ABSTRACT

Title of dissertation: COMPACT-RECONSTRUCTION WEIGHTED ESSENTIALLY NON-OSCILLATORY SCHEMES FOR HYPERBOLIC CONSERVATION LAWS

Debojyoti Ghosh, Doctor of Philosophy, 2012

Dissertation directed by: Professor James D. Baeder
Department of Aerospace Engineering

A new class of non-linear compact interpolation schemes is introduced in this dissertation that have a high spectral resolution and are non-oscillatory across discontinuities. The Compact-Reconstruction Weighted Essentially Non-Oscillatory (CRWENO) schemes use a solution-dependent combination of lower-order compact schemes to yield a high-order accurate, non-oscillatory scheme. Fifth-order accurate CRWENO schemes are constructed and their numerical properties are analyzed. These schemes have lower absolute errors and higher spectral resolution than the WENO scheme of the same order.

The schemes are applied to scalar conservation laws and the Euler equations of fluid dynamics. The order of convergence and the higher accuracy of the CRWENO schemes are verified for smooth solutions. Significant improvements are observed in the resolution of discontinuities and extrema as well as the preservation of flow features over large convection distances. The computational cost of the CRWENO schemes is assessed and the reduced error in the solution outweighs the additional expense of the implicit scheme, thus resulting in higher numerical

efficiency. This conclusion extends to the reconstruction of conserved and primitive variables for the Euler equations, but not to the characteristic-based reconstruction. Further improvements are observed in the accuracy and resolution of the schemes with alternative formulations for the non-linear weights.

The CRWENO schemes are integrated into a structured, finite-volume Navier-Stokes solver and applied to problems of practical relevance. Steady and unsteady flows around airfoils are solved to validate the scheme for curvi-linear grids, as well as overset grids with relative motion. The steady flow around a three-dimensional wing and the unsteady flow around a full-scale rotor are solved. It is observed that though lower-order schemes suffice for the accurate prediction of aerodynamic forces, the CRWENO scheme yields improved resolution of near-blade and wake flow features, including boundary and shear layers, and shed vortices. The high spectral resolution, coupled with the non-oscillatory behavior, indicate their suitability for the direct numerical simulation of compressible turbulent flows. Canonical flow problems – the decay of isotropic turbulence and the shock-turbulence interaction – are solved. The CRWENO schemes show an improved resolution of the higher wavenumbers and the small-length-scale flow features that are characteristic of turbulent flows.

Overall, the CRWENO schemes show significant improvements in resolving and preserving flow features over a large range of length scales due to the higher spectral resolution and lower dissipation and dispersion errors, compared to the WENO schemes. Thus, these schemes are a viable alternative for the numerical simulation of compressible, turbulent flows.

COMPACT-RECONSTRUCTION WEIGHTED ESSENTIALLY NON-OSCILLATORY SCHEMES FOR HYPERBOLIC CONSERVATION LAWS

by

Debojyoti Ghosh

Dissertation submitted to the Faculty of the Graduate School of the
University of Maryland, College Park in partial fulfillment
of the requirements for the degree of
Doctor of Philosophy
2012

Advisory Committee:
Dr. James D. Baeder, Chair/Adviser
Dr. Doron Levy
Dr. Anya Jones
Dr. Amir Riaz
Dr. James Duncan, Dean's Representative

Acknowledgments

Table of Contents

List of Tables

List of Figures

Chapter 1

Introduction

A large number of physical phenomena can be modeled using partial differential equations (PDEs) that are in the form of hyperbolic conservation laws. These phenomena are characterized by wave propagation or convective transport of quantities. The governing equations express the conservation of a quantity by equating its time derivative inside a control volume with the flux of that quantity through the boundary surfaces. Examples of such physical systems include compressible fluid dynamics, electromagnetics, and ideal plasma dynamics. The complexity of the governing equations and/or the physical domain makes an analytical solution impossible in engineering problems. Thus, a numerical solution is often sought where the equations are discretized in time and space. Numerical algorithms typically involve an interpolation or a reconstruction step where the solution is computed from discrete values to the desired accuracy. Hyperbolic PDEs admit discontinuities and sharp gradients in the solution and thus, interpolation schemes need to be modified to prevent spurious oscillations resulting from high-order polynomial interpolation. Several such schemes have been presented in the literature [1, 2] and applied to problems in fields such as fluid dynamics, electromagnetics and ideal magnetohydrodynamics.

The solutions to hyperbolic conservation laws are often characterized by a
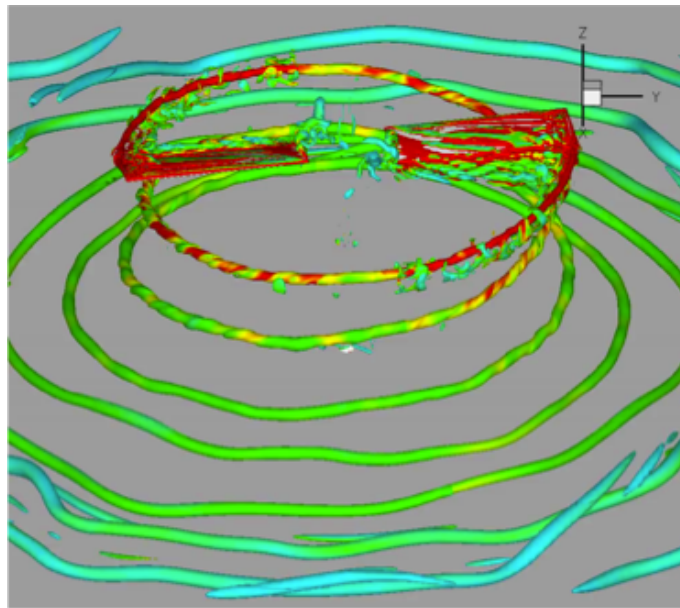
range of spatial and temporal scales. This dissertation focuses on numerical schemes for compressible gasdynamics, especially for flow problems that are characterized by a large range of length scales. Compressible flows are governed by the Navier-Stokes equations [3], which form a hyperbolic-parabolic system of equations. The simulation of turbulent flows requires the accurate resolution of small length scales of turbulent structures as well the characteristic length scales of the flow. Figure 1.1(a) shows the interaction of a shock wave with a turbulent flow field. Such an interaction results in the amplification of turbulence intensity downstream of the shock and a transfer of energy to smaller length scales. This canonical problem is representative of the interaction of shock waves with turbulent boundary layers. A numerical scheme with high spectral resolution is required to resolve all relevant length scales. In addition, the presence of a shock wave requires the scheme to be non-oscillatory across discontinuities.

Figure 1.1(b) shows the flow around a two-bladed rotor operating in ground effect. The wake flow is dominated by helical tip vortices shed from the rotor blades. Modeling of the wake flow requires the accurate resolution of these vortices as they convect over large distances and interact with each other as well as the ground plane. Thus, the length scales in the flow range from the rotor radius to the core radii of the tip vortices. In addition, flow on the advancing side of the rotor is highly compressible and may have local pockets of supersonic flows and shock structures, thus making it is essential for the numerical scheme to be non-oscillatory.

A new class of high-resolution, non-oscillatory numerical schemes is introduced

(a) Shock – turbulence interaction (retrieved from: *http://shocks.stanford.edu/image/M2_Mt015_eddies.jpg*)

(b) Numerical solution of the flow around a two-bladed rotor in ground effect (Kalra, Lakshminarayan & Baeder, American Helicopter Society 66th Annual Forum Proceedings, 2010)

Figure 1.1: Examples of flows requiring high-order accurate schemes with low dissipation errors and high spectral resolution

in this thesis, focusing on such problems. The numerical properties are analyzed

and demonstrated for simplified physical systems and then applied to flow problems

of practical relevance (in particular, to those referenced above). Although the ap-

plications presented in this study are particular to compressible gasdynamics, the

numerical schemes may be applied to other physical systems that are characterized

by a range of length scales.

1.1   Hyperbolic Conservation Laws

A hyperbolic conservation law in can be expressed in the differential form as

$$\frac{\partial \mathbf{u}}{\partial t} + \frac{\partial \mathbf{f_i}(\mathbf{u})}{\partial x_i} = 0 \qquad \text{in } \Omega; \quad i = 1, \dots, D \tag{1.1}$$

$$\mathbf{u}(\mathbf{x}, 0) = \mathbf{u}_0(\mathbf{x}) \qquad \text{for } x \in \Omega \tag{1.2}$$

$$\mathbf{u}(\mathbf{x}, t) = \mathbf{g}(\mathbf{x}, t) \qquad \text{for } x \in \Gamma \subset \partial\Omega \tag{1.3}$$

where $\mathbf{u} \in \mathbb{R}^n$ is the vector of conserved quantities, $\mathbf{f}_i(\mathbf{u})$ are the flux functions

in each space dimension i, D is the number of space dimensions, $\mathbf{u}_0$ is the initial

condition specified inside the domain Ω and $\mathbf{g}$ is the boundary condition, specified

over a subset of the boundary $\partial\Omega$. The system is hyperbolic if the flux Jacobian

$A = \partial \mathbf{F}/\partial \mathbf{x}$; $\mathbf{F} = \{\mathbf{f}_i\}$ is diagonalizable with all eigenvalues real. The eigenvalues

and the corresponding eigenvectors form the characteristic basis of the system that

defines the directions and speeds of wave propagation or advection of characteristic

quantities. Integrating Eqn. (1.1) over a control volume results in the integral form

of the equation, which is expressed as

$$\frac{\partial(\int_V \mathbf{u}dV)}{\partial t} + \int_S \mathbf{F}(\mathbf{u}).d\mathbf{S} = 0 \tag{1.4}$$

where V is the control volume and S is its boundary surface. The integral form demonstrates the conservation of the variable $\mathbf{u}$: any change (in time) of the volume-integrated quantity inside a control volume is equal to the total flux of that quantity through the boundary of the same control volume.

As an example, the linear advection equation is an example of a scalar, one-dimensional conservation law. It can be expressed as

$$u_t + au_x = 0 \tag{1.5}$$

where the flux function is given by $f(u) = a$. The solution is given by $u(x,t) = u_0(x - at)$ with $u_0(x) = u(x,0)$ as the initial condition, and represents a scalar wave advecting along the positive x-axis with speed a. The flux function is linear and thus, the solution is discontinuous if the initial condition u_0 is discontinuous. The inviscid Burgers' equation is an example of a scalar, non-linear conservation law. It can be expressed as

$$u_t + uu_x = 0; \quad u(x,0) = u_0(x) \tag{1.6}$$

where the flux function is given by $f(u) = u^2/2$. The solution is given by $u(x,t) = u_0(x - ut)$, which represents a wave with each point convecting at its local velocity. The flux function is non-linear and thus, discontinuities may develop even if the initial condition is smooth.

1.2 Numerical Solution

The numerical solution is obtained by discretizing Eqn. (1.1) or (1.4) in space and time to yield the finite difference or finite volume formulations respectively. As an example, a one-dimensional ($D = 1$) scalar conservation law is considered on a domain of unit length ($0 \le x \le 1$). The domain is represented by a grid with N points that are uniformly placed, as shown in Fig. 1.2. Discretizing the differential form of the conservation law in space, we get the semi-discrete equation as

$$\frac{du_j}{dt} + \frac{1}{\Delta x}\left(h_{j+1/2} - h_{j-1/2}\right) = 0 \tag{1.7}$$

where $u_j = u(x_j)$; $x_j = j\Delta x$ is the cell-centered value. The numerical flux function $h(x)$ is required to satisfy exactly

$$\left.\frac{\partial f}{\partial x}\right|_{x=x_j} = \frac{1}{\Delta x}[h(x_{j+1/2}, t) - h(x_{j-1/2}, t)] \tag{1.8}$$

and can thus be defined implicitly as

$$f(x) = \frac{1}{\Delta x}\int_{x-\Delta x/2}^{x+\Delta x/2} h(\xi)d\xi \tag{1.9}$$

Equation (1.7) represents a conservative finite difference formulation of Eqn. (1.1). The solution of this semi-discrete equation consists of two steps: *reconstruction* and *time marching*.

1.2.1 Reconstruction

The reconstruction step computes the solution at the interfaces from the cell-centered solution to the desired order of accuracy. An approximate flux function
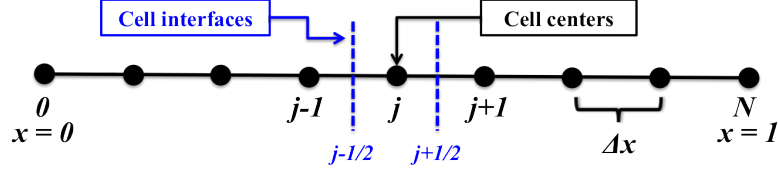
Figure 1.2: Schematic diagram illustrating the domain discretization.

$\hat{f}(x) \approx h(x)$ is found such that

$$
\begin{aligned}
\left.\frac{\partial f}{\partial x}\right|_{x=x_j} &= \frac{1}{\Delta x}\left(h_{j+1/2} - h_{j-1/2}\right) \\
&= \frac{1}{\Delta x}\left(\hat{f}_{j+1/2} - \hat{f}_{j-1/2}\right) + O(\Delta x^r)
\end{aligned}
\tag{1.10}
$$

where r is the desired order of the scheme. Thus, this step requires the interpolation of the approximate flux function $\hat{f}$ at the interfaces from neighboring cell-centered values $f_j = f(u_j)$. Several examples are presented below.

Two simple approximations of the interface flux can be expressed as

$$
\hat{f}^L_{j+1/2} = f_j \tag{1.11}
$$

$$
\hat{f}^R_{j+1/2} = f_{j+1} \tag{1.12}
$$

where the superscript denotes the stencil bias. These result in first-order left (L) and right (R) biased approximations of the first derivative, respectively:

$$
\left.\frac{\partial f}{\partial x}\right|^L_{x=x_j} = \frac{1}{\Delta x}\left(f_j - f_{j-1}\right) + O(\Delta x) \tag{1.13}
$$

$$
\left.\frac{\partial f}{\partial x}\right|^R_{x=x_j} = \frac{1}{\Delta x}\left(f_{j+1} - f_j\right) + O(\Delta x) \tag{1.14}
$$

Similarly, the interface flux can be approximated as

$$
\hat{f}^L_{j+1/2} = \frac{1}{2}\left(-f_{j-1} + 3f_j\right) \tag{1.15}
$$

$$
\hat{f}^C_{j+1/2} = \frac{1}{2}\left(f_j + f_{j+1}\right) \tag{1.16}
$$

$$
\hat{f}^R_{j+1/2} = \frac{1}{2}\left(3f_{j+1} - f_{j+2}\right) \tag{1.17}
$$

7

to yield second-order accurate left biased (L), central (C) and right biased (R) approximations of the first derivative, respectively:

$$\left.\frac{\partial f}{\partial x}\right|^{L}_{x=x_j} = \frac{1}{2\Delta x}\left(f_{j-2} - 4f_{j-1} + 3f_j\right) + O(\Delta x^2) \tag{1.18}$$

$$\left.\frac{\partial f}{\partial x}\right|^{C}_{x=x_j} = \frac{1}{2\Delta x}\left(f_{j+1} - f_{j-1}\right) + O(\Delta x^2) \tag{1.19}$$

$$\left.\frac{\partial f}{\partial x}\right|^{R}_{x=x_j} = \frac{1}{2\Delta x}\left(3f_{j+1} - 4f_{j+2} + f_{j+3}\right) + O(\Delta x^2) \tag{1.20}$$

Higher-order approximations to the flux derivative can be constructed along similar lines. Thus, interpolated values of the numerical flux function $\hat{f}$ are found at the interfaces such that the derivative of the flux function is approximated at the cell center to the desired accuracy using Eqn. (1.10).

The solution of a hyperbolic conservation law represents propagating waves or advection of quantities and the reconstruction step needs to respect the local directionality of advection or wave propagation through upwinding. At each interface, the eigenvalues and the eigenvectors of the flux Jacobian represent the characteristic speeds and directions. Thus, each eigenvalue and its corresponding eigenvector represent a wave with the eigenvalue as its propagation speed and the eigenvector as the direction in the variable space. The solution to the scalar conservation law comprises just one wave at each interface, with a propagation speed of $f'(u)$. As examples, the wave propagation speed for the linear advection equation, Eqn. (1.5), is a while for the inviscid Burgers' equation, Eqn. (1.6), the wave propagation speed is u. The wave nature of the solution is modeled through *upwinding* where the approximate flux function is interpolated using a biased stencil. This is illustrated as

follows:

$$\hat{f}_{j+1/2} = \hat{f}^L_{j+1/2} \text{ if } f'(u)_{j+1/2} > 0$$
$$= \hat{f}^R_{j+1/2} \text{ if } f'(u)_{j+1/2} < 0 \qquad (1.21)$$

The numerical flux at an interface is interpolated using a left-biased approximation if the wave speed is positive (i.e. traveling left to right) or a right-biased approximation if the wave speed is negative (i.e. traveling right to left). The left and right biased approximations, $\hat{f}^L_{j+1/2}$ and $\hat{f}^R_{j+1/2}$, are given by Eqns. (1.11) and (1.12) for a first-order accurate upwind scheme and by Eqns. (1.15) and (1.17) for a second-order accurate upwind scheme. The solution of a hyperbolic system of equations comprises multiple waves, each with its own characteristic speed. Thus, the flux at the interface is computed by decomposing it to its constituent waves and using an upwind approximation for each wave based on its wave speeds.

1.2.2 Time-Marching

Equation (1.7) can be rewritten as an ordinary differential equation (ODE) in time,

$$\frac{du}{dt} = L(u); \ L(u) = -\delta_x f(u); \ u(t=0) = u_0 \qquad (1.22)$$

where the $L(u)$ is the residual and $\delta_x f(u)$ is the finite difference approximation to the flux derivative computed in the previous section. The time interval for the numerical solution $[0, t_f]$ is discretized into T time steps with time step size as $\Delta t = t_f/T$. The time derivative term in Eqn. (1.22) is approximated by a finite difference discretization and the solution is evolved in time, starting with the initial

9

conditions u_0. A complete discussion of time-marching schemes is outside the scope of this thesis. However a few examples are presented of the time-marching schemes used in the present work.

A first-order explicit time marching (forward Euler) scheme is obtained by taking a backward-biased first-order discretization of the time derivative:

$$\frac{u^{n+1} - u^n}{\Delta t} = L(u^n) \tag{1.23}$$

where $u^n = u(n\Delta t)$ represents the solution at the n-th time level. Similarly, a first-order implicit (backward Euler) scheme is obtained by evaluating the residual at the new time level:

$$\frac{u^{n+1} - u^n}{\Delta t} = L(u^{n+1}) \tag{1.24}$$

The explicit scheme is conditionally stable, subject to time-step size restrictions but the implicit scheme is unconditionally stable.

High-order accurate time-marching schemes are used in algorithms with high-order spatial accuracy. The Runge-Kutta (RK) schemes are a family of multi-stage, high-order ODE solvers and the 3rd-order Total Variation Diminishing RK scheme (TVDRK3) [10] is used with high-order spatial reconstruction schemes in the present

study. The TVDRK3 scheme is given by:

$$
\begin{aligned}
v^{(0)} &= u^n \\
v^{(1)} &= v^{(0)} + \Delta t L(v^{(0)}) \\
v^{(2)} &= \frac{3}{4}v^{(0)} + \frac{1}{4}[v^{(1)} + \Delta t L(v^{(1)})] \\
v^{(3)} &= \frac{1}{3}v^{(0)} + \frac{2}{3}[v^{(2)} + \Delta t L(v^{(2)})] \\
u^{n+1} &= v^{(3)}
\end{aligned}
\tag{1.25}
$$

Since it is an explicit scheme, it has a time-step restriction and is not suitable for stiff problems. Stiff problems are cases where the time step size is restricted by stability requirements rather than accuracy. Implicit schemes are unconditionally stable. The second-order accurate Backward Differencing (BDF2) scheme, given by,

$$
\frac{3}{2}u^{n+1} - 2u^n + \frac{1}{2}u^{n-1} = \Delta t L(u^{n+1})
\tag{1.26}
$$

is used in this study for problems where the time step size of an explicit scheme is too restrictive.

1.3   ENO and WENO schemes

The solution of hyperbolic conservation laws may contain discontinuities (e.g. shock waves and contact discontinuities) and sharp transition layers. A numerical algorithm is required to capture the discontinuities without spurious oscillations as well as resolve smooth features of the solution with high-order accuracy. First-order numerical methods were proposed in the literature for problems in inviscid, compressible gasdynamics, such as the Godunov scheme [4] and the Roe scheme [5].

11

Though these schemes are monotonic across discontinuities, they are excessively dissipative resulting in smeared discontinuities and an inability to preserve smooth flow features. The basic structure of these schemes were used as building blocks for second-order accurate monotonic schemes such as the MUSCL scheme [6], the TVD scheme of Harten [7] and the Piecewise Parabolic Method (PPM) [8].

Second-order schemes provide better resolution of discontinuities and smooth solutions but higher-order accuracy is necessary to capture solutions that have discontinuities as well as complicated smooth features. Examples in fluid dynamics include turbulent eddies, vortical structures, acoustic waves, etc. and their interactions with each other as well as with shock waves. The high-order accurate Essentially Non-Oscillatory (ENO) scheme was introduced [9] for a finite-volume formulation and extended to a conservative finite difference formulation as well as systems of equations and multi-dimensional problems [10, 11]. The ENO schemes use an adaptive stenciling procedure that results in a non-oscillatory interpolation across discontinuities. As discussed in Section 1.2.1, a biased reconstruction of the flux at the interface is used to respect the wave-nature of the solution. Without loss of generality, if we consider the left-biased interpolation at a given interface, $\hat{f}^L_{j+1/2}$, there are r candidate interpolation stencils for an r-th order scheme, that contain the cell center left of the interface. For example, the two possible interpolation stencils for a second-order reconstruction of $\hat{f}^L_{j+1/2}$ are

$$\hat{f}^1_{j+1/2} = \frac{1}{2}\left(-f_{j-1} + 3f_j\right) \tag{1.27}$$

$$\hat{f}^2_{j+1/2} = \frac{1}{2}\left(f_j + f_{j+1}\right) \tag{1.28}$$

Similarly, the three candidate stencils for a third-order accurate reconstruction are:

$$\hat{f}_{j+1/2}^1 = \frac{1}{3}f_{j-2} - \frac{7}{6}f_{j-1} + \frac{11}{6}f_j \tag{1.29}$$

$$\hat{f}_{j+1/2}^2 = -\frac{1}{6}f_{j-1} + \frac{5}{6}f_j + \frac{1}{3}f_{j+1} \tag{1.30}$$

$$\hat{f}_{j+1/2}^3 = \frac{1}{3}f_j + \frac{5}{6}f_{j+1} - \frac{1}{6}f_{j+2} \tag{1.31}$$

The ENO scheme compares a hierarchy of undivided differences of the candidate stencils and chooses the one with the lowest magnitude. Stencils with discontinuities have higher undivided differences and the ENO procedure selects the smoothest amongst the candidate stencils to yield a non-oscillatory interpolation of the flux at the interface. Thus, using this stencil selection procedure, ENO schemes of the desired order of accuracy can be constructed.

The Weighted Essentially Non-Oscillatory (WENO) scheme was introduced [12] as an improvement over the ENO schemes by replacing the stencil selection by a weighted average of the candidate stencils. Smoothness-dependent weights are used such that they approach zero for candidate stencils with discontinuities. Thus, across discontinuities, the WENO schemes behave like the ENO schemes, while in smooth regions of the solution, the weighted average results in a higher-order approximation. The WENO schemes were extended to higher-order accuracy by defining improved smoothness indicators and applied to the finite difference formulation [13].

The underlying principle of the WENO schemes is the ability to combine lower-order interpolation schemes to get a higher-order scheme. For example, Eqns. (1.27) and (1.28) are two possible second-order accurate schemes. Multiplying them by $c_1 = 1/3$ and $c_2 = 2/3$ respectively and adding them, we get Eqn. (1.30), which

is a third-order accurate scheme. The WENO scheme calculates weights ω_1 and ω_2 that approach the optimal weights c_1 and c_2 respectively when the local solution is smooth, and approach zero when the local solution is discontinuous. To achieve this, the weights are defined as

$$\omega_k = \frac{\alpha_k}{\sum_k \alpha_k}; \ \alpha_k = \frac{c_k}{(\epsilon + \beta_k)^p}; \ i = 1, \ldots, r \tag{1.32}$$

where r is the order of candidate stencils ($r = 2$ in this example), ϵ is a small number to prevent division by zero, and β_k are the smoothness indicators of each candidate stencil. The optimal weights are divided by the smoothness indicators such that stencils containing discontinuities (and having a larger value of the smoothness indicator) have weights approaching zero. Extending the smoothness measurements of the ENO schemes, the WENO scheme in [12] used smoothness indicators based on undivided differences:

$$\beta_k = \sum_{l=1}^{r-1} \sum_{i=1}^{r-l} \frac{(f[j+i+k-r,l])^2}{r-l} \tag{1.33}$$

where $f[.,l]$ is the l-th undivided difference. For $r = 2$, the smoothness indicators are

$$\beta_1 = (f_j - f_{j-1})^2$$

$$\beta_2 = (f_{j+1} - f_j)^2 \tag{1.34}$$

Thus, the 3rd-order WENO scheme (WENO3) can be summarized as follows:

$$\hat{f}_{j+1/2}^L = \omega_1 \hat{f}_{j+1/2}^1 + \omega_2 \hat{f}_{j+1/2}^2 \tag{1.35}$$

where $\hat{f}_{j+1/2}^1$ and $\hat{f}_{j+1/2}^2$ are defined by Eqns. (1.27) and (1.28), and the weights ω_1 and ω_2 are defined by Eqns. (1.32) and (1.34). This results in a scheme that

14

is third-order accurate in smooth regions of the solution and non-oscillatory across discontinuities.

An improved smoothness indicator was introduced in [13] that is based on the L_2 norm of the derivatives of the interpolating polynomial:

$$\beta_k = \sum_{l=1}^{r-1} \int_{x_{j-1/2}}^{x_{j+1/2}} \Delta x^{2l-1} (q_k^{(l)})^2 dx \tag{1.36}$$

where $q_k^{(l)}$ is the l-th derivative of the interpolating polynomial $q_k(x)$ on the k-th candidate stencil. While the smoothness indicator of [12] allowed for the construction of a $(r+1)$-th order WENO scheme from r-th order candidate stencils, the smoothness indicators of [13] yield a $(2r-1)$-th order WENO scheme. The fifth-order WENO scheme (WENO5) $(r=3)$ was constructed in [13] based on the improved smoothness indicators and it can be expressed as:

$$\hat{f}_{j+1/2}^{L} = \omega_1 \hat{f}_{j+1/2}^{1} + \omega_2 \hat{f}_{j+1/2}^{2} + \omega_3 \hat{f}_{j+1/2}^{3} \tag{1.37}$$

where the three candidate third-order schemes $\hat{f}_{j+1/2}^{1,2,3}$ are given by Eqns. (1.29) to (1.31). The optimal coefficients are $c_1 = 1/10$, $c_2 = 6/10$, and $c_3 = 3/10$ respectively that result in the fifth-order scheme:

$$\hat{f}_{j+1/2}^{L} = \frac{1}{30} f_{j-2} - \frac{13}{60} f_{j-1} + \frac{47}{60} f_j + \frac{27}{60} f_{j+1} - \frac{1}{20} f_{j+2}$$

The weights are computed using Eqn. (1.32) and the smoothness indicators, given by Eqn. (1.36), are

$$\beta_1 = \frac{13}{12}(f_{j-2} - 2f_{j-1} + f_j)^2 + \frac{1}{4}(f_{j-2} - 4f_{j-1} + 3f_j)^2 \tag{1.38}$$

$$\beta_2 = \frac{13}{12}(f_{j-1} - 2f_j + f_{j+1})^2 + \frac{1}{4}(f_{j-1} - f_{j+1})^2 \tag{1.39}$$

$$\beta_3 = \frac{13}{12}(f_j - 2f_{j+1} + f_{j+2})^2 + \frac{1}{4}(3f_j - 4f_{j+1} + f_{j+2})^2 \tag{1.40}$$

15

The final form of the WENO5 scheme can be expressed as

$$\hat{f}^L_{j+1/2} = \frac{\omega_1}{3} f_{j-2} - \frac{1}{6}(7\omega_1 + \omega_2)f_{j-1} + \frac{1}{6}(11\omega_1 + 5\omega_2 + 2\omega_3)f_j$$
$$+ \frac{1}{6}(2\omega_2 + 5\omega_3)f_{j+1} - \frac{\omega_3}{6} f_{j+2} \qquad (1.41)$$

At smooth regions of the solution, the weights ω attain their optimal values c and Eqn. (1.41) is identical to Eqn. (1.38). At discontinuities, weights corresponding to the stencils containing the discontinuity tend to zero and the scheme behaves like a third-order ENO scheme.

In general, a $(2r - 1)$-th order WENO scheme can be constructed from r candidate interpolation schemes of r-th order accuracy. The interface flux is given by (omitting the superscript L or R):

$$\hat{f}_{j+1/2} = \sum_{k=1}^{r} \omega_k \hat{f}^k_{j+1/2} \qquad (1.42)$$

where $f^k_{j+1/2}$ is the interpolated flux at $x_{j+1/2}$ using the k-th candidate stencil and ω_k is the weight of k-th stencil in the convex combination. The weights are computed by Eqns. (1.32) and (1.36). The resulting scheme is $(2r-1)$-th order accurate in smooth regions of the solution and non-oscillatory near discontinuities. WENO schemes of very high-order accuracy ($r = 4, 5, 6$) have been constructed and presented in [14]. The development of the ENO and WENO schemes, and their application to systems of equations and multi-dimensional problems are summarized in [15].

1.3.1   Implementation of Non-Linear Weights

There have been several numerical issues with the way the non-linear weights have been defined by [13]. One such issue has been the debate regarding the role

of ϵ in Eqn. (1.32), which was introduced to prevent division by zero and set to 10^{-6} in [13]. Ideally, the numerical scheme should be insensitive to the value of ϵ. However, it was demonstrated in [16] that the WENO schemes show sub-optimal convergence for certain types of smooth problems and the order of convergence is dependent on the value of ϵ. For smooth problems that contain critical points (at which the first and higher derivatives vanish), the weights become sensitive to ϵ. A lower value of epsilon, e.g. 10^{-20} or 10^{-40} prevents the weights from attaining their optimal values, even though the solution is smooth. Thus, the scheme shows a sub-optimal rate of convergence. In addition, the non-optimal weights also reduce the accuracy and resolution, thus showing excessive dissipation for smooth solution features.

Several attempts have been presented in literature that improve the behavior of the WENO schemes for such cases. A mapping of the weights has been proposed [16] that causes the WENO weights to converge faster to their optimal values, defined by the function

$$g_k(\omega) = \frac{\omega(c_k + c_k^2 - 3c_k\omega + \omega^2)}{c_k^2 + \omega(1 - 2c_k)} \tag{1.43}$$

The mapped weights are given by

$$\alpha_k^M = g_k(\omega_k) \tag{1.44}$$

that are then normalized for convexity to give the mapped WENO weights. The WENO scheme with the mapped weights recovers the optimal order of convergence for smooth problems with critical points. The primary drawback of the mapping is the additional computational cost of the mapping function. Alternative formulations

17

for the weights have been suggested in the literature [17, 18, 19, 20] that have the same benefits as the mapping function without the additional expense. The weights are defined as

$$\alpha_k = c_k \left[1 + \left(\frac{\tau}{\epsilon + \beta_k} \right)^p \right] \tag{1.45}$$

The factor, τ, is initially defined as the absolute difference between the left-most and right-most smoothness indicators for a fifth-order scheme in [17] and later improved for higher-order schemes in [18]. The energy-stable WENO schemes [19, 20] define it as the square of the undivided difference of the appropriate order.

The value of ϵ has an effect on whether the WENO scheme tends towards the optimal higher-order central scheme or the adaptive lower-order ENO scheme. A higher value of ϵ biases the scheme towards the higher-order central scheme because higher magnitudes of β_k are required to dominate the denominator of Eqn. (1.32) and thus, scale the weight away from its optimal value. A lower value of ϵ biases the scheme towards the lower-order ENO scheme because the weights are sensitive to smaller values of the smoothness indicators. A variable-ϵ WENO scheme was proposed in [21] where the value of ϵ is solution-dependent. The ϵ at each interface is taken as

$$\epsilon = \epsilon_{max} \min \left(1, \frac{\min_k \beta_k}{\max_k \beta_k - \min_k \beta_k + \epsilon_{min}} \right) + \epsilon_{min} \tag{1.46}$$

where ϵ_{max} and ϵ_{min} are the upper and lower bounds (10^{-6} and 10^{-99}, respectively, in their implementation). Thus, a high value of ϵ is used for smooth regions of the solution, biasing the scheme towards a higher-order central scheme, and a low value of ϵ is used near discontinuities, biasing the scheme towards the ENO scheme.

These modifications to the WENO schemes have improved the accuracy and resolution for solutions with complicated but smooth features while preserving the non-oscillatory behavior across discontinuities. The WENO schemes have been extensively applied to several problems in compressible fluid dynamics that involve smooth flow features as well as shock waves. In addition, they have been applied to a wide range of engineering fields such as electromagnetics, astrophysics, semiconductor physics, and computational biology as well as non-PDE applications such as image processing. A review of the applications of the WENO schemes can be found in [22] and references therein.

1.4   Compact Schemes

Several engineering problems are characterized by a large range of length and time scales. The numerical solution of such problems requires the accurate modeling of all relevant scales. Spectral methods [23, 24] are a class of methods that capture the required range of scales exactly. However, these methods are restricted to problems on simple domains with periodic boundary conditions. Conventional finite difference schemes, including the higher-order ENO/WENO schemes described in the previous section, lack the spectral resolution to model higher wavenumbers on a given grid. Very fine grids are required to model such problems accurately such that all the relevant scales are represented. A new class of finite difference schemes was introduced [25] that have significantly higher spectral resolution. The schemes are formulated using the finite difference formulation and thus, can be applied to a

complicated domains as well as non-periodic boundary conditions.

Finite difference approximations to the first derivative of the flux function are linear combinations of the neighboring cell-centered values. Examples include the first and second-order accurate approximations given by Eqns. (1.13), (1.14), and (1.18) - (1.20). Compact schemes use a coupled formulation to compute the approximations to the derivatives such that the approximate flux derivative at a given cell center is dependent on those at neighboring cell centers. A general form of such schemes [25] can be expressed as:

$$
\begin{aligned}
\beta \hat{f}_{x,j-2} + \alpha \hat{f}_{x,j-1} \quad + \quad & \hat{f}_{x,j} + \alpha \hat{f}_{x,j+1} + \beta \hat{f}_{x,j+2} \\
= \quad & a \frac{f_{j+1} - f_{j-1}}{2\Delta x} + b \frac{f_{j+2} - f_{j-2}}{4\Delta x} + c \frac{f_{j+3} - f_{j-3}}{6\Delta x} \quad (1.47)
\end{aligned}
$$

where $\hat{f}_x$ is the finite difference approximation to the first derivative of the flux function f_x. Taylor series analysis yields constraints on the parameters that determine the order of accuracy for these schemes and these constraints are:

$$a + b + c = 1 + 2\alpha + 2\beta \qquad \text{Second order} \qquad (1.48)$$

$$a + 2^2 b + 3^2 c = 2 \frac{3!}{2!} (\alpha + 2^2 \beta) \qquad \text{Fourth order} \qquad (1.49)$$

$$a + 2^4 b + 3^4 c = 2 \frac{5!}{4!} (\alpha + 2^4 \beta) \qquad \text{Sixth order} \qquad (1.50)$$

$$a + 2^6 b + 3^6 c = 2 \frac{7!}{6!} (\alpha + 2^6 \beta) \qquad \text{Eighth order} \qquad (1.51)$$

$$a + 2^8 b + 3^8 c = 2 \frac{9!}{8!} (\alpha + 2^8 \beta) \qquad \text{Tenth order} \qquad (1.52)$$

Thus, we get a four-parameter family of second-order schemes, a three-parameter family of fourth-order schemes, a two-parameter family of sixth-order schemes, a one-parameter family of eighth-order schemes and a single tenth-order scheme. The

20

result is a system of equations for the unknown derivative values that is penta-diagonal for $\alpha, \beta \neq 0$ and tri-diagonal for $\alpha \neq 0, \beta = 0$. The schemes revert to the conventional non-compact schemes with $\alpha = \beta = 0$. The sparse nature of the system of equations allows a solution with $O(N)$ computational complexity.

To understand the advantages of a compact interpolation scheme for numerical solutions involving a large range of length scales, the spectral resolution of the compact schemes is compared with that of non-compact schemes. Assuming the flux function to be a periodic sinusoidal wave over a domain of unit length,

$$f(x) = e^{2\pi i k x} = e^{2\pi i k (j\Delta x)} \tag{1.53}$$

the phase error in the finite difference approximation of the flux derivative given by Eqn. (1.47) is given by
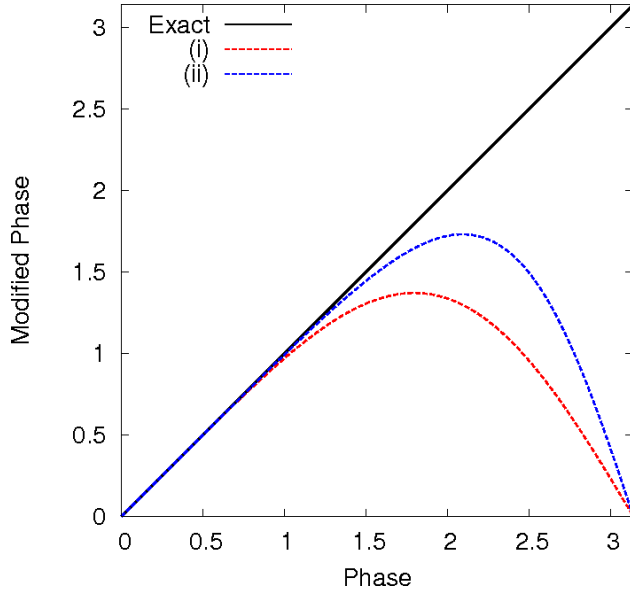
$$k'\Delta x = \frac{a \sin(k\Delta x) + \frac{b}{2}\sin(2k\Delta x) + \frac{c}{3}\sin(3k\Delta x)}{1 + 2\alpha \cos(k\Delta x) + 2\beta \cos(2k\Delta x)} \tag{1.54}$$

The spectral resolutions of fourth and sixth-order schemes are considered as examples. Fourth-order schemes can be constructed from Eqn. (1.47) with the constraint given by Eqns. (1.48) and (1.49). The non-compact fourth-order central scheme is obtained by $a = 4/3, b = -1/3, c = \alpha = \beta = 0$:
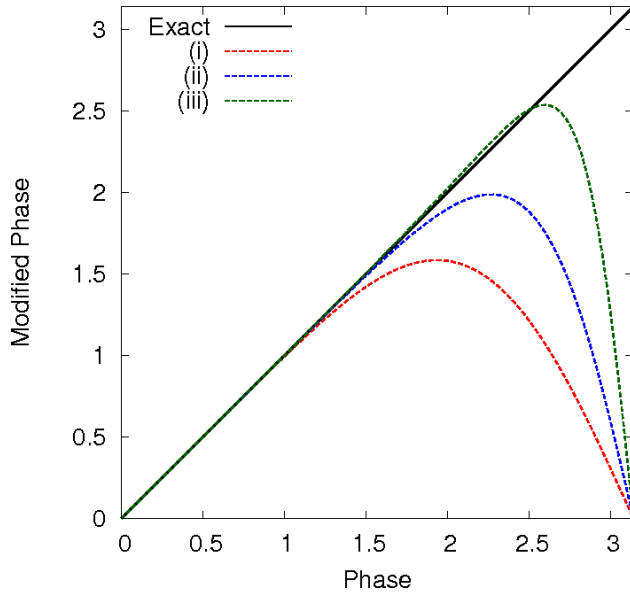
$$\hat{f}_{x,j} = \frac{f_{j-2} - 8f_{j-1} + 8f_{j+1} - f_{j+2}}{12\Delta x} \tag{1.55}$$

A compact fourth-order scheme approximation is obtained by $\alpha = 1/4, \beta = 0, a = 3/2, b = c = 0$:

$$\frac{1}{4}\hat{f}_{x,j-1} + \hat{f}_{x,j} + \frac{1}{4}\hat{f}_{x,j+1} = \frac{3(f_{j+1} - f_{j-1})}{4\Delta x} \tag{1.56}$$

21

(a) Fourth-order schemes: (i) Non-compact central Eqn. (1.55), (ii) Compact (tridiagonal) Eqn. (1.56)

(b) Sixth-order schemes: (i) Non-compact central Eqn. (1.57), (ii) Compact (tridiagonal) Eqn. (1.58) (iii) Compact (pentadiagonal) Eqn. (1.59)

Figure 1.3: Spectral resolutions for compact and non-compact schemes

that results in a tridiagonal system of equations. Figure 1.3(a) shows the modified phase as a function of the actual phase for the two schemes. Although both schemes are of fourth-order accuracy, the compact scheme is able to resolve a larger range of

wavenumbers than the non-compact scheme.

Sixth-order accurate interpolation schemes can be constructed from Eqn. (1.47) by using the constraints given by Eqns. (1.48) to (1.50). The non-compact sixth-order central scheme is obtained by taking $\alpha = \beta = 0, a = 3/2, b = -3/5, c = 1/10$:

$$\hat{f}_{x,j} = \frac{3(f_{j+1} - f_{j-1})}{4\Delta x} - \frac{3(f_{j+2} - f_{j-2})}{20\Delta x} + \frac{f_{j+3} - f_{j-3}}{60\Delta x} \qquad (1.57)$$

A sixth-order compact scheme that results in a tridiagonal system can be obtained by taking $\alpha = 1/3, \beta = 0, a = 14/9, b = 1/9, c = 0$:

$$\frac{1}{3}\hat{f}_{x,j-1} + \hat{f}_{x,j} + \frac{1}{3}\hat{f}_{x,j+1} = \frac{14(f_{j+1} - f_{j-1})}{9\Delta x} + b\frac{f_{j+2} - f_{j-2}}{36\Delta x} \qquad (1.58)$$

and a penta-diagonal sixth-order compact scheme can be constructed by taking $\alpha = 1/2, \beta = 1/24, a = 13/9, b = 23/36, c = 0$:

$$\frac{1}{24}\hat{f}_{x,j-2} + \frac{1}{2}\hat{f}_{x,j-1} + \hat{f}_{x,j} + \frac{1}{2}\hat{f}_{x,j+1} + \frac{1}{24}\hat{f}_{x,j+2}$$
$$= \frac{13(f_{j+1} - f_{j-1})}{18\Delta x} + \frac{23(f_{j+2} - f_{j-2})}{144\Delta x} \qquad (1.59)$$

The modified phase due to the finite difference approximation as a function of the actual phase is shown in Fig. 1.3(b). The compact schemes resolve a larger range of wavenumbers compared to the non-compact scheme and the penta-diagonal scheme has a higher spectral resolution than the tri-diagonal scheme.

These schemes have been applied to the simulation of incompressible [26, 27] and compressible [28, 29] flows as well as to computational aeroacoustics [29, 30] and electromagnetics [31]. The improved resolution of compact schemes has resulted in their application to direct numerical simulation (DNS) and large-eddy simulation (LES) of turbulent flows [32, 33]. The compact schemes, originally formulated for

finite differences on a uniform grid, have been extended to the finite volume formulation [34, 35] and non-uniform grids [36, 37, 38]. Linear compact schemes yield oscillatory solutions for discontinuities, such as shock waves and contact discontinuities, and thus a limiter is needed to ensure non-oscillatory behavior. A non-linearly stable compact scheme with a total variation bounded (TVB) limiter was introduced [39] for shock calculations and further improved [40].

1.5   Motivation

The numerical solution of several complex physical systems is challenging due to the presence of a large range of length and time scales. One such example is compressible, turbulent fluid dynamics where the length scales range from very fine turbulent eddies to the characteristic length of the flow. Accurate modeling of the convection and interaction of the turbulent eddies is required for the prediction of the flowfield as well derived characteristics such as aerodynamics forces and sound generation. Supersonic compressible flows contain shock waves while subsonic, high-speed turbulent flows may have local pockets of supersonic flows resulting in shocklets. In addition, such flows are characterized by thin boundary and shear layers near solid walls and mixing of jets, where the flow has steep gradients.

The motivation of this thesis is to develop a high-order accurate algorithm for such problems. One of the application areas is the accurate simulation of the wake flow around aircraft and rotorcraft. Although lower-order numerical schemes are sufficient to predict the aerodynamic forces, a high-order accurate scheme is

necessary to resolve the wake flow. Accurate modeling of the interaction of wake vortices with each other, the fuselage (if present), and the ground plane (for rotor-craft operating in ground effect) requires the preservation of vortex strength and shape over large convection distances and on relatively coarse grids (such that the computational cost of the simulations is not too large). Thus, a numerical scheme with very low dissipation and dispersion errors is desirable.

Another application area focussed on in this thesis is the direct numerical simulation of turbulent flows. Such simulations do not employ a turbulence model to account for the effect of scales that are not well-resolved. Thus, it is essential to accurately resolve the small-length-scale turbulent eddies in the flow. The numerical solution of such flows requires a numerical scheme with a high spectral resolution. In addition, a non-oscillatory interpolation is required to resolve high-gradients and discontinuities that develop in compressible flows.

As discussed in previous sections, compact schemes are a family of interpolation schemes that are characterized by high spectral resolution. They capture accurately a larger range of length scales compared to the non-compact schemes of the same order of convergence. However, these schemes, in their original form cannot handle discontinuities and need some form of modification to ensure non-oscillatory interpolation for discontinuous solutions. The WENO schemes, on the other hand, have been successfully applied to a large number of problems containing discontinuities. The adaptive stenciling algorithm yields solutions that high-order accurate in smooth regions and non-oscillatory across discontinuities. This has led to their application to problems that contain complex smooth features as well as

steep gradients and discontinuities. However, the spectral resolution of the underlying high-order accurate interpolation scheme compare poorly to that of the compact schemes. As a result, the WENO schemes are excessively dissipative at smaller length scales and require a very fine mesh for the accurate representation of such flow features. Thus, a high-resolution non-oscillatory algorithm is developed in this thesis that combines the advantages of the compact schemes with those of the WENO schemes.

1.6 Review of Previous Work

There have been several attempts in the literature to combine the ENO/WENO schemes with compact schemes, with a similar motivation as described in the previous section. One such class of schemes is the hybrid compact-ENO/WENO schemes where the smoothness of the solution is used to switch between the compact scheme and the ENO or WENO scheme. A hybrid compact-ENO scheme was introduced in [41] where asymetric coefficients were used for the compact scheme to provide the necessary dissipation for upwinding (unlike in [25], where symmetric coefficients resulted in central schemes with no dissipation). Two types of compact schemes were introduced, requiring the inversion of penta-diagonal matrices. A discontinuity detector is used to identify grid cells (along with a buffer region) where a discontinuity is present. The ENO scheme is used to calculate the flux derivatives at these cells. A first-order discontinuity detector is used where the slopes of the flux function are compared. The grid cells are identified as containing discontinuous data if the

magnitude of the slope exceeds a threshold value or attains a local maximum. The hybrid compact-ENO scheme was used for the direct numerical simulation of turbulent flow over a compression ramp [42]. This concept was further improved in [43] where a hybrid compact-WENO scheme was developed. The WENO scheme is used at cells where discontinuities are present since it provides higher-order accuracy with the same complexity as the ENO scheme. In addition, the compact scheme is formulated in the conservative form that improves the coupling with the shock-capturing WENO scheme. The coupling between a non-conservative compact scheme and a shock-capturing ENO scheme results in the generation of spurious waves in [41]. A tridiagonal compact scheme is used in [43] that reduces the numerical cost of matrix inversion. A characteristic-based compact-WENO hybrid scheme was presented in [44] where the interpolation is carried out on the characteristic variables with a Roe-type upwinding. A characteristic-based reconstruction reduces the smearing of the discontinuities, compared to the previous hybrid schemes that use the Lax-Friedrichs flux-splitting. However, this results in a block-tridiagonal system of equations and is thus, computationally more expensive. The hybrid scheme of [44] also uses a weighted average of the fluxes computed by the compact and WENO schemes. This results in a smooth transition between the two schemes, instead of an abrupt switch. The smoothness-based weighting function is a continuous function of the slope of the flux function.

One of the primary drawbacks of the hybrid schemes is that they revert to a non-compact scheme at and around discontinuities (depending on the size of the buffer region). This results in a loss of spectral resolution as well as higher dissi-

pative errors at these cells. These errors propagate to the rest of the domain as the simulation proceeds in time. The loss of resolution undermines the benefits of using a compact scheme even more so in problems involving the interaction of small-length-scale features with the discontinuities. In addition, hybrid schemes require a discontinuity detector to switch between the two schemes and this introduces an arbitrary parameter in the scheme. The switching mechanism in [41, 43] based on the slope magnitudes exceeding a certain specified threshold value and this value is likely to significantly affect the performance of the scheme for solutions involving discontinuities and waves of very small length scales.

An alternative way of implementing non-linear compact schemes with ENO adaptive stenciling was presented in [45]. The basic formulation is based on Eqn. (1.47) but on a staggered mesh, where the flux values on the right hand side are specified at the interfaces while the derivatives on the left hand side are evaluated at the cell centers. This can be expressed as:

$$\alpha \hat{f}_{x,j-1} + \hat{f}_{x,j} + \alpha \hat{f}_{x,j+1} = a \frac{f_{j+1/2} - f_{j-1/2}}{\Delta x} \tag{1.60}$$

that results in a tridiagonal scheme. Compact finite difference approximations on a staggered mesh are discussed in [25] and it is observed that they have a significantly higher spectral resolution. Thus, the algorithm presented in [45] requires a two-stage reconstruction step where the flux at the interfaces is computed and then used for the computation of the derivatives. The flux at the interfaces is interpolated in a non-oscillatory manner by using an adaptive compact scheme. Candidate compact interpolation schemes are identified for each interface and a smoothness indicator

based on the first and second undivided differences is used to choose the smoothest scheme. When a discontinuity is present, a biased (away from the discontinuity) bidiagonal compact scheme is used while for smooth data, a tridiagonal compact scheme is used. This results in a decoupling of the interpolation at the discontinuities, thus avoiding spurious oscillations. Third and fourth-order schemes were presented for the interface flux calculation and the first derivatives are calculated using Eqn. (1.60) to fourth-order accuracy.

The non-linear compact schemes presented in [45] were further improved in [46]. The basic formulation is identical to Eqn. (1.60) for a fourth-order approximation for the first derivative and has additional terms on the right hand side for a fifth-order approximation. However, one of the major drawbacks in the schemes implemented in [45] was the requirement of three tridiagonal inversions while calculating the flux at the interfaces. The other drawback, which is characteristic of ENO schemes, is that data from only one of the several candidate stencils is used although computations are done for all. Thus, the schemes presented in [46] use the non-compact WENO schemes to compute the interface flux. In addition, a characteristic reconstruction is used for a more robust scheme. Since the characteristic reconstruction is computationally more expensive, a density-based criterion is used to switch between a characteristic reconstruction and a component-wise reconstruction. A Fourier analysis of these schemes was presented and it was observed that the spectral resolutions of these schemes are only marginally higher than a non-compact upwind interpolation scheme of the same order. Although the staggered compact approximation to the first derivative has a very high spectral resolution,

a non-compact interpolation of the terms on the right hand side of Eqn. (1.60) compromises the spectral resolution of the overall scheme. A similar algorithm was presented in [47] where the flux was interpolated directly instead of the conserved variable. An ENO-Padé scheme was presented in [48] that uses Eqn. (1.60) as the basic formulation, but with additional terms on the right hand side to achieve sixth-order accuracy. The interpolation of the interface fluxes on the right hand side is carried out using a modified ENO scheme. The stencil selection procedure of the ENO scheme is biased towards a preferred, central stencil such that a biased stencil is chosen only when gradients are substantially large. The aim of this biasing is to improve the performance of the ENO scheme for problems with large, but continuous, gradients. As with the schemes presented in [46, 47], the spectral resolution of this scheme is only marginally better than non-compact schemes because a non-compact scheme is used for the interpolation of interface fluxes.

A weighted compact scheme, based on a conservative finite difference approximation of the first derivative, was constructed in [49]. The final compact scheme is a weighted combination of lower-order compact interpolation schemes. In their implementation, the candidate stencils are two biased third-order compact stencils and a central fourth-order compact stencil. The optimal interpolation, for smooth solutions, is a sixth-order central compact interpolation. While the work is a novel attempt at a non-oscillatory scheme, there are a few drawbacks. The underlying scheme, being central (and without additional dissipation), lacks the upwinding necessary to yield robust solutions to the Euler equations. The smoothness indicators that are used are the same as those of Jiang and Shu [13] and are designed

for third-order non-compact stencils. Their application to a fourth-order central stencil may not be correct. The extension of the scalar interpolation techniques to vector quantities is unclear in their study and it is not discussed if their schemes are implemented in the characteristic space. It is well known that a characteristic reconstruction is necessary to yield non-oscillatory solutions for inviscid flow problems. These drawbacks resulted in limited applicability of their algorithm to the Euler system.

1.7 Objectives

The aim of this thesis is to develop a high-resolution, non-oscillatory scheme by applying the WENO algorithm to compact schemes. As discussed in Section 1.3, the WENO schemes use a solution-dependent algorithm to yield high-order accuracy when the solution is smooth and non-oscillatory interpolation across discontinuities. Lower-order interpolation schemes are identified and optimal weights are calculated such that the weighted sum is a higher-order scheme. The WENO weights are calculated from the optimal weights based on the smoothness of each of the lower-order interpolation stencils. The final scheme is high-order accurate in smooth regions of the solution and non-oscillatory across discontinuities. This algorithm is applied to compact interpolation schemes in this study with the aim that the resulting scheme will have the high-spectral resolution of a high-order accurate compact scheme and yield non-oscillatory solutions across discontinuities due to the solution-dependent stencil selection.

The objectives of this thesis can be summarized as follows:

- Development of the Compact-Reconstruction WENO (CRWENO) schemes (Chapter 2)

  – Formulation of the CRWENO schemes by identifying lower-order compact interpolation schemes, calculating the optimal coefficients such their weighted sum is a high-order accurate compact scheme, and application of the WENO weights to derive the final scheme.

  – Numerical analysis of the underlying optimal compact schemes and comparison of the numerical error and spectral properties with the non-compact WENO schemes as well as other high-resolutions schemes in the literature.

  – Application to smooth and non-smooth solutions of scalar conservation laws to verify accuracy, order of convergence and resolution of extrema and discontinuities; as well as analysis of computational efficiency of the new schemes.

  – Formulation and numerical analysis of various boundary treatments for aperiodic domains.

  – Comparison of the alternative formulations of the non-linear weights in the context of the CRWENO schemes.

- Application of the CRWENO schemes to the Euler equations (Chapter 3)

  – Extension of the scalar CRWENO schemes to vector quantities through

the reconstruction of conserved, primitive and characteristic variables; and an analysis of algorithm accuracy and robustness as well as computational cost for each of these approaches.

– Application of benchmark inviscid flow problems (smooth and non-smooth) and verification of accuracy, order of convergence and resolution of various flow features (shocks, vortices, small length-scale waves, etc).

- Integration with a structured, finite-volume, compressible Navier-Stokes flow solver with overset mesh capability (Chapter 4)

    – Validation and application to two-dimensional steady and unsteady flow around airfoils and three-dimensional flow around wings and rotors; as well as comparison of the resolution of near-blade and wake flow features with the non-compact WENO scheme.

    – Application to the direct numerical simulation (DNS) of benchmark turbulent flow problems – decay of isotropic, homegenous turbulence and the shock-turbulence interaction; and the demonstration of the improved spectral resolution of the new scheme for these problems

Chapter 2

Non-Linear Compact Schemes

In this chapter, the development and implementation of the Compact - Reconstruction Weighted Essentially Non-Oscillatory (CRWENO) schemes are described, with the specific example of the fifth-order CRWENO scheme. The resolution characteristics of the new schemes are analyzed and compared to the WENO schemes of the same order of accuracy. Solutions to the scalar conservation laws are obtained using the CRWENO and WENO schemes and the performance of the new schemes is demonstrated. The compact schemes involve a coupling of the interpolated flux function at each grid point and thus, they require the solution to a system of equations at each step. The computational expense of this scheme is studied and compared to that WENO scheme for solutions with comparable accuracy and resolution.

2.1 Overview of the CRWENO Scheme

The numerical solution of a hyperbolic PDE was described in Section 1.2. A conservative discretization requires the approximation of the primitive function $h(x)$ that satisfies Eqn. (1.9). Thus, the approximate flux function $\hat{f}$ is constructed such that, at each interface, it satisfies

$$\hat{f}(x_{j+1/2}) = h(x_{j+1/2}) + O(\Delta x^r) \tag{2.1}$$
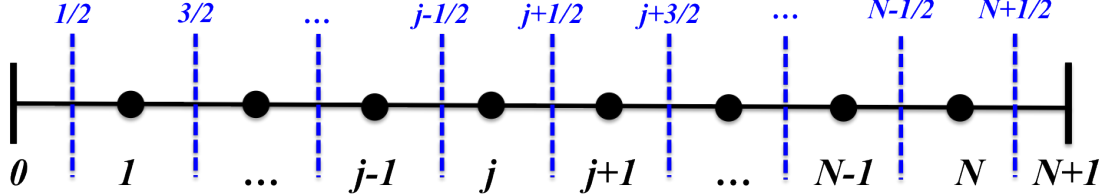
Figure 2.1: One-dimensional domain discretization showing interfaces and cell centers: Points 0 and $N+1$ correspond to boundaries

where r is the desired order of accuracy. The values of the approximate flux function at the interfaces are interpolated from the cell-centered values of the flux function $f(u)$ at neighboring cell centers.

The derivation of conservative compact schemes is described in [43]. Figure 2.1 shows a discretized one-dimensional domain with N cell-centers and $N+1$ interfaces. The boundary points are at $j = 0$ and $j = N + 1$. A general conservative compact approximation of the numerical flux at the interface can be expressed as

$$A\left(\hat{f}_{j+1/2-m}, \ldots, \hat{f}_{j+1/2}, \ldots, \hat{f}_{j+1/2+m}\right) = B\left(f_{j-n}, \ldots, f_j, \ldots, f_{j+n}\right) \qquad (2.2)$$

where the stencil operators A and B denote a linear combination of the terms inside the parentheses and the indices m and n control the width of the stencil operators. Although the equation above represents symmetric stencils on both the left and right hand sides, an asymmetric stencil can be represented in this form by setting some of the coefficients in A and B to zero. The above equation may also be represented in matrix form as

$$A\hat{\mathbf{f}} = B\mathbf{f} \qquad (2.3)$$

where $\hat{\mathbf{f}} = \left[\hat{f}_{1/2}, \ldots, \hat{f}_{N+1/2}\right]^T$ and $\mathbf{f} = [f_1, \ldots, f_N]^T$. It should be noted here that A is a $(N+1) \times (N+1)$ matrix while B is a $(N+1) \times N$ matrix. The computation of

the numerical flux at the interfaces requires the solution of this system of equations. Although the solution to a linear system is required, compact schemes that have been presented in the literature are usually tridiagonal ($m = 1$) or pentadiagonal ($m = 2$) systems and the computational complexity of solving such a system is $O(N)$. A non-compact scheme can be represented by Equation (2.2) by setting $m = 0$ which results in A in Equation (2.3) being the identity matrix.

The application of a linear compact scheme, given by Eqn. (2.2), to discontinuous functions results in a coupling of the function values across the discontinuity. This results in the introduction of spurious oscillations. Section 1.6 reviews several attempts at constructing non-oscillatory compact schemes. The basic thrust of all these efforts has been to decouple the solution of Eqn. (2.3) at the discontinuities. As a result, the matrix A on the left hand side comprises independent blocks that represent a locally coupled solution in smooth regions of the solution, bounded by discontinuities. The hybrid compact-ENO/WENO schemes achieve this by using a non-compact ENO/WENO scheme in regions around the discontinuities. The CRWENO schemes, presented in this section, seek to do the same while avoiding the reduction in spectral resolution that results from switching to a non-compact scheme.

The construction of the CRWENO schemes follows that of the WENO schemes, as described in Section 1.3. At each interface, it is possible to identify r candidate compact interpolation schemes of r-th order accuracy:

$$A_k^r \left(\hat{f}_{j+1/2-m}, \ldots, \hat{f}_{j+1/2+m} \right) = B_k^r \left(f_{j-n}, \ldots, f_{j+n} \right); \; k = 1, \ldots, r \qquad (2.4)$$

36

where the superscript r denotes the order of accuracy. There exist optimal coefficients c_k; $k = 1, \ldots, r$ such that the weighted sum results in a $(2r - 1)$-th order accurate compact interpolation scheme. This can be expressed as:

$$\sum_{k=1}^{r} c_k A_k^r \left(\hat{f}_{j+1/2-m}, \ldots, \hat{f}_{j+1/2+m} \right) = \sum_{k=1}^{r} c_k B_k^r \left(f_{j-n}, \ldots, f_{j+n} \right)$$
$$\Rightarrow A^{2r-1} \left(\hat{f}_{j+1/2-m}, \ldots, \hat{f}_{j+1/2+m} \right) = B^{2r-1} \left(f_{j-n}, \ldots, f_{j+n} \right) \qquad (2.5)$$

The WENO weights ω_k are calculated from the optimal coefficients, based on the smoothness of the solution, as expressed by Eqn. (1.32). The candidate interpolation schemes are then combined using the WENO weights to result in the $(2r - 1)$-th order CRWENO scheme:

$$\sum_{k=1}^{r} \omega_k A_k^r \left(\hat{f}_{j+1/2-m}, \ldots, \hat{f}_{j+1/2+m} \right) = \sum_{k=1}^{r} \omega_k B_k^r \left(f_{j-n}, \ldots, f_{j+n} \right) \qquad (2.6)$$

The present implementation of the CRWENO schemes uses identical definitions of the weights and the smoothness indicators as the WENO schemes. In smooth regions of the solution, the weights attain their optimal values ($\omega_k \to c_k$) and Eqn. (2.6) is identical to Eqn. (2.5). Across discontinuities, one or more of the weights approach zero resulting in a lower-order interpolation stencil that is biased away from the discontinuity.

Equation (2.6) can be expressed in the matrix form given by Eqn. (2.3), with A and B being banded matrices. However, it should be noted that these matrices are solution-dependent for the CRWENO scheme since the elements are a function of the weights that are computed based on the solution at each iteration. Thus, the solution to the linear system is required at each time step and cannot be computed as a preprocessing step.

2.2 5th Order CRWENO Schemes

Fifth-order CRWENO schemes are constructed in this section and applied to various problems in subsequent chapters. A fifth-order compact approximation to the interface flux can be expressed as

$$\frac{3}{10}\hat{f}_{j-1/2} + \frac{6}{10}\hat{f}_{j+1/2} + \frac{1}{10}\hat{f}_{j+3/2} = \frac{1}{30}f_{j-1} + \frac{19}{30}f_j + \frac{1}{3}f_{j+1} \tag{2.7}$$

and is the optimal scheme underlying the fifth-order CRWENO scheme. The solution requires the solution of a tridiagonal system of equations. The CRWENO scheme requires the identification of three third-order interpolation schemes that can be combined to result in the fifth-order scheme above. There are several such combinations.

Similar to the fifth-order WENO scheme, three third-order non-compact schemes can be used to construct the fifth-order compact scheme. However, the non-compact schemes are considered at different interfaces to restrict the total stencil to that of Eqn. (2.7). They can be expressed as:

$$\hat{f}_{j-1/2} = \frac{1}{6}\left(2f_{j-1} + 5f_j - f_{j+1}\right); \qquad c_1 = \frac{3}{10} \tag{2.8}$$

$$\hat{f}_{j+1/2} = \frac{1}{6}\left(-f_{j-1} + 5f_j + 2f_{j+1}\right); \qquad c_2 = \frac{6}{10} \tag{2.9}$$

$$\hat{f}_{j+3/2} = \frac{1}{6}\left(2f_{j-1} - 7f_j + 11f_{j+1}\right); \qquad c_3 = \frac{1}{10} \tag{2.10}$$

Using the optimal coefficients c_1, c_2 and c_3, the weighted sum is the fifth-order compact scheme. The optimal coefficients are replaced by the WENO weights and

thus, the resulting CRWENO scheme is:

$$\omega_1 \hat{f}_{j-1/2} \quad + \quad \omega_2 \hat{f}_{j+1/2} + \omega_3 \hat{f}_{j+3/2} = \frac{1}{6}[(2\omega_1 - \omega_2 + 2\omega_3)f_{j-1}$$

$$+ \quad (5\omega_1 + 5\omega_2 - 7\omega_3)f_j + (-\omega_1 + 2\omega_2 + 11\omega_3)f_{j+1}] \qquad (2.11)$$

The resulting tridiagonal system has the WENO weights on each diagonal. The weights are at their optimal (non-zero) values for smooth solutions and thus, the system is solvable. However, across or near discontinuities, one or more weights may approach zero and the system of equations may not be well defined.

An alternative combination of third-order schemes that constitute the fifth-order compact scheme can be formulated using two third-order compact schemes and one non-compact scheme. The three constituent schemes are given by:

$$\frac{2}{3}\hat{f}_{j-1/2} + \frac{1}{3}\hat{f}_{j+1/2} = \frac{1}{6}\left(f_{j-1} + 5f_j\right); \qquad c_1 = \frac{9}{20} \qquad (2.12)$$

$$\hat{f}_{j+1/2} = \frac{1}{6}\left(-f_{j-1} + 5f_j + 2f_{j+1}\right); \qquad c_2 = \frac{5}{20} \qquad (2.13)$$

$$\frac{2}{3}\hat{f}_{j+1/2} + \frac{1}{3}\hat{f}_{j+3/2} = \frac{1}{6}\left(f_j + 5f_{j+1}\right); \qquad c_3 = \frac{6}{20} \qquad (2.14)$$

The resulting CRWENO scheme is a tridiagonal system that can be expressed as

$$\frac{2}{3}\omega_1 \hat{f}_{j-1/2} + \left(\frac{1}{3}\omega_1 + \omega_2 + \frac{2}{3}\omega_3\right)\hat{f}_{j+1/2} + \frac{1}{3}\omega_3 \hat{f}_{j+3/2}$$

$$= \frac{1}{6}\left[(\omega_1 - \omega_2)f_{j-1} + (5\omega_1 + 5\omega_2 + \omega_3)f_j + (2\omega_2 + 5\omega_3)f_{j+1}\right] \qquad (2.15)$$

Thus, the main diagonal element is a combination of all the three weights and can never be zero.

Finally, the fifth-order compact scheme can be expressed as a combination of
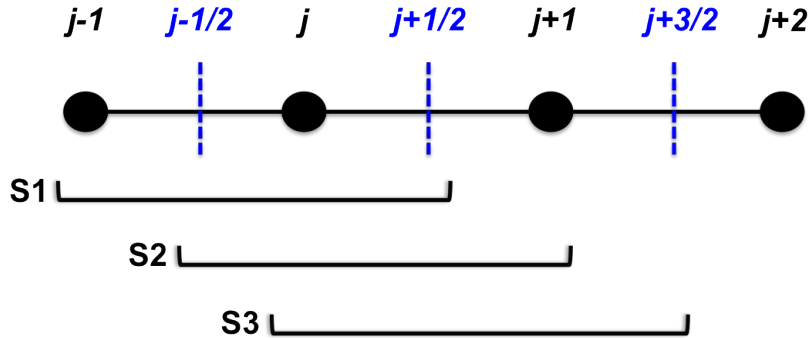
Figure 2.2: Constituent compact stencils for the fifth-order CRWENO scheme: S1 - Eqn. (2.16), S2 - Eqn. (2.17), S3 - Eqn. (2.18)

three third-order compact schemes:

$$\frac{2}{3}\hat{f}_{j-1/2} + \frac{1}{3}\hat{f}_{j+1/2} = \frac{1}{6}\left(f_{j-1} + 5f_j\right); \qquad c_1 = \frac{2}{10} \tag{2.16}$$

$$\frac{1}{3}\hat{f}_{j-1/2} + \frac{2}{3}\hat{f}_{j+1/2} = \frac{1}{6}\left(5f_j + f_{j+1}\right); \qquad c_2 = \frac{5}{10} \tag{2.17}$$

$$\frac{2}{3}\hat{f}_{j+1/2} + \frac{1}{3}\hat{f}_{j+3/2} = \frac{1}{6}\left(f_j + 5f_{j+1}\right); \qquad c_3 = \frac{3}{10} \tag{2.18}$$

Figure 2.2 shows the three constituent third-order stencils. The resulting CRWENO scheme as

$$\left(\frac{2}{3}\omega_1 + \frac{1}{3}\omega_2\right)\hat{f}_{j-1/2} + \left[\frac{1}{3}\omega_1 + \frac{2}{3}(\omega_2 + \omega_3)\right]\hat{f}_{j+1/2} + \frac{1}{3}\omega_3\hat{f}_{j+3/2}$$

$$= \frac{\omega_1}{6}f_{j-1} + \frac{5(\omega_1 + \omega_2) + \omega_3}{6}f_j + \frac{\omega_2 + 5\omega_3}{6}f_{j+1} \tag{2.19}$$

The tridiagonal system is well defined even if one or more weights approach zero near a discontinuity.

In the current implementation of the CRWENO schemes, the definition of the weights and the smoothness indicators are identical to the fifth-order WENO scheme. The weights are computed using Eqn. (1.32) where $r = 3$ and smoothness

indicators are given by

$$\beta_1 = \frac{13}{12}(f_{j-2} - 2f_{j-1} + f_j)^2 + \frac{1}{4}(f_{j-2} - 4f_{j-1} + 3f_j)^2 \qquad (2.20)$$

$$\beta_2 = \frac{13}{12}(f_{j-1} - 2f_j + f_{j+1})^2 + \frac{1}{4}(f_{j-1} - f_{j+1})^2 \qquad (2.21)$$

$$\beta_3 = \frac{13}{12}(f_j - 2f_{j+1} + f_{j+2})^2 + \frac{1}{4}(3f_j - 4f_{j+1} + f_{j+2})^2 \qquad (2.22)$$

Although the CRWENO scheme is compact and uses a smaller stencil for the interpolation, the smoothness indicators use function values from a larger stencil. The final stencil width, in terms of the number of grid points necessary for the complete scheme, is thus the same as that of the fifth-order WENO scheme.

Equations (2.11), (2.15) and (2.19) are three possible formulations of the fifth-order CRWENO scheme. The weights attain their optimal values for smooth solutions and they are identical to Eqn. (2.7). However, their behavior is different for solutions with discontinuities. As mentioned earlier, zero weights, resulting from a discontinuity, may render the system of equations unsolvable for Eqn. (2.11). Equation (2.15) comprises two compact and one non-compact schemes. Thus, in presence of discontinuities, the non-compact scheme may dominate the final interpolation scheme and thus, result in a reduction in the spectral resolution. Results were obtained using this formulation to test the accuracy and non-oscillatory nature of the scheme, however, they are not presented in this thesis and the scheme was not applied to problems of practical relevance. A CRWENO scheme comprising three third-order compact schemes is given by Eqn. (2.19). The scheme is a fifth-order compact scheme for smooth solutions, while across and near discontinuities, it is a non-oscillatory combination of third-order compact interpolation schemes. Thus,

the superior spectral resolution of the compact schemes is maintained at the discontinuities. A more complete discussion on the spectral properties of this scheme is presented in the next section.

Examination of Eqn. (2.19), or the other formulations for the fifth-order CR-WENO scheme, and the smoothness indicators shows the decoupling of the compact interpolation at the discontinuities in the domain. Consider a discontinuity located between x_{j+1} and $x_{j+3/2}$, which would imply $\beta_3 \gg \beta_{1,2}$ and thus $\omega_3 \to 0$. This would result in Eqn. (2.19) reducing to a bidiagonal system, biased away from the discontinuity. Similar, a discontinuity located between $x_{j-1/2}$ and x_j would result in $\omega_{1,2}$ approaching zero. This would once again result in a bidiagonal system biased away from the discontinuity. Thus, the WENO weights prevent the coupling of the flux calculation from crossing the discontinuities and result in a non-oscillatory compact interpolation scheme.

As an example, consider a solution that is smooth everywhere except a discontinuity located between $x_{j+1/2}$ and x_{j+1},

$$f(x) = \quad \cos(x), \ x \leq x_{j+1/2} + \delta$$

$$10 + \cos(x), \ x > x_{j+1/2} + \delta \tag{2.23}$$

where $0 < \delta < \Delta x/2$. Without loss of generality, assume that $x_{j-1} = 0$. Figure 2.3 shows the grid and the solution in the neighborhood of the discontinuity. Evaluating the flux at interface $x_{j-1/2}$, the smoothness indicators are obtained for this function

by Eqns. (2.20) - (2.22) as:

$$\beta_1 = \frac{13}{12}[\cos(2\Delta x) - 2\cos(\Delta x) + 1]^2 + \frac{1}{4}[\cos(2\Delta x) - 4\cos(\Delta x) + 3]^2$$

$$\beta_2 = \frac{13}{12}[2\cos(\Delta x) - 2]^2$$

$$\beta_3 = \frac{13}{12}[1 - 2\cos(\Delta x) + 10 + \cos(2\Delta x)]^2 + \frac{1}{4}[3 - 4\cos(\Delta x) + 10 + \cos(2\Delta x)]^2$$

An estimate is made of the approximate values of the smoothness indicators and the weights. Assuming $\Delta x \to 0$, the values for the smoothness indicators are: $\beta_1 = 0, \beta_2 = 0, \beta_3 = 400/3$. Thus, the weights are: $\omega_1 = 2/7, \omega_2 = 5/7, \omega_3 = 0$. Substituting these values in Eqn. (2.19), the left hand side coefficients for $\hat{f}_{j-3/2}, \hat{f}_{j-1/2}$ and $\hat{f}_{j+1/2}$ are $3/7, 4/7$ and 0, respectively. Similarly, Eqn. (2.19) is applied to the interface $x_{j+1/2}$. The smoothness indicators for this interface are:

$$\beta_1 = \frac{13}{12}[2\cos(\Delta x) - 2]^2 + \frac{1}{4}[\cos(4\Delta x) - 4]^2$$

$$\beta_2 = \frac{13}{12}[1 - 2\cos(\Delta x) + 10 + \cos(2\Delta x)]^2 + \frac{1}{4}[1 - 10 - \cos(2\Delta x)]^2$$

$$\beta_3 = \frac{13}{12}[\cos(\Delta x) - 2\{10 + \cos(2\Delta x)\} + 10 + \cos(3\Delta x)]^2$$
$$+ \frac{1}{4}[3\cos(\Delta x) - 4\{10 + \cos(2\Delta x)\} + 10 + \cos(3\Delta x)]^2$$

Once again, assuming $\Delta x \to 0$, the values of the smoothness indicators are: $\beta_1 = 0, \beta_2 = 400/3, \beta_3 = 1000/3$. The weights are: $\omega_1 = 1, \omega_2 = 0$ and $\omega_3 = 0$. The resulting left-hand side coefficients for $\hat{f}_{j-1/2}, \hat{f}_{j+1/2}$ and $\hat{f}_{j+3/2}$ are $2/3, 1/3$ and 0 respectively.

Evaluating the smoothness indicators and the weights in a similar manner at interface $x_{j+3/2}$ yields the left-hand side coefficients of $\hat{f}_{j+1/2}, \hat{f}_{j+3/2}$ and $\hat{f}_{j+5/2}$ as
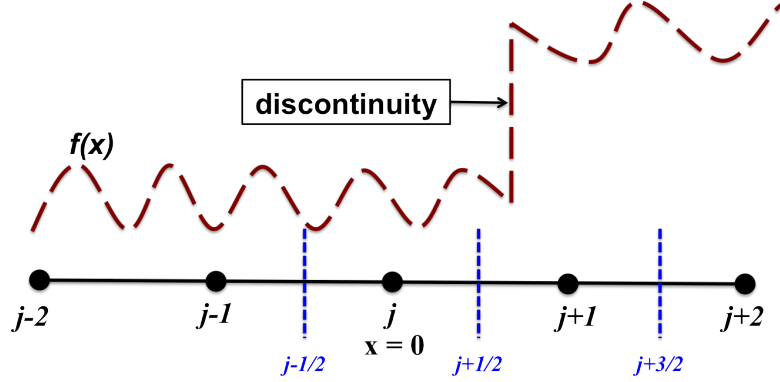
Figure 2.3: Example of a solution with a discontinuity and smooth regions.

$0, 2/3$ and $1/3$ respectively (with $\omega_{1,2} = 0, \omega_3 = 1$). The interpolation at $x_{j+5/2}$ yields the left-hand side coefficients of $\hat{f}_{j+3/2}, \hat{f}_{j+5/2}$ and $\hat{f}_{j+7/2}$ as $5/24, 2/3$ and $1/8$ (with $\omega_1 = 0, \omega_2 = 5/8$ and $\omega_3 = 3/8$). Expressing these equations in the matrix form, given by Eqn. (2.3), we get the left-hand side as:

$$
A\hat{\mathbf{f}} =
\left[
\begin{array}{ccccc|ccccc}
\bullet & \bullet & \bullet & 0 & \ldots & \ldots & \ldots & \ldots & \ldots & 0 \\
0 & \bullet & \bullet & \bullet & \ldots & \ldots & \ldots & \ldots & \ldots & \bullet \\
\cdot & \ldots & 3/7 & 4/7 & 0 & \ldots & \ldots & \ldots & \ldots & \cdot \\
\cdot & \ldots & \ldots & 2/3 & 1/3 & 0 & \ldots & \ldots & \ldots & \cdot \\
\hline
\cdot & \ldots & \ldots & \ldots & 0 & 2/3 & 1/3 & \ldots & \ldots & \cdot \\
\cdot & \ldots & \ldots & \ldots & \ldots & 5/24 & 2/3 & 1/8 & \ldots & \cdot \\
\cdot & \ldots & \ldots & \ldots & \ldots & \ldots & \bullet & \bullet & \bullet & 0 \\
0 & \ldots & \ldots & \ldots & \ldots & \ldots & 0 & \bullet & \bullet & \bullet \\
\end{array}
\right]
\left[
\begin{array}{c}
\bullet \\
\hat{f}_{j-3/2} \\
\hat{f}_{j-1/2} \\
\hat{f}_{j+1/2} \\
\hline
\hat{f}_{j+3/2} \\
\hat{f}_{j+5/2} \\
\hat{f}_{j+7/2} \\
\bullet \\
\end{array}
\right]
$$

The decoupling across the discontinuity that results from the WENO weights is observed in the matrix. The discontinuity separates the matrix A into two separate blocks. The interface fluxes on each side of the discontinuity are independently solved. Thus, the final system involves the coupled calculation of the interface fluxes within the smooth regions of the solutions.

A bandwidth-optimized WENO scheme was presented in [50] that improved the resolution characteristics of the WENO scheme. The optimal interpolation

scheme, given by Eqn. (1.38), is modified to increase the spectral resolution. This is achieved by adding an additional point to the stencil such that the overall stencil is central instead of upwind biased. However, the coefficients are biased to introduce the dissipation required for a stable solution. This is done at the cost of the order of spatial convergence, but the modified coefficients yield an interpolation scheme with lower dissipation and dispersion errors, compared to Eqn. (1.38). A similar approach is utilized here to construct a fifth-order CRWENO scheme with lower dissipation than Eqn. (2.19).

Equation (2.7) uses an upwind-biased stencil for a fifth-order compact interpolation at $x_{j+1/2}$. Addition of the cell-centered flux at x_{j+2} to the right-hand side results in a central stencil, which yields a sixth-order compact interpolation with symmetric coefficients. However, a sixth-order scheme does not have the dissipation necessary for stable solutions to hyperbolic problems. A biased, fifth-order compact scheme can be constructed using the central stencil by using asymmetric coefficients and can be expressed as:

$$\frac{5}{20}\hat{f}_{j-1/2} + \frac{12}{20}\hat{f}_{j+1/2} + \frac{3}{20}\hat{f}_{j+3/2} = \frac{1}{120}(3f_{j-1} + 67f_j + 49f_{j+1} + f_{j+2}) \qquad (2.24)$$

Although the order of convergence is the same, the absolute error is lower than that of Eqn. (2.7) (a more complete discussion on the numerical properties of these schemes is presented in the next section). A low dissipation CRWENO scheme can be constructed that has Eqn. (2.24) as the underlying optimal scheme. The

constituent third-order compact schemes and their optimal coefficients are:

$$\frac{2}{3}\hat{f}_{j-1/2} + \frac{1}{3}\hat{f}_{j+1/2} = \frac{1}{6}(f_{j-1} + 5f_j); \qquad c_1 = \frac{3}{20} \qquad (2.25)$$

$$\frac{1}{3}\hat{f}_{j-1/2} + \frac{2}{3}\hat{f}_{j+1/2} = \frac{1}{6}(5f_j + f_{j+1}); \qquad c_2 = \frac{9}{20} \qquad (2.26)$$

$$\frac{2}{3}\hat{f}_{j+1/2} + \frac{1}{3}\hat{f}_{j+3/2} = \frac{1}{6}(f_j + 5f_{j+1}); \qquad c_3 = \frac{7}{20} \qquad (2.27)$$

$$\frac{1}{3}\hat{f}_{j+1/2} + \frac{2}{3}\hat{f}_{j+3/2} = \frac{1}{6}(5f_{j+1} + f_{j+2}); \qquad c_2 = \frac{1}{20} \qquad (2.28)$$

The first three schemes are the same as those constituting Eqn. (2.7) while an additional downwind stencil is added such that the final scheme has a central stencil. The optimal coefficients are biased towards the upwind constituents to provide the upwinding necessary for a stable solution. Replacing the optimal coefficients with the WENO weights, the fifth-order low-dissipation CRWENO scheme can be expressed as:

$$\frac{2\omega_1 + \omega_2}{3}\hat{f}_{j-1/2} + \frac{\omega_1 + 2(\omega_2 + \omega_3) + \omega_4}{3}\hat{f}_{j+1/2} + \frac{\omega_3 + 2\omega_4}{3}\hat{f}_{j+3/2}$$

$$= \frac{\omega_1}{6}f_{j-1} + \frac{5(\omega_1 + \omega_2) + \omega_3}{6}f_j + \frac{\omega_2 + 5(\omega_3 + \omega_4)}{6}f_{j+1} + \frac{\omega_4}{6}f_{j+2} \qquad (2.29)$$

Equations (2.20) - (2.22) are the smoothness indicators for the first three constituent schemes. Evaluating Eqn. (1.36), the smoothness indicator for the fourth constituent scheme is obtained as:

$$\beta_4 = \frac{13}{12}(f_{j+1} - 2f_{j+2} + f_{j+3})^2 + \frac{1}{4}(-5f_{j+1} + 8f_{j+2} - 3f_{j+3})^2 \qquad (2.30)$$

The fourth smoothness indicator is modified by taking a maximum of itself and the third smoothness indicator ($\beta_4 = \max\beta_{3,4}$) to ensure that the weight for the fourth stencil is always less than or equal to the third stencil. This prevents a completely downwind interpolation.

Thus, to summarize, Eqns. (2.19) and (2.29) are two fifth-order CRWENO schemes introduced in this thesis. The concept of upwinding required for stable solutions of hyperbolic PDEs was briefly discussed in Section 1.2.1. The final interpolated flux at the interface is a linear combination of the left and right biased interpolations, depending on the sign of the local advection velocity. The interpolation schemes presented in this section correspond to the reconstruction of a left-biased flux. The corresponding expressions for the right-biased fluxes can be easily derived. The numerical properties, accuracy and convergence properties, and computational efficiency of the schemes introduced here are analyzed and discussed in subsequent sections. The application to compressible fluid dynamics is presented in later chapters.

2.3 Numerical Analysis

The numerical properties of the compact differencing schemes introduced in the previous section are analyzed in this section and compared to non-compact schemes as well as other compact differencing schemes in the literature. The accuracy, convergence and resolution of these schemes are studied.

2.3.1 Taylor series analysis

A Taylor series analysis is used to analyze the accuracy and convergence properties. The optimal scheme underlying the fifth-order WENO scheme is given by Eqn. (1.38). The resulting approximation for the first derivative of the flux function,

using Eqn. (1.10), is given by:

$$
\begin{aligned}
f_x &= \frac{1}{\Delta x}\left(\frac{-1}{30}f_{j-3} + \frac{1}{4}f_{j-2} - f_{j-1} + \frac{1}{3}f_j + \frac{1}{2}f_{j+1} - \frac{1}{20}f_{j+2}\right) \\
&\quad + \frac{1}{60}\left.\frac{\partial^6 f}{\partial x^6}\right|_j \Delta x^5 + \frac{1}{140}\left.\frac{\partial^7 f}{\partial x^7}\right|_j \Delta x^6 + O(\Delta x^7)
\end{aligned} \tag{2.31}
$$

The underlying optimal schemes for the fifth-order CRWENO schemes are given by Eqns. (2.7) and (2.24). The resulting approximations for the first derivative of the flux function and the leading error terms are:

$$
\begin{aligned}
\frac{3}{10}f_{x,j-1} + \frac{6}{10}f_{x,j} + \frac{1}{10}f_{x,j+1} &= \frac{1}{\Delta x}\left(\frac{-1}{30}f_{j-2} - \frac{18}{30}f_{j-1} + \frac{9}{30}f_j + \frac{10}{30}f_{j+1}\right) \\
\Rightarrow f_{x,j} = f_{\Delta,j} + \frac{1}{600}\left.\frac{\partial^6 f}{\partial x^6}\right|_j \Delta x^5 &+ \frac{1}{2100}\left.\frac{\partial^7 f}{\partial x^7}\right|_j \Delta x^6 + O(\Delta x^7)
\end{aligned} \tag{2.32}
$$

for the fifth-order upwind compact scheme, Eqn. (2.7); and

$$
\begin{aligned}
\frac{1}{4}f_{x,j-1} &+ \frac{6}{10}f_{x,j} + \frac{3}{20}f_{x,j+1} \\
&= \frac{1}{\Delta x}\left(\frac{-3}{120}f_{j-2} - \frac{64}{120}f_{j-1} + \frac{18}{120}f_j + \frac{48}{120}f_{j+1} + \frac{1}{120}f_{j+2}\right) \\
\Rightarrow f_{x,j} &= f_{\Delta,j} + \frac{1}{1200}\left.\frac{\partial^6 f}{\partial x^6}\right|_j \Delta x^5 + \frac{1}{2100}\left.\frac{\partial^7 f}{\partial x^7}\right|_j \Delta x^6 + O(\Delta x^7)
\end{aligned} \tag{2.33}
$$

for the central low-dissipation compact scheme, Eqn. (2.24). The term f_Δ denotes the finite difference approximation to the first derivative. The two leading error terms representing the dissipation and dispersion errors are included. The three interpolation schemes are fifth-order accurate. However, the dissipation error for the upwind compact scheme, Eqn. (2.32), is an order of magnitude lower than that of the non-compact scheme, Eqn. (2.31). The dissipation error for the low-dissipation central compact scheme, Eqn. (2.33), is half that of the upwind compact scheme. Thus, for the same order of convergence, the compact schemes have a

significantly lower dissipation error than the non-compact scheme at the same grid refinement. Similarly, a comparison of the dispersion error reveals that the error for the compact schemes is (1/15)-th times that for the non-compact scheme. An implication of the lower absolute error is the grid resolution required to obtain solutions of similar accuracy. Considering that these are fifth-order schemes, the upwind compact scheme would require a grid that is $(1/10)^{1/5} \approx 0.63$ times as fine as the grid for the non-compact scheme, to obtain a solution with the same absolute error. Similarly, the low-dissipation compact scheme would require a grid that is $(1/20)^{1/5} \approx 0.55$ as fine as the grid for the non-compact scheme. Although the compact schemes are more expensive because each iteration requires a tridiagonal solution, the lower grid size leads to lower expense for solutions of the same accuracy. The computational efficiency of these schemes are studied in Section 2.6.

2.3.2   Fourier analysis

The primary motivation for the development of the CRWENO schemes is the accurate resolution of small scales for physical problems involving a large range of scales. Thus, a Fourier analysis is performed for the optimal schemes to assess their spectral properties. The flux function is assumed to be a periodic sinusoidal wave, given by Eqn. (1.53), and the dispersion and dissipation is calculated as a function of the grid wavenumber $k\Delta x$. Figure 2.4(a) shows the real and imaginary parts of the modified phase of the flux derivative that indicate the dissipation and dispersion errors respectively. The optimal schemes underlying the CRWENO schemes, given

by Eqns. (2.7) and (2.24), are compared with the fifth-order non-compact scheme, given by Eqn. (1.38), as well as the ninth-order non-compact scheme. These schemes are the optimal schemes underlying fifth and ninth-order WENO schemes. The modified phase is shown in Fig. 2.4(b) as a function of the actual phase. It is observed from both these figures that the fifth-order compact differencing schemes have a significantly higher spectral resolution than the non-compact schemes. The range of wavenumbers that are accurately captured by the numerical approximation is much higher with the compact schemes. In fact, a fifth-order compact scheme has a higher spectral resolution than a ninth-order non-compact scheme. The low-dissipation central compact scheme has a lower spectral resolution than the upwind compact scheme.

The bandwidth resolving efficiency was introduced in [25] as a quantitative measure of the spectral resolution. It is defined as the maximum phase (as a fraction of π) for which the normalized error in phase does not exceed a given tolerance, i.e.,

$$\epsilon_f = \frac{|k'\Delta x - k\Delta x|}{k\Delta x} \leq \epsilon_t \tag{2.34}$$

The bandwidth resolving efficiencies for the compact schemes are compared with the non-compact schemes with an error tolerance of $\epsilon_t = 0.01$. Figure 2.4(c) shows the normalized phase error ϵ_f as a function of the normalized phase $k\Delta x/\pi$, where the resolving efficiency can be calculated from the x-value at which the normalized error crosses the horizontal line denoting an error of 0.01. The resolving efficiency of a fifth-order non-compact scheme is 0.35 while that of a ninth-order non-compact scheme is 0.48. The compact schemes have significantly higher resolving efficiency.

50

(a) Eigenvalues

(b) Modified Phase

(c) Normalized Phase Error
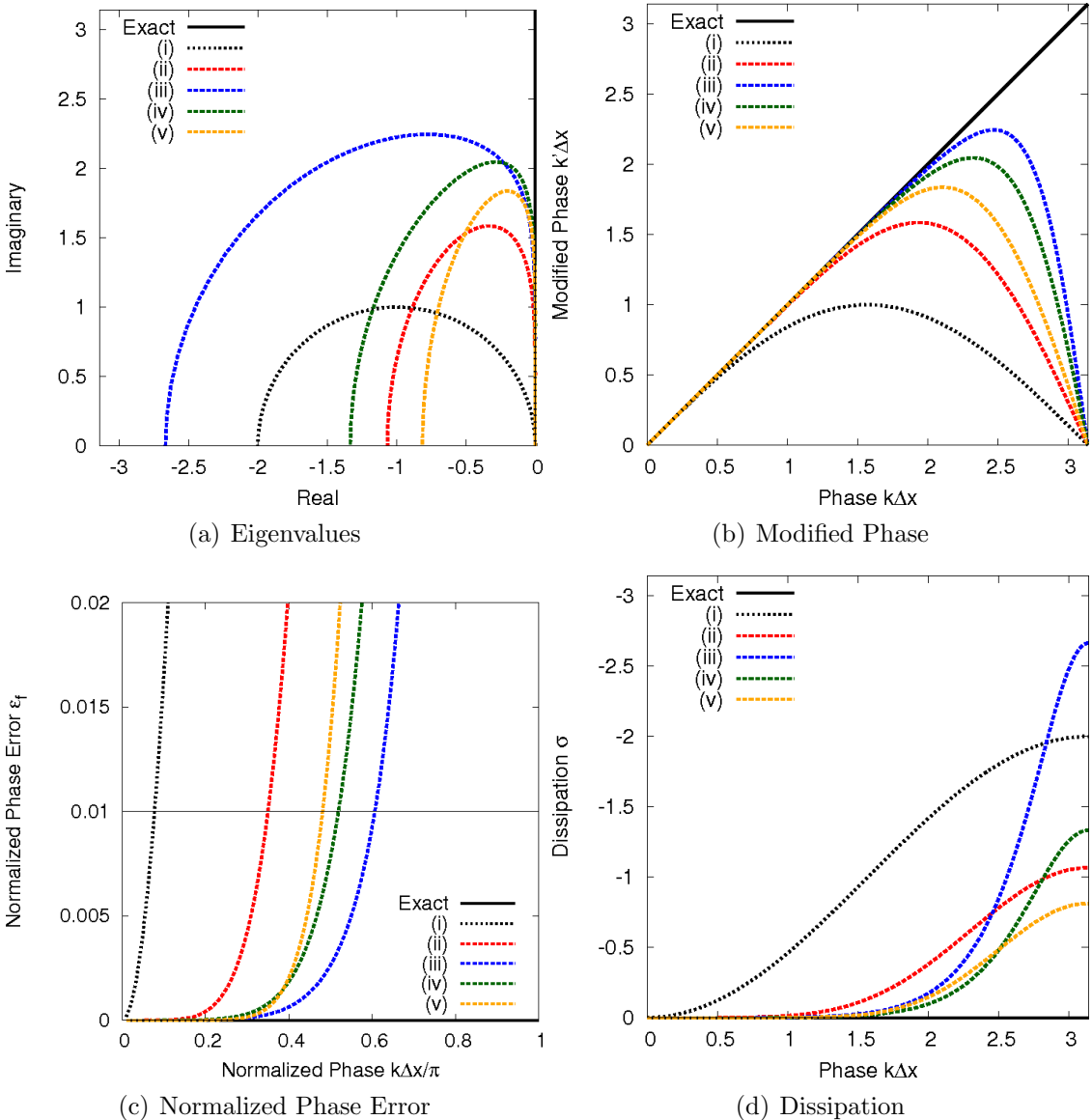
(d) Dissipation

Figure 2.4: Fourier analysis of compact and non-compact conservative differencing schemes: (i) 1st-order upwind, Eqn. (1.11); (ii) 5th-order non-compact, Eqn. (1.38); (iii) 5th-order compact, Eqn. (2.7); (iv) 5th-order low-dissipation compact, Eqn. (2.24); and (v) 9th-order non-compact

The fifth-order upwind compact scheme has an efficiency of 0.61 while that of the low-dissipation compact scheme is 0.52. Thus, a quantitative comparison of the spectral resolution for the various schemes is obtained.
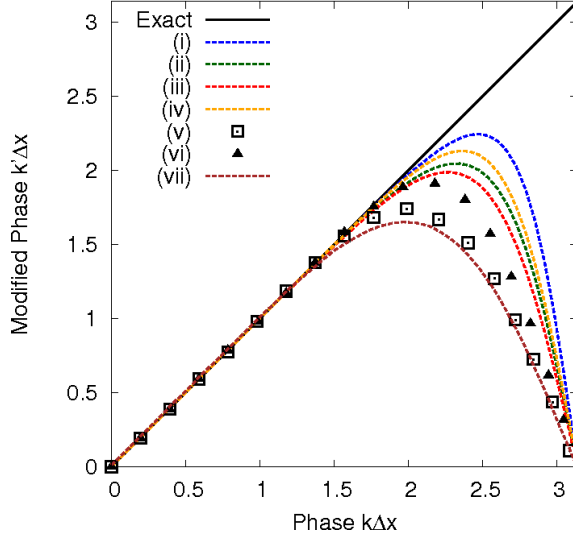
Figure 2.5: Comparison of spectral resolutions: (i) 5th-order upwind compact, Eqn. (2.7); (ii) 5th-order low-dissipation upwind compact, Eqn. (2.24); (iii) 6th-order central compact [25]; (iv) 8th-order central compact [25]; (v) WENO-SYMBO ($r = 3$) [50]; (vi) WENO-SYMBO ($r = 4$) [50]; and (vii) WCNS-5 [46]

The dissipation for the schemes is shown in Fig. 2.4(d) as a function of the phase. It is observed that for the wavenumbers that are accurately resolved, the dissipation for the fifth-order upwind compact scheme is significantly lower than the fifth-order non-compact scheme, and comparable to that of the ninth-order non-compact scheme. At higher wavenumbers, the dissipation is significantly higher for the upwind compact scheme. However, these wavenumbers are not accurately captured by any of the schemes and thus, the higher dissipation is useful in damping out the high-wavenumber errors in the solution. The low-dissipation compact scheme has a lower dissipation than that of the upwind compact scheme, as expected.

2.3.3 Comparison with previous work

The conservative compact differencing schemes that underlie the CRWENO schemes have superior spectral properties compared to the non-compact schemes of the same or higher order. Thus, the CRWENO schemes are expected to show an improved resolution and preservation of small-scale structures, compared to the WENO schemes, while retaining the non-oscillatory behavior across discontinuities. Figure 2.5 compares the spectral resolution of the fifth-order conservative compact schemes with that of various high-resolution schemes presented in the literature. The spectral resolutions of the tridiagonal sixth and eighth-order compact schemes, introduced in [25], are shown. As discussed in Section 1.6, a family of non-oscillatory compact schemes were presented that used the cell-centered compact scheme to compute the first derivative and a WENO scheme to compute the flux at the interfaces [46]. The spectral resolution for the fifth-order scheme (WCNS-5) that uses a sixth-order compact scheme for the first derivative and a fifth-order WENO scheme for the interface flux is shown. The spectral resolutions for the WENO-SYMBO schemes [50] are also shown, where the interpolation coefficients for the non-compact WENO schemes are optimized to improve the spectral resolution. The schemes with $r = 3$ and $r = 4$ that correspond to the regular fifth and seventh-order WENO schemes are shown here.

The spectral resolution of the conservative compact schemes compare well with those of schemes presented in the literature. The WCNS-5 scheme uses a non-compact WENO interpolation to compute the interface fluxes and thus, the

Table 2.1: Bandwidth resolving efficiencies for various schemes for an error tolerance of 0.01

Scheme	Bandwidth Resolving Efficiency
5th-order non-compact Eqn. (1.38)	0.35
7th-order non-compact	0.42
9th-order non-compact	0.48
5th-order upwind compact Eqn. (2.7)	0.61
5th-order low-dissipation compact Eqn. (2.24)	0.52
WENO-SYMBO ($r = 3$) [50]	0.49
WENO-SYMBO ($r = 4$) [50]	0.56
6th-order central compact (tridiagonal) [25]	0.50
8th-order central compact (tridiagonal) [25]	0.58

resulting scheme has a spectral resolution that is marginally better than the regular fifth-order WENO scheme. The WENO-SYMBO schemes resolve a larger range of wavenumbers, with the $r = 4$ scheme having a spectral resolution comparable to the sixth-order central compact scheme [25]. The fifth-order upwind compact scheme has a higher spectral resolution than the sixth and eighth-order central compact schemes presented in [25] while the low-dissipation compact scheme has a spectral resolution comparable to that of the sixth-order central compact scheme. Table 2.1 summarizes the bandwidth resolving efficiencies of the various compact and non-compact schemes. It is observed that the spectral resolution of the optimal schemes underlying the CRWENO schemes compares well with those of high-resolution schemes

Table 2.2: Summary of interpolation schemes (referred to in the text)

Description	Name of Scheme	Equation
5th-order non-compact	NonCompact5	Eqn. (1.38)
5th-order compact	Compact5	Eqn. (2.7)
5th-order low-dissipation compact	Compact5-LD	Eqn. (2.24)
5th-order WENO	WENO5	Eqn. (1.41)
5th-order CRWENO	CRWENO5	Eqn. (2.19)
5th-order low-dissipation CRWENO	CRWENO5-LD	Eqn. (2.29)

presented in the literature.

2.4 Application: Scalar Conservation Laws

The CRWENO schemes introduced in the previous sections are applied to scalar conservation laws. The numerical properties of accuracy, convergence and resolution are verified and compared to the WENO schemes. The conclusions drawn from the numerical analysis of the optimal schemes, as presented in the previous section, are verified. The applicability of the WENO weights, as implemented in [13], to compact schemes is tested. Numerical results are presented in the subsequent sections and the schemes, as they are referred to in the text, are summarized in Table 2.2. The NonCompact5, Compact5 and Compact5-LD schemes are the optimal schemes underlying the WENO5, CRWENO5 and CRWENO5-LD schemes, respectively.

2.4.1 Linear Advection Equation

The linear advection equation is the simplest example of a hyperbolic conservation law and represents the advection of a scalar quantity. The initial value problem on an infinite domain can be described as:

$$\frac{\partial u}{\partial t} + \frac{\partial u}{\partial x} = 0 \tag{2.35}$$

$$u(x, 0) = u_0(x) \tag{2.36}$$

The exact solution is given as:

$$u(x, t) = u_0(x - t) \tag{2.37}$$

and represents the advection of u with unit velocity in the positive x-direction. Upwinding requires a biased interpolation of the flux function depending on the sign of the local advection velocity, which is a positive constant in this case ($f'(u) = 1$). Thus, a left-biased interpolation is used for the numerical solution. The solution is marched in time using the TVD-RK3 scheme given by Eqn. (1.25).

The accuracy and convergence properties of the schemes are analyzed for a smooth solution. The initial conditions are taken as

$$u_0(x) = \sin(x), \ 0 \leq x \leq 2\pi \tag{2.38}$$

on a periodic domain. The solution is obtained after one cycle over the domain and the errors for the schemes are compared. Tables 2.3 - 2.5 shows the L_1, L_2 and L_∞ error norms and the rates of convergence (r_c) for the NonCompact5, Compact5 and Compact5-LD schemes. The grid is progressively refined from 20 points to 640

56

Table 2.3: L_1 errors and convergence rates for the optimal schemes with smooth initial data

N	NonCompact5 Error	r_c	Compact5 Error	r_c	Compact5-LD Error	r_c
20	2.067E-04	-	3.346E-05	-	2.425E-05	-
40	6.518E-06	4.99	9.510E-07	5.14	6.390E-07	5.25
80	2.042E-07	5.00	2.756E-08	5.11	1.788E-08	5.16
160	6.384E-09	5.00	8.231E-10	5.07	5.197E-10	5.10
320	2.003E-10	5.00	2.588E-11	4.99	1.629E-11	5.00

Table 2.4: L_2 errors and convergence rates for the optimal schemes with smooth initial data

N	NonCompact5 Error	r_c	Compact5 Error	r_c	Compact5-LD Error	r_c
20	2.287E-04	-	3.749E-05	-	2.827E-05	-
40	7.233E-06	4.98	1.036E-06	5.18	7.268E-07	5.28
80	2.267E-07	5.00	3.012E-08	5.10	1.990E-08	5.19
160	7.090E-09	5.00	9.053E-10	5.06	5.740E-10	5.12
320	2.225E-10	4.99	2.857E-11	4.99	1.799E-11	5.00

Table 2.5: L_∞ errors and convergence rates for the optimal schemes with smooth initial data

N	NonCompact5 Error	r_c	Compact5 Error	r_c	Compact5-LD Error	r_c
20	3.207E-04	-	5.792E-05	-	6.021E-05	-
40	1.021E-05	4.97	1.412E-06	5.36	1.388E-06	5.44
80	3.204E-07	4.99	4.166E-08	5.08	4.119E-08	5.07
160	1.003E-08	5.00	1.280E-09	5.02	1.355E-09	4.93
320	3.145E-10	4.99	4.042E-11	4.99	4.307E-11	4.98

points for the convergence analysis. The initial CFL is 0.1 for the 20-point grid and is reduced by a factor of $2/(2^{5/3})$ at each refinement to ensure that the errors due to time discretization converge at the same rate as those due to the spatial discretization. A low CFL number is chosen to ensure that the time discretization errors are significantly lower.

The three schemes show 5th-order convergence in all the three norms. How-

ever, it is observed that the absolute value of the error is an order of magnitude lower for the Compact5 scheme, as compared to the NonCompact5 scheme. The errors for the Compact5-LD scheme are approximately half those of the Compact5 scheme for the same grid resolution. These observations are consistent with the results from the Taylor series analysis presented in the last section. Thus, the Compact5 and Compact5-LD schemes yield solutions with significantly lower error than the NonCompact5 for the same order of convergence.

Tables 2.6 - 2.8 show the error norms and convergence rates for the WENO5, CRWENO5 and CRWENO5-LD schemes. The solution is smooth and thus, the implementation of the WENO weights dictate that these schemes be identical to their optimal counterparts (NonCompact5, Compact5 and Compact5-LD, respectively). The absolute values of the errors are identical to those obtained by the optimal schemes and all three schemes show 5th-order convergence. Thus, it is verified that the CRWENO5 and CRWENO5-LD schemes, given by Eqns. (2.19) and (2.29), converge to the optimal schemes given by Eqns. (2.7) and (2.24) respectively for smooth solutions. The conclusions drawn regarding the accuracy of the optimal schemes extend to the CRWENO schemes. The CRWENO5 and CRWENO5-LD schemes yield solutions with significantly lower absolute errors (1/10-th and 1/20-th, respectively) compared to the WENO5 scheme with the same order of convergence.

While the smooth solution considered above demonstrated the accuracy and convergence properties of the compact schemes, the spectral resolution of the schemes

Table 2.6: L_1 errors and convergence rates for the WENO and CRWENO schemes with smooth initial data

N	WENO5 Error	r_c	CRWENO5 Error	r_c	CRWENO5-LD Error	r_c
20	2.067E-04	-	3.346E-05	-	2.426E-05	-
40	6.518E-06	4.99	9.510E-07	5.14	6.390E-07	5.25
80	2.042E-07	5.00	2.756E-08	5.11	1.788E-08	5.16
160	6.384E-09	5.00	8.231E-10	5.07	5.197E-10	5.10
320	2.004E-10	4.99	2.588E-11	4.99	1.629E-11	5.00

Table 2.7: L_2 errors and convergence rates for the WENO and CRWENO schemes with smooth initial data

N	WENO5 Error	r_c	CRWENO5 Error	r_c	CRWENO5-LD Error	r_c
20	2.288E-04	-	3.749E-05	-	2.828E-05	-
40	7.233E-06	4.98	1.036E-06	5.18	7.268E-07	5.28
80	2.267E-07	5.00	3.012E-08	5.10	1.989E-08	5.19
160	7.090E-09	5.00	9.053E-10	5.06	5.740E-10	5.12
320	2.225E-10	4.99	2.857E-11	4.99	1.799E-11	5.00
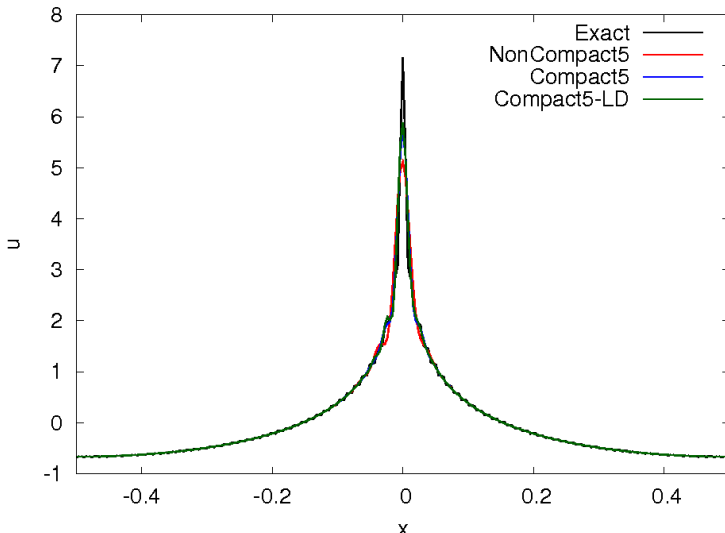
Table 2.8: L_∞ errors and convergence rates for the WENO and CRWENO schemes with smooth initial data

N	WENO5 Error	r_c	CRWENO5 Error	r_c	CRWENO5-LD Error	r_c
20	3.199E-04	-	5.797E-05	-	6.025E-05	-
40	1.021E-05	4.97	1.412E-06	5.36	1.388E-06	5.44
80	3.204E-07	4.99	4.166E-08	5.08	4.119E-08	5.07
160	1.003E-08	5.00	1.280E-09	5.02	1.355E-09	4.93
320	3.145E-10	4.99	4.042E-11	4.99	4.307E-11	4.98
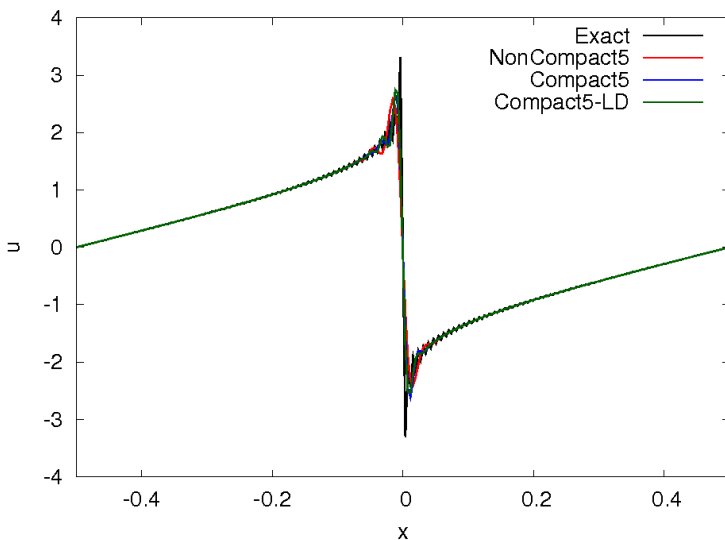
are verified and compared with that of the non-compact scheme for a solution containing a range of length scales. The discrete initial condition is the sum of sinusoidal waves of all length scales that are supported by the grid:

$$u_0(j) = \sum_{k=1}^{N/2} A(k)\cos\left(2\pi jk\Delta x + \phi(k)\right); \; j = 1, \ldots, N \tag{2.39}$$

where the periodic domain is taken as $[0, 1]$, k is the discrete wavenumber and ϕ is the phase. The amplitude $A(k) = k^{-5/6}$ is taken such that the energy, as a function of the

(a) $\phi = 0$

(b) $\phi = \pi/2$

Figure 2.6: Solution after one cycle for initial conditions with all frequencies supported by the grid

wavenumber, follows the $E(k) \propto k^{-5/3}$ distribution that is characteristic of turbulent flows. The initial phase $\phi(k)$ is taken as 0 and $\pi/2$, such that the solutions resemble an extremum and a discontinuity respectively. Figure 2.6 shows the initial conditions and the solutions after one cycle over the domain for both the values of the initial
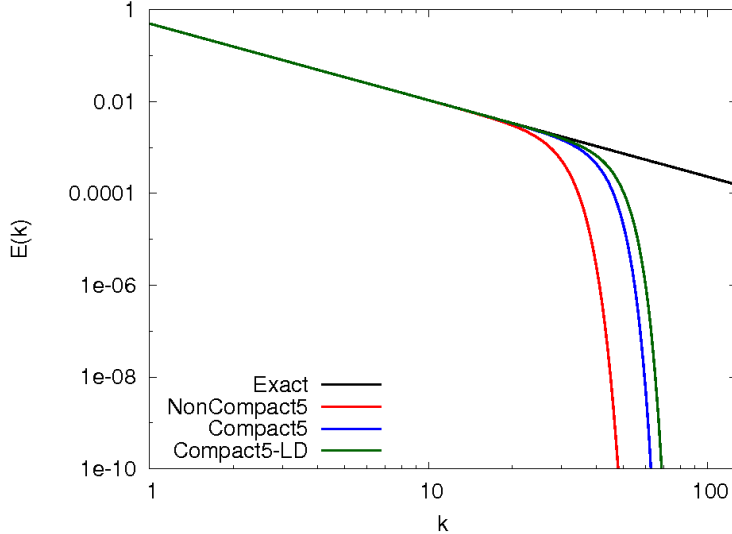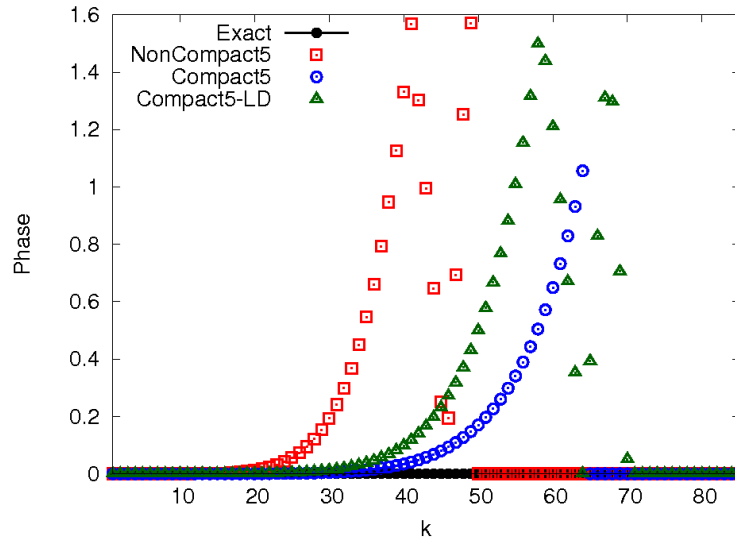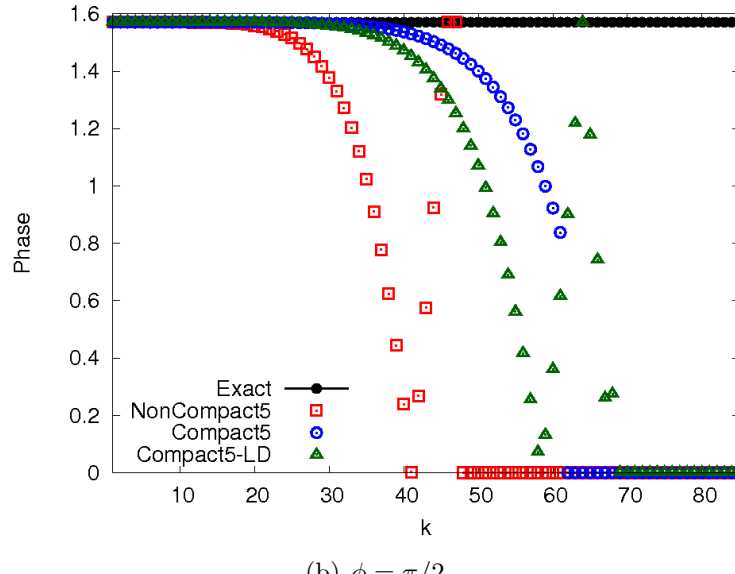
Figure 2.7: Energy spectrum for a smooth solution containing all the frequencies supported by the grid

phase on a grid with $N = 256$ points. The CRWENO5 and CRWENO5-LD schemes show a higher resolution of the extremum and a lower smearing of the discontinuity than the WENO5 scheme. The energy spectrum and phase errors are calculated. Figure 2.7 shows the energy (defined as $E(k) = |\hat{u}(k)|^2$, where $\hat{u}$ is the Fourier transform of u) as a function of the discrete wavenumber k for the initial conditions with $\phi = 0$. The energy spectrum for the case with $\phi = \pi/2$ is similar. The Compact5 and NonCompact5-LD schemes show an improved resolution of the higher frequencies due to their higher bandwidth resolving efficiencies. These observations are consistent with the spectral analysis presented in the previous section. The modified phase as a function of the wavenumber is shown in Fig. 2.8(a) for the two different values of the initial phase. The Compact5 and Compact5-LD schemes show a significantly lower phase error than the NonCompact5 scheme over a large range of wavenumbers. It should be noted that random values, followed by a zero phase,

(a) $\phi = 0$

(b) $\phi = \pi/2$

Figure 2.8: Phase errors for a smooth solution containing all the frequencies supported by the grid
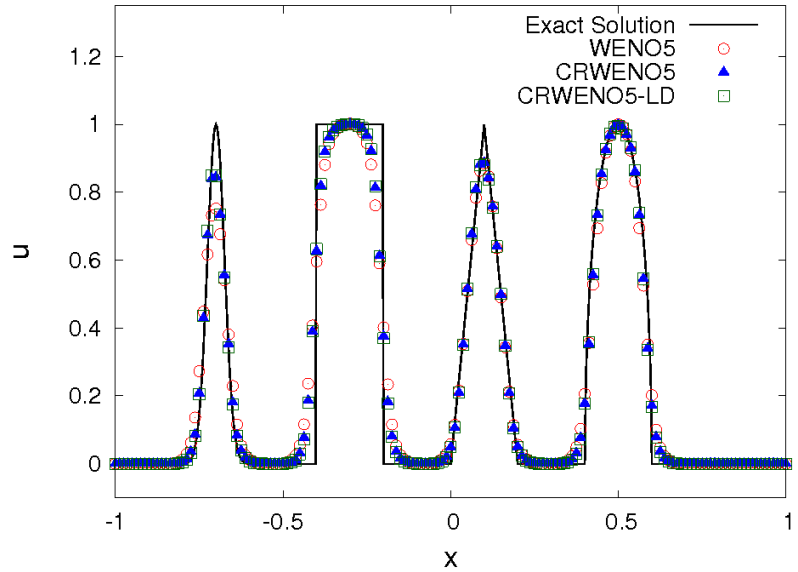
are observed for the modified phase beyond a certain wavenumber for each scheme. This is because the high dissipation at these wavenumbers reduces the amplitudes to near-machine-zero values and thus, the calculated values for the phase are not reliable.

Next, the behavior of the schemes across discontinuities is analyzed. The initial conditions are
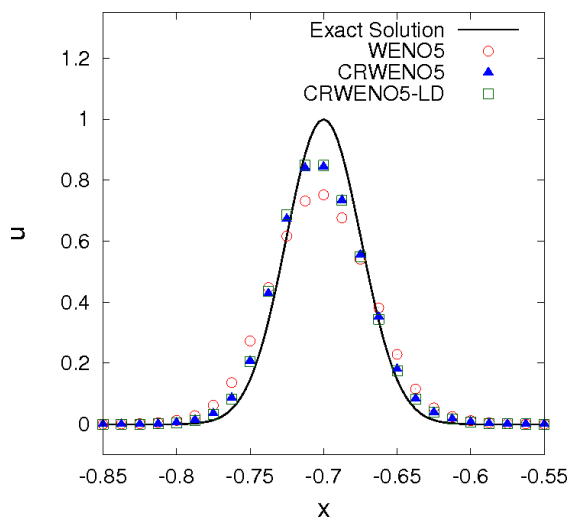
$$
\begin{aligned}
u_0(x) &= \exp\left(-\log(2)\frac{(x+7)^2}{0.0009}\right) \text{ if } -0.8 \leq x \leq -0.6 \\
&= 1 \text{ if } -0.4 \leq x \leq -0.2 \\
&= 1 - |10(x - 0.1)| \text{ if } 0 \leq x \leq 0.2 \\
&= [1 - 100(x - 0.5)^2]^{1/2} \text{ if } 0.4 \leq x \leq 0.6 \\
&= 0 \text{ otherwise} \quad\quad\quad\quad\quad\quad (2.40)
\end{aligned}
$$

thus consisting of exponential, square, triangular and parabolic waves. The domain is $-1 \leq x \leq 1$. Periodic boundary conditions are applied and the solution is obtained after one cycle over the domain at a CFL of 0.1.
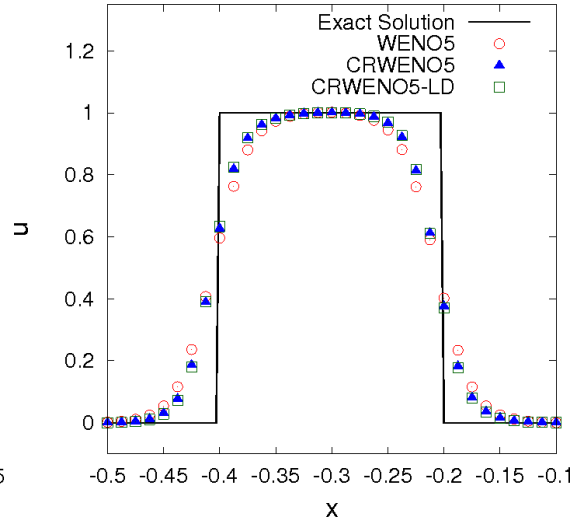
Figure 2.9(a) shows the solution on a grid with 160 points for the WENO5, CRWENO5 and CRWENO5-LD schemes after one cycle, while Fig. 2.9(b) and Fig. 2.9(c) show the magnified solution for the exponential and square waves. The CRWENO schemes show significantly reduced clipping of the extrema for the exponential wave and the discontinuities in the square waves show reduced smearing. The overall solution is essentially non-oscillatory, thus verifying the essentially non-oscillatory nature of the CRWENO schemes. As discussed in Sec. 2.2, the smoothness-dependent WENO weights are able to effectively decouple the interpolation of fluxes across the discontinuities. Figure 2.10 shows the triangular and parabolic waves after 100 cycles over the periodic domain. Although the difference in the solutions for these two waves is insignificant after 1 cycle, the lower errors

63

(a) Complete solution after 1 cycle

(b) Exponential wave after 1 cycle

(c) Square wave after 1 cycle

Figure 2.9: Comparison of WENO5, CRWENO5, and CRWENO5-LD schemes for a solution containing exponential, square, triangular and parabolic waves

from the CRWENO schemes result in better preservation of waves for long-term convection.

Thus, to summarize, the three cases of the linear advection equation demonstrate the numerical properties of the CRWENO schemes, with respect to the WENO

(a) Triangular wave after 100 cycles   (b) Parabolic wave after 100 cycles
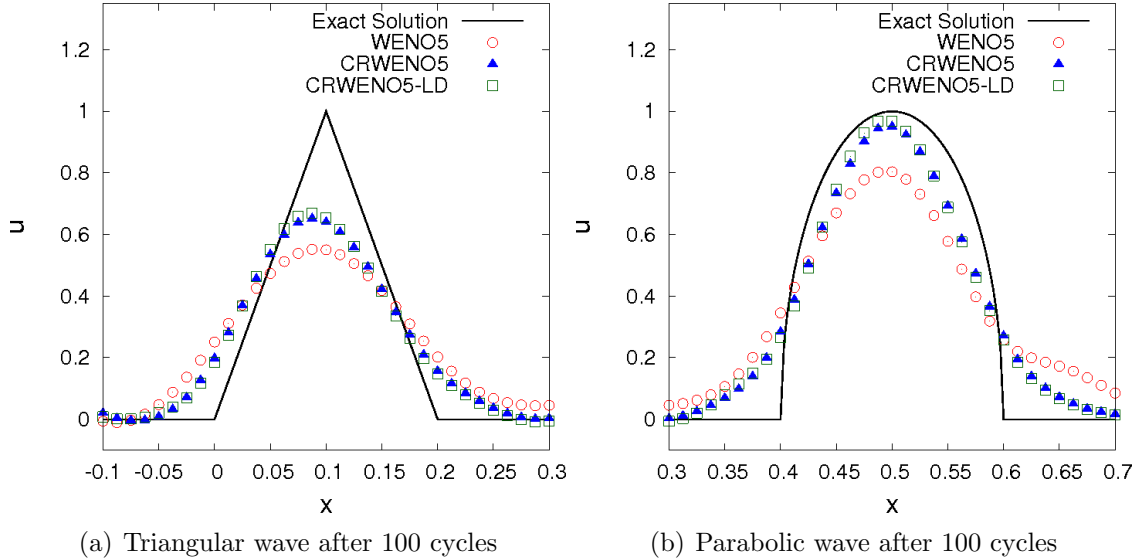
Figure 2.10: Comparison of schemes for long-term convection of discontinuous waves

scheme of the same order. The CRWENO schemes yield solutions with significantly lower errors for the same order of convergence as the WENO scheme. In addition, the improved spectral resolution results in a more accurate capturing of the higher wavenumbers or smaller length scales. The non-oscillatory nature of the scheme is verified for a problem with discontinuous waveforms and it is shown that the CRWENO schemes result in reduced clipping and smearing of extrema and discontinuities.

2.4.2   Inviscid Burgers Equation

The inviscid Burgers equation is an example of a scalar non-linear hyperbolic PDE, given by

$$u_t + uu_x = 0 \tag{2.41}$$

with the flux function as $f(u) = u^2/2$. The characteristic speed is $f'(u) = u$ and therefore, the solution consists of a wave propagating at the local value of u. A biased interpolation is used for the flux reconstruction at the interface, as expressed in Eqn. (1.21). The non-linearity of the equation implies that discontinuities may develop from smooth initial conditions. The shock formation from an initially smooth solution is examined. The problem provides an initial flow during which the solution is smooth, thus allowing for accuracy and order of convergence analyses. After a certain time, a shock forms in the solution and the non-oscillatory nature of the schemes can be verified. The initial condition is a sinusoidal wave given by

$$u_0(x) = \frac{1}{2\pi t_s} \sin(2\pi x) \tag{2.42}$$

where t_s is a free parameter specifying the time of shock formation ($t_s = 2$ in this example). Periodic boundary conditions are implemented and the exact solution, prior to shock formation, is defined implicitly as

$$u(x,t) = \frac{1}{2\pi t_s} \sin[2\pi(x - u(x,t)t)] \tag{2.43}$$

An iterative procedure with an initial guess is used to compute the exact solution to machine zero accuracy. The numerical solution is marched in time using the TVD-RK3 scheme.

Convergence analysis is done for solutions obtained at $t = 1$, prior to shock formation. The grid is progressively refined from 20 to 640 points. The initial CFL (for the grid with 20 points) is 0.1 and is reduced at each refinement to ensure that

66

(a) L_2 error and convergence behavior

(b) Solution shock formation
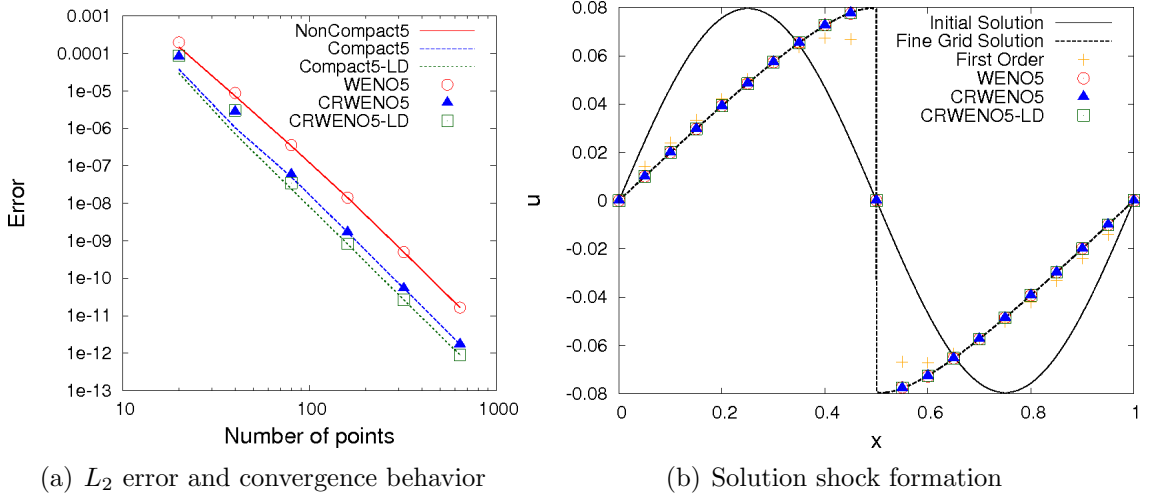
Figure 2.11: Inviscid Burgers equation - errors and convergence analysis before shock formation and solution with various schemes after shock formation
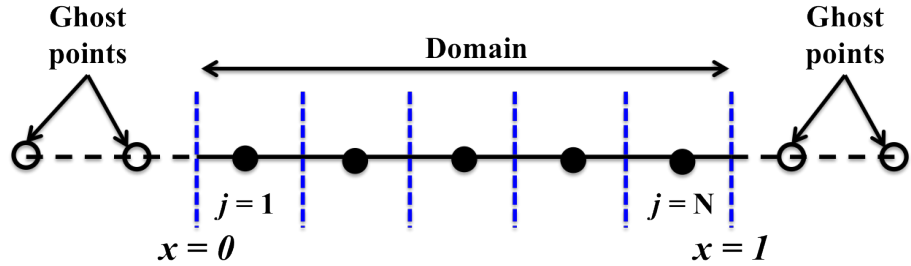
time discretization errors converge at the same order as space discretization ones. The L_2 errors are plotted against grid size in Fig. 2.11(a) for the WENO5, CRWENO5 and CRWENO5-LD schemes. Errors from the NonCompact5, Compact5 and Compact5-LD schemes are also plotted for comparison because the behavior should be identical for a smooth solution. It is observed that the WENO limiting results in non-optimal weights at very coarse grids. However, at finer grids, the WENO schemes attain their optimal accuracy and the errors are identical to the schemes without the non-linear weights. As in the case of the linear advection equation, the CRWENO5 scheme shows significantly lower errors (almost an order of magnitude lower) at all grid resolution, compared to the WENO5 scheme. The CRWENO5-LD scheme has an even lower error (half that of the CRWENO), except on very coarse meshes. The accuracy and convergence behavior of the CRWENO schemes are thus validated on a non-linear problem.

Figure 2.11(b) shows the solution at $t = 3$ after the formation of a shock on a grid with 20 points for a CFL of 0.5. Solutions obtained using the first-order, WENO5, CRWENO5 and CRWENO5-LD schemes are shown. The "fine grid solution" is the solution obtained on a grid of 2000 points with the WENO5 scheme since the exact solution is not available in analytical form. The solutions obtained using the WENO5, CRWENO5 and CRWENO5-LD schemes are seen to be nearly identical for this problem. The non-oscillatory nature of the CRWENO schemes is thus validated for a non-linear problem.
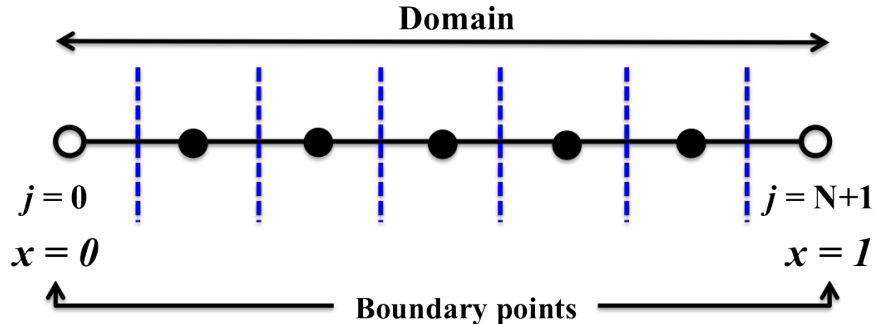
2.5   Boundary Closures

The numerical test cases presented in the previous section involved periodic boundaries representing an infinite domain. The implementation of boundary closures for the CRWENO schemes on a finite domain is discussed in this section. Compact schemes involve the coupled solution of the interface fluxes and thus, the formulation of a boundary closure is crucial to the stability and accuracy of the overall scheme.

Figure 2.12 shows two possible alignments between the physical domain and the grid for a one-dimensional domain $[0, 1]$ and N degrees of freedom. A grid used to discretize the domain for a finite-volume scheme is usually generated such that the cell interfaces align with the physical boundary. The interface flux may be calculated by extending the physical domain through "ghost" cells and applying the numerical

(a) Finite-volume discretization

(b) Finite-difference discretization

Figure 2.12: Two possible alignments between the grid and the domain boundary

scheme from the interior. The number of ghost cells required is proportional to the order of the interior scheme (and thus its stencil size). The values in the ghost cells are such that the computed flux at the boundary interface is consistent with the physical boundary conditions. The primary advantage of the "ghost" cell technique is that the reconstruction schemes from the interior may be applied to the boundary interface without modification.

Finite-difference methods are usually applied to grids where the boundary coincides with a grid point. The solution is specified at the first and last grid points and the governing equations are not solved for at these points. Since the domain does not extend beyond these points, a high-order numerical scheme cannot be applied to the interior points adjacent to these boundary points. Thus, a reduced-order and/or

biased numerical scheme is used at the grid points that do not have the sufficient number of neighbors required for the numerical scheme in the interior.

Although non-compact schemes may be applied without modification to the boundary interfaces for an interface-aligned boundary through ghost points (Fig. 2.12(a)), the application of compact schemes is not possible due to the absence of ghost interfaces. Specification of the flux at interfaces outside the physical domain may not be possible, except for very simple problems. In this study, the non-compact fifth-order WENO scheme (WENO5) is applied at the boundary interfaces along with the CRWENO5 scheme at the interior interfaces. Expressing this in the matrix-vector form of Eqn. (2.3), we obtain the complete numerical scheme for the left-biased flux at the interfaces as:

$$A\hat{\mathbf{f}} = B\mathbf{f} + \mathbf{b} \tag{2.44}$$

where

$$
A = \begin{bmatrix}
1 & & & & & \\
\frac{3}{10} & \frac{6}{10} & \frac{1}{10} & & & \\
& \frac{3}{10} & \frac{6}{10} & \frac{1}{10} & & \\
& & \ddots & \ddots & \ddots & \\
& & & \frac{3}{10} & \frac{6}{10} & \frac{1}{10} \\
& & & & & 1
\end{bmatrix}, \quad
B = \begin{bmatrix}
\frac{27}{60} & -\frac{1}{20} & & & & \\
\frac{19}{30} & \frac{1}{3} & & & & \\
\frac{1}{30} & \frac{19}{30} & \frac{1}{3} & & & \\
& & \ddots & \ddots & \ddots & \\
& & & \frac{1}{30} & \frac{19}{30} & \frac{1}{3} \\
& & & \frac{1}{30} & -\frac{13}{60} & \frac{47}{60}
\end{bmatrix} \tag{2.45}
$$

and the boundary terms are given by

$$\mathbf{b} = \begin{bmatrix} \frac{1}{30} f_{-2}^G - \frac{13}{60} f_{-1}^G + \frac{47}{60} f_0^G \\[1em] \frac{1}{30} f_0^G \\[2em] \\ \vdots \\ \\[2em] \frac{27}{60} f_{N+1}^G - \frac{1}{20} f_{N+2}^G \end{bmatrix} \tag{2.46}$$

with the superscript G denoting ghost cell values. The above expressions for A, B and $\mathbf{b}$ assume the optimal fifth-order compact and non-compact schemes, given by Eqns. (2.7) and (1.38) respectively. The corresponding expressions can be derived for the CRWENO5 scheme with WENO5 scheme at the boundaries by replacing the optimal coefficients with the WENO weights.

The boundary closure of the scheme for the second type of grid alignment (Fig. 2.12(b)) requires a biased and/or lower-order numerical scheme at the interfaces adjacent to the boundaries due to the unavailability of the complete stencil of the CRWENO5 scheme in the interior. It should be noted that although the stencil for the fifth-order compact scheme, given by Eqn. (2.7), is $[j - 1, j, j + 1]$, the calculation of the smoothness indicators requires a wider stencil $[j - 2, ..., j + 2]$ and thus, the overall CRWENO5 scheme has the larger stencil of $[j - 2, j + 2]$. Referring to Fig. 2.12(b), it can be seen that the CRWENO5 scheme can be applied to interfaces $j + 1/2, j = 2, N - 1$ and a biased numerical scheme is required for the remaining interfaces. In the present study, third-order boundary closures are

proposed as follows:

$$j = 0 \quad : \quad \frac{2}{3}\hat{f}_{j+1/2} + \frac{1}{3}\hat{f}_{j+3/2} = \frac{1}{6}\left(f_j + 5f_{j+1}\right) \tag{2.47}$$

$$j = 1 \quad : \quad \frac{1}{3}\hat{f}_{j-1/2} + \frac{2}{3}\hat{f}_{j+1/2} = \frac{1}{6}\left(5f_j + f_{j+1}\right) \tag{2.48}$$

$$j = N \quad : \quad \frac{2}{3}\hat{f}_{j-1/2} + \frac{1}{3}\hat{f}_{j+1/2} = \frac{1}{6}\left(f_{j-1} + 5f_j\right) \tag{2.49}$$

These boundary schemes correspond to the left-biased flux at the interfaces and are thus upwinded accordingly, subject to the physical domain constraint. It is also possible to use a fourth-order central compact scheme for $j = 1$. Similarly, the right-biased flux calculation would require a biased numerical scheme at interfaces $j = 1, N, N+1$ and the CRWENO5 scheme at all other interfaces. The complete left-biased discretization scheme resulting from the boundary closures given by Eqn. (2.47) can be expressed in the form of Eqn. (2.44) where

$$A = \begin{bmatrix} \frac{2}{3} & \frac{1}{3} & & & \\ \frac{1}{3} & \frac{2}{3} & & & \\ & \frac{3}{10} & \frac{6}{10} & \frac{1}{10} & \\ & & \ddots & \ddots & \ddots \\ & & \frac{3}{10} & \frac{6}{10} & \frac{1}{10} \\ & & & \frac{2}{3} & \frac{1}{3} \end{bmatrix}, \quad B = \begin{bmatrix} \frac{5}{6} & & & \\ \frac{5}{6} & \frac{1}{6} & & \\ \frac{1}{30} & \frac{19}{30} & \frac{1}{3} & \\ & \ddots & \ddots & \ddots \\ & \frac{1}{30} & \frac{19}{30} & \frac{1}{3} \\ & & \frac{1}{6} & \frac{5}{6} \end{bmatrix}, \quad \mathbf{b} = \begin{bmatrix} \frac{1}{6}f_0 \\ 0 \\ \vdots \\ \vdots \\ 0 \end{bmatrix}$$

$$\tag{2.50}$$

Note that f_0 is a boundary node with the solution specified and the boundary node f_{N+1} is not used since this is a left-biased interpolation.
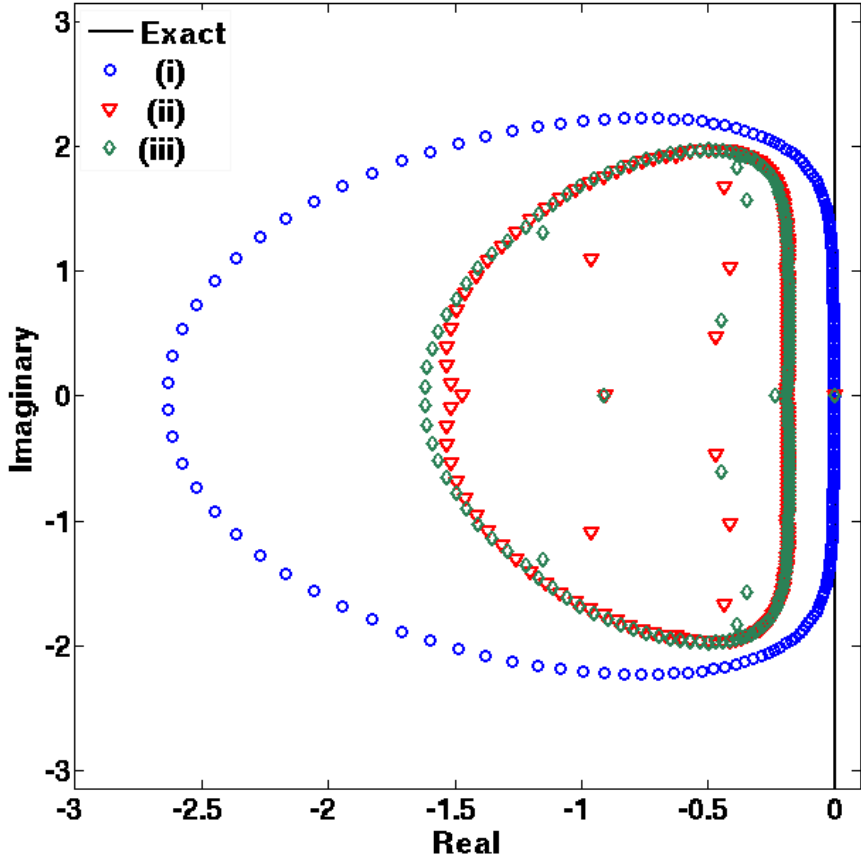
Figure 2.13: Eigenvalues of the CRWENO5 and its boundary closures – (i) Periodic CRWENO5, (ii) CRWENO5 with WENO5 at the boundaries (ghost cells), (iii) CRWENO5 with biased 3rd-order compact schemes on the boundaries

The numerical stability of the complete schemes can be analyzed by expressing

the vector of first derivatives as

$$\mathbf{f}' = \frac{1}{\Delta x}\mathbf{C}\hat{\mathbf{f}}$$

$$\Rightarrow \mathbf{f}' = \frac{1}{\Delta x}\mathbf{C}\mathbf{A}^-1\left(\mathbf{B}\hat{\mathbf{f}} + \mathbf{b}\right) \qquad (2.51)$$

where C is a $N \times (N+1)$ matrix given by

$$\mathbf{C} = \begin{bmatrix} -1 & 1 & & \\ & \ddots & \ddots & \\ & & -1 & 1 \end{bmatrix} \qquad (2.52)$$

The eigenvalues of the matrix $(CA^{-1}B)$ are evaluated numerically and shown in Fig. 2.13 for $N = 200$. The application of boundary closures increases the dissipation of the overall scheme at lower wavenumbers and reduces the spectral resolution. All the eigenvalues, for both the implementations considered in this section, have negative real parts confirming that the overall scheme is stable.

2.6 Computational Efficiency
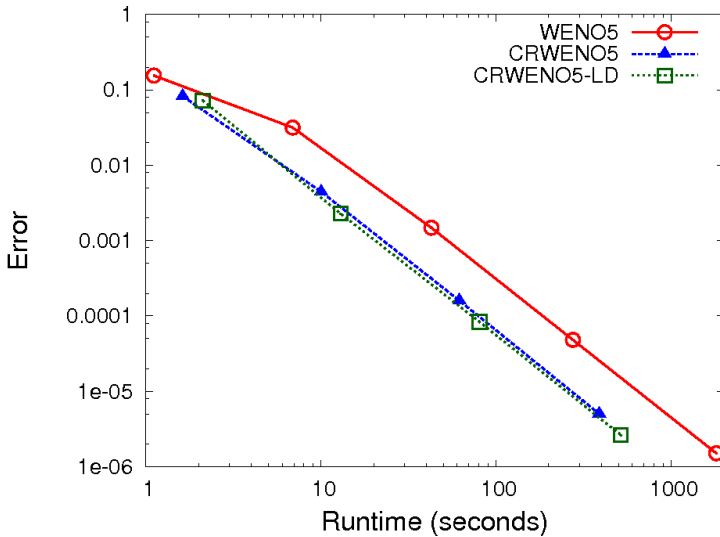
The CRWENO schemes require a coupled solution to the interpolated flux function. The reconstruction step results in a system of equations that can be expressed in matrix form as Eqn. (2.3). The left hand side is a tridiagonal matrix whose elements are solution-dependent. Thus, the solution to a tridiagonal system is required at each iteration and a pre-factoring of the matrix is not possible. However, the computational complexity of a tridiagonal solution scales linearly with the number of grid points. A one-dimensional problem requires one tridiagonal solution for each iteration, while for a multi-dimensional problem, the system is solved along each grid line in each dimension. As an example, for a two-dimensional problem, discretized on a grid with $NI \times NJ$ points, the number of tridiagonal solutions required is $NI + NJ$. Thus, at the same grid resolution, the CRWENO schemes are more expensive than the WENO schemes, keeping in mind that the calculation of smoothness indicators and the WENO weights is identical for the two schemes.

However, it has been shown in the previous section that the CRWENO schemes yield results that are substantially more accurate than the WENO scheme of the
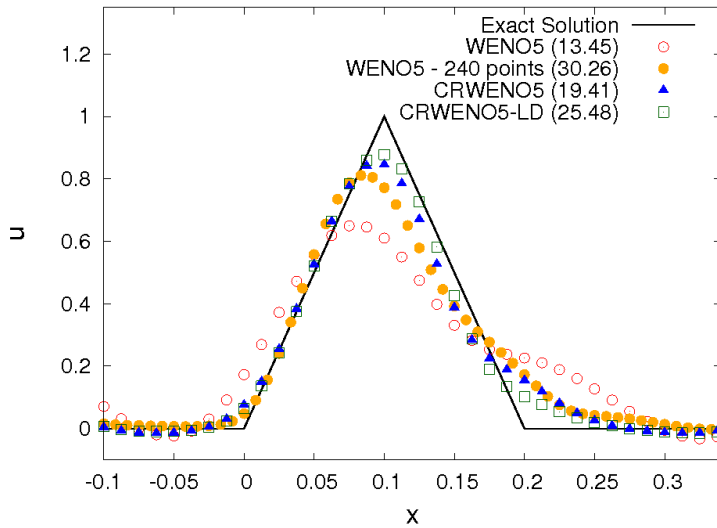
same order of convergence. Taylor series analysis, as well as numerical examples from the previous section, shows that the absolute error in solutions obtained by the CRWENO5 scheme is 1/10-th of the error in solutions obtained by the WENO5 scheme. Similarly, the error in solutions obtained by the CRWENO5-LD scheme is 1/20-th. This would imply that the CRWENO5 scheme is theoretically capable of obtaining a solution of the same accuracy as the WENO5 scheme on a grid with 0.63 times the number of points. The CRWENO5-LD scheme is capable of obtaining solutions of the same accuracy on a grid with 0.55 times the number of points. These represent substantial reduction in the computational expense, especially for multi-dimensional problems (for example, a three-dimensional grid with 0.63 times the number of points in each dimension has only 1/4-th the total number of points as the original grid). Thus, when comparing solutions with the same absolute errors, the CRWENO schemes are less expensive.

Table 2.9: Errors and computational run-time (in seconds) with smooth initial data

N	WENO5		CRWENO5		CRWENO5-LD	
	Error	T	Error	T	Error	T
20	1.549E-01	1.11	8.236E-02	1.62	7.201E-02	2.11
30	8.416E-02	2.45	-	-	-	-
40	3.155E-02	6.89	4.436E-03	10.02	2.277E-03	12.94
60	5.729E-03	15.20	-	-	-	-
80	1.480E-03	42.73	1.603E-04	61.66	8.343E-05	80.53
120	2.033E-04	95.28	-	-	-	-
160	4.824E-05	268.85	5.047E-06	388.24	2.635E-06	516.89
240	6.404E-06	602.76	-	-	-	-

(a) Error vs. computational run-time for a smooth problem

(b) Comparison of solution and runtimes on a 160-point grid for a discontinuous problem (Number inside parentheses in the legend indicates runtimes)

Figure 2.14: Computational efficiencies of various schemes

Table 2.9 shows the L_2 errors and the corresponding computational run-time (T) for solutions of the linear advection equation, obtained after 500 cycles over the periodic domain. Smooth initial conditions are specified, as given in Eqn. (2.38). The grid is progressively refined starting with 20 points. The errors for the CR-

76

WENO5 and CRWENO5-LD are an order of magnitude lower than those of the WENO5 scheme. In addition, corresponding to each grid resolution, the error and the run-time for a solution obtained by WENO5 scheme on a grid that is 1.5 as fine are also shown. The CRWENO schemes are more expensive than the WENO5 scheme for the same grid resolution, as expected. However, a comparison of the errors show that the errors in the CRWENO solutions are comparable to those in the WENO solutions on grids that are 1.5 times as fine. Thus, the run-time for the CRWENO scheme is lower when solutions with similar errors are compared. As an example, the CRWENO5 scheme on a 80-point grid has an error slightly lower than that of the WENO5 scheme on a 120 point grid, while the run-time is lower by a factor of around 2/3. The L_2 norm of the error as a function of the computational run-time is shown in Fig. 2.14(a). The WENO5, CRWENO5 and CRWENO5-LD schemes are compared and the previous conclusions are reiterated. The CRWENO schemes have a significantly lower computational cost when comparing solutions with similar errors.

Although the Taylor series analysis does not hold for solutions with discontinuities, the resolution of the solutions obtained with the WENO5, CRWENO5 and CRWENO5-LD schemes are compared for a problem with discontinuous waves. Figure 2.14(b) shows the magnified solution around the triangular wave for the initial conditions specified by Eqn. (2.40). The solutions are obtained after 100 cycles over the periodic domain on a grid of 160 points. The number inside the parentheses in the legend indicates the run-times. As observed in the previous section, the CRWENO5 and CRWENO5-LD schemes yield solutions with sharper resolu-

77

tion than the WENO5 schemes. The run-times for these schemes are larger than the WENO5 scheme on the same grid, as expected. The solution obtained by the WENO5 scheme on a 240-point grid is included in the figure. The resolution of the solutions obtained with the CRWENO schemes is comparable, or better than, to that of the WENO5 solution on the finer grid. However, the run-time for the WENO5 scheme on the 240-point is higher than that of the CRWENO schemes on the 160-point grid. Thus, it is observed that for solutions with discontinuities, the CRWENO schemes are computationally less expensive when solutions of the same resolution are compared.

The computational efficiency of the CRWENO schemes is demonstrated for the scalar conservation laws in one-dimension. Although the tridiagonal solution at each iteration renders these schemes more expensive for a given grid, the resulting improvements in accuracy and resolution justify the expense. The CRWENO schemes are less expensive than the WENO schemes when solutions of similar accuracy and resolution are compared. The computational efficiency of these schemes for systems of equations is discussed in subsequent chapters where the application of the CRWENO schemes to the Euler and Navier-Stokes equations is presented.

2.7   Implementation of Non-Linear Weights

The implementation of the non-linear weights affects the numerical properties of the WENO schemes and was briefly discussed in Section 1.3.1. The numerical properties of the various implementations are discussed in the present section in the

context of the CRWENO schemes. The fifth-order CRWENO schemes described in Section 2.2 use weights as defined in [13]. The WENO weights are calculated as:

$$\alpha_k \;=\; \frac{c_k}{(\epsilon + \beta_k)^p} \tag{2.53}$$

$$\omega_k \;=\; \frac{\alpha_k}{\sum_k \alpha_k} \tag{2.54}$$

with $\epsilon = 10^{-6}$ and $p = 2$. The first step scales the optimal weights with the corresponding smoothness indicators while the second step makes the weights convex. The smoothness indicators are defined as Eqn. (1.36) that results in Eqn. (1.38) - (1.40) for the fifth-order WENO and CRWENO schemes. Thus, for $r = 3$, the smoothness indicators are the sum of the divided differences approximating the first and second derivatives of the solution. In the subsequent discussion and following chapters, the fifth-order CRWENO scheme using the implementation of the weights as defined by Eqn. 2.53 is referred to as CRWENO5-JS.

The parameter ϵ was introduced in [13] to prevent division by zero. Although it is not desirable that the numerical properties of the scheme be dependent on the value of ϵ, numerical experiments [16] reveal that the convergence properties of the WENO schemes is severely influenced by ϵ for a certain class of smooth solutions. The convergence of the WENO schemes was studied for a smooth problem with critical points where the first and higher derivatives vanish. It was shown that for such problems, the WENO schemes converged at their optimal order for $\epsilon = 10^{-6}$ but showed sub-optimal convergence for $\epsilon = 10^{-40}$. At critical points, the smoothness indicators approach zero ($\beta_k \to 0$) and the denominator in Eqn. (2.53) is dominated by ϵ. A higher value of ϵ results in the weights being nearly optimal and the WENO

schemes converge at their optimal order. However, if the value of ϵ that is of the same or lower order than the machine representation of zero, the differences in the values of the smoothness indicators, which are of the order of machine zero, result in non-optimal weights.

A mapping function was introduced in [16] to partially correct the dependence of the convergence rate on ϵ. The mapping function, given by Eqn. (1.43), causes the non-linear weights to converge more rapidly to their optimal values. The weights, calculated using Eqn. (2.53) and (2.54), are then mapped by Eqn. (1.44) followed by Eqn. (2.54) for convexity. The CRWENO5 scheme with the mapped weights is referred to as CRWENO5-M in this thesis.

The non-linear weights, as defined in [13], seek to reduce or eliminate the contribution of the constituent interpolation stencils that contain discontinuities. This results in a smearing of discontinuities due to dissipation. The mapping function results in increasing the weights corresponding to the discontinuous data, without compromising the non-oscillatory nature of the scheme. Thus, the numerical results in [16] show sharper resolution of discontinuities. The primary drawback of the mapping function is the additional computational expense required to calculate the mapped weights. An alternative implementation for the non-linear weights was proposed in [17], that resulted in optimal convergence of the WENO scheme for smooth problems containing critical points. The weights are defined as

$$\omega_k = c_k \left[1 + \left(\frac{\tau_5}{\beta_k + \epsilon} \right)^p \right] \tag{2.55}$$

followed by Eqn. (2.54) for convexity. The factor τ_5 (the subscript denotes the

optimal order) is defined as

$$\tau_5 = |\beta_1 - \beta_3| \tag{2.56}$$

and is a measure of the higher derivatives of the solution using the information from all points in the interpolation stencil. The magnitude of τ_5 is much lower than β_k for a solution that is smooth and thus, the weights attain their optimal values. In the presence of a discontinuity, τ_5 is large as it contains information from the complete higher-order stencil but β_k is small for the sub-stencils that are smooth. This results in lower weights for the stencils that contain a discontinuity. The CRWENO5 scheme using the weights as defined above is referred to as CRWENO-Z in the text.

The definition of the non-linear weights as given by Eqn. (2.55) was further improved in [19, 20] for a fifth-order scheme. Definition of $\tau_5 = |\beta_1 - \beta_3|$ results in a loss of accuracy at points where $\beta_1 - \beta_3$ changes sign. Thus, the improved definition of τ_5 is

$$\tau_5 = (f_{j-2} - 4f_{j-1} + 6f_j - 4f_{j+1} + f_{j+2})^2 \tag{2.57}$$

which is the fourth-degree undivided difference. The CRWENO5 scheme with the weights defined as Eqn. (2.55) and (2.57) is referred to as CRWENO5-YC in subsequent discussion. Table 2.10 summarizes the implementations of the CRWENO5 scheme that are studied in this thesis.

The convergence properties of the various implementations of the non-linear weights are studied on a smooth problem that has critical points. The initial conditions are given as:

$$u_0(x) = \sin\left(\pi x - \frac{\sin(\pi x)}{\pi}\right) \tag{2.58}$$

Table 2.10: Implementation of non-linear weights for the CRWENO5 scheme (referred to in the text)

Name of Scheme	Implementation of Weights	Author(s)
CRWENO5-JS	Eqn. (2.53)	Jiang & Shu [13]
CRWENO5-M	Eqns. (2.53), (1.44)	Henrick, Aslam & Powers [16]
CRWENO5-Z	Eqns. (2.55), (2.56)	Borges, et. al. [17]
CRWENO5-YC	Eqns. (2.55), (2.57)	Yamaleev & Carpenter [19, 20]

Table 2.11: L_2 errors and convergence rates for the CRWENO5-JS

N	$\epsilon = 10^{-6}$		$\epsilon = 10^{-20}$	
	Error	r_c	Error	r_c
20	3.825E-03	-	3.825E-03	-
40	2.172E-04	4.14	2.174E-04	4.14
80	1.082E-05	4.33	1.096E-05	4.31
160	6.178E-07	4.13	7.059E-07	3.96
320	2.089E-08	4.89	5.266E-08	3.74

Table 2.12: L_2 errors and convergence rates for the CRWENO5-M

N	$\epsilon = 10^{-6}$		$\epsilon = 10^{-20}$	
	Error	r_c	Error	r_c
20	6.785E-04	-	6.786E-04	-
40	1.387E-05	5.61	1.388E-05	5.61
80	3.649E-07	5.25	3.659E-07	5.25
160	1.061E-08	5.10	1.069E-08	5.10
320	3.229E-10	5.04	3.242E-10	5.04

with the domain as $-1 \leq x \leq 1$. Periodic boundary conditions are applied at both ends and the solution is marched in time using the TVD-RK3 scheme. A grid convergence study is carried out for each of the schemes listed in Table 2.10 for $\epsilon = 10^{-6}$ and $\epsilon = 10^{-20}$.

Tables 2.11 - 2.14 show the L_2 error norms and the rates of convergence (r_c) for the CRWENO5-JS, CRWENO5-M, CRWENO5-Z and CRWENO5-YC schemes
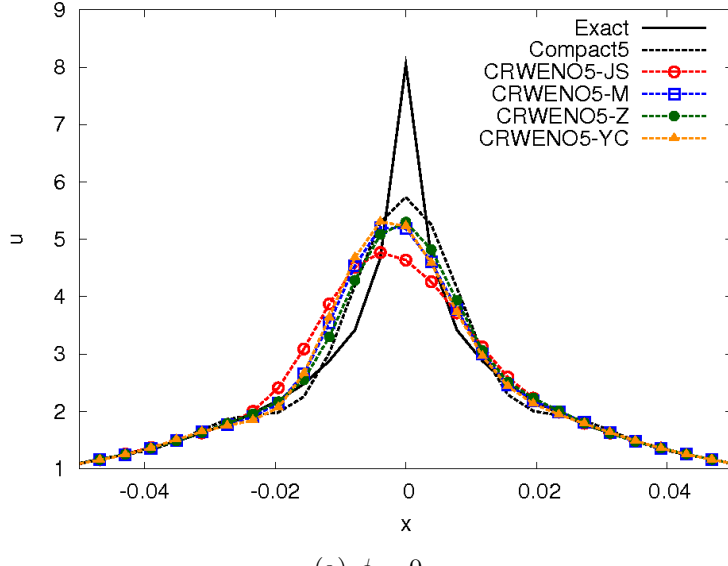
Table 2.13: L_2 errors and convergence rates for the CRWENO5-Z

| N | $\epsilon = 10^{-6}$ | | $\epsilon = 10^{-20}$ | |
	Error	r_c	Error	r_c
20	1.312E-03	-	1.313E-03	-
40	2.336E-05	5.81	2.342E-05	5.81
80	4.430E-07	5.72	4.511E-07	5.70
160	1.085E-08	5.35	1.147E-08	5.30
320	3.229E-10	5.07	3.324E-10	5.11
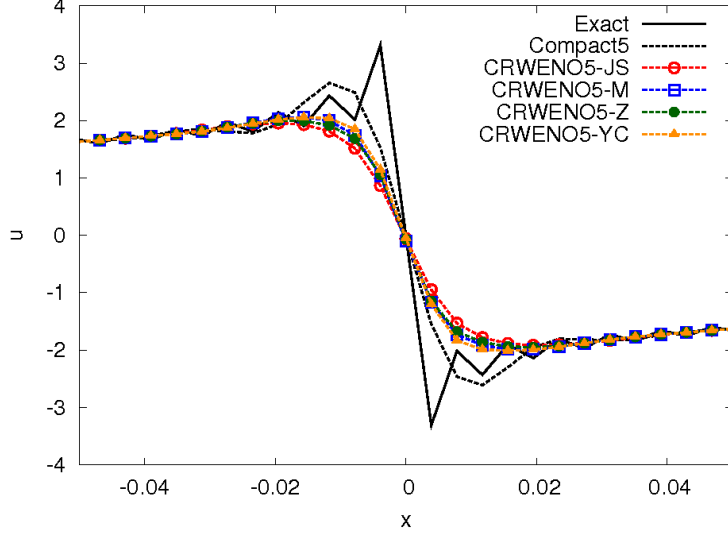
Table 2.14: L_2 errors and convergence rates for the CRWENO5-YC

| N | $\epsilon = 10^{-6}$ | | $\epsilon = 10^{-20}$ | |
	Error	r_c	Error	r_c
20	4.530E-04	-	4.529E-04	-
40	1.226E-05	5.21	1.226E-05	5.21
80	3.528E-07	5.12	3.528E-07	5.12
160	1.056E-08	5.06	1.059E-08	5.06
320	3.229E-10	5.03	3.229E-10	5.03

for the two different ϵ values. It is observed that the CRWENO5-JS scheme does not converge at the optimal order for this problem. The smoothness indicators approach zero at the critical points and the weights are sensitive to ϵ. The order of convergence is closer to 5th-order for a higher ϵ. The accuracy and convergence are improved by the mapping of the weights, as seen by the errors in the solution obtained by the CRWENO-M scheme. The optimal order of convergence is recovered and the absolute errors have similar values for the two different ϵ, thus indicating insensitivity to ϵ. A similar observation regarding the absolute errors is made for the CRWENO-Z scheme; however, the order of convergence is higher than 5th-order for coarse grids, indicating non-optimal weights. The CRWENO5-YC scheme yields solutions that converge at the optimal order, for both ϵ. The errors are insensitive to ϵ and are lower than those for the other schemes on coarse grids.

(a) $\phi = 0$

(b) $\phi = \pi/2$

Figure 2.15: Solution after one cycle for initial conditions with all frequencies supported by the grid

The dependence of the spectral resolution on the implementation of the nonlinear weights is assessed by solving the linear advection equation with the initial conditions given by Eqn. (2.39) for $\phi = 0$ and $\phi = \pi/2$. The solution is obtained after one cycle over the periodic domain and the TVD-RK3 scheme is used for ad-
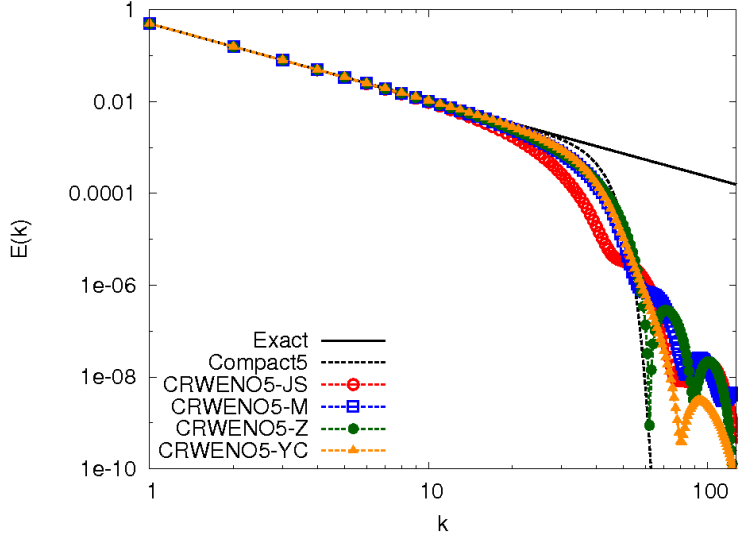
Figure 2.16: Energy spectrum for various implementations of the non-linear weights

vancing the solution in time. Figure 2.15 shows the solution for both the values of ϕ

obtained on a grid with 256 points. The solution is magnified around the extremum

and the discontinuity. The CRWENO5-JS scheme shows significant dissipative and

dispersive errors for the extremum and a considerable amount of smearing for the

discontinuity. The alternate implementations of the weights result in a sharper res-

olution of both the solutions. Figure 2.16 shows the energy $E(k)$ as a function of

the wavenumber for the solutions to the initial conditions with $\phi = 0$. The so-

lutions are obtained with the various CRWENO5 schemes ($\epsilon = 10^{-6}$) as well as

the optimal Compact5 schemes. Although the solution is smooth, the CRWENO5

schemes are more dissipative than the optimal scheme at the higher wavenumbers.

At these wavenumbers, the waves are resolved by very few points and thus, the

gradients in the solution are large. The weights are not optimal, resulting in ex-

cessive dissipation. The CRWENO5-M, CRWENO5-Z and CRWENO5-YC show

an improved resolution compared to the CRWENO5-JS scheme. A similar energy

(a) $\phi = 0$

(b) $\phi = \pi/2$
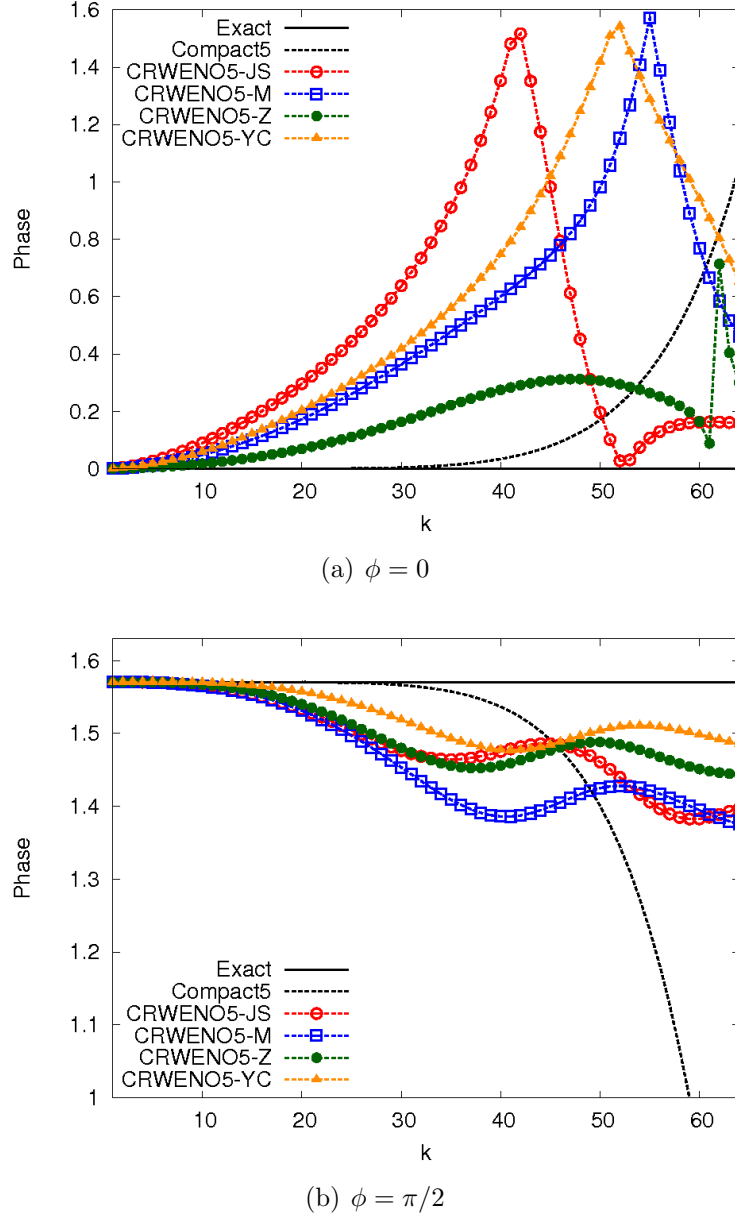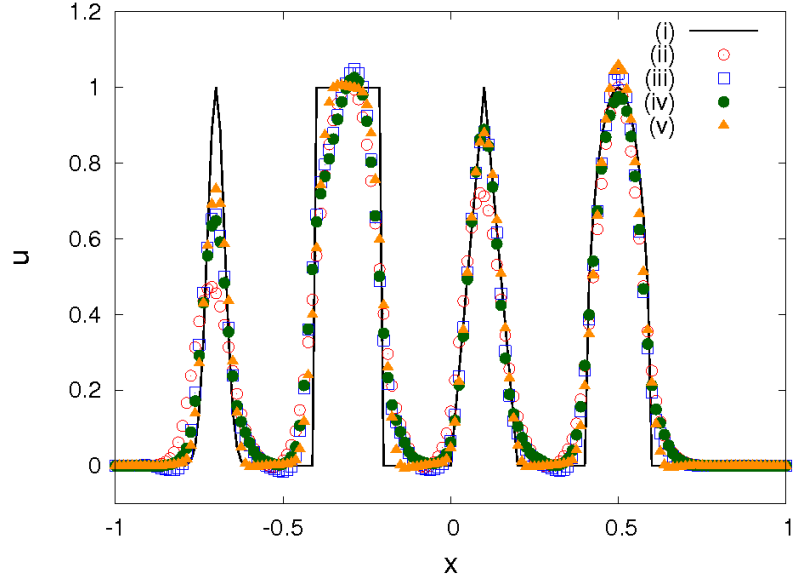
Figure 2.17: Phase errors for various implementations of the non-linear weights

spectrum is observed for the initial conditions with $\phi = \pi/2$. The phase errors for

the various schemes are shown in Fig. 2.17(a) for the two different values of the

initial phase ϕ. The CRWENO5-JS shows a significant error in phase for a large

range of wavenumbers for the solution with $\phi = 0$ (extremum). The CRWENO5-M

and CRWENO5-YC schemes also show a significant phase error, compared to the
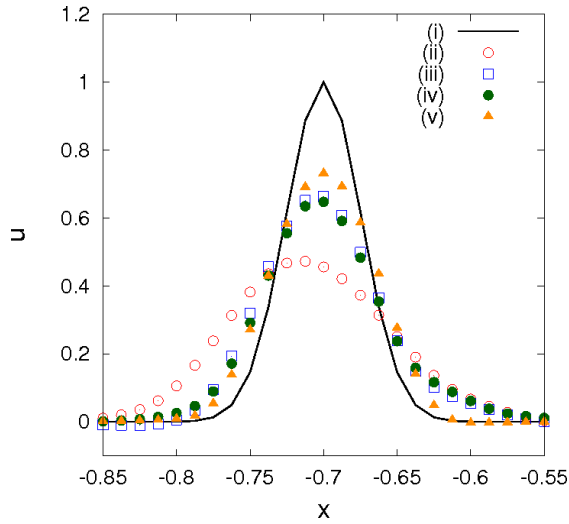
Compact5 scheme, while the CRWENO5-Z scheme results in relatively low phase errors. However, for the solution with $\phi = \pi/2$ (discontinuity), the CRWENO5-YC scheme results in solutions with the least phase error while the CRWENO5-M scheme exhibits significantly large errors. The phase errors in the solutions obtained by the CRWENO5-JS and CRWENO5-Z schemes are similar except at very high wavenumbers.

The behavior of the weights is analyzed for a problem consisting of discontinuous waves. The initial conditions are given by Eqn. (2.40) over the periodic domain $-1 \leq x \leq 1$. The solution is advanced in time using the TVD-RK3 scheme for 50 cycles over the domain. The solutions obtained using the CRWENO5-JS, CRWENO5-M, CRWENO5-Z and CRWENO5-YC schemes are shown in Fig. 2.18. The alternative formulations for the non-linear weights improve the resolution of the solution. Figures 2.18(b) and 2.18(c) show the solution magnified around the exponential and square waves respectively. The dissipation across the exponential wave is significantly reduced with the mapping of weights or reformulating them with Eqn. (2.55), with CRWENO5-YC scheme showing the least dissipation. The smearing of the discontinuities for the square wave is reduced with the CRWENO5-M and CRWENO5-Z schemes while the solution obtained using the CRWENO5-YC scheme exhibits the least amount of smearing and distortion.
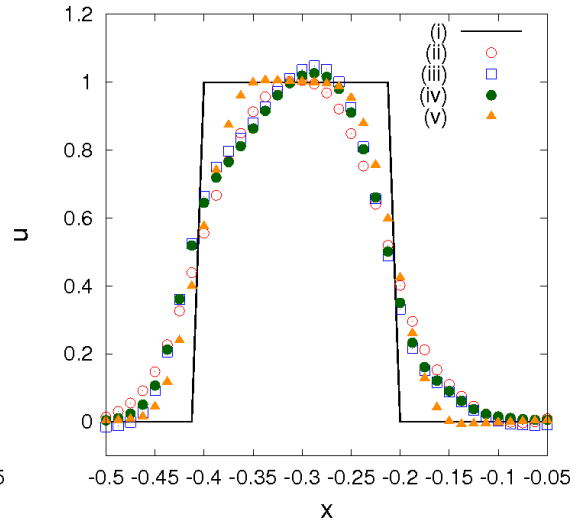
The effect of the various implementations of the non-linear weights is compared for this particular problem. Figure 2.19 shows the three weights ($\omega_{1,2,3}$) over the domain for the various schemes. The solution consists of sharp discontinuities with

(a) Complete solution after 50 cycles

(b) Exponential wave after 50 cycles

(c) Square wave after 50 cycles

Figure 2.18: Comparison of CRWENO5 scheme with the various non-linear weights for a discontinuous solution: (i) Exact Solution, (ii) CRWENO5-JS, (iii) CRWENO5-M, (iv) CRWENO5-Z, (v) CRWENO5-YC

smooth regions in between. The weights computed by the CRWENO5-JS scheme are far from optimal throughout the domain. The mapping function causes the weights to converge more rapidly to their optimal values and this is observed for the weights computed by CRWENO5-M. A similar observation is made for the CRWENO5-Z

(a) CRWENO5-JS

(b) CRWENO5-M

(c) CRWENO5-Z
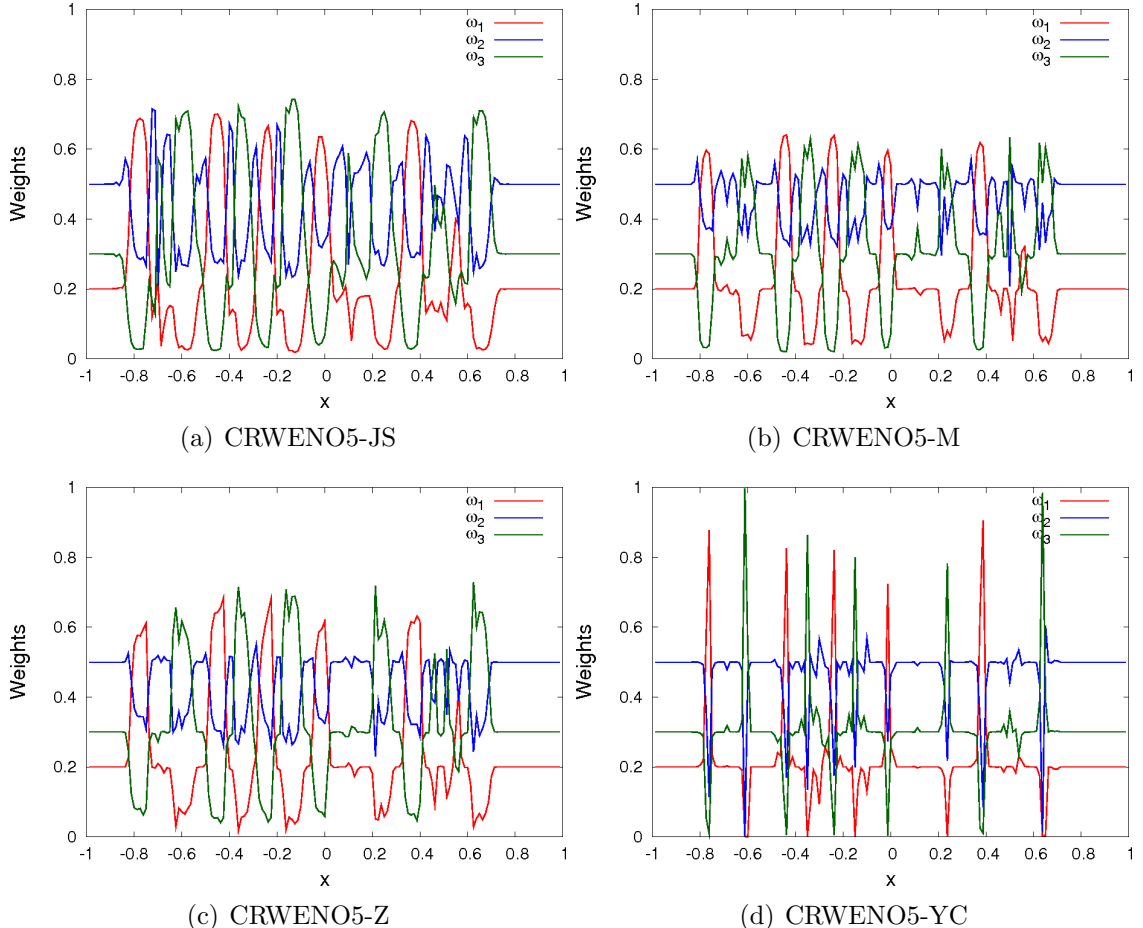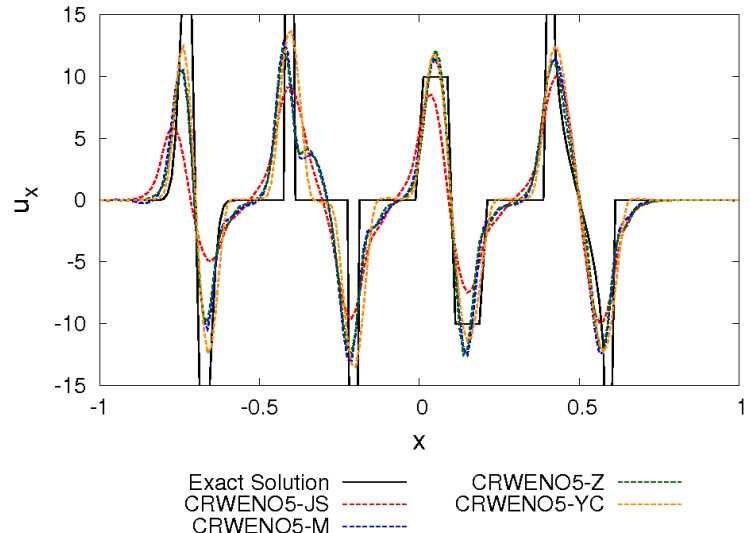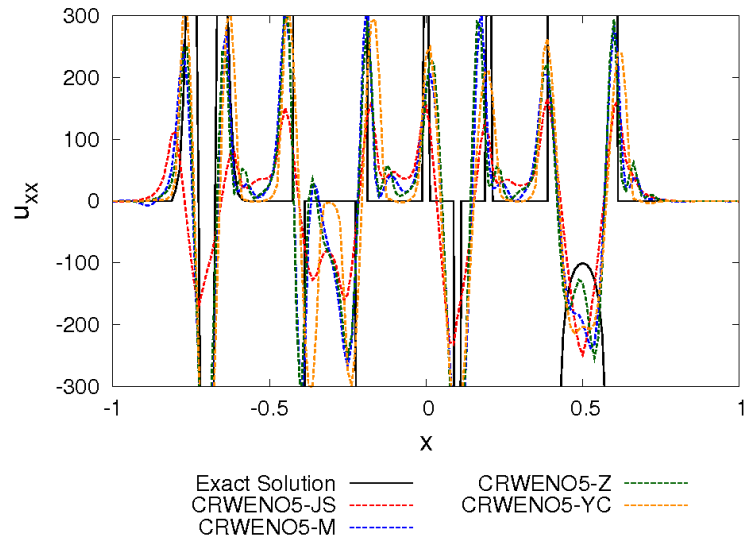
(d) CRWENO5-YC

Figure 2.19: Comparison of the weights for a discontinuous solution after one cycle

with the computed weights being nearer to their optimal values compared to the

CRWENO5-JS scheme. The weights computed by the CRWENO5-YC scheme are

observed to be the closest to their optimal values in the smooth regions of the

solution. The weights for stencils containing the discontinuities go to zero at the

discontinuity with minimal smearing.

The solutions obtained by the various implementations of the weights are non-

oscillatory for discontinuities. However, oscillations in the higher derivatives may

exist. Figure 2.20 shows the first and second derivatives for the same solution shown

in Fig. 2.18. The improved resolution of the solution with the alternative implemen-

(a) First derivative

(b) Second derivative

Figure 2.20: Effect of non-linear weights on higher derivatives for a discontinuous solution

tation of weights is also visible for the higher derivatives, with the solution obtained using the CRWENO5-JS scheme being very dissipative. However, the CRWENO5-M and CRWENO5-Z schemes show slight oscillations in the first derivative (around $x = -0.4$). The oscillations are more pronounced in the second derivative where CRWENO5-JS, CRWENO5-M and CRWENO5-Z show oscillations in the smooth

regions between the discontinuities. The solution obtained using the CRWENO5-YC scheme is observed to be non-oscillatory in this case for the higher derivatives.

2.8   Summary of Chapter

The Compact-Reconstruction WENO schemes are introduced in this chapter. Lower-order conservative compact schemes are identified for the interpolation of the interface fluxes. The optimal coefficients are calculated such that the weighted sum results in a higher-order conservative compact interpolation scheme for the interface flux. The CRWENO scheme is obtained by replacing the optimal coefficients with solution-dependent weights that are a function of the local smoothness of the solution. The weights approach the optimal coefficients for smooth solutions and approach zero in the presence of a discontinuity. A fifth-order accurate CRWENO scheme is given by Eqn. (2.19) and a low-dissipation variant is given by Eqn. (2.29).

The solution-dependent weights result in an interpolation scheme that is high-order accurate when the solution is locally smooth. At and near discontinuities, the scheme behaves like a biased compact scheme such that the grid cells containing the discontinuity are avoided. The calculation of the right-hand sides of Eqns. (2.19) and (2.29) avoids the discontinuities in a way similar to the traditional WENO schemes. The WENO weights result in a decoupling of the solution across the discontinuities by appropriately biasing the terms on the left-hand side. The resulting system of equations involves a coupling of the solution within the smooth regions of the solution. The decoupling of the solution across the discontinuities avoids spurious

oscillations in the solution.

The numerical properties of the linear, high-order compact schemes underlying the fifth-order CRWENO schemes are studied. A Taylor series analysis is carried out and the dissipation and dispersion errors are calculated. The dissipation error for the fifth-order compact scheme is 1/10-th that of the fifth-order non-compact scheme that underlies the traditional WENO scheme. The dissipation error for the low-dissipation compact scheme is 1/20-th that of the non-compact scheme. A comparison of the dispersion error shows that the compact schemes have an error that is 1/15-th that of the non-compact scheme. Thus, it is expected that the compact schemes will yield a solution of the same accuracy on a coarser grid. A Fourier analysis is used to find the spectral resolution of the schemes. The compact schemes have a significantly higher spectral resolution than the non-compact scheme. It is found that the fifth-order compact schemes had a higher spectral resolution than the ninth-order non-compact scheme. The bandwidth resolving efficiency is compared and the conservative compact schemes presented in this chapter compare well with high-resolution schemes presented in the literature.

The CRWENO schemes are applied to the linear advection equation. The accuracy and order of convergence are studied for a smooth problem and the conclusions drawn from the Taylor series analysis are verified. The convergence of the WENO weights to the optimal coefficients is verified. The spectral properties are assessed for a smooth problem comprising all length scales supported by the interpolation scheme. The dissipation and phase errors are compared as a function of the wavenumber. The higher spectral resolution of the compact schemes

is demonstrated. The non-oscillatory behavior of the compact schemes is verified for a problem with various discontinuous waveforms. The resolution of the waveforms and the ability to preserve the waves for long-term convection is compared and the CRWENO schemes show an improved behavior compared to the WENO scheme. The accuracy, convergence and non-oscillatory behavior are also verified for the inviscid Burger's equation.

The CRWENO schemes require a tridiagonal solution at each iteration and this introduces a computational overhead. At the same grid resolution, the CRWENO schemes are more expensive than the WENO scheme. The absolute errors and the computational run-time are studied for a smooth problem at various grid refinement levels. It is demonstrated that the CRWENO schemes are less expensive when comparing solutions with the same absolute error because a coarser grid can be used with the CRWENO scheme. Similarly, for discontinuous problems, CRWENO schemes yield solutions with comparable resolution on a coarser grid and are less expensive. Thus, the CRWENO schemes have a higher computational efficiency.

Finally, the implementation of the solution-dependent weights is studied. The drawbacks of the implementation given in [13] are explored in the context of the CRWENO5 scheme and the alternative implementations [16, 17, 19, 20] are studied. The accuracy and convergence of the various implementations are assessed on a smooth problem with critical points. The optimal order of convergence is recovered with the alternative formulations. These formulations for the non-linear weights are also observed to improve the spectral properties of the CRWENO5 scheme. The resolution and smoothness of the solution as well as its higher derivatives are studied

for the problem consisting of discontinuous waveforms. The alternative formulations result in higher resolution. Although the solution is smooth, oscillations are observed in the higher derivatives that are absent for the CRWENO5-YC scheme.

The CRWENO5 schemes are applied to the Euler equations in the next chapter. The extension of these schemes to a system of equations is described. The schemes are applied to the conserved, primitive and characteristic variables and results are compared. Several inviscid flow problems are solved to validate the CRWENO schemes, as well as demonstrate its superior numerical properties on benchmark problems. The numerical cost of the compact schemes is studied and the computational efficiency is compared with the WENO scheme.

Chapter 3

Application to Euler Equations

The Compact-Reconstruction WENO schemes were introduced in the preceding chapter. The adaptive stenciling of the WENO schemes is applied to the compact schemes. The resulting CRWENO schemes have higher accuracy and spectral resolution for the same order of convergence. The schemes were applied to the scalar conservation laws and the numerical properties were verified for smooth problems as well as problems with discontinuities. The numerical cost of the schemes was analyzed and the CRWENO schemes were shown to be more computationally efficient than the traditional WENO schemes. The present chapter extends these schemes to the Euler equations of fluid dynamics.

The Euler equations form a hyperbolic system of partial differential equations. The numerical solution of this system along with the application of the CRWENO schemes is presented. The relative merits and demerits of applying the compact schemes to the primitive, conserved and characteristic variables are discussed. The convergence and accuracy of the CRWENO schemes are verified on a smooth, one-dimensional problem and compared with the WENO schemes. Several one- and two-dimensional benchmark problems are solved to validate the schemes as well as demonstrate their numerical properties.

3.1 Euler Equations

The Euler equations govern inviscid flows [2] and are derived from the Navier-Stokes equations by assuming zero viscosity and heat conduction. The equations represent the conservation of mass, momentum and energy for a given flow. Mathematically, the compressible Euler equations are a system of hyperbolic conservation laws. The equations are expressed as:

$$\frac{\partial \rho}{\partial t} + \frac{\partial \rho u_i}{\partial x_i} = 0 \tag{3.1}$$

$$\frac{\partial \rho u_j}{\partial t} + \frac{\partial \rho u_i u_j}{\partial x_i} = -\frac{\partial p}{\partial x_j} \tag{3.2}$$

$$\frac{\partial e}{\partial t} + \frac{\partial (e + p) u_i}{\partial x_i} = 0 \tag{3.3}$$

where $i, j = 1, \ldots, D$ with D being the number of dimensions. The density is given by ρ, the velocity components along each dimension is u_i, p is the pressure and the internal energy e is related to the flow variables by the equation of state:

$$e = \frac{p}{\gamma - 1} + \frac{1}{2} \rho u_i u_i \tag{3.4}$$

where γ is the ratio of specific heats.

Equations (3.1) - (3.3) form a system of conservation laws that can be expressed as Eqn. (1.1) with the vector of conserved quantities $\mathbf{u}$ and the flux vector $\mathbf{f}_i$ as

$$\mathbf{u} = \begin{bmatrix} \rho \\ \rho u_j \\ e \end{bmatrix} ; \quad \mathbf{f}_i = \begin{bmatrix} \rho u_i \\ \rho u_i u_j + \delta_{ij} p \\ (e + p) u_i \end{bmatrix} \tag{3.5}$$

where δ_{ij} is the Kronecker delta function.

3.1.1 Characteristic Decomposition

The hyperbolic nature of the Euler equations implies that the solution consists of waves propagating at their characteristic speeds. Thus, the equations can be decoupled into a set of independent scalar conservation laws, each representing a wave. The characteristic decomposition of the Euler equations along each dimension yields the wave propagation speeds as well as the characteristic variables that are propagated along each wave. As an example, the one-dimensional Euler equations are considered, which are obtained by letting $i, j = 1$ in Eqns. (3.1) - (3.3). The resulting system is given by

$$\frac{\partial \mathbf{u}}{\partial t} + \frac{\partial \mathbf{f}}{\partial x} = 0 \tag{3.6}$$

$$\mathbf{u} = \begin{bmatrix} \rho \\ \rho u \\ e \end{bmatrix} \quad ; \quad \mathbf{f} = \begin{bmatrix} \rho u \\ \rho u^2 + p \\ (e + p)u \end{bmatrix}$$

which can be expressed as

$$\frac{\partial \mathbf{u}}{\partial t} + \mathrm{A}\frac{\partial \mathbf{u}}{\partial x} = 0 \tag{3.7}$$

where A is the flux Jacobian given by

$$\mathrm{A} = \frac{\partial \mathbf{f}}{\partial \mathbf{u}} = \begin{bmatrix} 0 & 1 & 0 \\ \frac{\gamma-3}{2}u^2 & (3-\gamma)u & \gamma-1 \\ -\gamma u e + (\gamma-1)u^3 & \gamma e - \frac{3}{2}(\gamma-1)u^2 & \gamma u \end{bmatrix} \tag{3.8}$$

The wave nature of solutions to the Euler equations can be understood by the eigenstructure of the flux Jacobian matrix. The system of equations given by Eqn. (3.7) is hyperbolic if and only if the matrix A is diagonalizable. Thus, the flux Jacobian

97

can be expressed as

$$X^{-1}AX = \Lambda \tag{3.9}$$

where Λ is a diagonal matrix whose elements λ_i are the eigenvalues of A, X is a matrix whose columns are the right-eigenvectors of A satisfying $A\mathbf{r}_i = \lambda_i \mathbf{r}_i$, and X^{-1} is a matrix whose rows are the left-eigenvectors of A satisfying $\mathbf{l}_i^T A = \lambda_i \mathbf{l}_i^T$. The eigenvalues and eigenvectors are given by

$$
\begin{aligned}
\Lambda &= \operatorname{diag}\left[u, u+a, u-a\right] \\[4pt]
X^{-1} &= \frac{\gamma-1}{\rho a}
\begin{bmatrix}
\frac{\rho}{a}\left(-\frac{u^2}{2}+\frac{a^2}{\gamma-1}\right) & \frac{\rho}{a}u & -\frac{\rho}{a} \\[8pt]
\frac{u^2}{2}-\frac{au}{\gamma-1} & -u+\frac{a}{\gamma-1} & 1 \\[8pt]
-\frac{u^2}{2}-\frac{au}{\gamma-1} & u+\frac{a}{\gamma-1} & -1
\end{bmatrix} \\[10pt]
X &=
\begin{bmatrix}
1 & \frac{\rho}{2a} & -\frac{\rho}{2a} \\[8pt]
u & \frac{\rho}{2a}\left(u+a\right) & -\frac{\rho}{2a}\left(u-a\right) \\[8pt]
\frac{u^2}{2} & \frac{\rho}{2a}\left(\frac{u^2}{2}+\frac{a^2}{\gamma-1}+au\right) & -\frac{\rho}{2a}\left(\frac{u^2}{2}+\frac{a^2}{\gamma-1}-au\right)
\end{bmatrix}
\end{aligned}
\tag{3.10}
$$

where $a^2 = \gamma p/\rho$ is the speed of sound. Equation (3.7) can be transformed into the characteristic space as

$$\frac{\partial \boldsymbol{\alpha}}{\partial t} + \Lambda \frac{\partial \boldsymbol{\alpha}}{\partial x} = 0 \tag{3.11}$$

where $\boldsymbol{\alpha} = X^{-1}\mathbf{u}$ is the vector of characteristic variables. The matrix Λ is a diagonal matrix and therefore, Eqn. (3.11) represents a set of decoupled scalar advection equations, where α_i are the characteristic variables being advected at the characteristic speeds $\lambda_i = u, u \pm a$. Thus, solutions to the Euler equations comprise waves that propagate with the local flow velocity and the relative speed of sound in each direction.

3.2 Numerical Solution

The numerical solution of a one-dimensional scalar conservation law is described in Section 1.2 and can be easily extended to a system of equations. A conservative, finite-difference discretization of Eqn. (3.6) in space can be expressed as:

$$\frac{d\mathbf{u}_j}{dt} + \frac{1}{\Delta x}\left(\mathbf{h}_{j+1/2} - \mathbf{h}_{j-1/2}\right) = 0 \tag{3.12}$$

where j is the grid index. The numerical flux function $\mathbf{h}(x)$ satisfies the vector equivalent of Eqn. (1.8) and the reconstruction step requires the approximation of $\mathbf{h}(x)$ at the interfaces to the desired accuracy.

Equation (3.12) is a system of ODEs in time and is solved using the time-marching schemes described in Section 1.2.2. The present chapter deals with the inviscid Euler equations on uniform grids, and thus, the third-order TVD Runge-Kutta (TVDRK3) scheme, given by Eqn. (1.25), is used for time-marching. The application of the CRWENO schemes to viscous flow problems and problems on non-uniform meshes is described in the next chapter and the second-order Backward Differencing Scheme (BDF2), given by Eqn. (1.26), is used for cases where the time step size is restricted by stability rather than accuracy.

3.2.1 Reconstruction

The reconstruction step requires the approximation of the numerical flux function $\mathbf{h}(x)$ from the discrete values at grid points. An approximate flux function is

found that satisfies

$$\hat{\mathbf{f}}(x) = \mathbf{h}(x) + O(\Delta x^{r+1})$$

$$\Rightarrow \left.\frac{\partial \mathbf{f}}{\partial x}\right|_{x_j} = \frac{1}{\Delta x}\left(\hat{\mathbf{f}}_{j+1/2} - \hat{\mathbf{f}}_{j-1/2}\right) + O(\Delta x^r) \tag{3.13}$$

where r is the desired order of accuracy. The resulting ODE in time is given by

$$\frac{d\mathbf{u}_j}{dt} + \frac{1}{\Delta x}\left(\hat{\mathbf{f}}_{j+1/2} - \hat{\mathbf{f}}_{j-1/2}\right) = 0 \tag{3.14}$$

The reconstruction of the flux function for the Euler equations consists of two steps: *interpolation* and *upwinding*. The interpolation step involves the construction of an approximate flux function from the discrete values at grid points. Section 1.2.1 described the interpolation process for a scalar function and the extensions to a vector function (in the context of the Euler equations) are discussed subsequently. At a given interface, there are several different possibilities for a r-th order interpolation of the flux function and the upwinding step is required to select an appropriate combination that respects the direction of wave propagation. The wave nature of solutions to the Euler equations is described in the previous section. At a given grid point or an interface, the solution is composed of waves propagating at their characteristic speeds. Thus, the solution or the flux function can be split into its constituent waves. The upwinding step finds a combination of the different possible interpolations such that each of the constituent waves is interpolated from data that is biased according to its direction of propagation. A detailed discussion on the theory behind upwinding, in the context of hyperbolic PDEs, can be found in [1].

The previous chapters described the interpolations of a scalar function using the fifth-order CRWENO schemes. Equations (2.19) and (2.29) are the CRWENO5
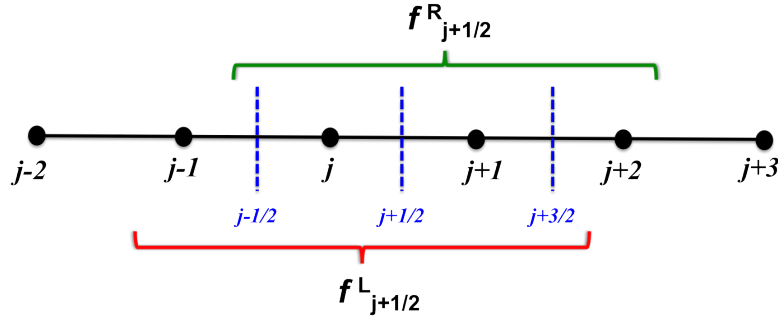
Figure 3.1: Interpolation stencils for the left and right-biased approximations to the interface flux.

and CRWENO5-LD schemes for a scalar conservation laws. In particular, they describe a left-biased interpolation scheme that corresponds to a positive advection speed in the linear advection equation. There are three possible ways of extending the scalar reconstruction schemes to the Euler equations. These involve the reconstruction of the conserved, primitive or the characteristic variables.

A simple extension involves the component-wise interpolation of the vectors in Eqn. (3.14). This involves the interpolation of the conserved variables. As an example, the CRWENO5 scheme, given by Eqn. (2.19), can be rewritten for each component as:

$$
\left(\frac{2}{3} \omega_1^k + \frac{1}{3} \omega_2^k \right) \hat{f}_{j-1/2}^{L,k} + \left[\frac{1}{3} \omega_1^k + \frac{2}{3} (\omega_2^k + \omega_3^k) \right] \hat{f}_{j+1/2}^{L,k} + \frac{1}{3} \omega_3^k \hat{f}_{j+3/2}^{L,k}
$$
$$
= \frac{\omega_1^k}{6} f_{j-1}^k + \frac{5(\omega_1^k + \omega_2^k) + \omega_3^k}{6} f_j^k + \frac{\omega_2^k + 5\omega_3^k}{6} f_{j+1}^k; \ k = 1, \dots, D+2 \ (3.15)
$$

where the superscript L denotes that this is a left-biased interpolation at $x_{j+1/2}$, k is the index for each component in the vector and D is the number of dimensions. This represents $D+2$ independent tridiagonal solutions corresponding to each component of the flux and solution vectors. Similarly, the right-biased interpolation at the same

101

interface can be written for each component as:

$$\left(\frac{2}{3}\omega_1^k + \frac{1}{3}\omega_2^k\right)\hat{f}_{j+3/2}^{R,k} + \left[\frac{1}{3}\omega_1^k + \frac{2}{3}(\omega_2^k + \omega_3^k)\right]\hat{f}_{j+1/2}^{R,k} + \frac{1}{3}\omega_3^k\hat{f}_{j-1/2}^{R,k}$$

$$= \frac{\omega_1^k}{6}f_{j+2}^k + \frac{5(\omega_1^k + \omega_2^k) + \omega_3^k}{6}f_{j+1}^k + \frac{\omega_2^k + 5\omega_3^k}{6}f_j^k; \quad k = 1,\ldots,D+2 \quad (3.16)$$

which is obtained by reflecting the left-biased interpolation at interface $x_{j+1/2}$. Figure 3.1 shows the stencils used to compute the left and right-biased interpolations. Thus, Eqns. (3.15) and (3.16) yield the left and right-biased approximations to the flux vector, $\hat{\mathbf{f}}_{j+1/2}^L$ and $\hat{\mathbf{f}}_{j+1/2}^R$. Similar expressions can be obtained for the reconstruction of the conserved variables using the CRWENO5-LD scheme.

An alternative to the interpolation of the conserved variables is the interpolation of the primitive flow variables. At each iteration, the density, velocity and pressure are extracted from the conserved variables at each grid point. These primitive variables are then interpolated at the interfaces and the flux vector computed from the interpolated flow variables. Replacing $\hat{f}^k$ and f^k with $\hat{\rho}$ and ρ respectively in Eqns. (3.15) and (3.16), or the corresponding expressions for the CRWENO5-LD scheme, we obtain the left and right-biased approximations to the density at the interfaces ($\hat{\rho}$ is the numerical approximation to ρ). The left and right-biased approximations to each component of the velocity vector u and pressure p can be similarly obtained. As with the reconstruction of conserved variables, this process requires $D + 2$ independent tridiagonal solutions each for the left and right-biased computations. The interpolated values of the primitive variables at the interface are thus used to compute the left and right-biased interface fluxes, $\hat{\mathbf{f}}_{j+1/2}^L$ and $\hat{\mathbf{f}}_{j+1/2}^R$.

The final flux at the interface $\hat{\mathbf{f}}_{j+1/2}$ is obtained from the left and right-biased

fluxes through the upwinding step. In the present study, the Roe flux-differencing scheme [5] is used. The scheme uses the solution of a local Riemann problem at each interface to compute the left and right running waves. The final flux can be expressed as the sum of the left-biased flux and the left-running waves or the right-biased flux minus the right-running waves; or an average of the two. The upwind flux is thus expressed as:

$$\hat{\mathbf{f}}_{j+1/2} = \frac{1}{2}(\hat{\mathbf{f}}^L_{j+1/2} + \hat{\mathbf{f}}^R_{j+1/2}) - \frac{1}{2}|\hat{A}(\hat{\mathbf{u}}^L_{j+1/2}, \hat{\mathbf{u}}^R_{j+1/2})|(\hat{\mathbf{u}}^L_{j+1/2} + \hat{\mathbf{u}}^R_{j+1/2}) \qquad (3.17)$$

where $\hat{\mathbf{u}}^{L,R}$ are the approximations to $\mathbf{u}$, computed in the same way as the approximations to the flux function $\hat{\mathbf{f}}^{L,R}$; and

$$|\hat{A}(\hat{\mathbf{u}}^L_{j+1/2}, \hat{\mathbf{u}}^R_{j+1/2})| = X_{j+1/2}|\Lambda_{j+1/2}|X^{-1}_{j+1/2} \qquad (3.18)$$

The eigenvalues and eigenvectors at the interface on the right-hand side of the above equation are calculated by Roe-averaging $\mathbf{u}^L_{j+1/2}$ and $\mathbf{u}^R_{j+1/2}$. The entropy correction of Harten [7] is used to prevent the formation of unphysical expansion shocks.

The third approach is the reconstruction of the characteristic variables and is the most robust, especially for problems with strong discontinuities [9, 13]. The characteristic decomposition of the one-dimensional Euler equations is discussed in Section 3.1.1. It is shown that the flux Jacobian matrix is diagonalizable and the system of equations can be transformed to the characteristic space, where it decouples into a set of independent scalar advection equations. Thus, the application of the scalar interpolation schemes to the characteristic variables is the most natural choice that respects the underlying physics of the problem. At each interface $x_{i+1/2}$, the Roe-averaged state is computed from $\mathbf{u}_i$ and $\mathbf{u}_{i+1}$, and the eigenvalues and
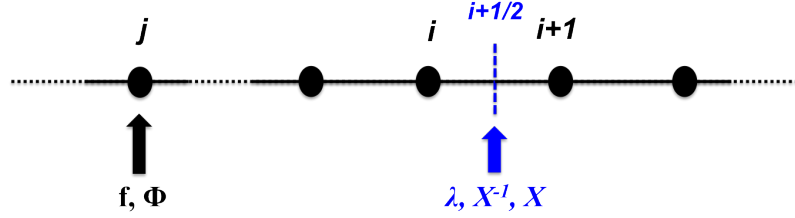
Figure 3.2: Characteristic-based reconstruction of the flux at j for interface $i+1/2$.

eigenvectors are evaluated. The characteristic fluxes at each grid point j, based on the eigen-decomposition at $i+1/2$, are defined as

$$\boldsymbol{\Phi}_j = X_{i+1/2}^{-1}\mathbf{f}_j \tag{3.19}$$

where the k-th component of $\boldsymbol{\Phi}_j$ denotes the component of the flux vector at x_j along the k-th left-eigenvector at the $i+1/2$-th interface. Figure 3.2 shows the interface at which the eigenvalues and eigenvectors are evaluated and the grid point at which the characteristic flux is calculated. The scalar interpolation schemes, given by Eqns. (2.19) or (2.29), are applied to characteristic flux vector:

$$\hat{a}\hat{\boldsymbol{\Phi}}_{j-1/2}^{L} + \hat{b}\hat{\boldsymbol{\Phi}}_{j+1/2}^{L} + \hat{c}\hat{\boldsymbol{\Phi}}_{j+3/2}^{L} = a\boldsymbol{\Phi}_{j-1} + b\boldsymbol{\Phi}_j + c\boldsymbol{\Phi}_{j+1} + d\boldsymbol{\Phi}_{j+2} \tag{3.20}$$

where $\hat{a}, \hat{b}, \hat{c}$ and a, b, c, d are the corresponding coefficients from the CRWENO5 or CRWENO5-LD schemes. Substituting Eqn. (3.19) into the above equation, we get

$$\hat{a}X_{j+1/2}^{-1}\hat{\mathbf{f}}_{j-1/2}^{L} + \hat{b}X_{j+1/2}^{-1}\hat{\mathbf{f}}_{j+1/2}^{L} + \hat{c}X_{j+1/2}^{-1}\hat{\mathbf{f}}_{j+3/2}^{L} = a\boldsymbol{\Phi}_{j-1} + b\boldsymbol{\Phi}_j + c\boldsymbol{\Phi}_{j+1} + d\boldsymbol{\Phi}_{j+2} \tag{3.21}$$

The left-eigenvectors, X^{-1}, in the above equation are evaluated at interface $x_{j+1/2}$ since the above equation represents the reconstruction at this interface. The corresponding expression for the right-biased approximation can be similarly derived.

104

Examination of Eqn. (3.21) shows that the solutions to the three components of the flux vector are coupled, since X^{-1} is a full matrix. The resulting system of equations is block tridiagonal, with the block size as $D + 2$. This is in contrast to the reconstruction of the conserved or primitive variables, where $D + 2$ separate tridiagonal systems of equations were solved, one for each scalar variable.

The reconstruction of the characteristic variables is marginally more expensive for a non-compact scheme due to the additional cost of evaluating the eigenvectors at each interface and transforming between the conserved variables and characteristic variables. The numerical cost is significantly increased for a non-linear compact scheme because in addition to these calculations, the solution to a block tridiagonal system is required at each iteration, as opposed to several tridiagonal systems. If $\tau(N)$ is the operation count for a tridiagonal system with N variables, the operation count of $D+2$ such solutions is $(D+2)\tau(N)$. This corresponds to the reconstruction of conserved or primitive variables. In contrast, reconstruction of characteristic variables require one block tridiagonal solution with block size $D + 2$, for which the operation count is $O[(D + 2)^2]\tau(N)$, which is significantly larger. Section 2.6 discusses the computational expense and efficiency of the CRWENO5 schemes for a scalar problem. These issues are revisited in the context of the Euler equations in subsequent sections.

The left and right-biased approximations obtained using the interpolation of characteristic variables can be combined using Eqn. (3.17) to give the final flux at the interface. An alternative to Eqn. (3.17) is the characteristic form of the Roe scheme, where the upwinding is carried out for each characteristic and then the final

flux at the interface is computed from the upwind characteristic flux. The Roe-Fixed (RF) flux formulation [11, 15] is obtained by incorporating the local Lax-Friedrich flux splitting [52] as an entropy fix to the Roe solver [5]. It can be expressed as

$$
\hat{\phi}^k_{j+1/2} = \begin{cases} \hat{\phi}^{L,k}_{j+1/2} & \text{if } \lambda_{j,j+1/2,j+1} > 0 \\ \hat{\phi}^{R,k}_{j+1/2} & \text{if } \lambda_{j,j+1/2,j+1} < 0 \\ \frac{1}{2}\left[\hat{\phi}^{L,k}_{j+1/2} + \hat{\phi}^{R,k}_{j+1/2} + \tilde{\lambda}(\hat{\alpha}^{L,k}_{j+1/2} - \hat{\alpha}^{R,k}_{j+1/2})\right] & \text{otherwise} \end{cases} \quad (3.22)
$$

where $\hat{\phi}^k$ is the k-th component of $\hat{\boldsymbol{\Phi}}$ and $\hat{\boldsymbol{\alpha}} = X^{-1}\hat{\boldsymbol{u}}$ is the vector of characteristic variables. The term $\tilde{\lambda} = \mu\lambda_{max}[j, j + 1/2, j + 1]$ provides the necessary dissipation in the entropy fix. The dissipation parameter μ is usually between 1.1 and 1.3. In the present study, the RF flux formulation is used along with the reconstruction of characteristic variables.

3.3   One-Dimensional Inviscid Flow Problems

The application of the CRWENO scheme to the one-dimensional Euler equations is discussed in this section. The accuracy and convergence properties are studied on a smooth problem that involves the advection of an entropy wave. The non-oscillatory nature of the schemes and the resolution of discontinuities are studied on the one-dimensional Riemann problems. The Shu-Osher problem, that describes the interaction of a shock wave with an entropy wave, is studied. The solution consists of waves of high wavenumbers as well as discontinuities and is representative of compressible turbulent flows. The nomenclature of the various schemes considered in this section is summarized in Table 2.2.

3.3.1 Advection of Entropy Wave

The advection of a smooth density wave over a periodic domain is considered in this problem. The pressure and velocity are constant, thus reducing the Euler equations to a linear advection equation for density, with the advection speed as the freestream velocity. The exact solution is given by:

$$
\begin{aligned}
\rho(x,t) &= \rho_\infty + A\sin\left[\pi(x - u_\infty t)\right] \\
u(x,t) &= u_\infty \\
p(x,t) &= p_\infty
\end{aligned}
\tag{3.23}
$$

In the present example, the freestream conditions are taken as $\rho_\infty = u_\infty = p_\infty = 1$ and the amplitude of the entropy wave is taken as $A = 0.1$. The domain is taken as $[0,2]$ and periodic boundaries are assumed on both sides. The solution is obtained after one cycle $(t = 2)$ and the errors are compared.

Tables 3.1 - 3.3 show the L_1, L_2 and L_∞ errors (density) and the corresponding rates of convergence for the optimal schemes (NonCompact5, Compact5 and Compact5-LD). The solutions are obtained by the reconstruction of characteristic variables. An initial grid with 15 points is taken and progressively refined. The CFL number corresponding to the grid with 15 points is 0.1 and is decreased with each grid refinement, to ensure that errors due to time discretization converge at the same order as those due to space discretization. The TVD-RK3 scheme is used to evolve the solution in time. Fifth-order convergence is verified for all the schemes as expected. The Compact5 schemes yields solutions with errors that are almost 1/10-th those of the NonCompact5 scheme. At finer grid resolutions, the Compact5-

Table 3.1: L_1 errors and convergence rates for the optimal schemes for entropy wave advection

N	NonCompact5 Error	r_c	Compact5 Error	r_c	Compact5-LD Error	r_c
15	8.359e-05	-	1.289e-05	-	9.313e-06	-
30	2.676e-06	4.97	3.548e-07	5.18	2.253e-07	5.36
60	8.395e-08	4.99	9.929e-09	5.16	5.906e-09	5.25
120	2.626e-09	5.00	2.888e-10	5.10	1.623e-10	5.18
240	8.184e-11	5.00	8.567e-12	5.07	4.686e-12	5.11

Table 3.2: L_2 errors and convergence rates for the optimal schemes for entropy wave advection

N	NonCompact5 Error	r_c	Compact5 Error	r_c	Compact5-LD Error	r_c
15	9.293e-05	-	1.483e-05	-	1.141e-05	-
30	2.967e-06	4.97	3.877e-07	5.25	2.717e-07	5.39
60	9.321e-08	4.99	1.083e-08	5.16	6.854e-09	5.30
120	2.916e-09	5.00	3.172e-10	5.09	1.843e-10	5.21
240	9.097e-11	5.00	9.597e-12	5.04	5.473e-12	5.07

Table 3.3: L_∞ errors and convergence rates for the optimal schemes for entropy wave advection

N	NonCompact5 Error	r_c	Compact5 Error	r_c	Compact5-LD Error	r_c
15	1.311e-04	-	2.600e-05	-	2.556e-05	-
30	4.196e-06	4.97	5.913e-07	5.45	6.007e-07	5.41
60	1.317e-07	4.99	1.733e-08	5.09	1.732e-08	5.11
120	4.124e-09	5.00	5.338e-10	5.02	5.734e-10	4.92
240	1.308e-10	4.98	1.647e-11	5.01	2.080e-11	4.78

LD scheme yields solutions with errors that are 1/2 those of the Compact5 scheme. These conclusions are consistent with the results from the numerical analysis presented in Section 2.3.1, as well as the conclusions drawn from smooth solutions of the linear advection equation (Section 2.4.1). Tables 3.4 - 3.5 show the density errors and rates of convergence for the WENO5, CRWENO5 and CRWENO5-LD schemes. The mapped weights are used for the data shown in these tables and a more detailed

Table 3.4: L_1 errors and convergence rates for the WENO and CRWENO schemes for entropy wave advection

N	WENO5		CRWENO5		CRWENO5-LD	
	Error	r_c	Error	r_c	Error	r_c
15	9.465e-05	-	1.689e-05	-	1.317e-05	-
30	2.696e-06	5.13	3.612e-07	5.54	2.289e-07	5.84
60	8.399e-08	5.00	9.940e-09	5.18	5.911e-09	5.27
120	2.626e-09	5.00	2.889e-10	5.10	1.623e-10	5.18
240	8.185e-11	5.00	8.565e-12	5.07	4.685e-12	5.11

Table 3.5: L_2 errors and convergence rates for the WENO and CRWENO schemes for entropy wave advection

N	WENO5		CRWENO5		CRWENO5-LD	
	Error	r_c	Error	r_c	Error	r_c
15	1.028e-04	-	1.899e-05	-	1.597e-05	-
30	2.988e-06	5.10	3.945e-07	5.58	2.758e-07	5.85
60	9.325e-08	5.00	1.084e-08	5.18	6.860e-09	5.32
120	2.917e-09	5.00	3.172e-10	5.09	1.843e-10	5.21
240	9.098e-11	5.00	9.593e-12	5.04	5.471e-12	5.07

Table 3.6: L_∞ errors and convergence rates for the WENO and CRWENO schemes for entropy wave advection

N	WENO5		CRWENO5		CRWENO5-LD	
	Error	r_c	Error	r_c	Error	r_c
15	1.309e-04	-	3.266e-05	-	3.268e-05	-
30	4.199e-06	4.96	5.999e-07	5.76	6.124e-07	5.73
60	1.317e-07	4.99	1.734e-08	5.11	1.731e-08	5.14
120	4.124e-09	5.00	5.338e-10	5.02	5.734e-10	4.92
240	1.308e-10	4.98	1.644e-11	5.02	2.079e-11	4.79

discussion regarding the non-linear weights is presented in Section 3.5. The solution is smooth and these schemes should be identical to their optimal counterparts. At very coarse grids, the non-linear schemes show some irregularities. However, at finer grids the errors are identical to those of the optimal schemes, indicating that the weights converge to their optimal values. The conclusions regarding the accuracy of the various schemes extend to the WENO5, CRWENO5 and CRWENO5-LD
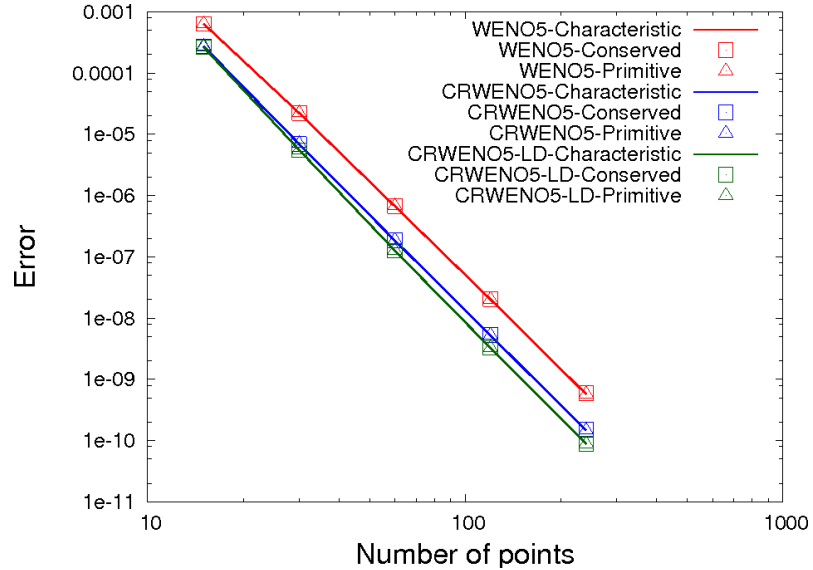
Figure 3.3: Comparison of L_2 errors for the reconstruction of characteristic, conserved and primitive variables.

schemes.

The extension of the scalar interpolation schemes to the Euler equations is described in Section 3.2.1. The interpolation schemes can be applied to the conserved, primitive and the characteristic variables. It is well known that the reconstruction of the characteristic variables result in a robust algorithm that yields non-oscillatory solutions for problems with strong discontinuities. However, for smooth problems, the reconstruction of conserved or primitive variables suffices to yield accurate solutions. Figure 3.3 shows the L_2 error as a function of the number of points. The WENO5, CRWENO5 and CRWENO5-LD schemes are compared and the solutions obtained through the reconstruction of conserved, primitive and characteristic variables are shown. The CRWENO schemes are more accurate than the WENO scheme for the same order of convergence. However, there are no differences in the solutions obtained through the reconstruction of characteristic, conserved and primitive

variables for a given scheme.
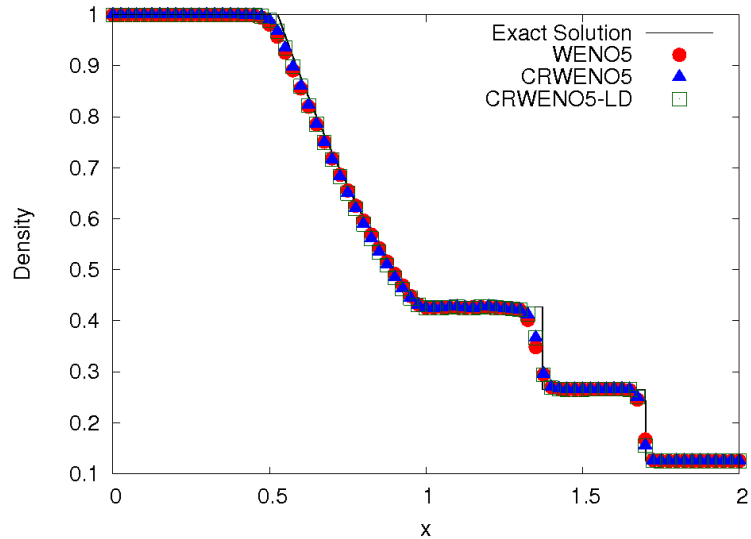
3.3.2 1D Riemann Problems

The non-oscillatory nature of the CRWENO schemes and the resolution of discontinuities are assessed on the one-dimensional Riemann problems. These problems consist of an initial discontinuity that decomposes into a rarefaction wave, a contact discontinuity and a shock wave, corresponding to each of the characteristic fields of the Euler equations. The Sod shock tube problem [51] and the Lax shock tube problem [52] are benchmark inviscid problems. The exact solutions to these problems are obtained using a Riemann solver.
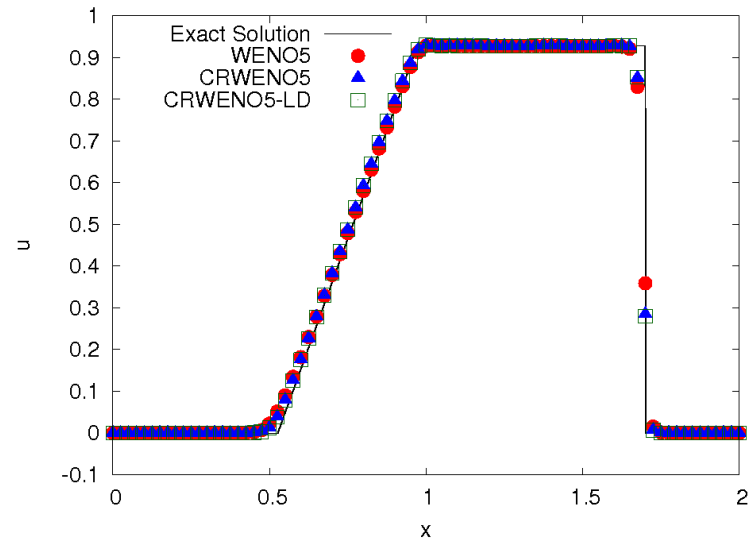
The initial conditions to the Sod shock tube problem is given by:

$$\rho_L, u_L, p_L \;\; = \;\; 1, 0, 1$$
$$\rho_R, u_R, p_R \;\; = \;\; 0.125, 0, 0.1 \tag{3.24}$$

The domain is taken as $[0, 2]$ and the initial discontinuity is placed at $x = 1$. Zero-gradient boundary conditions are applied at both boundaries. The solution is obtained on a grid with 80 points at $t = 0.4$ with a CFL number of 0.5. The TVD-RK3 scheme is used for time-marching. The WENO5, CRWENO5 and CRWENO5-LD schemes are compared and a characteristic-based reconstruction is used to ensure non-oscillatory solutions. Figure 3.4(a) and 3.4(b) show the density and velocity respectively. The left-running rarefaction wave and the right-running contact discontinuity and shock wave can be observed in the solution. The CRWENO5 and

111
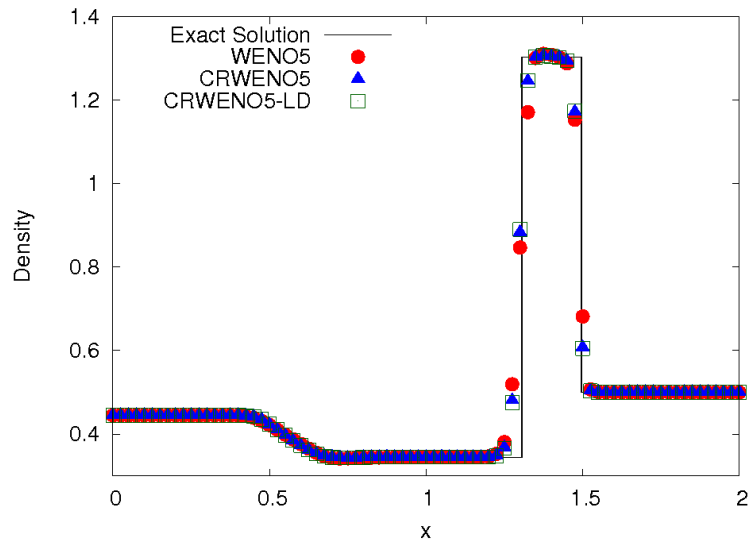
(a) Density
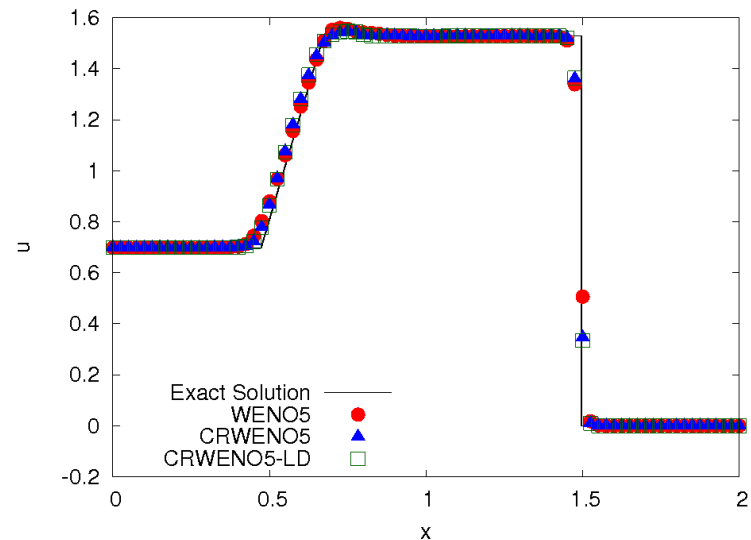
(b) Velocity

Figure 3.4: Solutions to the Sod shock tube problem.

CRWENO5-LD schemes yield solutions that are non-oscillatory across the discontinuities, like the WENO5 scheme. Thus, the non-oscillatory nature of the schemes and the applicability of the WENO weights to the compact schemes are validated for a non-linear system of equations. Examination of the shock wave shows that the CRWENO5 and CRWENO5-LD schemes show a significantly lower smearing across

(a) Density

(b) Velocity

Figure 3.5: Solutions to the Lax shock tube problem.

the discontinuity.

The initial conditions of the Lax shock tube are given by

$$\rho_L, u_L, p_L = 0.445, 0.698, 3.528$$

$$\rho_R, u_R, p_R = 0.5, 0, 0.571 \tag{3.25}$$

Table 3.7: L_1 errors and convergence rates for the Lax shock tube problem

	WENO5		CRWENO5		CRWENO5-LD	
N	Error	r_c	Error	r_c	Error	r_c
15	7.003E-02	-	5.403E-02	-	5.343E-02	-
30	3.716E-02	0.91	3.167E-02	0.77	3.153E-02	0.76
60	2.153E-02	0.79	1.836E-02	0.79	1.821E-02	0.79
120	1.081E-02	0.99	8.869E-03	1.05	8.732E-03	1.06
240	5.810E-03	0.90	4.716E-03	0.91	4.596E-03	0.93

with the domain as $[0, 2]$ and the initial discontinuity located at $x = 1$. The solution is evolved in time till $t = 0.2$ at a CFL of 0.5 using the TVD-RK3 scheme. Zero-gradient boundary conditions are applied at both boundaries. Figure 3.5(a) and 3.5(b) show the solutions obtained by the WENO5, CRWENO5 and CRWENO5-LD schemes on a grid with 80 points. The schemes use a characteristic-based reconstruction. The CRWENO5 and CRWENO5-LD schemes yield non-oscillatory solutions and show significantly lower smearing for the contact discontinuity and the shock wave.

Table 3.7 shows the L_1 errors (density) and convergence plots for the Lax shock tube. The CFL for the initial grid of 15 points is 0.1 and reduced with each successive refinement. The solution is discontinuous and thus, the Taylor series analysis for the schemes does not hold. However, the errors for the CRWENO5 and CRWENO5-LD schemes are observed to be substantially lower compared to the WENO5 scheme. At finer grids, the L_1 convergence approaches 1 for all the three schemes, which is consistent with results in the literature [16].

3.3.3 Shock – Entropy Wave Interaction

The interaction of a shock wave with an entropy wave was proposed in [11] and is a simplified one-dimensional representation of compressible turbulent flows. The solution consists of discontinuities as well as waves of very small length scales. The initial conditions, which consist of a Mach 3 shock wave interacting with a density wave, are given by [16]
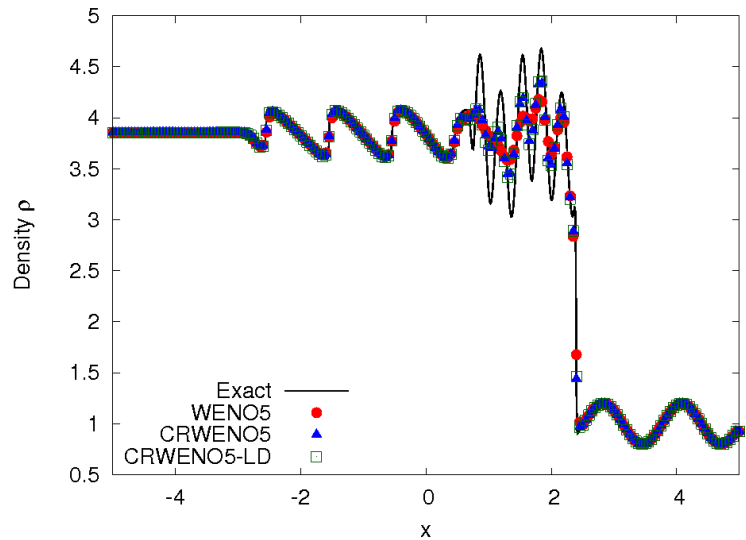
$$
(\rho, u, p) = \begin{cases} \left(\frac{27}{7}, \frac{4\sqrt{35}}{9}, \frac{31}{3}\right) & \text{if } x < -4 \\[2mm] \left(1 + \frac{1}{5}\sin 5x, 0, 1\right) & \text{if } x \geq -4 \end{cases} \tag{3.26}
$$

The domain is taken as $[-5, 5]$ and zero-gradient boundaries are applied at both boundaries.
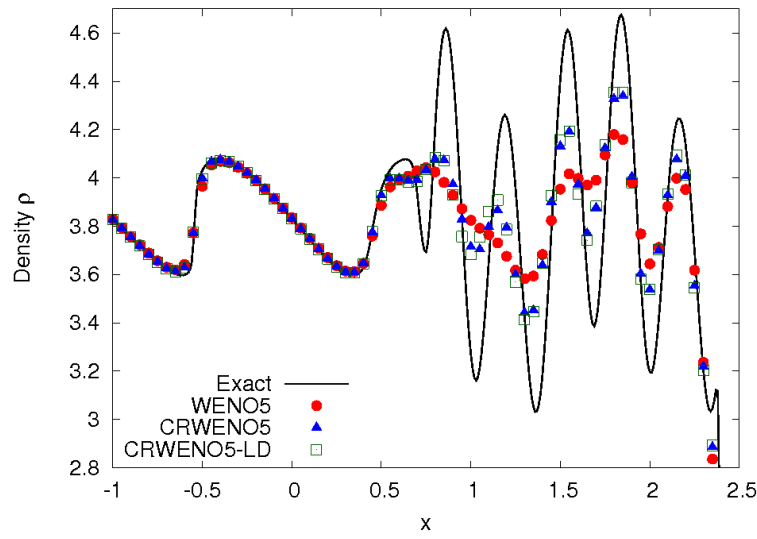
The solution is obtained at $t = 1.8$ at a CFL of 0.1 on a grid with 200 points. The CRWENO5 and CRWENO5-LD schemes are compared with the WENO5 scheme and a characteristic-based reconstruction is used. Figure 3.6(a) shows the density on the complete domain while Fig. 3.6(b) shows the same solution, magnified around the post-shock region. The "Exact Solution" refers to the solution obtained by the WENO5 scheme on a grid with 2000 points and is used as the reference solution in absence of an analytical one. The interaction of the shock wave with the entropy wave results in the formation of smaller shock waves and high-wavenumber density waves.

The CRWENO5 and CRWENO5-LD schemes show non-oscillatory behavior across the discontinuities as well as lower smearing than the WENO5 scheme. The high-wavenumber density waves behind the shock wave are smooth, but have large

gradients. The performance of a numerical scheme for such flow features is representative of its ability to accurately model small length scales characteristic of turbulent flows. The WENO5 shows significant dissipation of the density waves. The higher spectral resolution of the CRWENO5 and CRWENO5-LD schemes results in a more accurate representation of these waves. Thus, the CRWENO schemes show

(a) Complete solution

(b) Discontinuities and small length-scale waves

Figure 3.6: Solutions to the shock – entropy wave interaction problem.

a higher resolution of smooth flow features of small length scales, while maintaining non-oscillatory behavior across discontinuities.

3.4   Computational Efficiency

The numerical cost of the CRWENO schemes and their computational efficiency were discussed in Section 2.6 in the context of a scalar equation. The CRWENO schemes are more expensive than the WENO scheme on the same grid due to the requirement of a tridiagonal solution at each time step. However, when comparing solutions with the similar errors, the CRWENO schemes are less expensive. The validity of these conclusions is verified for a system of equations. As discussed before, the reconstruction of conserved or primitive variables require $D + 2$ tridiagonal solutions, while the reconstruction of the characteristic variables require one block tridiagonal solution with a block size of $D + 2$. Thus, the computational expense of the characteristic-based reconstruction is substantially higher.

The advection of an entropy wave (Section 3.3.1) is considered. Table 3.8 shows the L_2 errors and computational run-times for the solutions obtained by using the WENO5, CRWENO5 and CRWENO5-LD schemes on the conserved variables. The solutions are obtained at grid sizes of 30, 60, 120 and 240 points. Solutions are also obtained using the WENO5 scheme at grid sizes that are 1.5 times each of these grid sizes (i.e., 45, 90, 180 and 360 points) and the errors and run-times shown. It is observed that the compact schemes are more expensive for the same grid size. However, a comparison of the error shows that the errors in the solutions obtained

Table 3.8: L_2 errors and computational run-time (in seconds) for WENO5, CR-WENO5 and CRWENO5-LD with conserved variables reconstruction

	WENO5		CRWENO5		CRWENO5-LD	
N	Error	T	Error	T	Error	T
30	2.999E-05	1.01	3.823E-06	1.33	2.230E-06	1.62
45	3.967E-06	2.29	-	-	-	-
60	9.359E-07	6.27	1.076E-07	8.29	5.976E-08	10.30
90	1.241E-07	14.37	-	-	-	-
120	2.928E-08	39.13	3.209E-09	51.63	1.733E-09	66.10
180	3.879E-09	90.25	-	-	-	-
240	9.136E-10	258.23	9.723E-11	329.54	5.222E-11	399.04
360	1.204E-10	576.41	-	-	-	-

by the CRWENO5 scheme is comparable to the error in the solution obtained by the WENO5 scheme on the grid that is 1.5 times finer. This conclusion holds true at all refinement levels. A comparison of the run-times shows that the CRWENO5 schemes are less expensive than the WENO5 schemes for solutions of the same accuracy. Figure 3.7(a) shows the error as a function of the computational run-time of the various schemes for the reconstruction of the conserved variables. The CRWENO5 and CRWENO5-LD schemes are more efficient.

The same conclusions do not extend to the reconstruction of the characteristic variables where the solution of a block tridiagonal system is needed. Table 3.9 shows the L_2 errors and computational run-times for the solutions obtained by applying the reconstruction schemes to the characteristic variables. The errors are identical to those obtained by reconstructing the conserved variables, however the computational expense of the CRWENO schemes is significantly larger. The WENO5 scheme
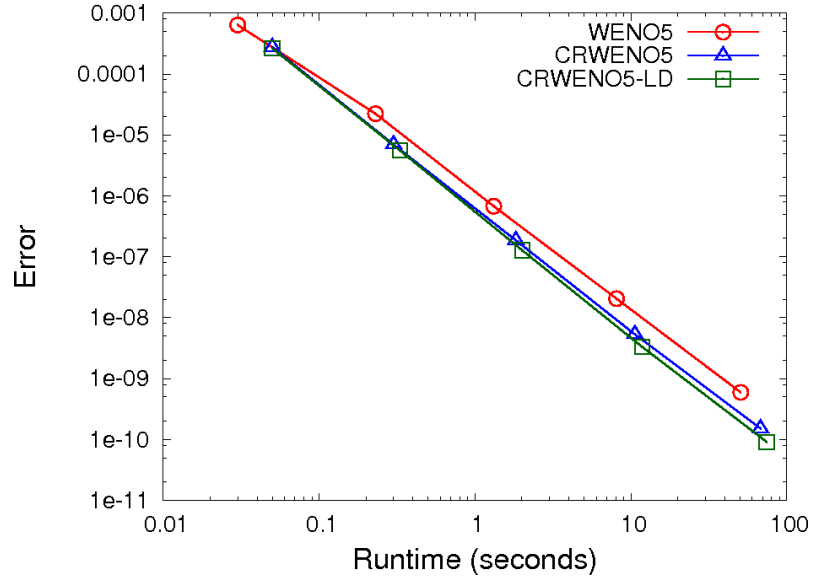
Table 3.9: L_2 errors and computational run-time (in seconds) for WENO5, CR-WENO5 and CRWENO5-LD with characteristic based reconstruction

| | WENO5 | | CRWENO5 | | CRWENO5-LD | |
N	Error	T	Error	T	Error	T
30	2.998E-05	1.24	3.824E-06	5.58	2.229E-06	5.85
45	3.967E-06	2.81	-	-	-	-
60	9.359E-07	7.78	1.076E-07	34.97	5.976E-08	36.57
90	1.241E-07	17.61	-	-	-	-
120	2.928E-08	50.11	3.209E-09	221.75	1.733E-09	233.67
180	3.879E-09	110.92	-	-	-	-
240	9.136E-10	314.19	9.722E-11	1405.66	5.223E-11	1498.15
360	1.204E-10	702.10	-	-	-	-
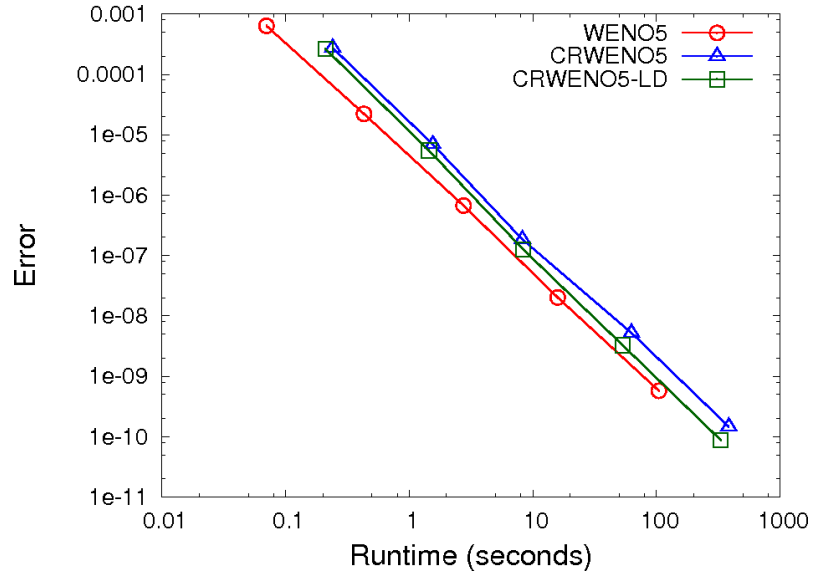
is less expensive, even when comparing solutions with comparable errors. Figure 3.7(b) shows the error as a function of the computational run-time of the various schemes for a characteristic-based reconstruction. The CRWENO5 and CRWENO5-LD schemes are more expensive for the same error and are less efficient.

Sections 3.3.2 and 3.3.3 show results for inviscid problems that have strong discontinuities. The results are obtained using a characteristic-based reconstruction. The CRWENO schemes show superior resolution of the discontinuities but they are computationally less efficient than the WENO scheme. The WENO5 scheme is expected to show the same resolution of a finer grid and would be less expensive. The results are shown to validate and demonstrate the numerical properties of the CRWENO schemes on benchmark problems that are representative of practical flows.

Although the CRWENO schemes are less efficient for a characteristic-based reconstruction, their applicability to compressible flow problems is not limited. There

(a) Reconstruction of conserved variables

(b) Reconstruction of characteristic variables

Figure 3.7: Errors and runtime for the various schemes.

are two reasons for this. The primary reason is that a characteristic-based recon-struction is not necessary in many problems of practical relevance. It has been observed in the literature that the reconstruction of characteristic variables is re-quired for non-oscillatory solutions to inviscid flow problems. However, for smooth problems as well as viscous flow problems, reconstruction of primitive or conserved

variables suffice, even when shock waves are present in the solution. Several such examples are presented in the next chapter. The CRWENO schemes are more efficient for the reconstruction of primitive or conserved variables. The second reason is that the numerical cost of reconstruction is a small fraction of the overall cost (of each time step) for a practical flow solver. Thus, even if the reconstruction of characteristic variables is necessary, the total increase in the computational expense may be marginal.

3.5   Implementation of Non-Linear Weights

The implementation of the non-linear weights in Eqn. (3.15) or (3.21) (or their right-biased counterparts) affects the accuracy, convergence and resolution of the solution. The drawbacks of the weights proposed in [13] and the various alternatives proposed [16, 17, 19, 20] were discussed in Section 1.3.1 and explored in the context of the CRWENO schemes in Section 2.7. The numerical properties of the various implementations were studied for scalar problems. Table 2.10 summarizes the CRWENO schemes with the various implementation of the non-linear weights. The CRWENO5-M, CRWENO5-Z and CRWENO5-YC schemes were observed to recover the optimal order of convergence for a smooth solution with optimal points. These schemes also showed an improved spectral resolution as compared to the CRWENO5-JS scheme. The resolution of discontinuities showed significant improvements, especially for long-term convection over a periodic domain. Although the solution was observed to be smooth for the various CRWENO schemes,
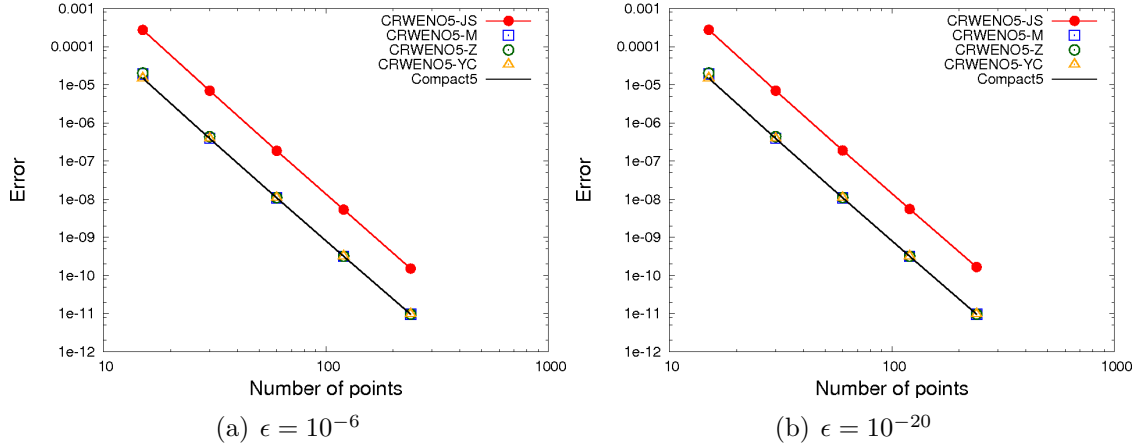
Figure 3.8: Errors and runtime for various implementations of the non-linear weights.

higher derivatives of the solution showed spurious oscillations for the CRWENO5-JS, CRWENO5-M and CRWENO5-Z schemes. These oscillations were absent in the CRWENO5-YC scheme. The effect of the non-linear weights and their implementation is studied in this section in the context of the inviscid Euler equations.

Figure 3.8 shows the L_2 errors as a function of the number of grid points for the advection of a smooth entropy wave (Section 3.3.1). The solution is evolved in time using the TVD-RK3 scheme and the initial CFL number, corresponding to the grid with 15 points, is 0.1. The solution is smooth and the weights are expected to be at their optimal values. Errors in the solutions obtained using the CRWENO5-JS, CRWENO5-M, CRWENO5-Z and CRWENO5-YC are shown in the figure. In addition, the error in the solution obtained using the underlying optimal scheme, Compact5, is included. The CRWENO5-JS yields solutions that have a significantly higher error than that of the Compact5 scheme at all grid sizes. The alternative formulations, CRWENO5-M, CRWENO5-Z and CRWENO5-YC, yield solutions with

122

errors identical to that of the Compact5 scheme. Figure 3.9 shows the three weights for each of the CRWENO5 schemes on a grid with 30 points, for the characteristic field corresponding to the eigenvalue u for $\epsilon = 10^{-6}$. The problem involves the advection of an entropy wave and thus, this is the only characteristic field contributing to the solution. Weights are shown for the left-biased interpolation. The weights calculated using the CRWENO5-JS scheme show a departure from their optimal values at the extrema that results in the loss of accuracy. The CRWENO5-M, CRWENO5-Z and CRWENO5-YC schemes result in optimal weights, as expected

(a) CRWENO5-JS   (b) CRWENO5-M

(c) CRWENO5-Z   (d) CRWENO5-YC
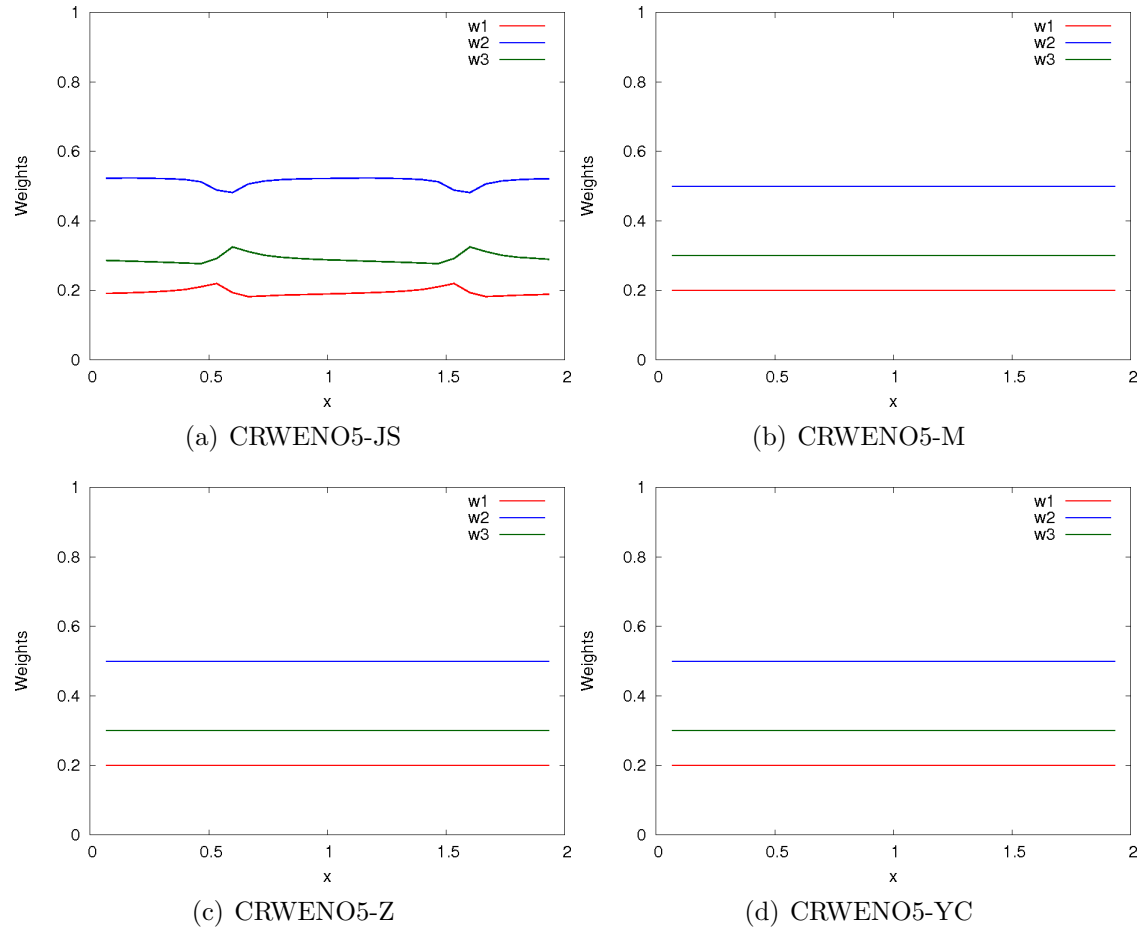
Figure 3.9: Entropy wave advection: Weights for the left-biased reconstruction of characteristic field u ($\epsilon = 10^{-6}$).
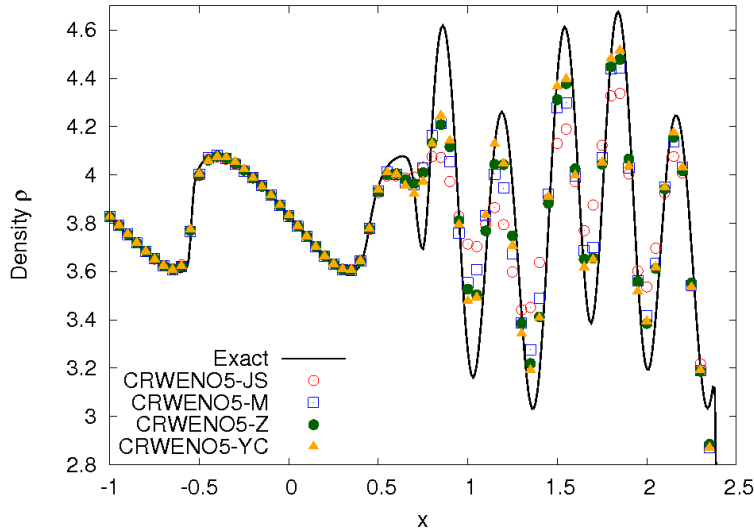
Figure 3.10: Solutions to the shock – entropy wave interaction problem with various implementations of non-linear weights.

for this smooth problem.

The implementation of the non-linear weights has a significant effect on solutions to flows with small length scales. Such flow features are smooth but have high gradients due to their resolution with a small number of grid points. The accurate representation of the small scales require the non-linear weights to be as close to optimal as possible. However, due to the large gradients, the behavior of the weights may be similar to their behavior across a discontinuity. The resulting solution would show significant dissipation of the small length scales. The various implementations of the CRWENO5 scheme are applied to the interaction of the shock wave with an entropy wave (Section 3.3.3). The resolution of the post-shock high-wavenumber density waves is compared for the various schemes.

Figure 3.10 shows the solution to the shock – entropy wave interaction problem obtained by the CRWENO schemes with the various implementations of non-linear

weights. The solutions are evolved in time using the TVD-RK3 scheme on a grid with 200 points. The characteristic-based reconstruction is used and the CFL number is 0.1. The solution is magnified around the post-shock region. The alternative formulations for the weights show significant improvements in the solution, compared to the CRWENO5-JS scheme. The CRWENO5-Z and CRWENO5-YC yield solutions that show slightly lower dissipation than that obtained by the CRWENO5-M scheme. The difference in the solutions is explained by examining the weights in the post-shock region. The density waves correspond to the characteristic field with eigenvalue u and the corresponding weights for a left-biased reconstruction are

(a) CRWENO5-JS

(b) CRWENO5-M

(c) CRWENO5-Z

(d) CRWENO5-YC
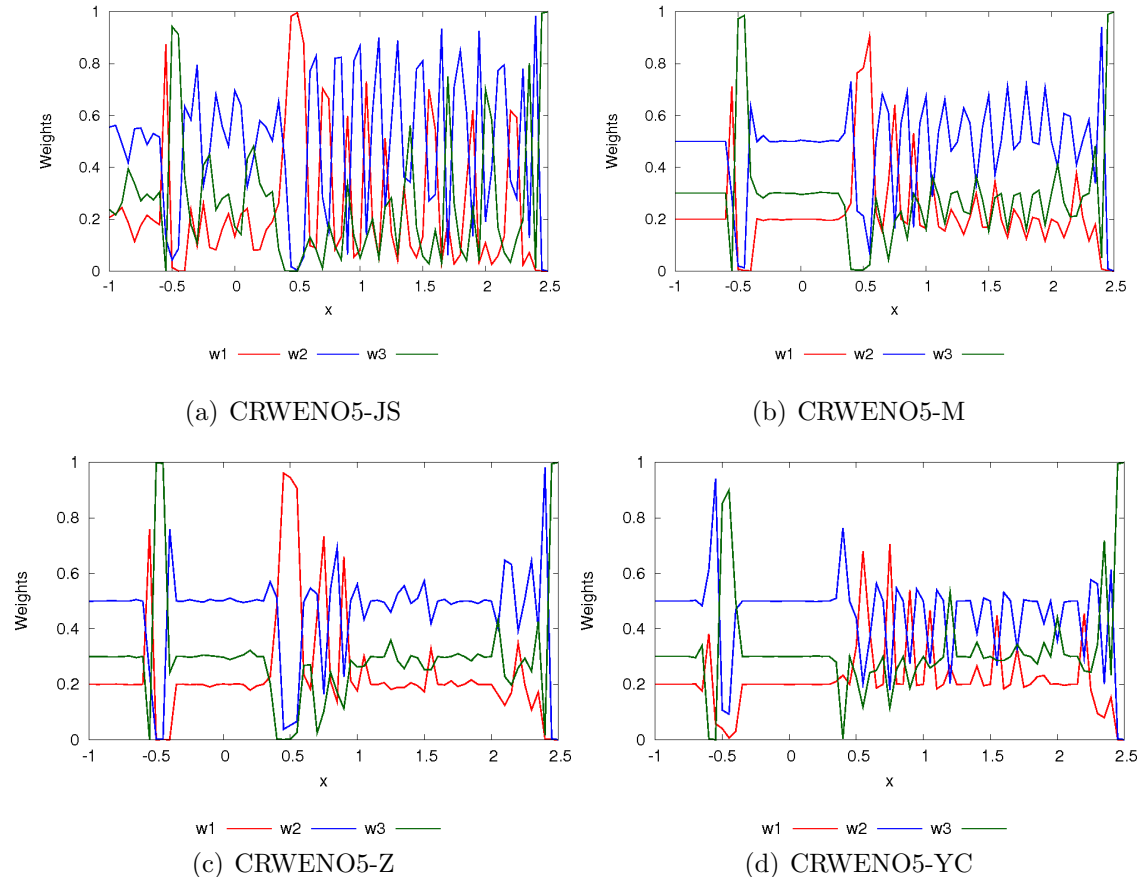
Figure 3.11: Shock – entropy wave interaction: Weights for the left-biased reconstruction of characteristic field u ($\epsilon = 10^{-6}$).

shown in Fig. 3.11 for the CRWENO schemes. The weights computed using the CRWENO5-JS implementation are far from optimal. The CRWENO5-M scheme results in a slight improvement, where the weights are closer to their optimal values. The CRWENO5-Z and CRWENO5-YC implementations show significant improvements in the weights and this results in the higher resolution of the solutions. The solutions shown in the previous figures are obtained with $\epsilon = 10^{-6}$ and are identical for $\epsilon = 10^{-20}$.

Thus, to summarize, the CRWENO5 scheme with the weights proposed in [13] show significant dissipation and loss of accuracy. The computed weights are observed to be non-optimal for extrema of smooth flows on coarse grids as well as high-wavenumber flow features. The alternative formulations for the non-linear weights result in weights that are closer to their optimal values, while retaining the non-oscillatory nature of the scheme across discontinuities. This results in a significant improvement of the resolution of small length-scale flow features.

3.6   Two-Dimensional Inviscid Flow Problems

The CRWENO schemes are applied to two-dimensional inviscid flow problems to assess and validate their performance in multiple dimensions. The present section considers inviscid flows solved on a domain discretized by an equi-spaced Cartesian grid. The numerical solution of the one-dimensional Euler equations is described in Section 3.2 and their extension to the two-dimensional Euler equations is trivial. The CRWENO schemes are applied along each grid line in each dimension. The

reconstruction of conserved or primitive variables requires $(D+2)(NI+NJ)$ tridiagonal solutions at each iteration, where NI and NJ are the total number of points in each dimension and D is the number of dimensions. A characteristic-based reconstruction requires $(NI+NJ)$ block tridiagonal solutions at each iteration. Thus, it is important to verify the conclusions drawn regarding computational efficiency in Section 3.4 for a multi-dimension case.

3.6.1 Isentropic Vortex Convection

The long-term convection of an isentropic vortex with the freestream flow [15] is considered. An isentropic vortex is an exact solution of the two-dimensional Euler equations and convects with the freestream flow without dissipation or distortion. The performance of numerical schemes for this test problem indicates their ability to preserve the strength and shape of vortical structures for large durations of time.

The domain is taken as $[0, 10] \times [0, 10]$ in the present example and the freestream flow is

$$\rho_\infty = 1, \ u_\infty = 0.5, \ v_\infty = 0, \ p_\infty = 1$$

A vortex is introduced in the flow, specified as:

$$\rho = \left[1 - \frac{(\gamma-1)b^2}{8\gamma\pi^2} e^{1-r^2} \right]^{\frac{1}{\gamma-1}}; \ p = \rho^\gamma$$

$$\delta u = -\frac{b}{2\pi} e^{\frac{1-r^2}{2}}(y - y_c)$$

$$\delta v = \frac{b}{2\pi} e^{\frac{1-r^2}{2}}(x - y_c) \qquad (3.27)$$

where $r = ((x-x_c)^2 + (y-y_c)^2)^{1/2}$ is the distance from the vortex center and $b = 0.5$ is the vortex strength. Periodic boundary conditions are applied at all boundaries.

(a) Initial

(b) WENO5

(c) CRWENO5

(d) CRWENO5-LD
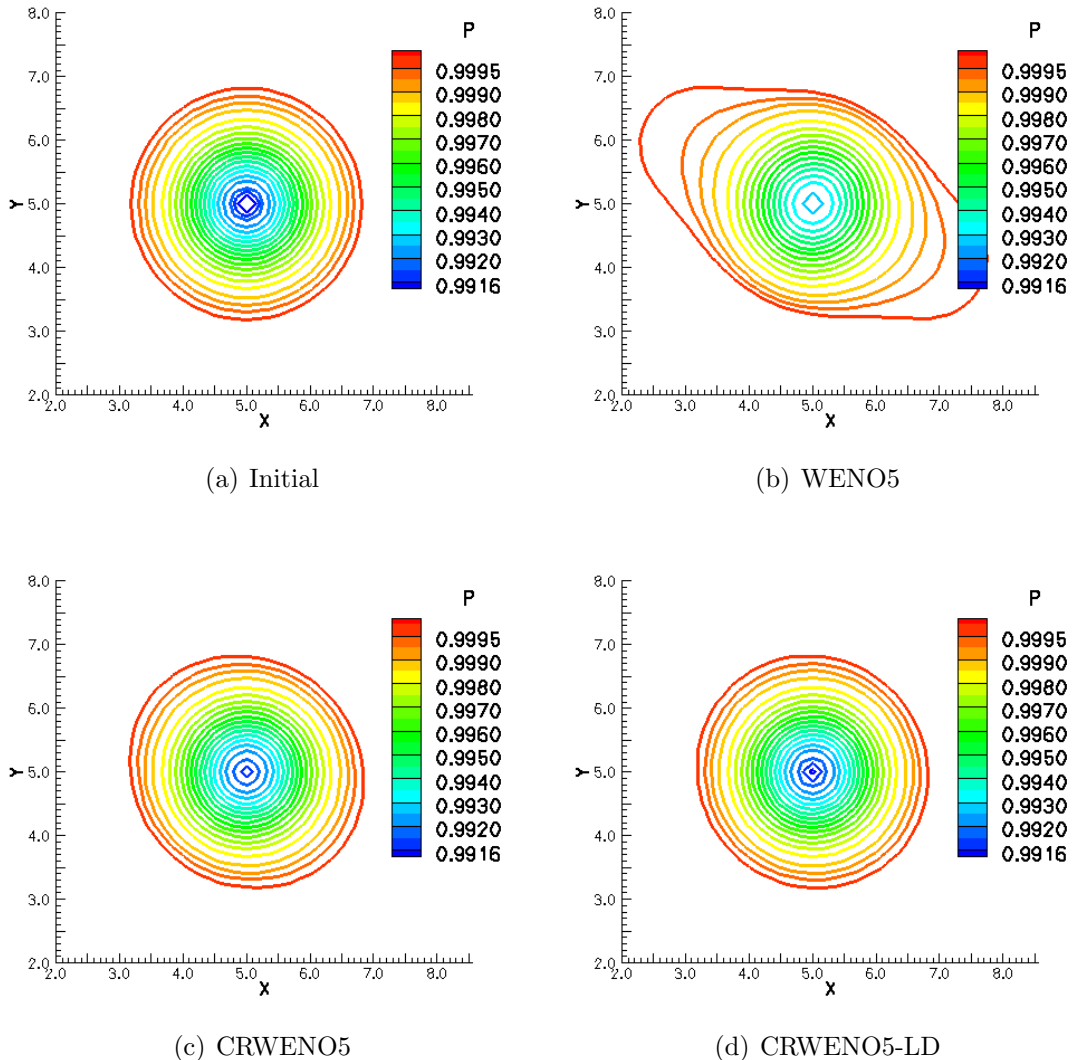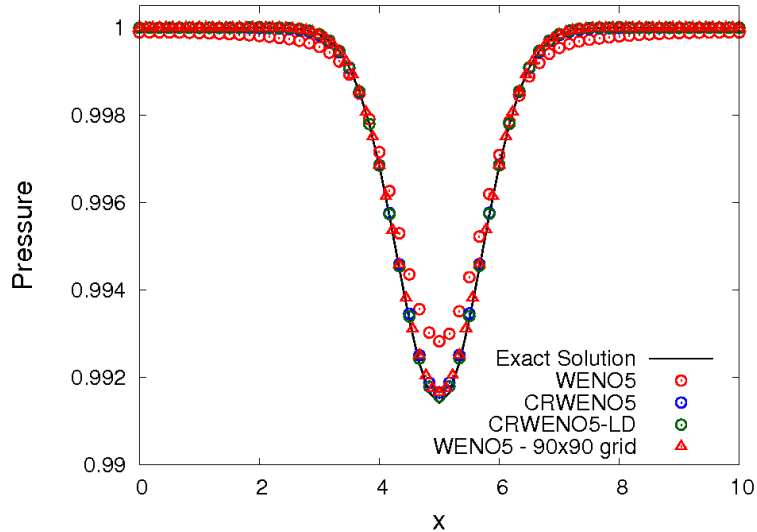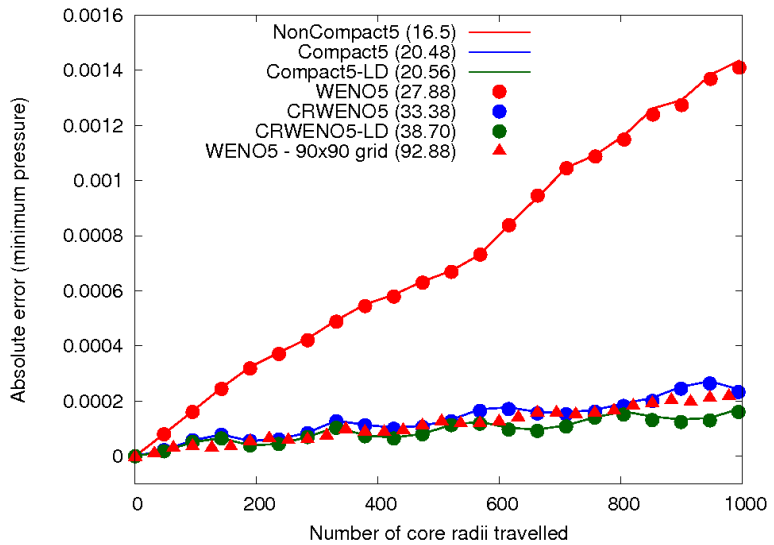
Figure 3.12: Pressure contours for isentropic vortex convection after travelling 1000 core radii

As the solution is evolved in time, the vortex convects over the periodic domain with a time period of $T = 20$.

Solutions are obtained on a 60×60 grid at a CFL number of 0.5. The TVD-RK3 scheme is used to evolve the solution in time. The WENO5, CRWENO5 and CRWENO5-LD schemes are applied to the reconstruction of conserved variables. The problem is smooth and the reconstruction of primitive or conserved variables

(a) Cross-sectional pressure

(b) Pressure error at core (Number in parentheses is the computational run-time)

Figure 3.13: Cross-sectional pressure contours and error in pressure at vortex core for solutions obtained on a 60×60 grid

suffices. The solutions are obtained after the vortex travels a distance of 1000 times the core radius. Figure 3.12 shows the pressure contours of the vortex corresponding to the initial conditions and the numerical solutions obtained by the WENO5, CRWENO5 and CRWENO5-LD schemes. The solution obtained by the WENO5

scheme shows significant dissipation of the vortex strength at the center as well as a distortion of the shape. The CRWENO5 and CRWENO5-LD schemes are able to preserve the vortex strength and shape as it convects over a large distance. Figure 3.13(a) shows the pressure variation through the cross-section of the vortex. In addition to the solutions obtained on a 60×60 grid, the solution obtained by the WENO5 scheme on a 90×90 grid is included. The WENO5 scheme causes significant dissipation of the pressure at the same grid resolution. The solutions obtained by the CRWENO schemes are comparable to that obtained by the WENO5 scheme on the 90×90 grid.

Figure 3.13(b) shows the non-dimensionalized absolute error in pressure at the vortex core as a function of the convection distance. The solutions obtained using the underlying optimal schemes, NonCompact5, Compact5 and Compact5-LD, are included as well as the solution obtained by the WENO5 scheme on a 90×90 grid. The solutions obtained by the WENO5, CRWENO5 and CRWENO5-LD schemes show a good agreement with their optimal counterparts, thus verifying that the weights attain their optimal values for a smooth solution. The solutions obtained using the CRWENO schemes have a significantly lower error than that obtained by the WENO5 scheme. This holds true for their optimal counterparts as well. The solution obtained by the WENO5 scheme on a 90×90 grid is comparable to those obtained by the CRWENO schemes on a 60×60 grid.

The computational efficiency of the CRWENO schemes is assessed for the reconstruction of conserved/primitive variables in two dimensions. The number in the parentheses inside the legend of Fig. 3.13(b) indicates the computational

run-time for each of the schemes. The schemes with the WENO limiting have larger run-times than the corresponding optimal schemes due to the computation of weights. The WENO5 scheme is less expensive at the same grid resolution as expected. However, the WENO5 scheme on a 90×90 grid is significantly more expensive than the CRWENO schemes on a 60×60 grid and yields results of similar accuracy. Thus, the conclusions drawn regarding the computational efficiency of CRWENO schemes in Section 3.4 extend to multiple dimensions.

3.6.2 Double Mach Reflection of a Strong Shock
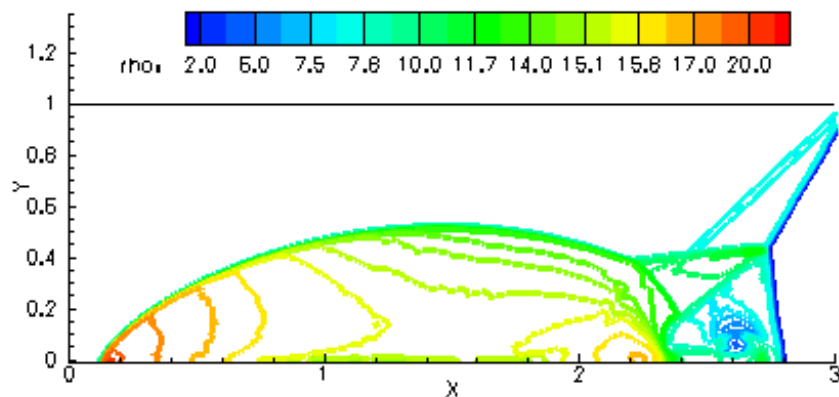
The double Mach reflection of a strong shock is a benchmark inviscid problem [53] to assess the performance of the algorithm for strong discontinuities. The flow involves the reflection of a strong shock wave from an inviscid wall resulting in secondary shock waves and contact discontinuities. The CRWENO schemes are applied to this problem to validate their non-oscillatory behavior for a two-dimensional flow dominated by strong discontinuities that are not grid-aligned.

The domain is a rectangle defined as $[0, 4] \times [0, 1]$ and the initial conditions consist of an oblique Mach 10 shock intersecting the bottom boundary $y = 0$ at $x = \frac{1}{6}$. The shock is at an angle of 60° to the x-axis. The flow upstream of the shock is initialized as $\rho, u, v, p = 1.4, 0, 0, 1$ and post-shock conditions are specified downstream. The left and right boundaries ($x = 0$ and $x = 4$) are set to the post- and pre-shock flow conditions respectively. The bottom boundary ($y = 0$) consists of an inviscid wall for $\frac{1}{6} < x \leq 4$ and post-shock flow conditions are imposed on
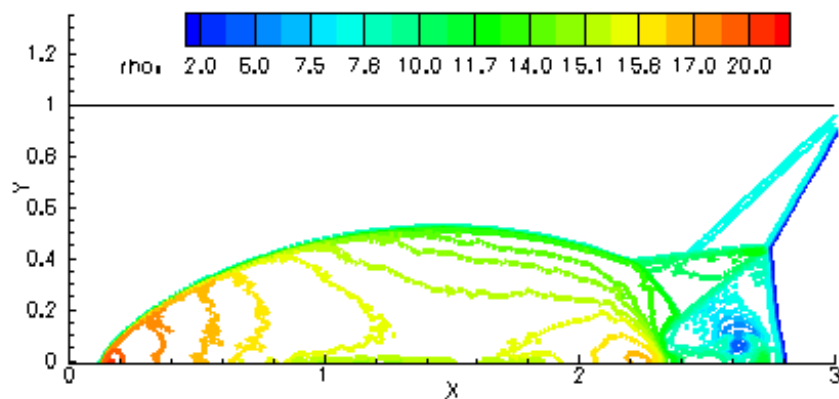
$x \le \frac{1}{6}$. The boundary conditions at the top of the domain $(y = 1)$ correspond to the exact motion of a Mach 10 oblique shock.

The flow is solved on a grid with 480×120 grid points. The presence of strong discontinuities requires the reconstruction of characteristic variables. Though the CRWENO schemes are computationally less efficient than the WENO scheme for a characteristic-based reconstruction, this problem is presented as a validation of the schemes for multi-dimensional problems with strong, non-grid-aligned discontinuities, as well as to demonstrate its numerical properties. The solution is obtained at $t = 0.2$ with the TVD-RK3 scheme and a CFL number of 0.5.
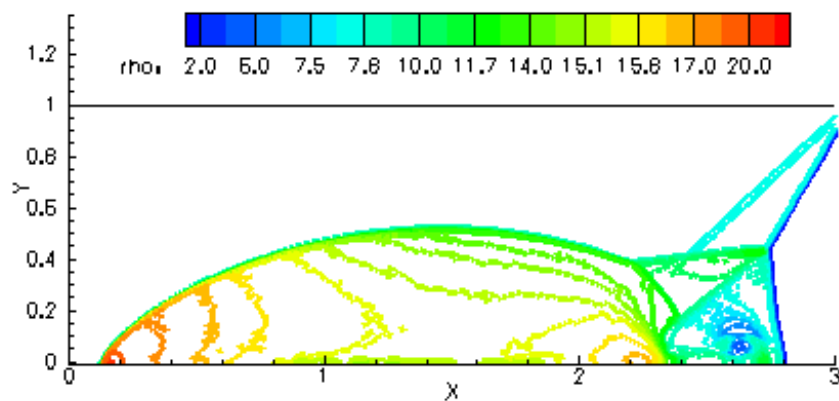
Figure 3.14 shows the density contours of the solution obtained with the WENO5, CRWENO5 and CRWENO5-LD schemes. The shock waves and the Mach stems are captured well with all the three schemes and the solutions agree well with those in the literature [13, 14]. Figure 3.15 shows the entropy contours for this problems, obtained on the 480×120 grid with the various schemes. The compact schemes show an improved resolution of the contact discontinuity roll-up at the base of the Mach stem. The solution obtained using the WENO5 scheme on a 720×180 grid is also included for comparison (Fig. 3.15(b)). The solutions obtained by the CRWENO schemes are comparable to the solution obtained by the WENO5 scheme on a finer grid. The resolution of the CRWENO schemes is comparable to that of the ninth-order MPWENO scheme in [14](see Fig. 7(b) on page 445 of that paper).

(a) WENO5
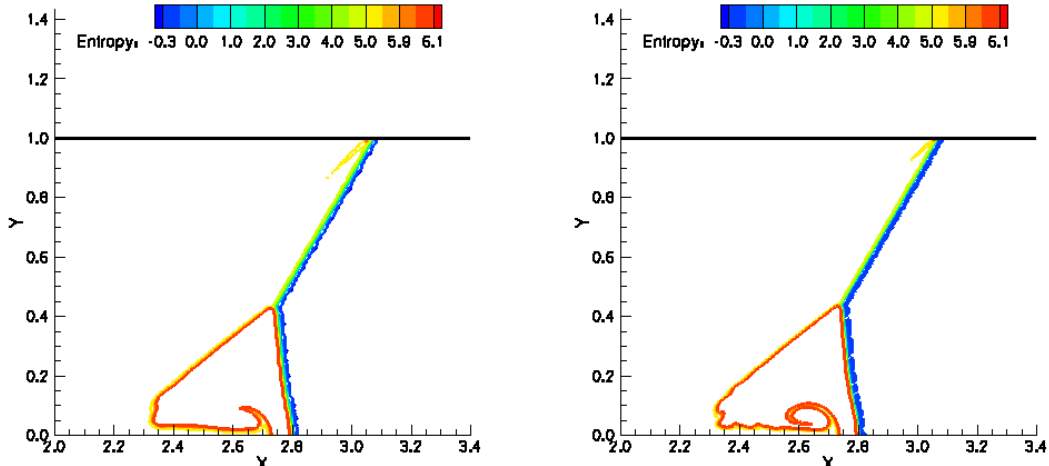
(b) CRWENO5
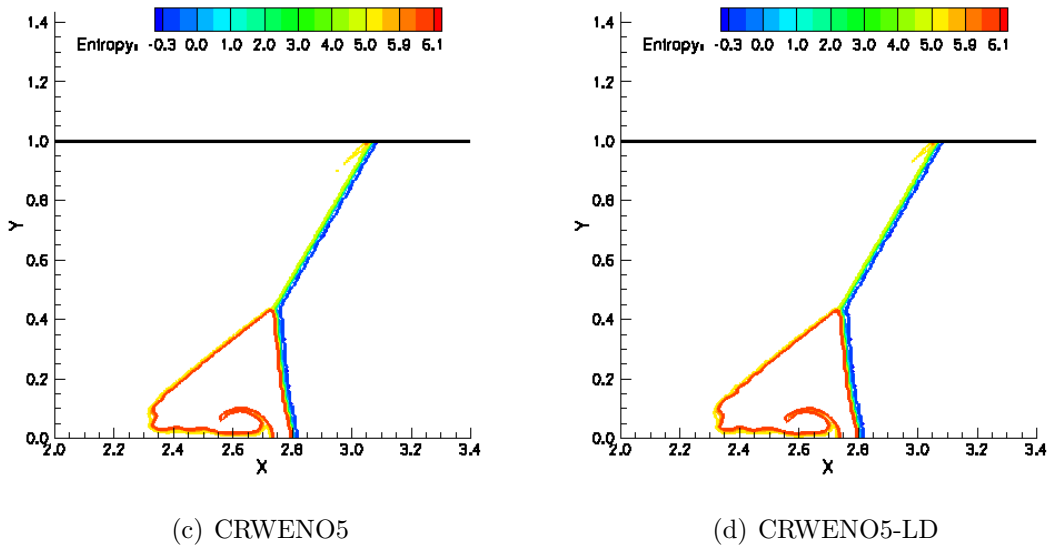
(c) CRWENO5-LD

Figure 3.14: Density contours for double Mach reflection problem on a 480×120 grid

(a) WENO5

(b) WENO5 (720×180 grid)

(c) CRWENO5

(d) CRWENO5-LD

Figure 3.15: Entropy contours for double Mach reflection problem on a 480×120 grid

3.6.3 Shock – Vorticity Wave Interaction

The interaction of a shock wave with a vorticity wave [11] is a two-dimensional, simplified representation of shock-turbulence interactions. This is a two-dimensional equivalent of the shock – entropy wave interaction discussed in Section 3.3.3. This
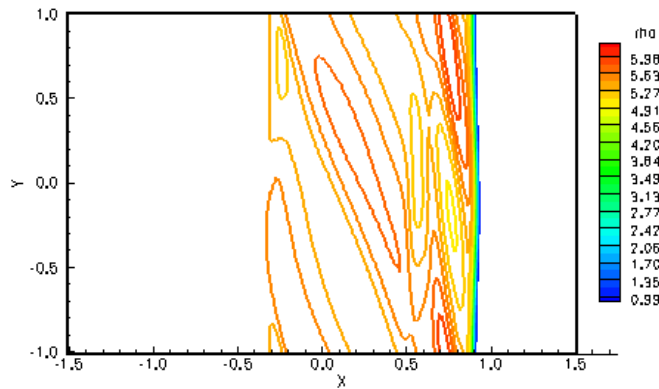
benchmark problem involves the accurate capturing of acoustic, vorticity and entropy waves and has been studied in [41, 43] using hybrid compact-ENO/WENO schemes.

The flow involves a Mach 8 shock wave interacting with a vorticity wave. The domain is taken as $[-1.5, 1.5] \times [-1, 1]$ and the shock is initially situated at $x = -1$. The vorticity wave, upstream of the shock, is defined as:

$$\rho = 1$$

$$u = -\sqrt{\gamma} \sin\theta \cos\left(2\pi x \cos\theta + 2\pi y \sin\theta\right)$$

$$v = \sqrt{\gamma} \cos\theta \cos\left(2\pi x \cos\theta + 2\pi y \sin\theta\right)$$

$$p = 1$$
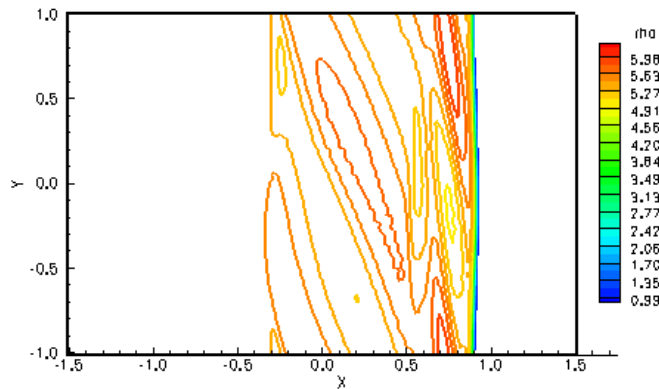
where $\theta = \pi/6$ is the angle of the vorticity wave with the shock wave. Uniform post-shock conditions are specified downstream of the shock that are related to the undisturbed upstream state by the Rankine-Hugoniot conditions. The solution is evolved to a time of $t = 0.2$ using the TVD-RK3 scheme. Periodic boundary conditions are enforced on the top and bottom boundaries $(y = \pm 1)$. Steady flow values corresponding to the flow conditions upstream and downstream of the shock are specified at the left and right boundaries $(x = \pm 1.5)$. The solutions are obtained at a CFL number of 0.5.
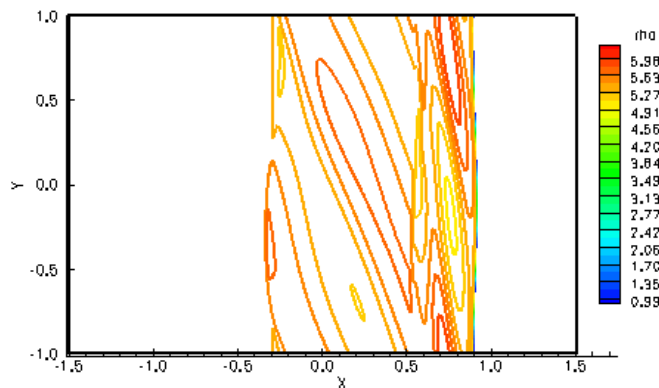
Solutions are obtained using the reconstruction of characteristic variables, since the problem involves discontinuities. Figure 3.16 shows the density contours

135
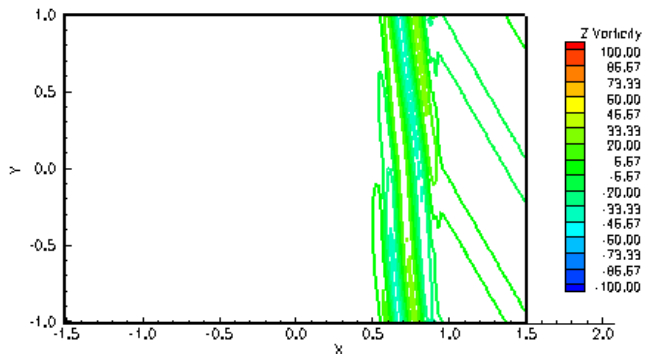
(a) WENO5 (192 × 128 grid)



(b) CRWENO5 (192 × 128 grid)
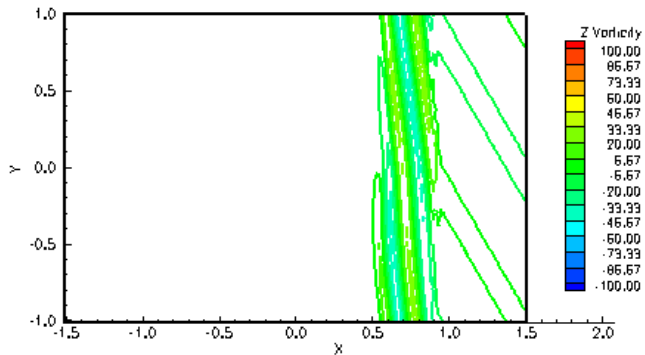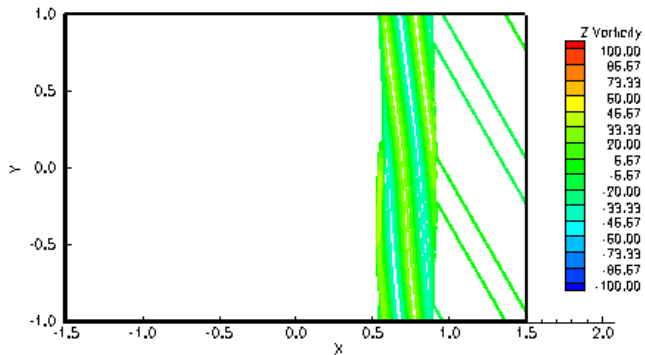
(c) WENO5 (960 × 640 grid)

Figure 3.16: Density contours for shock – vorticity wave interaction problem

(a) WENO5 (192×128 grid)

(b) CRWENO5 (192×128 grid)

(c) WENO5 (960×640 grid)

Figure 3.17: Vorticity contours for shock – vorticity wave interaction problem

using the WENO5 and CRWENO5 schemes on a 192×128 grid. The solution

obtained using the WENO5 scheme on a 960×640 grid is also included as the "ex-

act" solution, in the absence of an analytical one. Figure 3.17 shows the vorticity
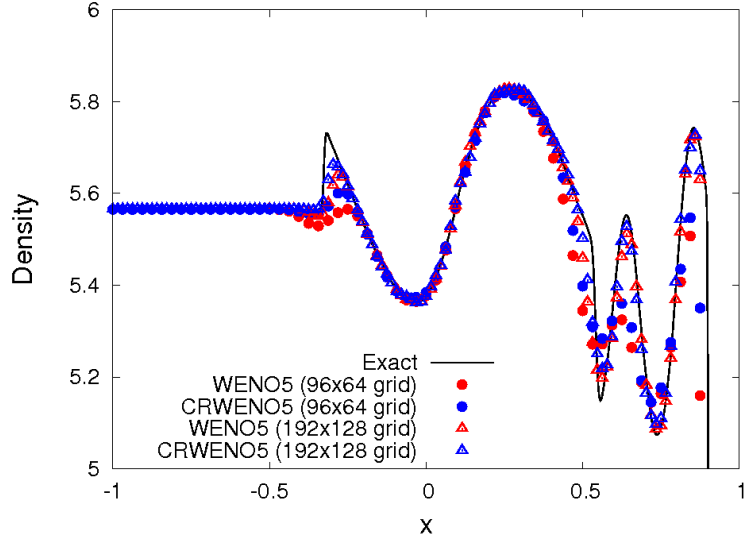
Figure 3.18: Cross-sectional density for shock – vorticity wave interaction problem

contours for the same solutions. The solutions show good agreement with those in the literature [11, 41, 43]. Figure 3.18 shows the cross-sectional density variation through $y = 0$, magnified around the post-shock region. The solution comprises fast left-running acoustic waves, and slow left-running entropy and vorticity waves. The acoustic and entropy-vorticity regions are demarcated by a sharp discontinuity around $x = 0.55$. The "exact" solution corresponds to the solution obtained using the WENO5 scheme on a 960×640 grid. Solutions obtained using the WENO5 and CRWENO5 schemes on two different grids, 96×64 and 192×128, are shown. The CRWENO5 scheme shows a sharper resolution of the solution at both grid refinement levels, for the acoustic, entropy and vorticity waves. This particular flow problem is not as numerically challenging since it involves waves of large wave-lengths and therefore, the differences in the solutions by WENO5 and CRWENO5 are slight. The solutions obtained here compare well with those obtained by the hybrid compact-WENO schemes in [43].
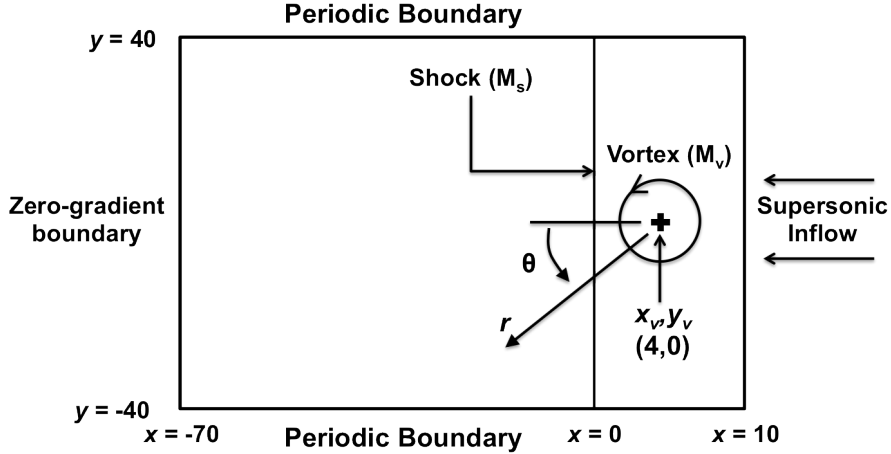
Figure 3.19: Schematic diagram of the initial conditions for the shock-vortex interaction

3.6.4 Sound Generation from Shock-Vortex Interaction

A significant cause of aerodynamic noise in compressible flows is shock – turbulence interactions. A simplified, benchmark problem representing the acoustics of shock – turbulence interactions is the interaction of an isolated vortex with a planar shock wave and the consequent formation of sound waves. There have been several experimental and computational studies [54, 55, 56] (and references therein) focusing on the effect of vortex and shock strengths on the generation of sound as well as the deformation of the vortex and the shock wave.
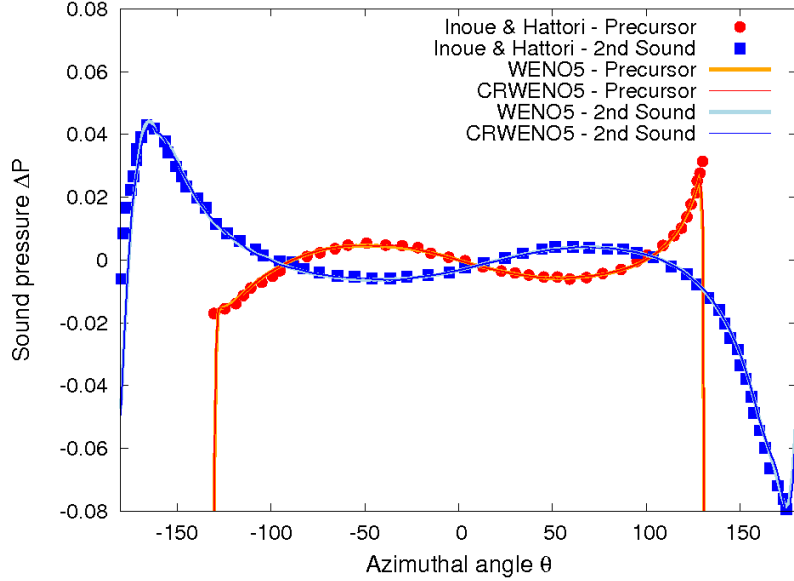
The initial conditions consist of a stationary shock in a rectangular domain given by $[-70, 10] \times [0, 10]$. A relatively large domain is taken such that the sound waves do not reach the boundaries within the simulation times. The shock is placed at $x = 0$ with a freestream Mach number (M_s) of 1.2, with the flow going from right to left. The right $(x = 10)$ boundary is supersonic inflow while zero gradients are enforced at the left $(x = -70)$ boundary. The top $(y = 40)$ and bottom $(y = -40)$

boundaries are periodic. The domain is initialized with $\rho, u, v, p = 1, -1.2, 0, 1/\gamma$ upstream of the shock and post-shock conditions downstream of the shock. An isentropic vortex is added to the flow at $(x_v = 4, \; y_v = 0)$ for which the density and velocity is given by
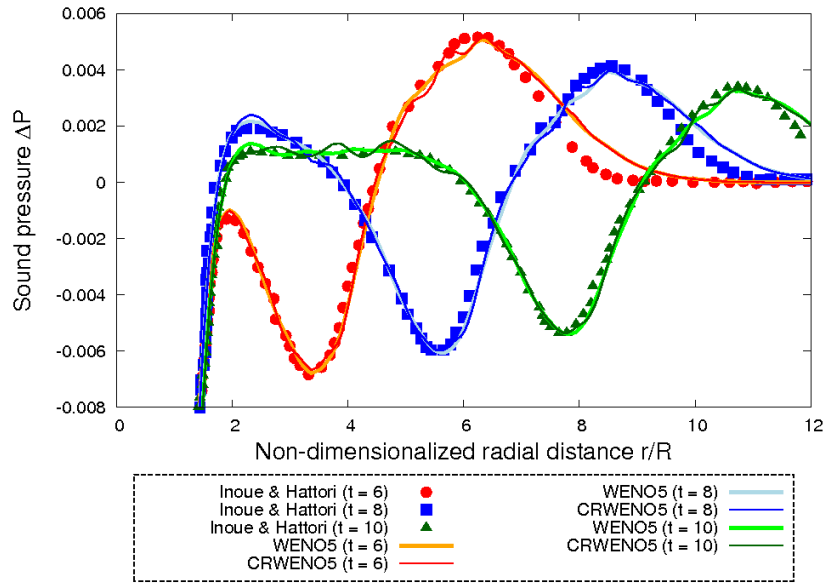
$$
\begin{aligned}
\rho &= \left(1 - \frac{1}{2}(\gamma - 1)M_v^2 e^{1-(r/R)^2}\right)^{\frac{1}{\gamma-1}} \\
\delta u &= -M_v e^{\frac{1}{2}(1-(r/R)^2)}(y - y_v) \\
\delta v &= M_v e^{\frac{1}{2}(1-(r/R)^2)}(x - x_v)
\end{aligned}
\tag{3.28}
$$

where M_v is the vortex strength, $r = \sqrt{(x - x_v)^2 + (y - y_v)^2}$ is the radial distance from the vortex center and $R = 1$ is the vortex radius. Figure 3.19 shows the domain with the initial and boundary conditions.

The weak interaction ($M_v = 0.25$) is solved to verify the algorithm. Solutions are obtained on a uniform 640×640 mesh with the TVD-RK3 time-stepping at a CFL number of 0.5. Figure 3.20 shows the radial and azimuthal sound pressure ($\Delta p = \frac{p - p_\infty}{p_\infty}$, where p_∞ is the post-shock freestream pressure) for the solutions obtained with the CRWENO5 and WENO5 schemes. Two sound waves – precursor and second sound – are generated as a result of the primary interaction of the vortex with the shock wave. Both sound waves are quadrupolar and out of phase with each other. The solutions are compared with those in [54], obtained using a 6th-order central compact scheme and 4th-order Runge-Kutta time-stepping; and a good agreement is observed.
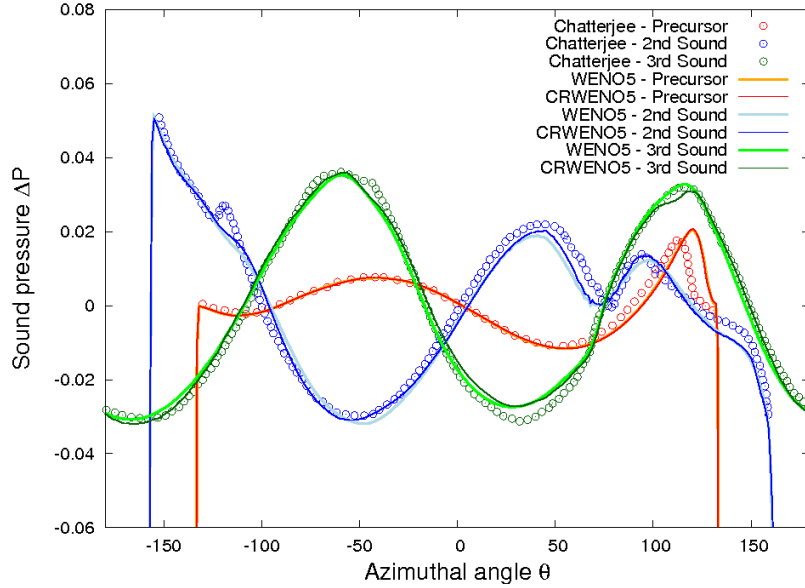
(a) Azimuthal variation at $t = 6$ ($r = 6.0$ - precursor, $r = 3.7$ - second sound)
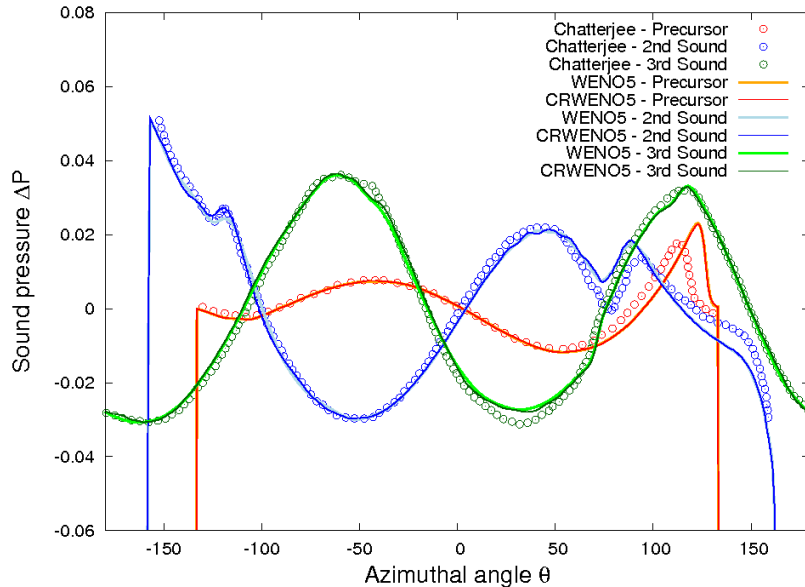

(b) Radial variation at $t = 6$ for $\theta = -45^{\circ}$

Figure 3.20: Sound pressure for the weak shock – vortex interaction

The strong interaction ($M_v = 1.0$) is solved with the 9th-order WENO (WENO9) scheme [14], along with the 5th-order WENO and CRWENO schemes. Solutions are obtained on uniform grids with 640×640 and 1050×1050 points and compared with those obtained in [56] using the 7th and 9th-order WENO schemes on iden-
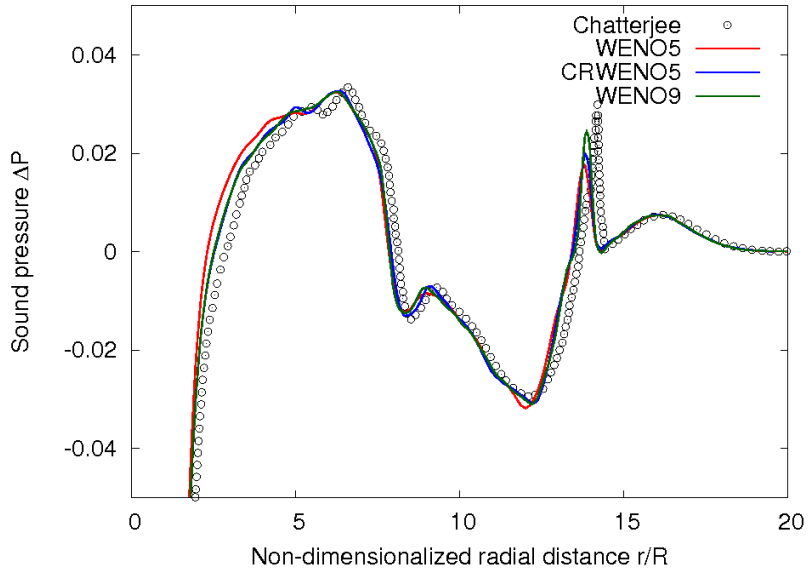
(a) 640×640 grid
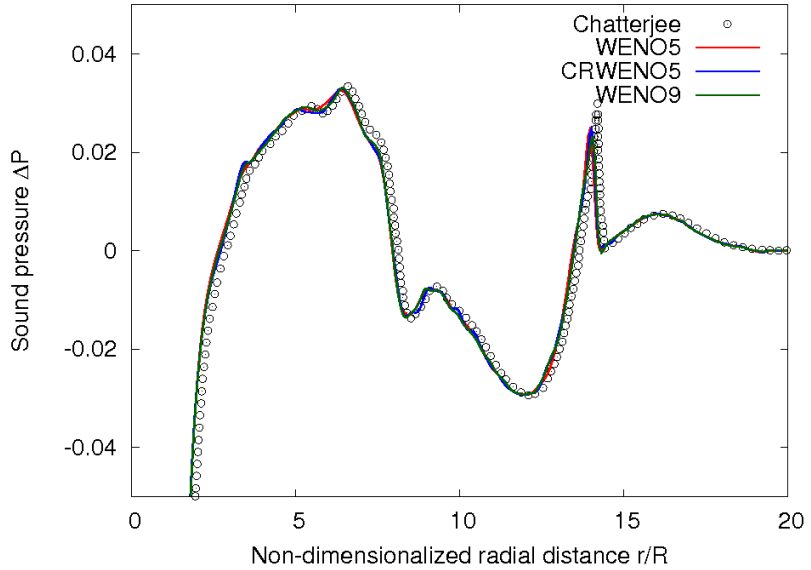
(b) 1050×1050 grid

Figure 3.21: Azimuthal variation of sound pressure at $t = 16$ ($r = 16.0$ - precursor, $r = 12.0$ - second sound, $r = 6.7$ - third sound) (strong interaction)

tical grids. The TVD-RK3 scheme is used to march in time at a CFL number of

0.5. Figure 3.21 shows the azimuthal variation of sound pressure at $t = 16$ for the

two different grid resolutions. Three quadrupolar sound waves – precursor, second

(a) 640×640 grid

(b) 1050×1050 grid

Figure 3.22: Radial variation of sound pressure at $\theta = -45^{\mathrm{o}}$ (strong interaction)

sound and third sound – are observed at different radial locations and consecutive

sound waves are out of phase with each other. These result from the multi-stage

interaction of the vortex with the shock wave as well as secondary shock structures

[55]. Figure 3.22 shows the radial variation of the sound pressure at $t = 16$ for

(a) $t = 16$

(b) $t = 20$

(c) $t = 34$
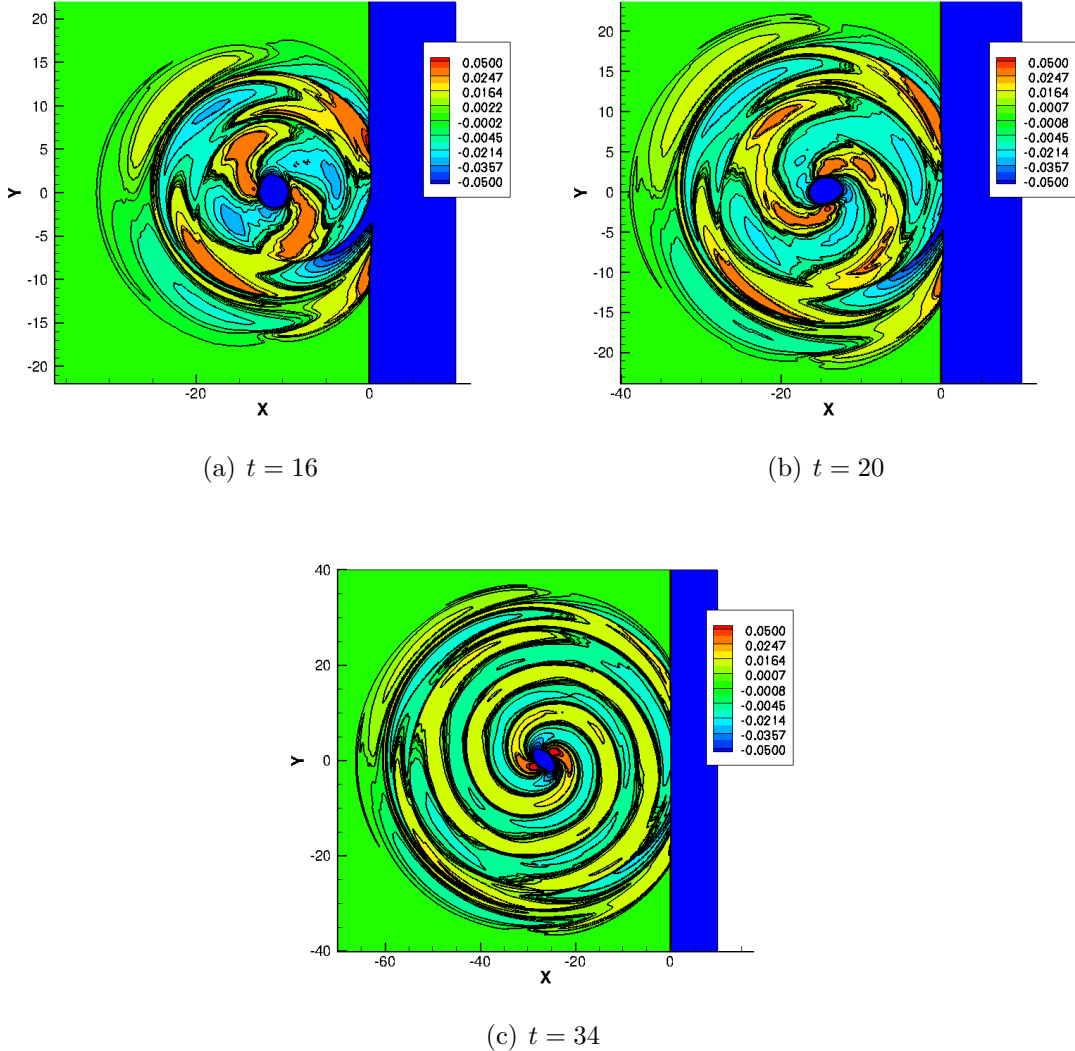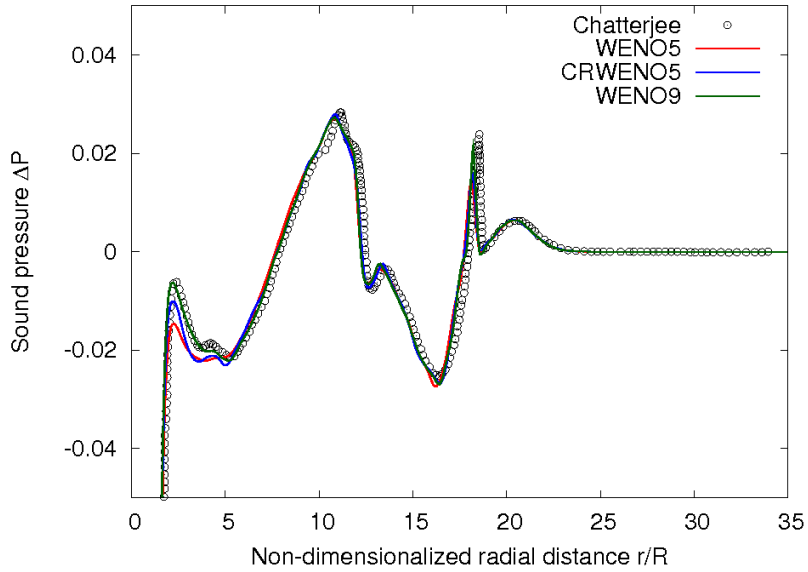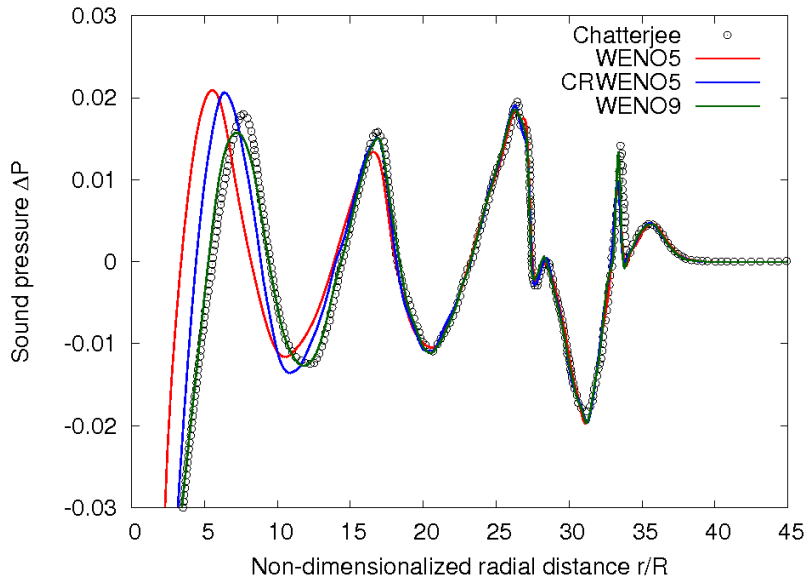
Figure 3.23: Sound pressure contours (strong interaction)

both grid resolutions. The three sound waves are visible as well as the secondary shock structure between the precursor and the second sound. At a grid resolution of 640×640 (Fig. 3.22(a)), the CRWENO5 scheme shows a sharper resolution of the secondary shock structure compared to the WENO5 scheme. The solutions agree well with the results in [56].

(a) $t = 20$

(b) $t = 34$

Figure 3.24: Radial variation of sound pressure on the 640×640 grid

The precursor, second and third sounds result from the primary and secondary shock – vortex interactions. These interactions result in the distortion of the initially circular vortex to an elliptical, rotating vortex that radiates additional quadrupolar sound waves. Figure 3.23 shows the sound pressure contours at $t = 16, 20, 34$ for

(a) CRWENO5   (b) WENO5   (c) WENO9
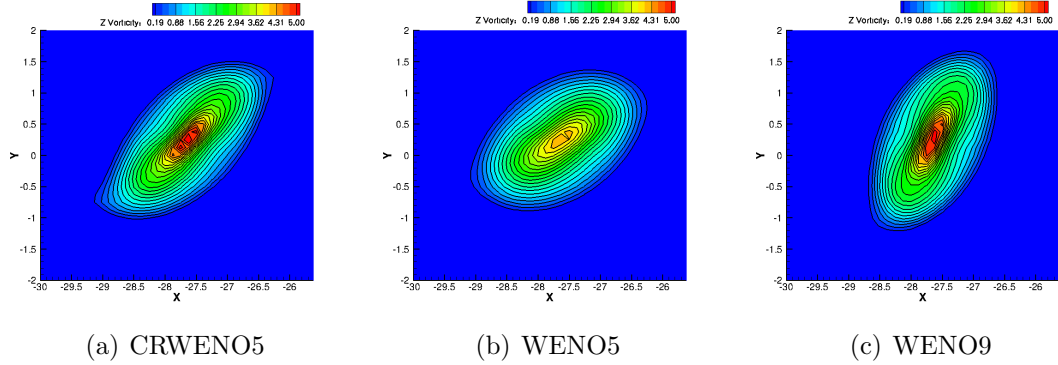
Figure 3.25: Out-of-plane vorticity contours at $t = 34$ (640×640 grid)

(a) CRWENO5   (b) WENO5   (c) WENO9
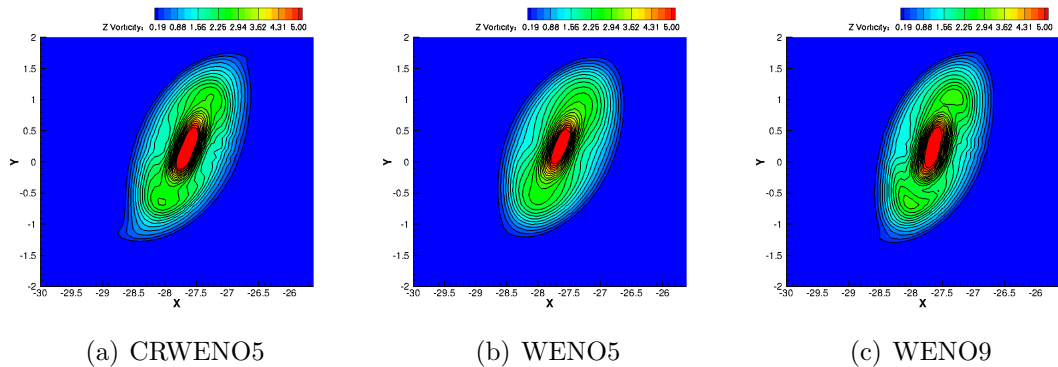
Figure 3.26: Out-of-plane vorticity contours at $t = 34$ (1050×1050 grid)

the solution obtained using the CRWENO5 scheme on the 1050×1050 grid. Three quadrupolar sound waves are identifiable at $t = 16$ that are generated from the interaction of the vortex with the primary and secondary shocks. At $t = 20$, the vortex takes on the elliptical shape causing the emission of additional sound waves. A fourth acoustic wavefront is identifiable. Finally, Fig. 3.23(c) shows the acoustic field at $t = 34$ for the rotating, elliptical vortex as it convects downstream emitting sound waves.

Figure 3.24 shows the radial variation of the sound pressure at $t = 20$ and $t = 34$. The additional sound waves generated due to the rotation of an elliptic vortex

146
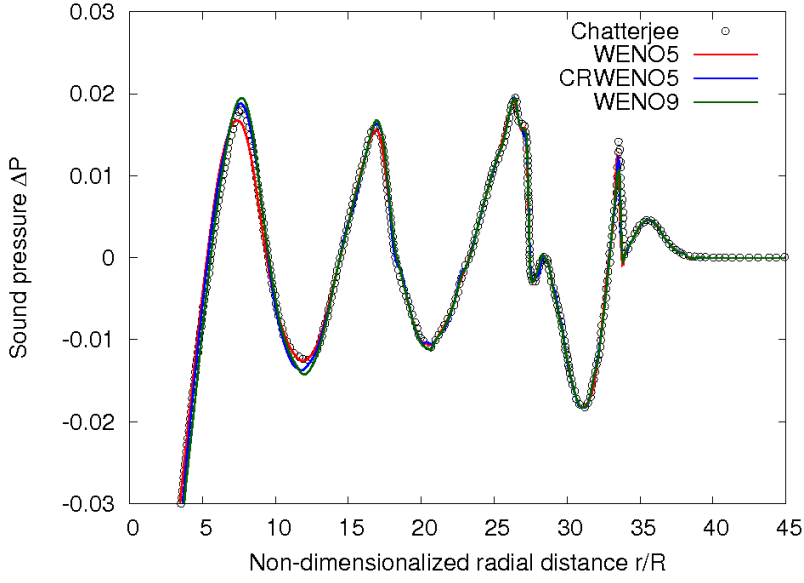
Figure 3.27: Radial variation of sound pressure at $t = 34$ on the 1050×1050 grid

are identifiable. At $t = 34$, seven sound waves are observed. The CRWENO5 shows

a sharper resolution of the sound waves at all times than the WENO5 scheme and the

solutions obtained with the CRWENO5 scheme are comparable to those obtained

with the WENO9 scheme. A disagreement in the sound pressure is observed between

the various schemes in Fig. 3.24(b) near the vortex core. This is a result of the

numerical error in the vortex strength and orientation. Figure 3.25 shows the out-

of-plane vorticity contours for the solutions at $t = 34$ obtained with the various

schemes on the 640×640 grid, while Fig. 3.26 shows the same on the 1050×1050

grid. The WENO5 scheme shows a significant dissipation of the vortex strength

as well as an error in the orientation on the coarse grid, compared to the WENO9

scheme. The orientation of the vortex at a given time instant depends on the

accurate numerical modeling of the shock – vortex interaction that results in the

distortion of the vortex. The CRWENO5 scheme shows a significant improvement

147

in preserving the vortex strength as well as predicting the correct rotational speed. The solutions obtained by the three schemes are similar on the finer grid. Figure 3.27 shows the radial variation of sound pressure at $t = 34$ on the 1050×1050 grid and the solutions obtained with the various schemes agree well with each other.

3.7   Summary of Chapter

The application of the CRWENO schemes, introduced in the last chapter, to the Euler equations is discussed in this chapter. The CRWENO schemes, given by Eqns. (2.19) and (2.29), describe the interpolation of a scalar variable. Three different extensions to a vector function, in the context of the Euler equations, are discussed and compared: reconstruction of primitive, conserved or characteristic variables.

The accuracy and convergence of the CRWENO schemes is verified on a smooth, one-dimensional problem. The conclusions regarding the improved accuracy for the same order of convergence, drawn in the last chapter for scalar equations, extend to the Euler equations. These observations are consistent with the Taylor series analysis of the schemes. The non-oscillatory nature of the schemes as well as the resolution of discontinuities is assessed on benchmark inviscid flow problems. The CRWENO schemes yield solutions with lower smearing of discontinuities. Specific to the case of a flow with discontinuities as well as small length-scale structures, the CRWENO schemes show a significant improvement in the resolution of the smaller scales without compromising on the non-oscillatory behavior across shock waves.

This property of the schemes indicates their suitability for simulation of compressible, turbulent flows.

The numerical cost of the CRWENO schemes is studied in the context of a system of equations. The CRWENO schemes are computationally more efficient for the reconstruction of primitive or conserved variables. The reconstruction of characteristic variables with non-linear compact schemes requires the solution of a block tridiagonal system and thus, the additional numerical cost is not justified by the increase in accuracy (compared to the WENO schemes). Although the reconstruction of the characteristic variables is required to yield non-oscillatory solutions for inviscid flows with strong discontinuities, it is shown in the next chapter that reconstruction of primitive/conserved variables suffice for viscous flows or flows without strong discontinuities. Thus, the applicability of the CRWENO schemes is not limited.

The CRWENO schemes are extended to the two-dimensional Euler equations, discretized on equi-spaced Cartesian grids. The schemes are validated on benchmark problems. The long-term convection of an isentropic vortex is studied and the CRWENO schemes show significant improvements in preserving the vortex strength and shape. This indicates their suitability towards the simulation of aircraft and rotorcraft wake flows, which involves the long-term convection and interactions of vortical structures. The schemes are validated for flows with strong discontinuities, especially one case that involves the interaction of a shock wave with a vorticity wave. This problem is representative of flows involving shock-turbulence interactions. The performance of the schemes is also verified for the accurate prediction of sound

generation from shock – vortex interactions.

The numerical results presented in this chapter demonstrate the ability of the CRWENO schemes to resolve smaller length scales and discontinuities, and preserve flow features while yielding non-oscillatory solutions across discontinuities. Based on these encouraging results for benchmark problems, the next chapter presents the integration of the schemes with an in-house flow solver and the application of the schemes to flows of practical relevance.

Chapter 4

Application to Navier-Stokes Equations

The application of the CRWENO schemes to one- and two-dimensional inviscid flow problems on equi-spaced grids was presented in the preceding chapter. The solutions were compared to those obtained using the traditional WENO schemes. The spectral properties of the CRWENO schemes result in an improved resolution of smaller length scales, while maintaining non-oscillatory behavior across discontinuities. The lower dissipation and dispersion errors result in reduced smearing of discontinuities as well as improved preservation of flow features for convection over large distances.

In the present chapter, the fifth-order CRWENO scheme is integrated into a structured, finite-volume, compressible Navier-Stokes solver and applied to flow problems of practical relevance. The scheme is validated for curvi-linear meshes as well as domains discretized by multiple, overset meshes with relative grid motion. Steady and unsteady flows around two-dimensional airfoils as well as three-dimensional wings are solved and the results are presented. It should be noted that a lower-order numerical scheme usually suffices for the prediction of integrated forces (lift and drag). However, in this thesis, the focus is on the accurate resolution of flow features near the airfoil/wing surfaces as well as in the wake. This chapter presents cases that show the improved performance of the CRWENO schemes in capturing

these features.

The CRWENO schemes are applied to the direct numerical simulation (DNS) of turbulent flows. Two benchmark problems are presented that demonstrate the ability of the schemes to accurately capture the smaller length scales of turbulent fluctuations. These results indicate the suitability of the CRWENO schemes for the numerical solution of compressible turbulent flows.

4.1   Governing Equations

The governing equations are the three-dimensional Navier-Stokes equations [3] that can be expressed as

$$\frac{\partial \mathbf{u}}{\partial t} + \frac{\partial \mathbf{f}}{\partial x} + \frac{\partial \mathbf{g}}{\partial y} + \frac{\partial \mathbf{h}}{\partial z} = \frac{\partial \mathbf{f}_v}{\partial x} + \frac{\partial \mathbf{g}_v}{\partial y} + \frac{\partial \mathbf{h}_v}{\partial z} + S \qquad (4.1)$$

where $\mathbf{u}$ is the vector of conserved variables, $\mathbf{f}$, $\mathbf{g}$ and $\mathbf{h}$ are the convective flux vectors, $\mathbf{f}_v$, $\mathbf{g}_v$ and $\mathbf{h}_v$ are the viscous flux vectors and S is a source term that represents body forces. In the present study, the source term comprises the pseudo-forces that are required when the equations are formulated in a non-inertial frame. The vectors in the above equations are given by:

$$\mathbf{u} = \begin{bmatrix} \rho \\ \rho u \\ \rho v \\ \rho w \\ e \end{bmatrix}, \ \mathbf{f} = \begin{bmatrix} \rho u \\ \rho u^2 + p \\ \rho uv \\ \rho uw \\ (e+p)u \end{bmatrix}, \ \mathbf{g} = \begin{bmatrix} \rho v \\ \rho uv \\ \rho v^2 + p \\ \rho vw \\ (e+p)v \end{bmatrix}, \ \mathbf{h} = \begin{bmatrix} \rho w \\ \rho uw \\ \rho vw \\ \rho w^2 + p \\ (e+p)w \end{bmatrix},$$

152

$$
\mathbf{f}_v \;=\; \begin{bmatrix} 0 \\[6pt] \tau_{xx} \\[6pt] \tau_{yx} \\[6pt] \tau_{zx} \\[6pt] u\tau_{xx} + v\tau_{yx} + w\tau_{zx} - q_x \end{bmatrix},
$$

$$
\mathbf{g}_v \;=\; \begin{bmatrix} 0 \\[6pt] \tau_{xy} \\[6pt] \tau_{yy} \\[6pt] \tau_{zy} \\[6pt] u\tau_{xy} + v\tau_{yy} + w\tau_{zy} - q_y \end{bmatrix},
$$

$$
\mathbf{h}_v \;=\; \begin{bmatrix} 0 \\[6pt] \tau_{xz} \\[6pt] \tau_{yz} \\[6pt] \tau_{zz} \\[6pt] u\tau_{xz} + v\tau_{yz} + w\tau_{zz} - q_z \end{bmatrix} \tag{4.2}
$$

where $q_{x,y,z}$ are the thermal conduction terms ($q_i = -k\frac{\partial T}{\partial x_i}$ with k as the thermal conductivity and T as the temperature). The equation of state is

$$
e = \frac{p}{\gamma - 1} + \frac{1}{2}\rho(u^2 + v^2 + w^2) \tag{4.3}
$$

and a perfect gas ($p = \rho R T$) is assumed where R is the gas constant. The mean stresses are expressed as:

$$
\tau_{ij} = \mu\left[\left(\frac{\partial u_i}{\partial x_j} + \frac{\partial u_j}{\partial x_i}\right) - \frac{2}{3}\frac{\partial u_k}{\partial x_k}\delta_{ij}\right] \tag{4.4}
$$

153

where μ is the laminar viscosity. The equations are solved in their non-dimensional form with the non-dimensionalized variables as:

$$t^* = \frac{ta_\infty}{L}, \ (x^*, y^*, z^*) = \frac{(x, y, z)}{L}, \ (u^*, v^*, w^*) = \frac{(u, v, w)}{a_\infty},$$

$$\rho^* = \frac{\rho}{\rho_\infty}, \ T^* = \frac{T}{T_\infty}, \ p^* = \frac{p}{\rho a_\infty^2}, \ e^* = \frac{e}{\rho a_\infty^2}, \ \mu^* = \frac{\mu}{\mu_\infty} \tag{4.5}$$

where the superscript $*$ denotes non-dimensionalized quantities, the subscript ∞ denotes freestream quantities, $a = \sqrt{\gamma p / \rho}$ is the speed of sound, and L is a reference length scale for the flow. The non-dimensional parameters are defined as:

$$\text{Reynolds number}: \quad Re_\infty = \frac{\rho_\infty u_\infty L}{\mu_\infty} \tag{4.6}$$

$$\text{Mach number}: \quad M_\infty = \frac{u_\infty}{a_\infty} \tag{4.7}$$

$$\text{Prandtl number}: \quad Pr_\infty = \frac{\mu C_p}{k} \tag{4.8}$$

where C_p is the specific heat at constant pressure. The Prandtl number is assumed as 0.72 for all the flow problems in this study. The mean stresses and thermal conduction terms for the non-dimensionalized system of equations are expressed as:

$$\tau_{ij} = \frac{\mu M_\infty}{Re_\infty} \left[\left(\frac{\partial u_i}{\partial x_j} + \frac{\partial u_j}{\partial x_i} \right) - \frac{2}{3} \frac{\partial u_k}{\partial x_k} \delta_{ij} \right] \tag{4.9}$$

$$q_i = -\frac{\mu M_\infty}{Re_\infty Pr (\gamma - 1)} \frac{\partial T}{\partial x_i} \tag{4.10}$$

where the superscript $*$ is omitted for convenience of notation.

4.1.1 Turbulence Modeling

Equation (4.1) is sufficient to describe flows that are inviscid or laminar. However, a large number of flows of practical relevance are turbulent and characterized

154

by chaotic motion of molecules and higher rates of momentum and energy transfer between different fluid elements. Section 4.4 describes the direct numerical simulation of turbulent flows where the grid is fine enough to capture the fluctuations that result from the chaotic motion. However, this technique is computationally expensive except for benchmark problems. Practical flow problems, such as those described in Section 4.3, are usually solved on grids that are not fine enough to capture the scales relevant to turbulent fluctuations. Thus, a turbulence model is required to account for the macroscopic effects of the sub-grid-scale motion.

The Reynolds-Averaged Navier-Stokes (RANS) equations [3] are used in this study, where the flow variables are decomposed into their mean and fluctuating parts, i.e.,

$$\phi = \overline{\phi} + \phi' \tag{4.11}$$

where ϕ' is the fluctuation and $\overline{\phi}$ is the mean, defined as,

$$\overline{\phi} = \frac{1}{\overline{\chi}} \lim_{\Delta t \to \infty} \frac{1}{\Delta t} \int_0^{\Delta t} \chi \phi(t) dt \tag{4.12}$$

The weighting function is $\chi = 1$ for pressure and density and $\chi = \rho$ for all other flow variables (velocity, internal energy, enthalpy and temperature). The RANS equations are obtained by expressing each of the variables in Eqn. (4.1) as Eqn. (4.11) and assuming that the magnitude of fluctuations are much lower than the mean value of each variable. The resulting system of equations for the mean variables is identical to Eqn. (4.1) with the addition of the Reynolds-stress tensor to the momentum and energy equations that accounts for the additional momentum and energy exchange due to turbulent fluctuations. This introduces additional terms in

155

the system of equations and a turbulence model is needed to close the equations. In the present study, the one-equation Spalart-Allmaras turbulence model [57] with the rotational correction [58] is used.

4.2 Baseline Flow Solver

A structured-mesh, compressible, unsteady, Reynolds-Averaged Navier-Stokes (RANS) solver developed in [59] is used in this chapter. The RANS equations are solved using a cell-averaged finite volume formulation [1]. The focus of this thesis is a high-order accurate spatial reconstruction scheme for the convective fluxes and thus, the application of scalar interpolation schemes described in the previous chapters to a discretization on a curvi-linear mesh is discussed in the next sub-section. A brief description of the other elements of the solution algorithm is presented in the following paragraphs.

The convective fluxes are computed using high-order accurate upwind schemes. In addition to the CRWENO schemes developed in this thesis, the flow solver incorporates the third-order MUSCL scheme with Koren's limiter [6, 60] and the fifth-order WENO scheme [13] with mapped weights [16] as given by Eqn. (1.41), and Eqns. (1.43) and (1.44). The conserved variables are reconstructed and the Roe scheme [5] with the Harten entropy fix is used to calculate the upwind inviscid flux at the interface.

The viscous fluxes are calculated using second-order central differences. The equations are marched in time using the third-order TVD Runge-Kutta (TVD-

RK3) scheme or the second-order Backward Differencing (BDF2) scheme. Viscous problems need very fine mesh sizes to resolve the boundary layer that results in a very restrictive stability limit for the time step size for an explicit time-marching scheme. Thus, for these problems the implicit BDF2 scheme is used. The resulting system of equations is solved using the diagonalized ADI [61, 62] or the LU-SGS [63, 64] schemes. Dual time-stepping [65] is used for unsteady problems on stretched meshes.

Several problems require the use of overset meshes for domain discretization. Examples include the simulation of flow around an airfoil in a wind tunnel and the wake flow around a helicopter rotor blade. The solution algorithm for overset meshes require the identification of overlap zones, donor and recipient grid points for each grid and interpolation of solution between the grids. The implicit hole-cutting technique [66, 68] is used in the present solver to identify the overlap regions and a tri-linear interpolation is used to transfer the solution between donor and recipient points.

A more detailed description of the above algorithms and their integration with each other is available in [67, 68]. It should be noted here that the present solver uses the ghost-point technique to enforce boundary conditions such that a reduced order reconstruction is not necessary at the boundaries.

4.2.1 Finite Volume Formulation and Reconstruction

The finite volume formulation is based on the integral form of a conservation law given by Eqn. (1.4). The Navier-Stokes equations can be expressed in this form by integrating them over a control volume and applying Stokes' theorem. The discretized convective flux can thus be expressed in the integral form as:

$$\sum_{l=0}^{N_{faces}} \mathbf{F}_l \cdot \hat{\mathbf{n}}_l dS_l; \ \ \mathbf{F} = \mathbf{f}\hat{\mathbf{i}} + \mathbf{g}\hat{\mathbf{j}} + \mathbf{h}\hat{\mathbf{k}} \qquad (4.13)$$

where N_{faces} is the number of discrete faces of a grid cell (control volume), $\mathbf{F}$ is the flux tensor with $\mathbf{f}, \mathbf{g}, \mathbf{h}$ as the convective fluxes in Eqn. (4.1), $\hat{\mathbf{n}}$ is the unit face normal vector for a given face, and dS is the face area. The vectors $\hat{\mathbf{i}}, \hat{\mathbf{j}}, \hat{\mathbf{k}}$ denote the Cartesian unit vectors along x, y and z directions respectively.

The domain is discretized using a structured grid, resulting in each grid cell being a quadrilaterally-faced hexahedron (in three dimensions). A grid cell centered at (i, j, k) has six faces ($N_{faces} = 6$), with face center indices as $(i \pm 1/2, j, k)$, $(i, j \pm 1/2, k)$ and $(i, j, k \pm 1/2)$. The reconstruction step requires the calculation of the flux tensor $\mathbf{F}$ at these faces from the discrete values at the cell centers. The reconstruction of the interface flux for a one-dimensional domain is described in Section 3.2.1 and is extended to a three-dimensional domain in this section. The calculation of the flux at the face $(i+1/2, j, k)$ is described and the flux at the other faces is similarly computed.

In the present study, the scalar interpolation schemes are applied to the conserved variables. Equations (3.15) and (3.16) with the appropriate indices are used to compute the left- and right-biased flux at the face $(i + 1/2, j, k)$ using the CR-

WENO5 scheme. These equations are applied to each component of the flux vectors $\mathbf{f}$, $\mathbf{g}$ and $\mathbf{h}$. Denoting the face-normal flux as

$$\mathbf{F}_n = \mathbf{F} \cdot \hat{\mathbf{n}} = \mathbf{f}n_x + \mathbf{g}n_y + \mathbf{h}n_z \tag{4.14}$$

the left and right biased face-normal numerical fluxes $\hat{\mathbf{F}}_n^{L,R}$ are thus computed using the CRWENO5 scheme. The final upwind flux is obtained by using the Roe scheme

$$
\begin{aligned}
\hat{\mathbf{F}}_{n,(i+1/2,j,k)} &= \frac{1}{2}(\hat{\mathbf{F}}^L_{n,(i+1/2,j,k)} + \hat{\mathbf{F}}^R_{n,(i+1/2,j,k)}) \\
&\quad - \frac{1}{2}\left|\hat{A}(\hat{\mathbf{u}}^L_{(i+1/2,j,k)}, \hat{\mathbf{u}}^R_{(i+1/2,j,k)})\right|(\hat{\mathbf{u}}^L_{(i+1/2,j,k)} + \hat{\mathbf{u}}^R_{(i+1/2,j,k)}) \tag{4.15}
\end{aligned}
$$

where

$$\left|\hat{A}(\hat{\mathbf{u}}^L_{(i+1/2,j,k)}, \hat{\mathbf{u}}^R_{(i+1/2,j,k)})\right| = X_{n,(i+1/2,j,k)}|\Lambda_{n,(i+1/2,j,k)}|X^{-1}_{n,(i+1/2,j,k)} \tag{4.16}$$

The subscript n in the right hand side of the above equation signifies that the eigenvalues and eigenvectors for the face are evaluated using the face-normal flow velocities [69].

4.3   Flow over Airfoils and Wings

The application of the CRWENO scheme to steady and unsteady flow over airfoils and wings is described in this section. The scheme is validated for curvilinear meshes as well as overset meshes with relative grid motion. Results are compared with experimental data available in the literature as well as the third-order MUSCL scheme with Koren's limiter (MUSCL3) and the fifth-order WENO scheme (WENO5). The flow around a NACA0005 airfoil undergoing simultaneous

pitching and plunging is studied as it is representative of a flapping-wing-based micro-air vehicle. The scheme is validated in three-dimensions for the steady flow around the ONERA-M6 wing and the unsteady flow around the Harrington-2 rotor. Although lower-order schemes suffice for calculating integrated forces, the solutions obtained using the CRWENO scheme show considerable improvement in capturing various flow features (for example, wake vortices).

4.3.1   Steady Turbulent Flow over RAE2822 Airfoil

The steady, transonic, turbulent flow around the RAE2822 airfoil is solved to validate the CRWENO5 scheme for a curvi-linear mesh. The domain is discretized by a stretched, C-type mesh with the outer boundaries 50 chord lengths away. Figure 4.1 shows the domain as well as a magnified view of the mesh near the airfoil. The mesh has 521 points in the wrap-around direction with 60 points in the wake and 401 points on the airfoil surface, and 171 points in the normal direction. The grid spacing at the airfoil surface is 4×10^{-6} times the chord length.

The freestream conditions correspond to "Case 6" in [70]. The Mach number is 0.725, the Reynolds number is 6.5 million (based on airfoil chord length) and the angle of attack is 2.92º. The experimental data was obtained inside a wind tunnel and thus, the freestream conditions for the computations are corrected [71]. The corrected angle of attack and freestream Mach number are 2.51º and 0.731 respectively.

(a) Complete domain

(b) Magnified view near the airfoil
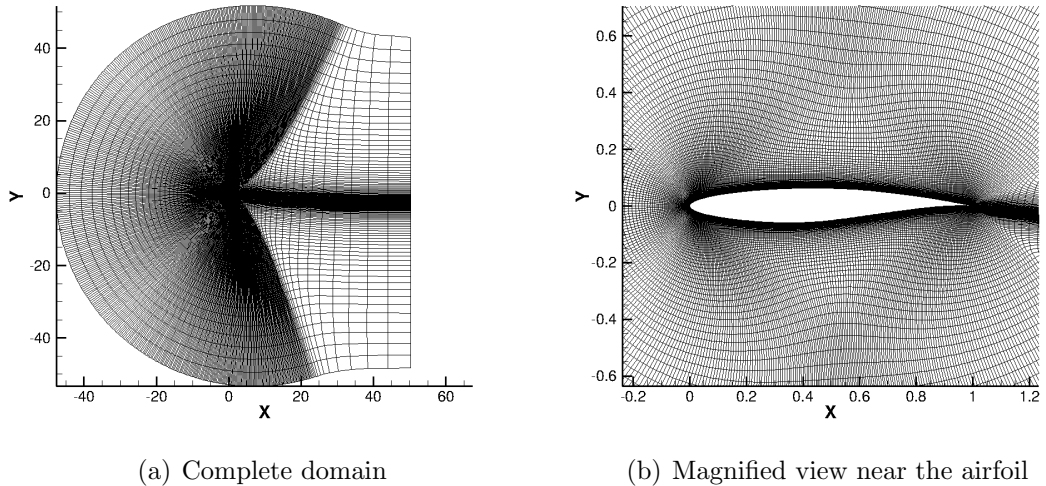
Figure 4.1: C-type mesh for the RAE2822 airfoil with 521×171 points
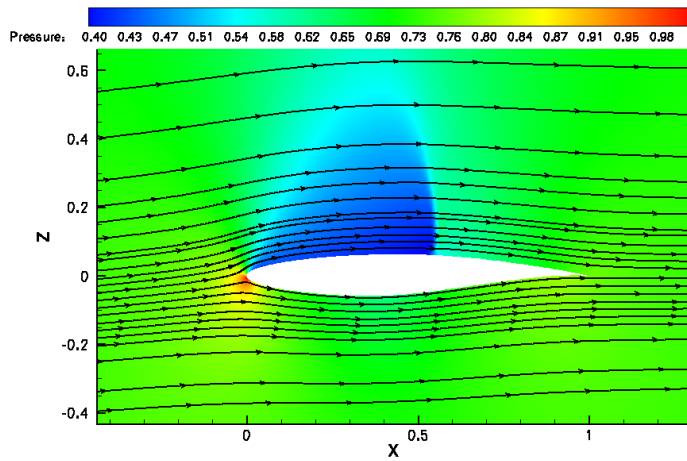
Figure 4.2: Transonic flow around the RAE2822 airfoil: pressure contours and streamlines

The numerical solution is obtained using the CRWENO5 scheme and the BDF2 scheme is used to march the solution in time to steady state. Characteristic-based freestream boundary conditions are enforced on the outer boundaries. No-slip wall boundary conditions are applied on the airfoil surface and wake averaging is used in the wake-cut of the C-type mesh. Figure 4.2 shows the pressure contours and the velocity streamlines for the flowfield. The stagnation point, locally supersonic flow

161
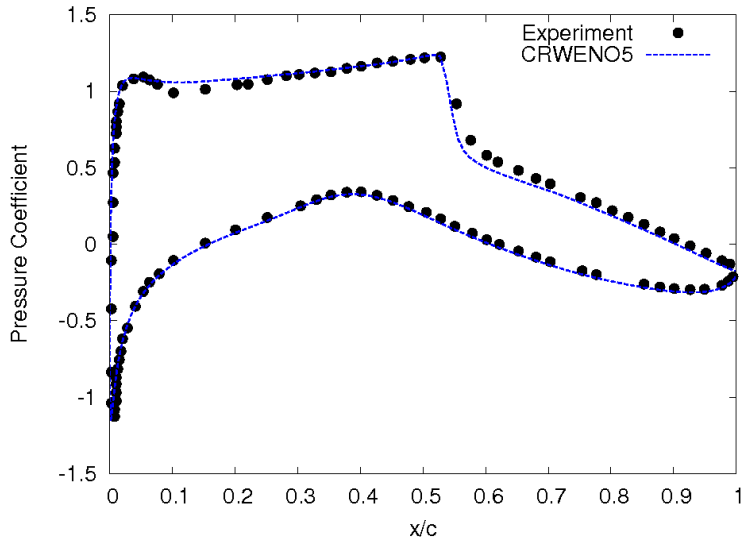
Figure 4.3: Coefficient of pressure on the surface for the RAE2822 airfoil



(a) $x/c = 0.319$

(b) $x/c = 1.025$
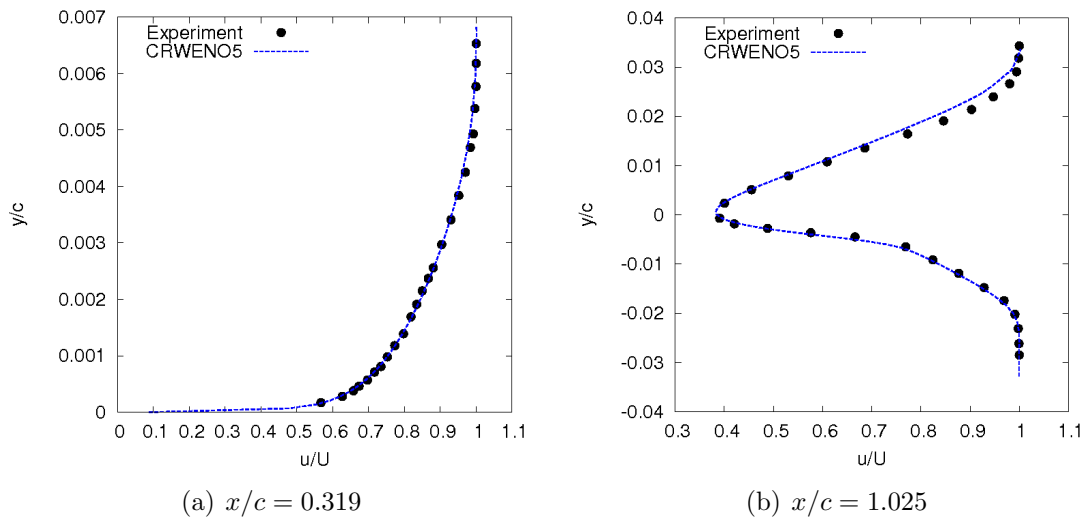
Figure 4.4: Boundary layer and wake velocity profiles for the RAE2822 airfoil (c is the airfoil chord)

on the upper surface and the shock that terminates it are clearly visible. Figure 4.3 shows the coefficient of pressure on the airfoil surface for the computed solution as well as the experimental data [70]. A good agreement is observed between the numerical solution and the experimental data. Figure 4.4 shows the velocity profiles at two locations: inside the boundary layer on the upper surface at $x/c = 0.319$
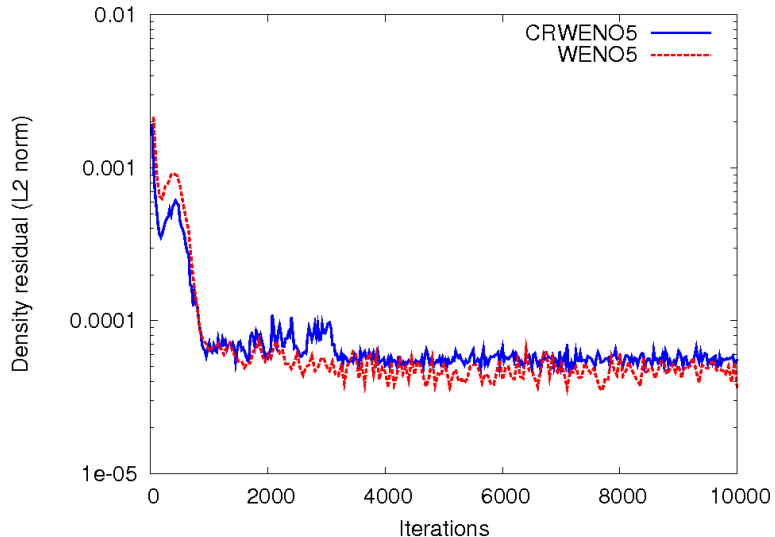
Figure 4.5: Convergence history for the RAE2822 airfoil

and inside the wake at $x/c = 1.025$. The numerical solution agrees well with the experimental data.

Figure 4.5 shows the density residual for the CRWENO5 scheme as well as the WENO5 scheme. Both these schemes show a residual drop of only one-and-a-half orders of magnitude. A component-wise reconstruction is used in the present study, along with the WENO weights as formulated by Jiang and Shu. The convergence of the WENO schemes for airfoil problems has been studied [72] and non-characteristic-based formulations were observed to show poor convergence. Although the current results agree well with experimental data, the improvement of convergence behavior for the CRWENO5 scheme is an area of active research.

(a) Complete domain - Wind tunnel and airfoil (b) Magnified view near the airfoil
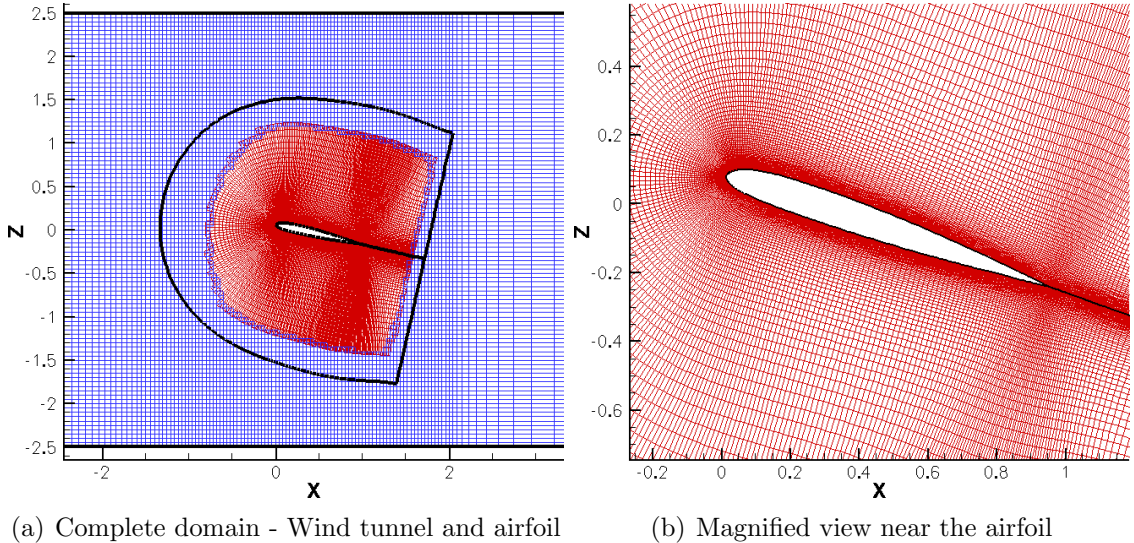
Figure 4.6: Overset mesh system for the SC1095 in a wind tunnel

4.3.2 Dynamic Stall of SC1095 Airfoil in Wind Tunnel

The dynamic stall of the SC1095 airfoil inside a wind tunnel is solved to
validate and demonstrate the CRWENO5 scheme for overset mesh systems with
relative motion between the meshes. The numerical solution of flows over such
domains require the identification of regions of overlap (between meshes) where
the solution is transferred from the donor mesh to the recipient mesh, as well as
blanked out regions within a mesh where the flow is solved for on a different mesh.
The solution update procedure is such that at a given instant in time, the solution
update at a blanked out point is zero. This may create a locally unphysical solution;
but as it does not influence interior field points (since it is separated by points in
the overlap region that use interpolated data) it does not contaminate the solution
field. In addition, if a blanked point becomes a field point at a future point in time
due to relative grid motion, there will always be a transition period where the data
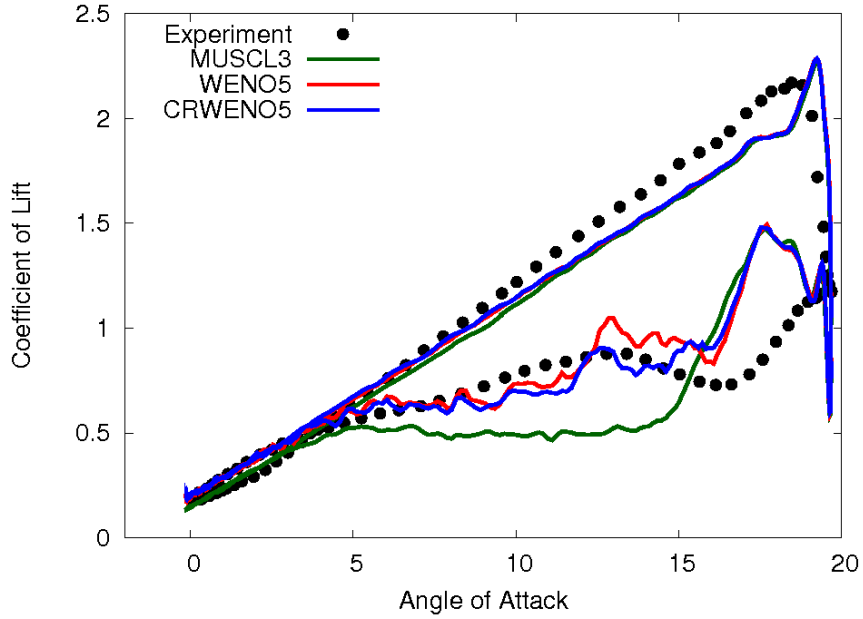
Figure 4.7: Lift vs. angle of attack for the pitching SC1095 airfoil

will be updated using interpolated data from another mesh.

A compact scheme results in a coupling of the interpolated interface fluxes with neighboring fluxes, i.e., the fluxes in the blanked out region are also solved as a part of the system of equations. Therefore, the treatment of the fluxes in the blanked out region is important. The CRWENO5 scheme uses an adaptive stenciling procedure based on the local smoothness of the solution. Section 2.2 discusses this in details and demonstrates how the system of equations is decoupled across a discontinuity. The unphysical values of flow variables inside the blanked out region of a mesh appears as a discontinuity to the reconstruction scheme. It is thus expected that the CRWENO5 scheme will result in a system of equations that is decoupled from the interface fluxes inside the blanked out region, preventing contamination of the flow domain and yielding smooth solutions across regions of overlap.

(a) Pressure (b) Vorticity
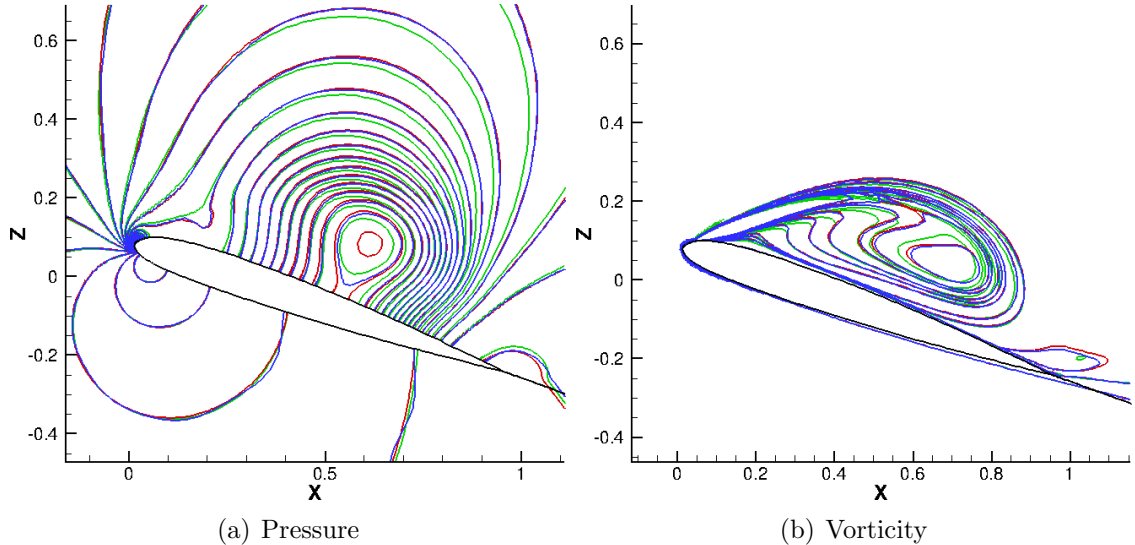
Figure 4.8: Comparison of pressure and vorticity contours for various schemes - MUSCL3 (green), WENO5 (red) and CRWENO5 (blue)

Figure 4.6(a) shows the airfoil and wind tunnel meshes for this problem. The wind tunnel height is $5c$ where c is the airfoil chord length. A clustered Cartesian grid with 151×101 points is used to discretize the wind tunnel. A C-type mesh is used for the airfoil that has 365 points in the wrap-around direction with 47 points in the wake, and 138 points in the normal direction. The figure shows the overlap region as well as the blanked out regions for the airfoil and wind tunnel meshes. The region around the airfoil is blanked out for the wind tunnel mesh as the flow in that region is solved on the body-conforming airfoil mesh. The outer regions of the airfoil mesh are blanked out since the stretching causes this mesh to be coarser than the wind tunnel mesh. Thus, the flow is solved on the wind tunnel mesh. A thin overlap region separates the blanked out regions of the two meshes, where the solution is transferred between them. Figure 4.6(b) shows a magnified view of the

166

(a) CRWENO5

(b) WENO5

(c) CRWENO5

(d) WENO5
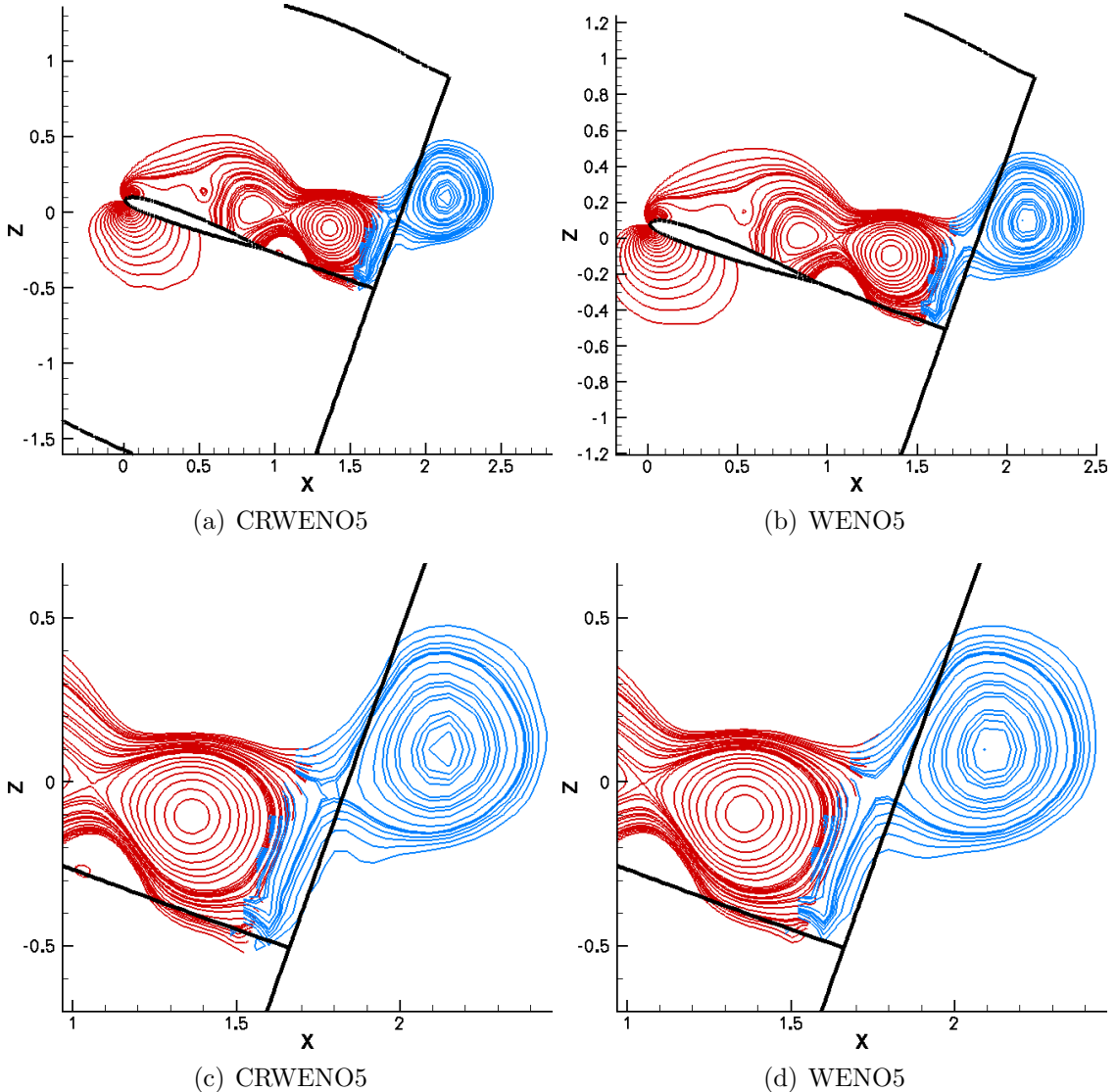
Figure 4.9: Comparison of pressure contours at 18.83º angle of attack for the overlap region - airfoil mesh (red) and wind tunnel mesh (blue)

grid near the airfoil. The grid spacing at the airfoil surface is 5×10^{-6} times the chord length.

The freestream Mach number is 0.302 and the Reynolds number (based on the airfoil chord length) is 3.92 million. The airfoil pitches with a mean angle of attack of 9.78º and the pitch amplitude is 9.9º at a reduced frequency of 0.099. The time step size is taken at 0.01, which results in 10, 500 iterations per cycle. The solution

is marched in time using the BDF2 scheme and dual time-stepping with 15 Newton sub-iterations. The simulation is run for four cycles and solutions are compared for the last cycle. The solution obtained using the CRWENO5 scheme is compared with those obtained using the non-compact MUSCL3 and WENO5 schemes. Figure 4.7 shows the lift as a function of the angle of attack over one complete cycle. The numerical solutions are validated against experimental data [73] and a good agreement is observed. Figure 4.8 show the pressure and vorticity contours around the airfoil for the three numerical schemes. The solutions are obtained at 18.94º angle of attack (upstroke). The figure shows the leading edge vortex after it has detached from the leading edge and has started convecting downstream. The solution obtained using the CRWENO5 scheme agrees well with solutions obtained with the non-compact schemes.

Figures 4.9(a) and 4.9(b) show the pressure contours for the flow when the airfoil is at 18.83º angle of attack (upstroke). The solutions for the compact scheme and non-compact WENO5 scheme are shown. The vortices shed from the upper surface are transferred from the airfoil mesh to the wind tunnel mesh as they convect downstream. A magnified view of the overlap region between the two meshes for the two schemes is shown in Figs. 4.9(c) and 4.9(d). The contours on the airfoil and wind tunnel meshes agree with each other in the overlap region and are continuous across the mesh boundary. Thus, the applicability of the compact scheme is verified for overset meshes requiring transfer of flow data between domains.

4.3.3 Flow over Pitching-Plunging NACA0005 Airfoil

Flow around a pitching-plunging airfoil at low Reynolds number is representative of the flowfield around a flapping-wing-based micro-air vehicle and has been previously studied using experimental and numerical techniques [74]. The combined pitching and plunging motion results in positive thrust (negative drag) when averaged over one cycle. Previous computational studies used Reynolds-Averaged Navier-Stokes (RANS) based algorithms with second-order spatial accuracies. These lower-order algorithms are sufficient for the prediction of lift and thrust. In this thesis, the focus is to capture the finer details of the flowfield near the airfoil surface including the formation and shedding of leading edge vortical structures. The CR-WENO5 scheme is used for spatial reconstruction and compared to MUSCL3 and WENO5 schemes. In addition to higher-order spatial schemes, the one-equation Spalart-Allmaras turbulence model [57] is used with the Delayed-Detached Eddy Simulation (DDES) modification in its two-dimensional form. It is expected that a higher-fidelity turbulence model with high-order accurate numerical scheme will improve the resolution of coherent vortical structures.

The domain is discretized using an O-type mesh with two different grid sizes – 241×241 and 361×361. A freestream Mach number of 0.1 is specified, which is higher than that used in [74]. A higher Mach number is used in this study to avoid the need for low Mach preconditioning. The Reynolds number based on airfoil chord length is 15000. The pitching motion is specified by a pitch amplitude of 40° around

a zero mean angle of attack and a reduced frequency of 0.795. The plunging motion has an amplitude of 1.0 and the same reduced frequency. The plunging motion is $\pi/2$ behind in phase than the pitching motion and the airfoil pitches around the leading edge.

The simulation is run over four cycles and the results from the final cycle are presented. The solution is advanced in time using the BDF2 scheme and dual time-stepping with 15 Newton sub-iterations. A time step size of 0.008 is taken resulting
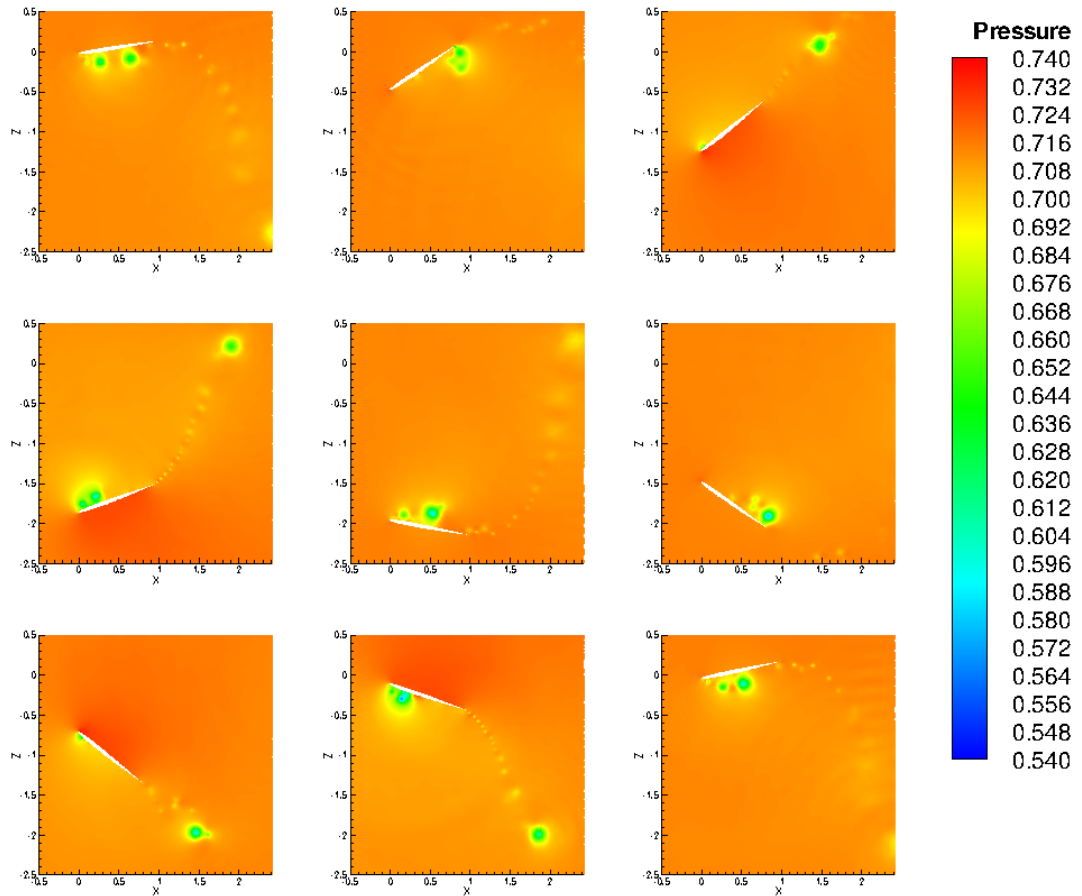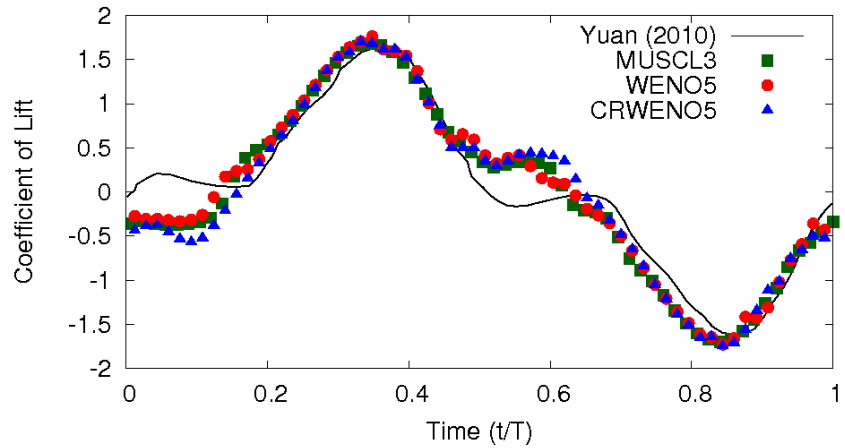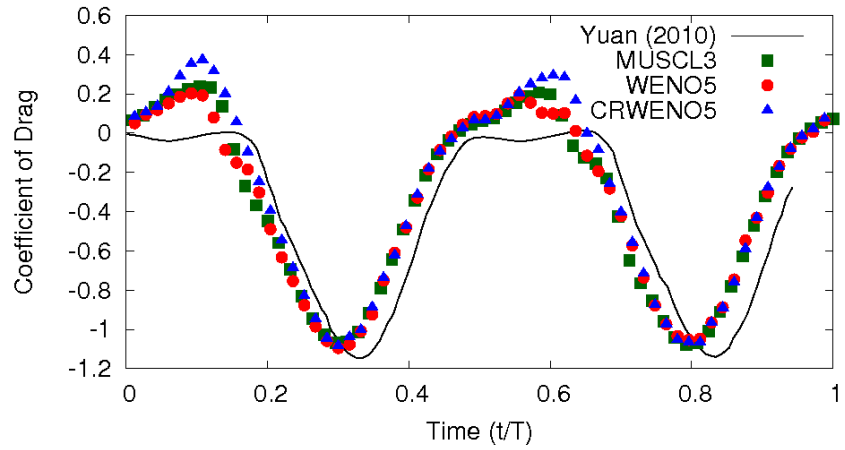

Figure 4.10: Pressure distribution over one time period - Ordering is from left to right and top to bottom

(a) Lift

(b) Drag

Figure 4.11: Integrated forces over one time period

in 5000 iterations per cycle. Figure 4.10 shows the pressure distribution around the

airfoil over one complete cycle on the 361×361 grid. The solutions are obtained using

the CRWENO5 scheme. As the airfoil plunges downwards, leading edge vortices are

(a) MUSCL3   (b) WENO5   (c) CRWENO5
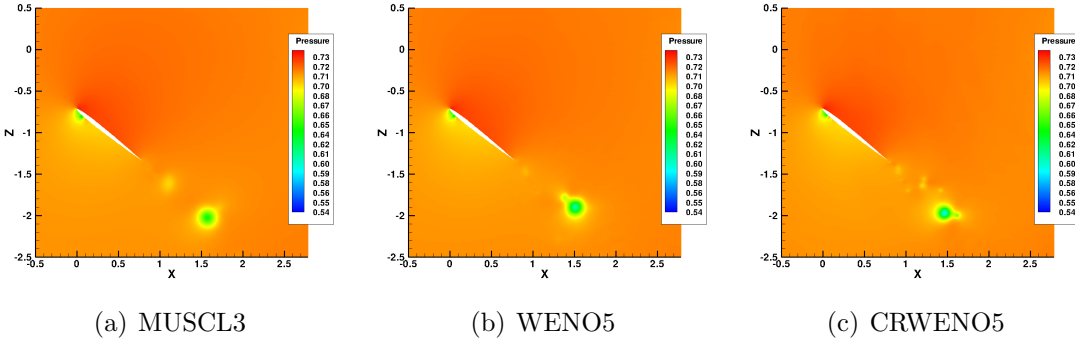
Figure 4.12: Pressure distribution for various schemes at $t/T = 0.75$ (Upstroke) (361×361 grid)

formed on the upper surface that grow in size and then detach from the surface. This results in a positive lift during the downstroke. Similarly, vortices form and shed from the lower surface during the upstroke resulting in negative lift. This results in a zero average lift over the entire cycle. Both strokes result in negative drag and the flapping motion causes the generation of positive thrust. The lift and drag variation over one cycle is shown in figure 4.11. Results from the CRWENO5, WENO5 and the MUSCL3 schemes are verified with the previous computational results [74] where the flow was solved using an incompressible, RANS-based algorithm with second-order accuracy in time and space. The integrated forces agree well with the previous results.

Figure 4.12 shows the pressure for the solutions obtained with the MUSCL3, WENO5 and CRWENO5 schemes on the 361×361 grid at $t/T = 0.75$ (where T is the time period). The CRWENO5 scheme shows an improved resolution of the vortical flow features in the wake. The numerical shadowgraph ($\nabla^2 \rho$) for the

(a) MUSCL3 (241×241 grid)   (b) WENO5 (241×241 grid)   (c) CRWENO5 (241×241 grid)

(d) MUSCL3 (361×361 grid)   (e) WENO5 (361×361 grid)   (f) CRWENO5 (361×361 grid)
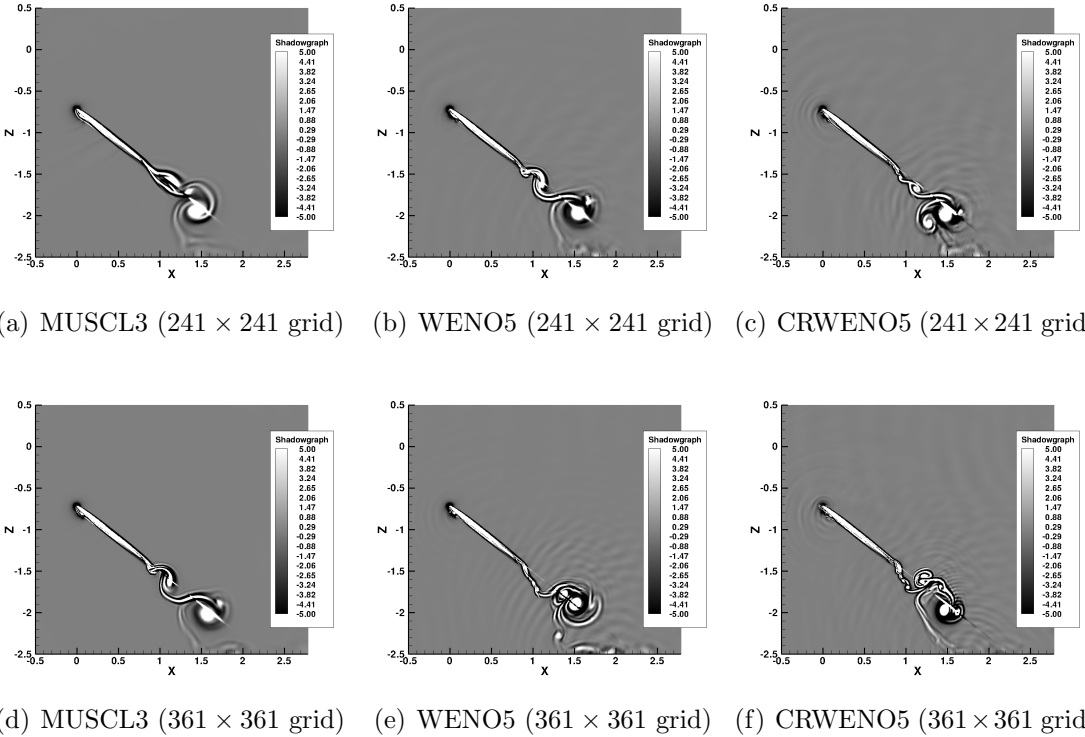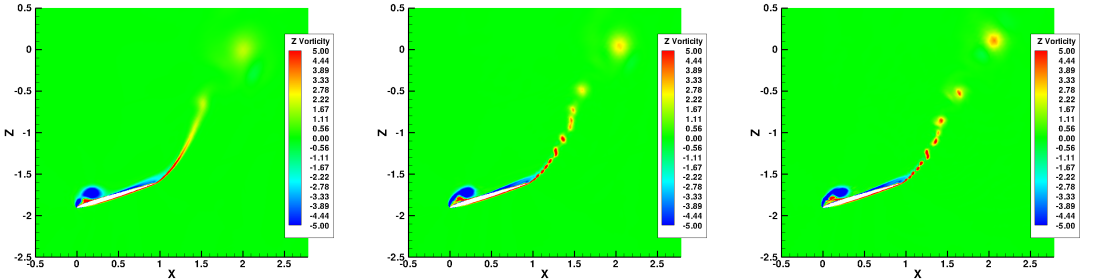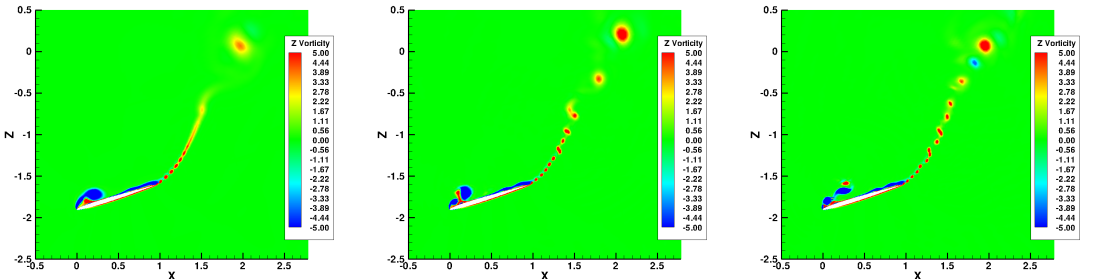
Figure 4.13: Numerical shadowgraph for various schemes at $t/T = 0.75$ (Upstroke)

solutions at the same time are shown in figures 4.13 for both grid sizes. Though the CRWENO5 and WENO5 schemes are of the same order, the resolution of the shed vortices is significantly better with the CRWENO5 scheme, at both grid sizes. Figure 4.14 shows out-of-plane vorticity at $t/T = 0.4$ for the three schemes on the two grids. It is observed on the finer grid that the CRWENO5 scheme is able to resolve the various vortices that form and detach from the airfoil surface. At both grid sizes, it is observed once again that the CRWENO5 is able to preserve the wake vortices over larger distances than the WENO5 scheme. A comparison of the three schemes show that while a second or third-order scheme is sufficient to predict the integrated forces like the lift and drag, a higher-order scheme is necessary to capture the separated vortical flow features near the airfoil surface as well in the wake.

(a) MUSCL3 (241×241 grid) (b) WENO5 (241×241 grid) (c) CRWENO5 (241×241 grid)

(d) MUSCL3 (361×361 grid) (e) WENO5 (361×361 grid) (f) CRWENO5 (361×361 grid)

Figure 4.14: Vorticity distribution for various schemes at $t/T = 0.40$ (Downstroke)

Although the CRWENO5 and WENO5 schemes are both fifth-order accurate, the increased spectral resolution capabilities of the CRWENO5 scheme yields a solution with higher resolution of the flow features than the WENO5 scheme.

## 4.3.4 Steady Flow over ONERA-M6 Wing
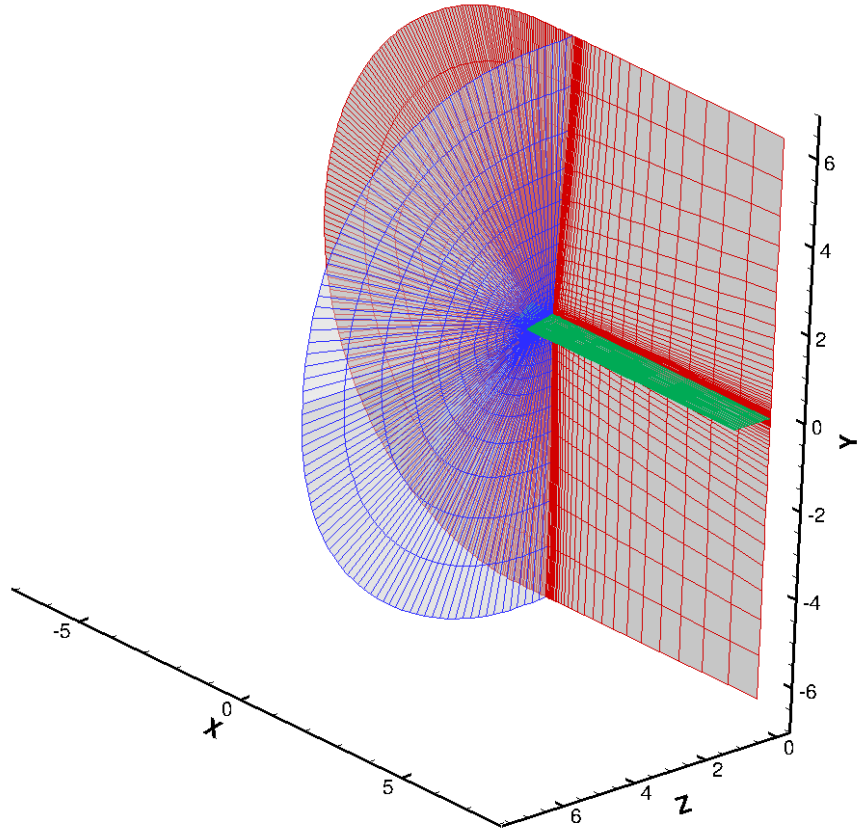
The steady flow around the ONERA-M6 wing is solved to validate the CR-WENO5 scheme for a three-dimensional problem, as well as compare its ability to capture and preserve the tip vortex in the wake. The numerical solution for the flow over airfoils and wings are usually obtained on a mesh that is clustered near the body. In absence of additional overset meshes specifically placed to capture the tip vortices, the rapid stretching of the mesh away from the body causes dissipation of

174

the vortices in the wake. A high-order accurate numerical scheme helps in significantly improving the resolution and preservation of wake flow features without the need of finer meshes.
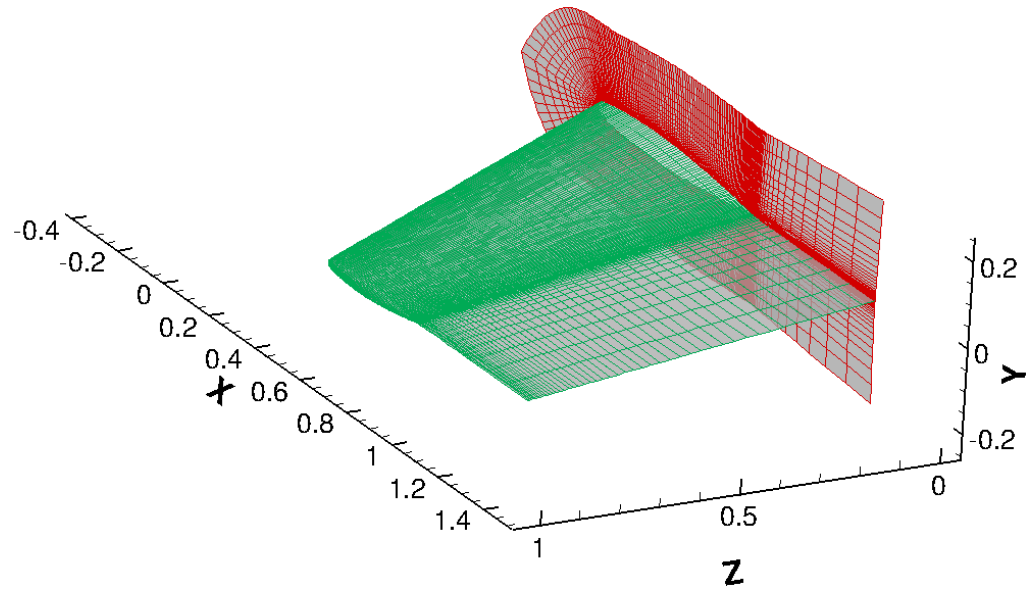
Figure 4.15 shows the single-block C-O mesh used to discretize the domain around the ONERA-M6 wing. The mesh has 289 points in the wrap-around direction, 65 points in the normal direction and 49 points in the spanwise direction. The grid is non-dimensionalized to have a unit semi-span. Characteristic-based freestream boundary conditions are enforced at all far-field boundaries. No-slip wall boundary conditions are enforced on the wing surface. Symmetry is assumed on the plane corresponding to the wing root. The Reynolds number based on mean aerodynamic chord is 11.7 million and the angle of attack is 3.06º. The freestream Mach number is 0.84.

The solution is marched in time using the BDF2 scheme till it reaches a steady state. Figure 4.16 shows the pressure coefficient on the wing surface at various span-wise locations. Solutions obtained by the CRWENO5 scheme are validated against experimental data [75]. A good agreement is observed, thus validating the CRWENO5 scheme for a three-dimensional steady flow problem.

The ability of the CRWENO5 scheme to accurately capture and preserve the tip vortex in the wake is compared to that of the MUSCL3 and WENO5 schemes. Figure 4.17 shows the surface pressure contours as well as the evolution of the tip vortex in the wake for the solutions obtained by the WENO5 and CRWENO5 schemes.

(a) Complete domain

(b) Magnified view near the wing

Figure 4.15: C-O type mesh for ONERA-M6 wing
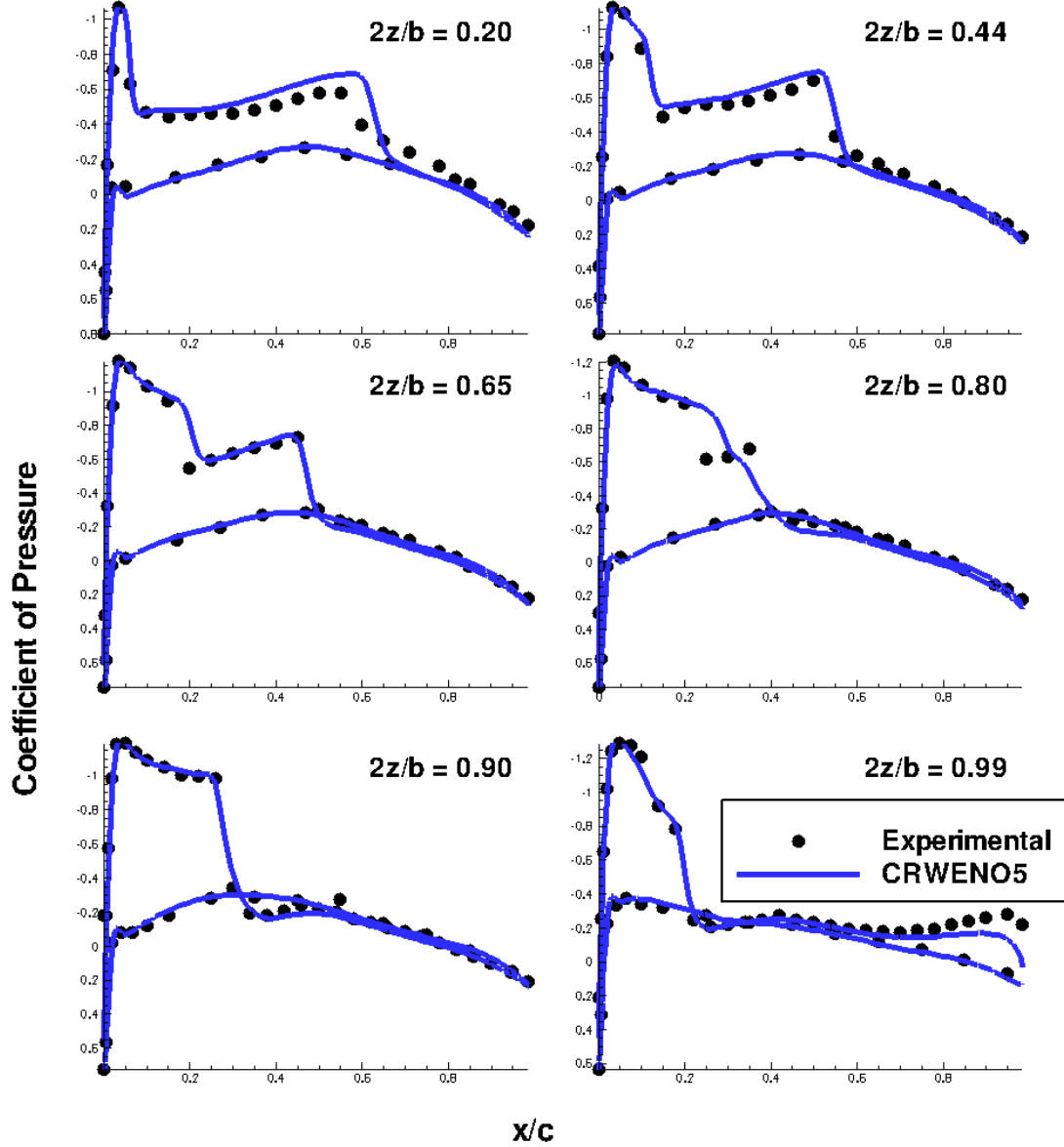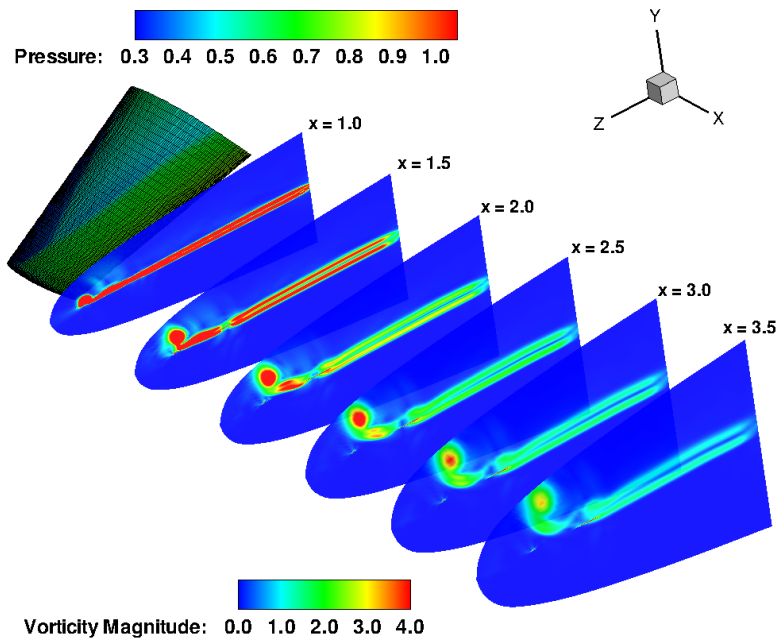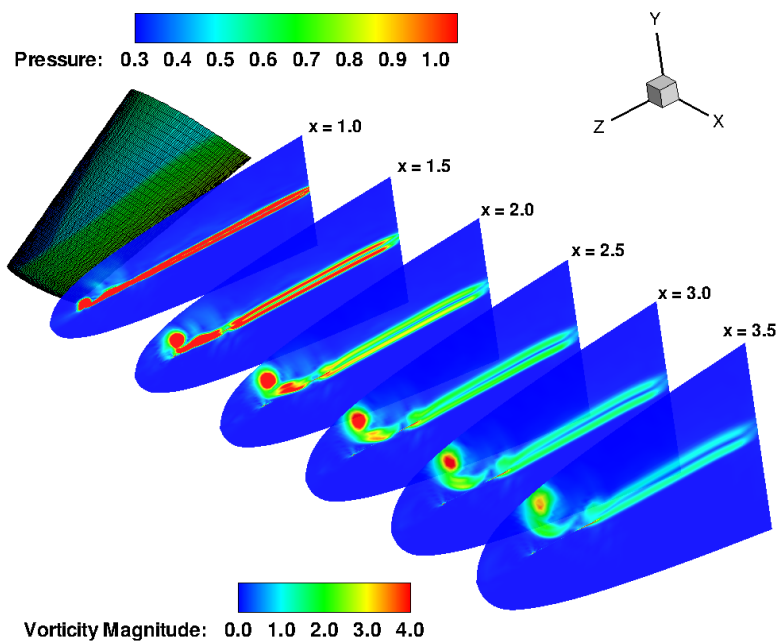
Figure 4.16: Pressure coefficient on wing surface at various span-wise locations for the ONERA-M6 wing

The wing surface is colored by the pressure while the slices in the wake are colored by the vorticity magnitude. Both the schemes capture the formation and convection of the tip vortex. The solutions are similar near the wing. However, further downstream, the CRWENO5 scheme shows an improvement in the preservation of

(a) WENO5

(b) CRWENO5

Figure 4.17: Surface pressure distribution and evolution of tip vortex in the wake for the ONERA-M6 wing
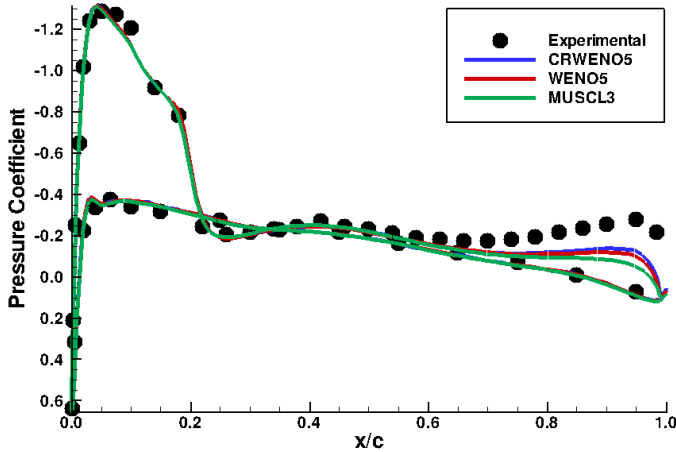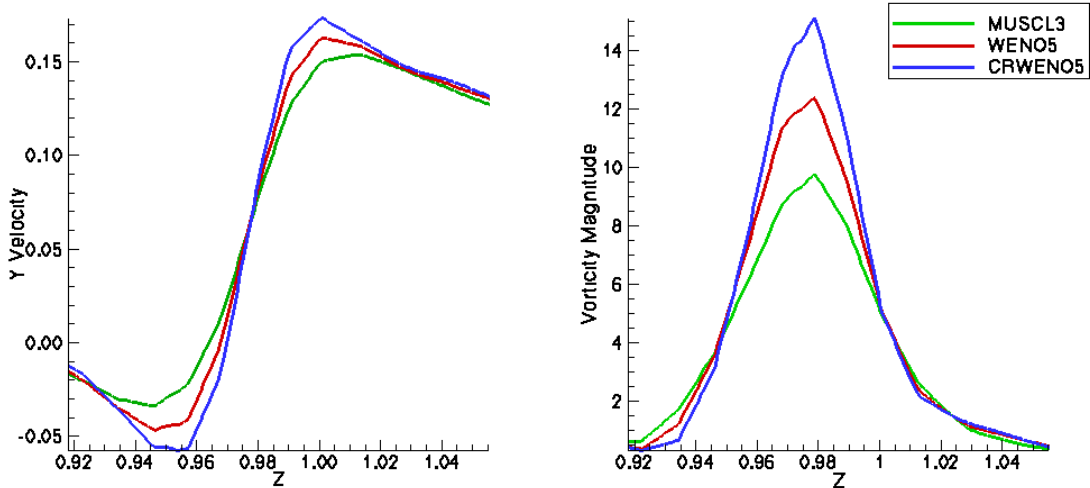
Figure 4.18: Comparison of wingtip pressure coefficient for various schemes
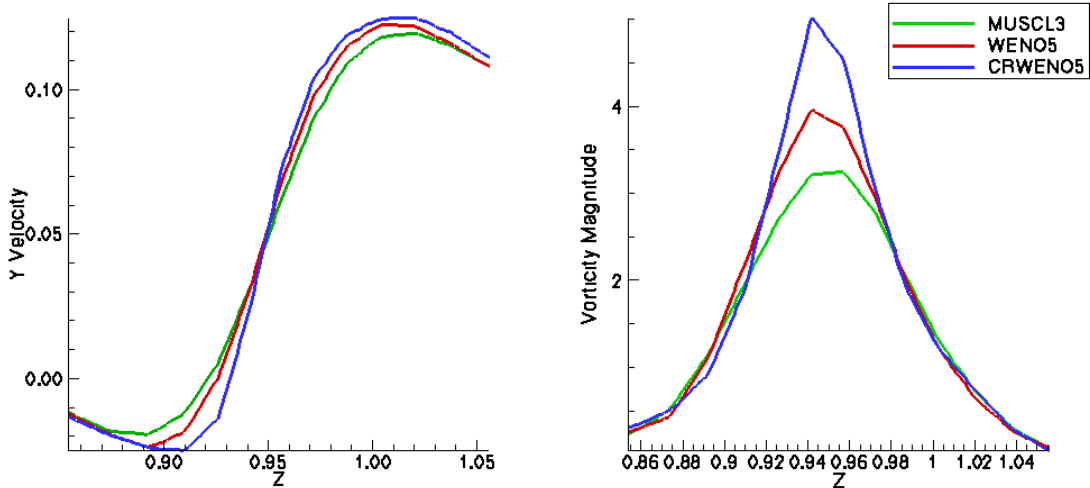
the tip vortex, as observed from the slices at $x = 3.0$ and $x = 3.5$.

The formation of the tip vortex at the wing is compared for the various schemes. Figure 4.18 compares the pressure coefficient on the wing surface at a span-wise location of $2z/b = 0.99$ (where $b = 2$ is the wing span). The suction peak at the trailing edge indicates the formation of the tip vortex. It is observed that the MUSCL3 scheme results in the formation of a significantly weaker vortex, compared to experimental data. The WENO5 and CRWENO5 schemes result in stronger tip vortices and the pressure distribution agrees better with the experimental data.

Figure 4.19 compares the swirl velocity and vorticity magnitude through the tip vortex core at two locations in the wake. The vortex is significantly weaker at the downstream location. At both these locations, the CRWENO5 scheme results in a stronger vortex as it convects downstream in the wake.

(a) $x = 1.5$

(b) $x = 3.0$
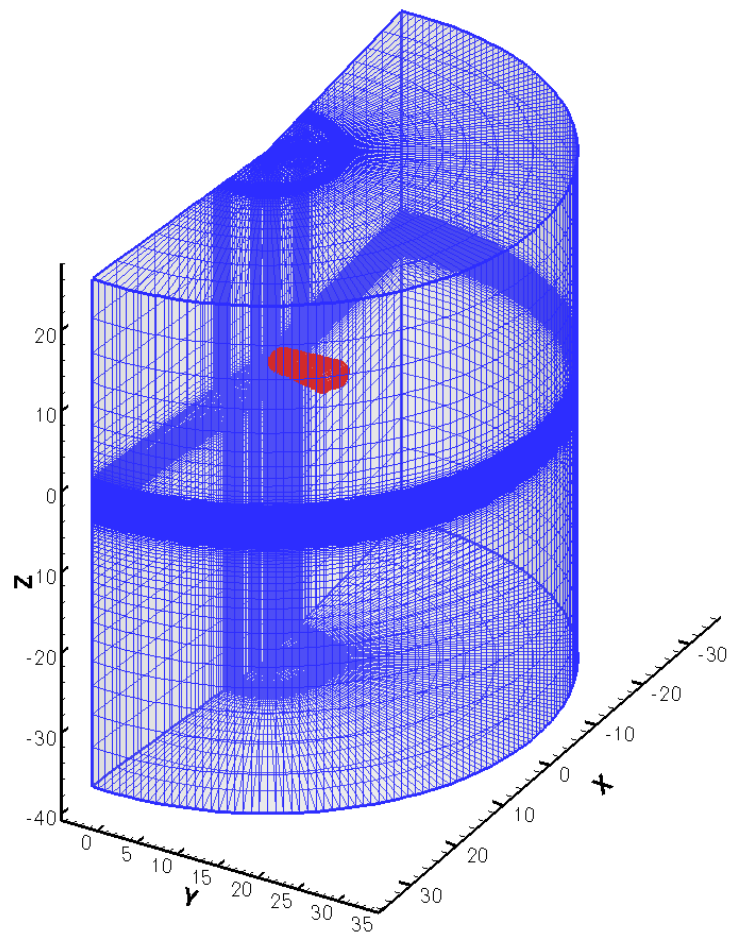
Figure 4.19: Comparison of swirl velocity and vorticity magnitude in the tip vortex for various schemes

4.3.5 Flow around Harrington Rotor
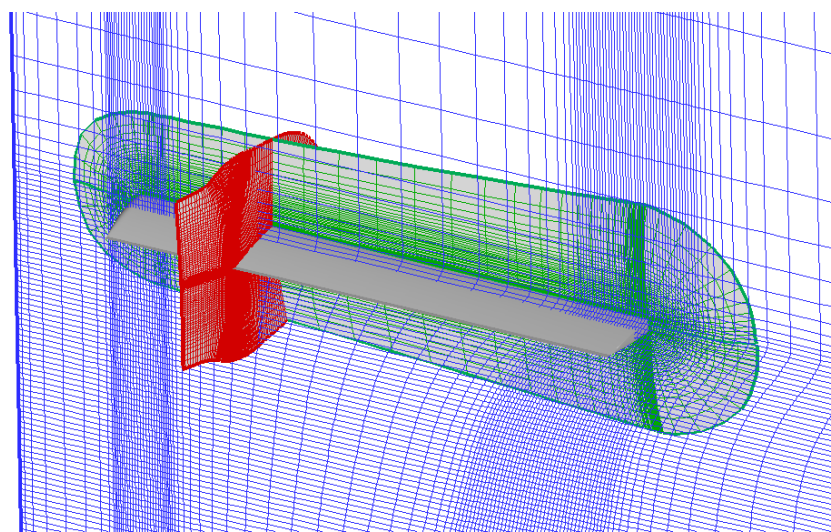
Section 4.3.2 demonstrated the performance of the CRWENO5 scheme on a domain involving overset grids with relative motion for a two-dimensional flow. The flow around an experimental Harrington two-bladed single rotor [76] is solved to

validate the scheme for a three-dimensional unsteady flow on overset, moving grids. The unsteady flow around a rotor, and in its wake, is characterized by vortical structures interacting with the rotor blade and each other. A lower-order numerical scheme is sufficient to predict the integrated airloads over the blades; however, a high-order accurate scheme is required to capture and preserve near-blade and wake flow features. This is necessary, for example, to study the sound generation from a rotor or to understand the flow-field near the ground plane for a rotorcraft operating in ground effect. In this section, the CRWENO5 scheme is compared with the non-compact schemes (MUSCL3 and WENO5).

The experimental setup (referred to as "Rotor-2" in [76]) consists of a two-bladed rotor with an aspect ratio of 8.33. The blade cross-section is the symmetric NACA airfoil with a linearly varying thickness of 27.5% at the hub ($0.2R$) to 15% at the tip ($1.0R$) where R is the rotor radius. The tip Mach number and Reynolds number are 0.352 and 3.5×10^6 respectively. The collective pitch is varied from 2º to 12º to obtain the variation of thrust with power. Figure 4.20 shows the domain discretization used in the present study. The domain consists of a cylindrical background mesh with $127 \times 116 \times 118$ points and a C-O type blade mesh with $267 \times 78 \times 56$ points. The background mesh is clustered near the blade mesh in the z-direction and at the hub and tip regions in the radial direction. The blade mesh is clustered at the hub and tip in the spanwise direction, as well as the blade surface along the surface-normal direction. The dimensions in Fig. 4.20(a) correspond to a unit chord length for the blade. The solution is extrapolated with zero gradients at

181
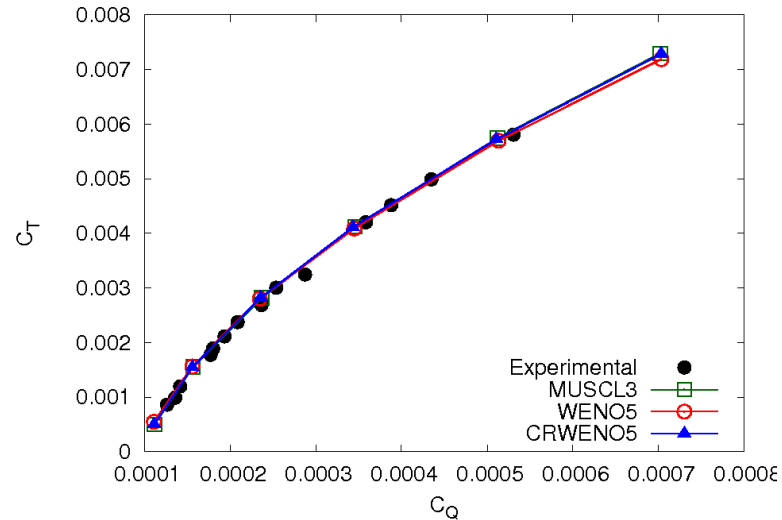
(a) Complete domain - Blade mesh (red) and background mesh (blue)
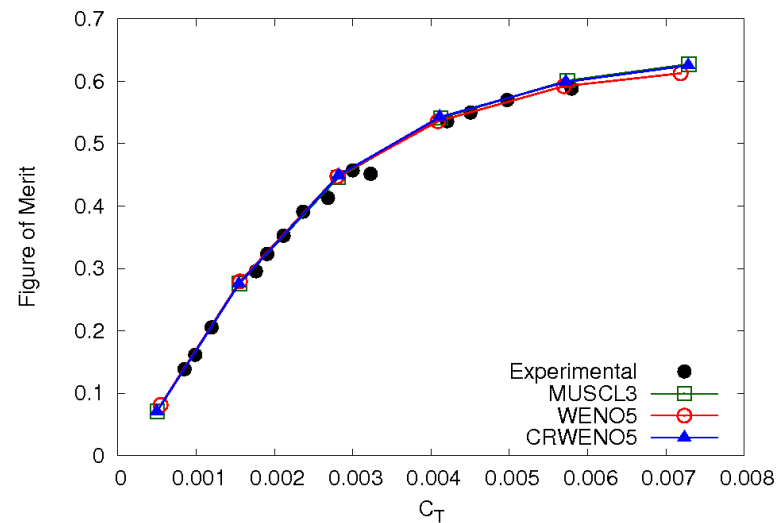
(b) Blade Mesh (red and green) overset on the background mesh (blue)

Figure 4.20: Computational domain for Harrington rotor

(a) c_T vs. c_Q

(b) Figure of merit

Figure 4.21: Thrust and power coefficients, and the figure of merit, for the Harring-ton rotor

the center of the cylindrical mesh, while periodic boundary conditions are applied

to the azimuthal boundaries. Characteristic-based freestream boundary conditions

are applied at all other boundaries.

Solutions are obtained using the BDF2 time-marching scheme with 8 Newton sub-iterations for time-accuracy. Figure 4.21(a) shows the thrust coefficient as a function of the power coefficient obtained using the three numerical schemes while Fig. 4.21(b) shows the figure of merit as a function of the thrust coefficient. The results obtained with the CRWENO5 scheme agree well with those obtained with the non-compact schemes and the experimental results [76], thus validating the CRWENO5 scheme for this problem.

The ability of the CRWENO5 scheme to capture and preserve the helical tip vortex in the wake is compared to that of the MUSCL3 and WENO5 schemes. The MUSCL3 is third-order accurate and is expected to be more dissipative than the fifth-order WENO and CRWENO schemes. The lower dissipation of the CRWENO5 scheme, as compared to the WENO5 scheme, is expected to result in an improved preservation of the wake vortices.

(a) Wake flow (b) Cross-section at 0° azimuth
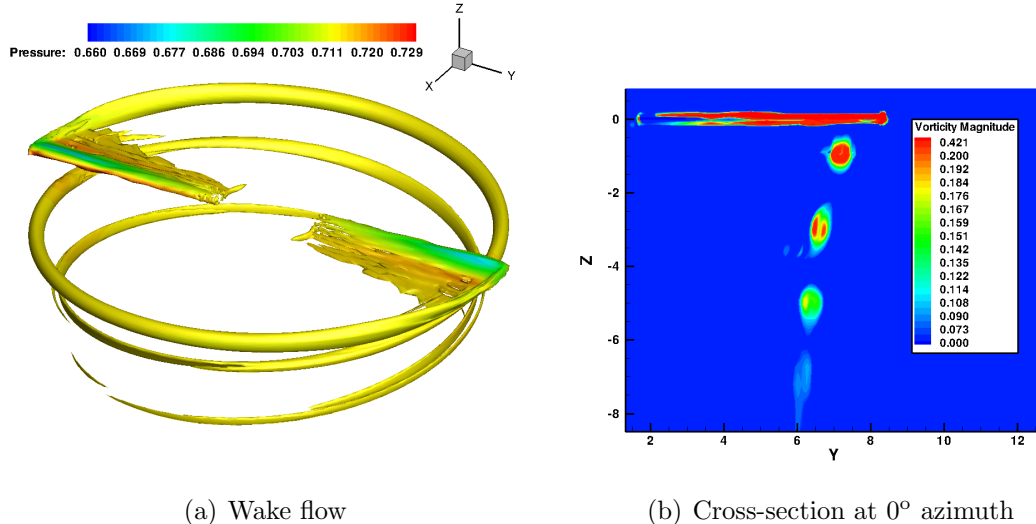
Figure 4.22: Wake flow-field for the Harrington rotor obtained with MUSCL3 scheme

(a) Wake flow

(b) Cross-section at 0° azimuth
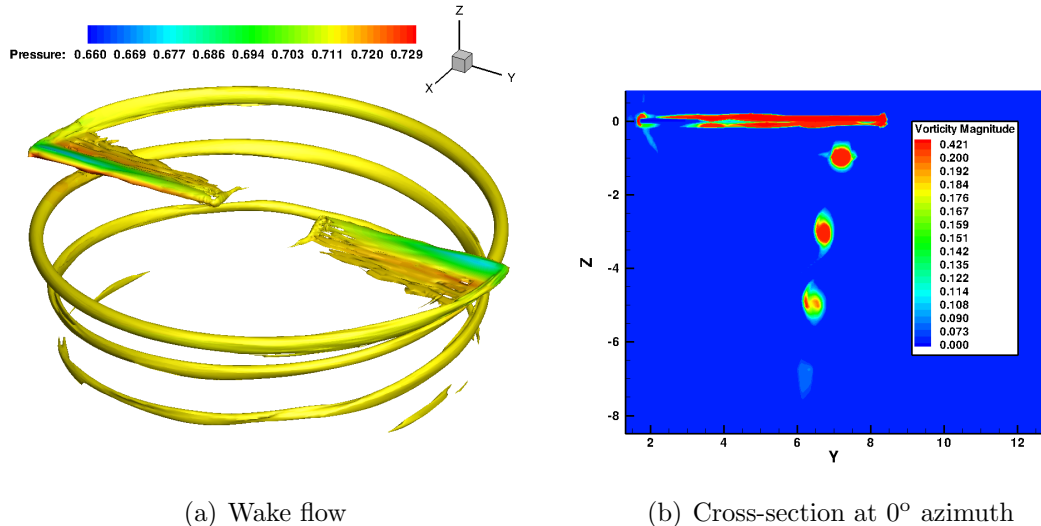
Figure 4.23: Wake flow-field for the Harrington rotor obtained with WENO5 scheme

(a) Wake flow

(b) Cross-section at 0° azimuth
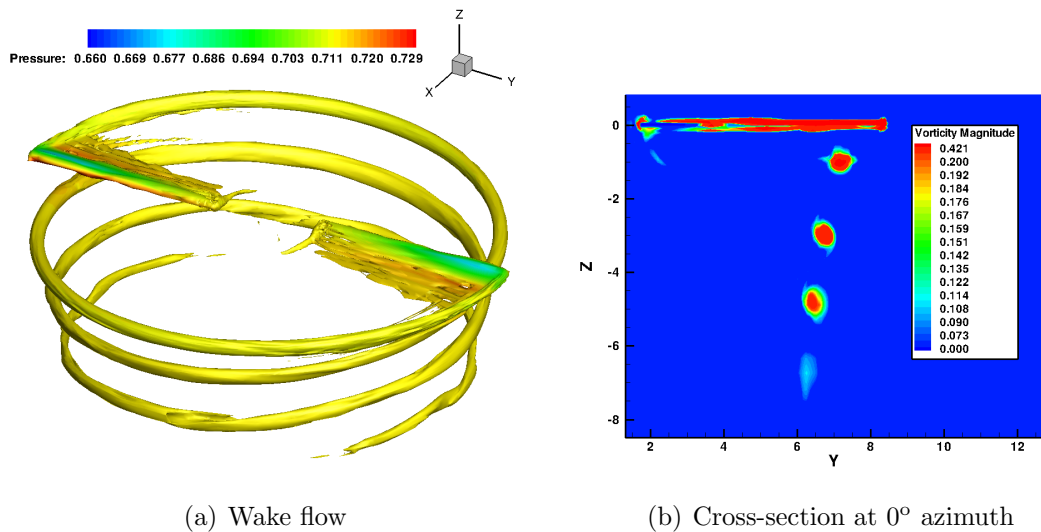
Figure 4.24: Wake flow-field for the Harrington rotor obtained with CRWENO5 scheme

Figures 4.22 – 4.24 show the helical tip vortices shed from the blades in the wake as well as a cross-section of wake at 0° azimuth after ten revolutions. The vorticity magnitude iso-surface, colored by the pressure, is shown in the figures on the left-hand side, while the cross-sectional vorticity magnitude contours are shown in the figures on the right-hand side. In the figures showing the cross-section of the

(a) MUSCL3
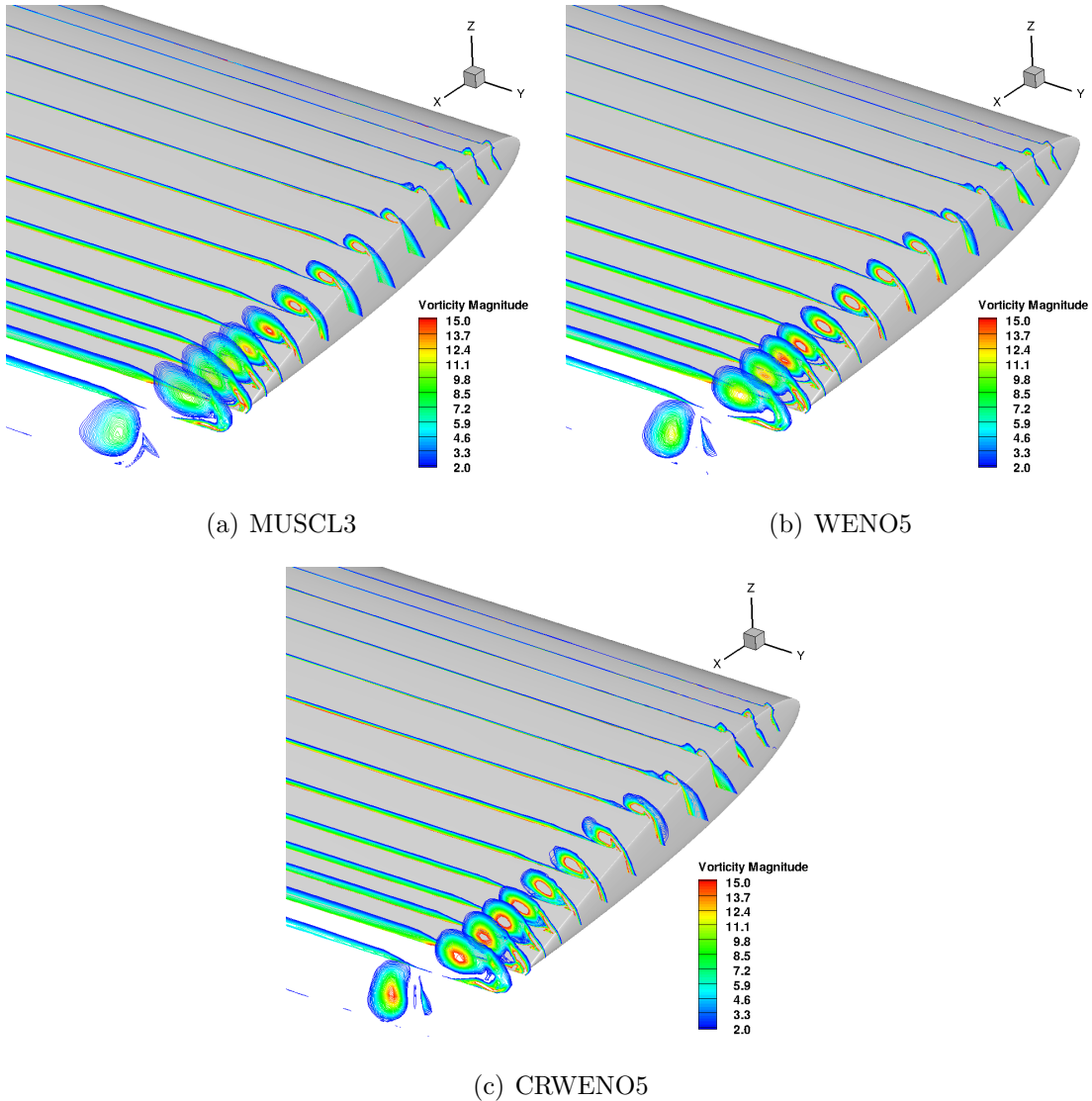
(b) WENO5

(c) CRWENO5

Figure 4.25: Comparison of the tip vortex for various numerical schemes

wake, the first vortex below the blade has a wake age of π radians, the second vortex has a wake age of 2π radians and so forth. It is observed that the CRWENO5 scheme shows a significant improvement in the preservation of the vortices as they convect through the domain. It is observed that the shape and strength of the tip vortex is preserved till a wake age of 3π in the solution obtained using the CRWENO5 scheme, while the vortex is significantly dissipated and distorted at this wake age

for the solution obtained with the MUSCL3 and WENO5 schemes.

Figure 4.25 shows the flow at the blade tip for the solutions obtained with the various schemes. The vorticity magnitude contours are shown at the various chordwise locations. The blade mesh is clustered at the tip to accurately capture the tip vortex. Although the tip vortex is captured with all the three schemes, the CRWENO5 scheme results in the formation of a stronger vortex and reduced smearing.

4.4   Direct Numerical Simulation of Compressible Turbulent Flows

Numerical simulation of compressible, turbulent flows requires the accurate resolution of small length scales characteristic of turbulent flows, as well as non-oscillatory behavior across shock waves and high-gradient shear layers. Non-compact, non-oscillatory schemes have been applied to such problems where the schemes are optimized for spectral resolution (at the cost of order of convergence) [50, 77, 78]. The application of compact schemes to such flows required hybrid schemes where the solution in the immediate vicinity of discontinuities is obtained using a non-compact ENO/WENO scheme [41, 43, 82]. This section demonstrates the performance of the CRWENO5 scheme for two canonical flows – decay of isotropic turbulence and the shock-turbulence interaction. The solutions are compared with the WENO5 scheme and the CRWENO5 scheme shows a significant improvement in the resolution of higher wavenumbers while maintaining the non-oscillatory nature of the WENO schemes. Thus, there is no special treatment of the solution around discontinuities

as is required in hybrid schemes, or a compromise in the order of accuracy and convergence.

4.4.1 Isotropic Turbulence Decay

The decay of three-dimensional, isotropic turbulence is a canonical flowfield that is representative of the small scales in turbulent flows. An initial energy spectrum of turbulent fluctuations is specified and the temporal decay involves a transfer of energy to smaller length scales. The flow is compressible for higher values of velocity fluctuations and thus, a non-oscillatory scheme is required to accurately capture the formation of shocklets. The initial condition is an incompressible flowfield consisting of random, isotropic velocity fluctuations that satisfy a prescribed energy spectrum [83, 84]. The domain is taken as a cube of edge length 2π with periodic boundaries and the initial velocity field is specified in the Fourier space as:

$$\hat{u}_i(\mathbf{k}) = \alpha e_i^1 + \beta e_i^2; \ i = 1, 2, 3 \tag{4.17}$$

where $\hat{u}_i$ is the Fourier transform of the velocity component u_i, and $\mathbf{e}^{1,2} = [e_1^{1,2}, e_2^{1,2}, e_3^{1,2}]^T$ are mutually orthogonal unit vectors that lie in the plane normal to the wavenumber vector $\mathbf{k}$. The complex coefficients α and β are given by:

$$\alpha = \left[\frac{E(k)}{4\pi k^2}\right] \exp(i\theta_1) \cos(\phi) \tag{4.18}$$

$$\beta = \left[\frac{E(k)}{4\pi k^2}\right] \exp(i\theta_2) \sin(\phi) \tag{4.19}$$
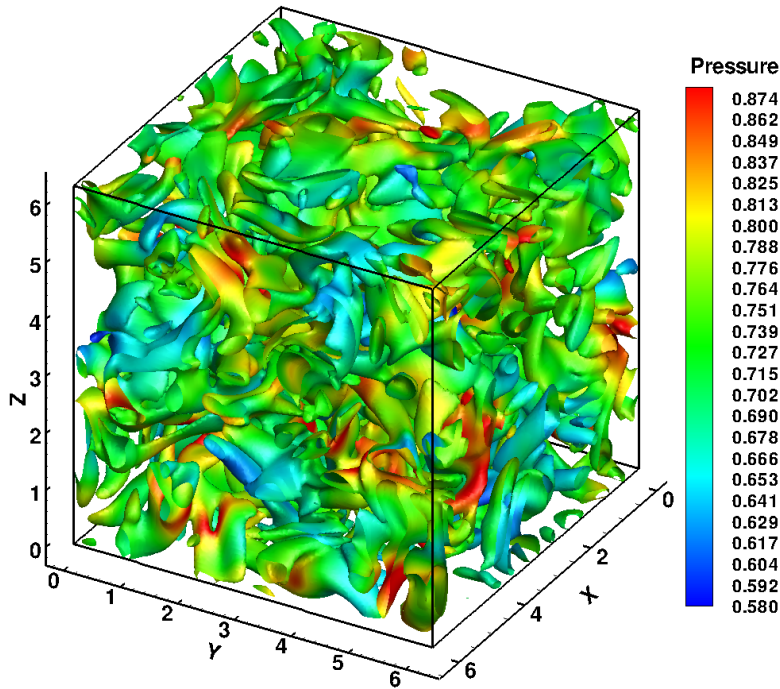
Figure 4.26: Isotropic turbulence decay – vorticity magnitude iso-surfaces colored by pressure

where $k = |\mathbf{k}|$ and θ_1, θ_2, ϕ are uniformly distributed random numbers in $[0, 2\pi]$.

The energy distribution of the fluctuations is prescribed in the present study as:

$$E(k) = 16\sqrt{\frac{2}{\pi}} \frac{u_0^2}{k_0} \left(\frac{k}{k_0}\right)^4 \exp\left[-2\left(\frac{k}{k_0}\right)^2\right] \tag{4.20}$$
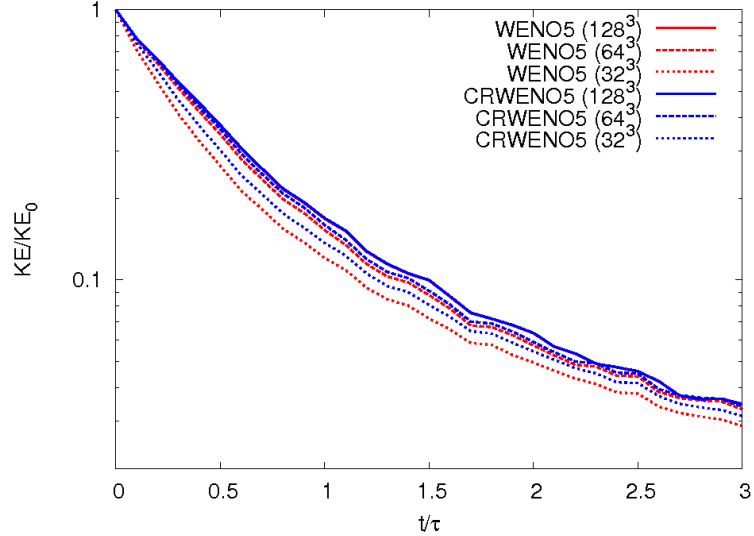
where u_0 is the RMS turbulence intensity and k_0 is the wavenumber corresponding to the highest energy [87]. This spectrum has the following properties:
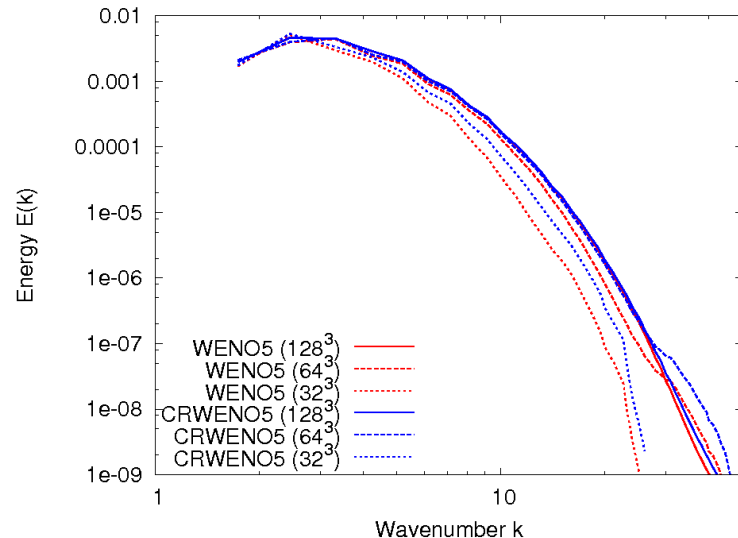
$$\text{Kinetic Energy}: KE = \frac{q^2}{2} = \int_0^\infty E(k)dk = \frac{3}{2}u_0^2 \tag{4.21}$$

$$\text{Taylor microscale Reynolds number}: Re_\lambda = \frac{u_0\lambda}{\nu} = 2\frac{u_0}{\nu k_0} \tag{4.22}$$

where ν is the kinematic viscosity and λ is the Taylor microscale. In the present study, the RMS turbulence intensity is taken as $u_0 = 0.3$ such that the resulting flow is compressible and the most energetic wavenumber is taken as $k_0 = 4$. Solutions

(a) Kinetic energy vs. time

(b) Energy Spectrum

Figure 4.27: Solution of isotropic turbulence decay at various grid resolutions are obtained at $Re_\lambda = 50$. The initial conditions are obtained by transforming the velocity fluctuations given by Eqn. (4.17) to the physical space and specifying constant density and pressure ($\rho = 1, p = 1/\gamma$) over the domain.

The solution is evolved till a final time of $t/\tau = 3.0$ where $\tau = \lambda/u_0$ is the turbulent time scale. The TVD-RK3 scheme is used to march the solution in time.

(a) 32^3 points

(b) 64^3 points
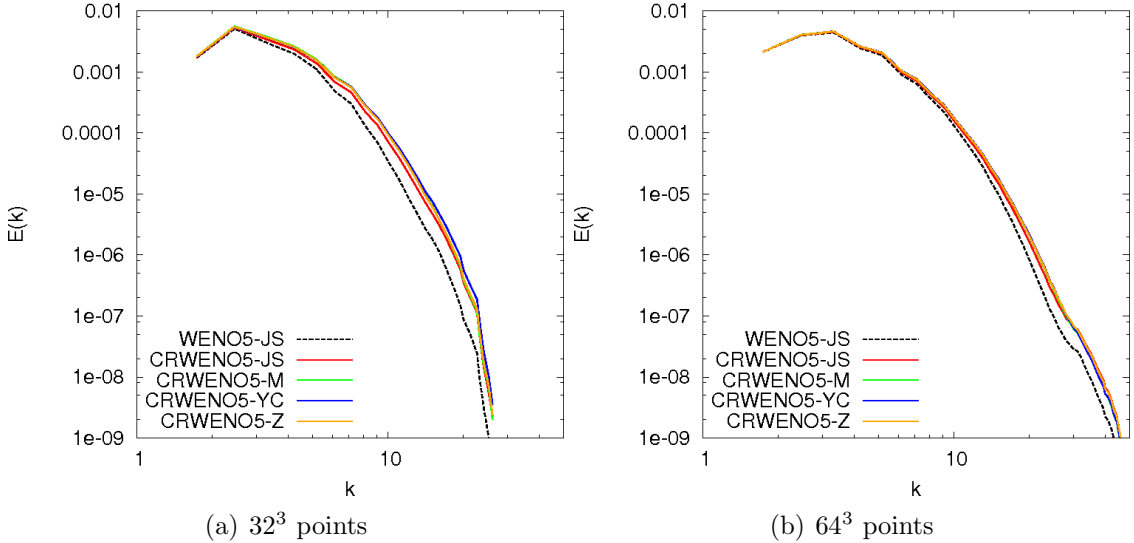
Figure 4.28: Solution of isotropic turbulence decay for the alternative formulations of the non-linear weights at two different grid resolutions

Figure 4.26 shows the solution obtained by the CRWENO5 scheme on a 128^3 grid at $t/\tau = 1$. The iso-surfaces of the vorticity magnitude are shown, colored by pressure. The decay of the kinetic energy (non-dimensionalized by the initial kinetic energy) is shown in Fig. 4.27(a) for the WENO5 and CRWENO5 schemes at three different grid resolutions – 32^3, 64^3 and 128^3. The CRWENO5 scheme shows significantly lower dissipation than the WENO5 scheme at grid resolutions of 32^3 and 64^3. The solution is well resolved on the grid with 128^3 points and the WENO5 and CRWENO5 schemes agree well with each other. Figure 4.27(b) shows the kinetic energy as a function of the wavenumber for the solution at $t/\tau = 1$. At lower grid resolutions, the CRWENO5 scheme shows an improved resolution of higher wavenumbers, compared to the WENO5 scheme. A grid-converged solution is obtained on the grid with 128^3 points, and the WENO5 and CRWENO5 schemes agree well.

The previous results are obtained with the non-linear weights as defined in [13] for both the WENO5 and CRWENO5 schemes. Section 2.7 and 3.5 discussed alternative formulations for the non-linear weights that improved their convergence to the optimal values. This resulted in an improved resolution across discontinuities and extrema. The solution to the decay of isotropic turbulence requires the accurate resolution of small length scales and thus, it is expected that the alternative formulations for the non-linear weights should improve the solution. Figure 4.28 shows the energy spectrum of the solution at $t/\tau = 1$ obtained with the WENO5-JS, CRWENO5-JS, and the CRWENO5 schemes with the alternative weights. Table 2.10 summarizes the various formulations of the non-linear weights and the corresponding CRWENO5 scheme. The alternative weights result in an improved resolution of the higher wavenumbers, compared to the CRWENO5-JS scheme. The difference is more visible for the solutions obtained on the coarse grid (32^3 points).

4.4.2   Shock-Turbulence Interactions

The interaction of a normal shock wave with an isotropic turbulent flowfield is representative of the interaction of shock waves with turbulent boundary layers, resulting in an amplification of the turbulence intensity downstream of the shock and a reduction of length scales. This canonical problem has been extensively studied [79, 80, 81, 82] (and references therein) through the development of linear analysis as well as direct numerical simulation. The performance of the CRWENO5 scheme is compared to that of the WENO5 scheme in this section.

The problem is solved in the reference frame of the shock wave. The domain is taken as $[-2\pi, 2\pi] \times [0, 2\pi] \times [0, 2\pi]$ and discretized with a uniform grid. The initial conditions consist of a stationary shock at $x = 0$ with $M_\infty = 2$, where M_∞ is the inflow Mach number. Uniform flow is specified upstream and downstream of the shock, with the upstream conditions as $\rho = 1$, $u = M_\infty$, $v, w = 0$ and $p = 1/\gamma$. Periodic boundary conditions are applied in the y and z directions. The outflow boundary at $x = 2\pi$ is treated with a sponge boundary condition: the domain is extended in the x-direction beyond $x = 2\pi$ and discretized with a grid that rapidly stretches in this direction (with uniform spacing in the y and z directions). This extension is referred to as the sponge zone henceforth. A sink term is added to the governing equations in the sponge zone in the form of $\sigma(\mathbf{u} - \mathbf{u}_{ps})$ where $\mathbf{u}_{ps}$ is the uniform post-shock flow and σ varies linearly from 0 at $x = 2\pi$ to 1 at the downstream end of the sponge zone. A combination of grid-stretching and the sink term is sufficient to damp out the fluctuations and avoid reflections from the outflow boundary [85, 86]. Characteristic-based outflow boundary conditions are applied at the downstream end of the sponge zone.

The inflow boundary conditions consist of a field of isotropic, turbulent fluctuations added to uniform, supersonic mean flow. The inflow turbulent fluctuations are generated from the solution to the decaying isotropic turbulence problem, discussed in the last section. Velocity fluctuations satisfying Eqn. (4.20) are added to a mean flow identical to flow conditions upstream of the shock and solved on a periodic domain of size $(2\pi)^3$. In the present study, $u_0 = 0.3$ and $k_0 = 4$ in Eqn.
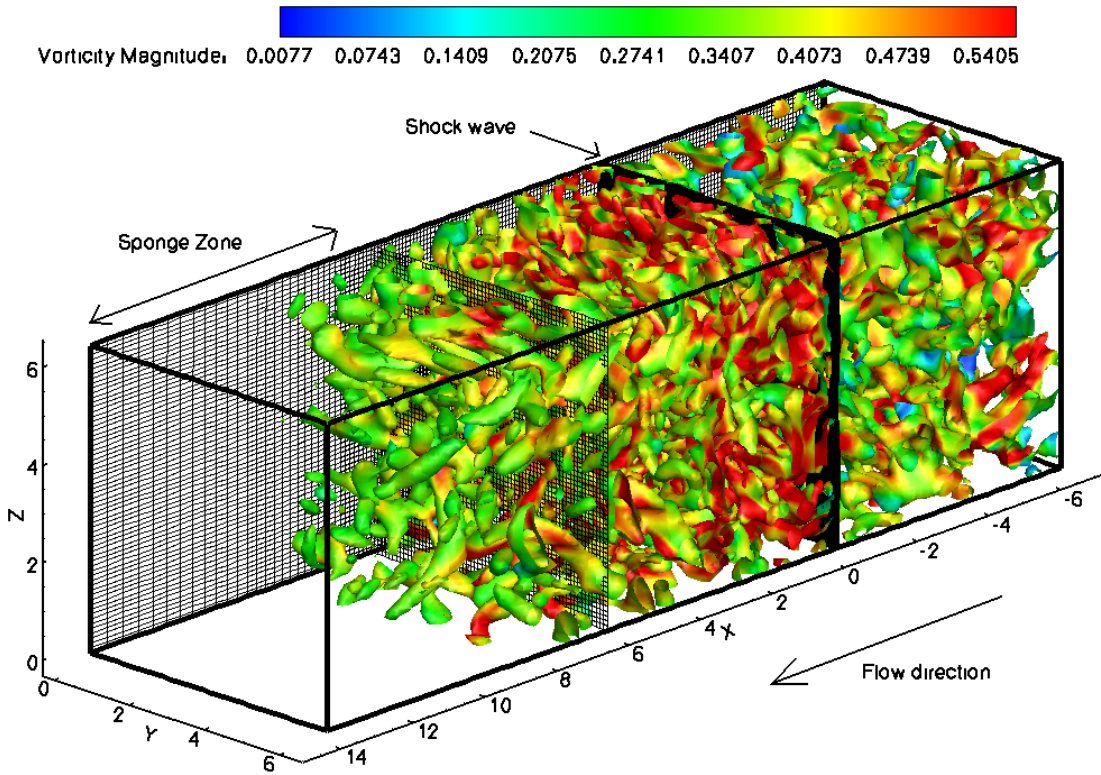
Figure 4.29: Solution of the shock-turbulence interaction problem obtained by the CRWENO5 on a $128 \times 64 \times 64$ grid: Iso-surfaces of the second invariant of the velocity gradient tensor colored by vorticity magnitude

(4.20). The decay of this turbulent flowfield is solved till $t/\tau = 1$ where τ is the turbulent time scale. The density, velocity and pressure fluctuations are extracted from the solution and transformed from the (x, y, z)-space to the (t, y, z)-space through $x = M_\infty t$. These fluctuations are then added to the uniform supersonic inflow. The unsteady, turbulent inflow is thus specified. A detailed description of this procedure is available in [87, 88]. It should be noted that the procedure described here results in a periodic inflow with a time period of $2\pi/M_\infty$. The procedure described in the references include a random "jitter" during each time period to remove this periodicity. Since the focus of the present study is the performance and comparison of
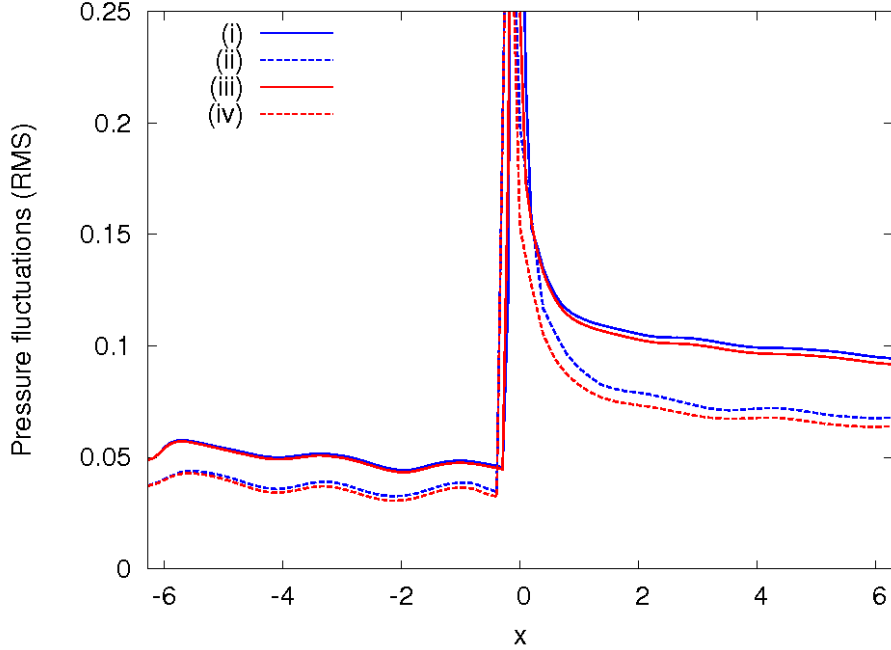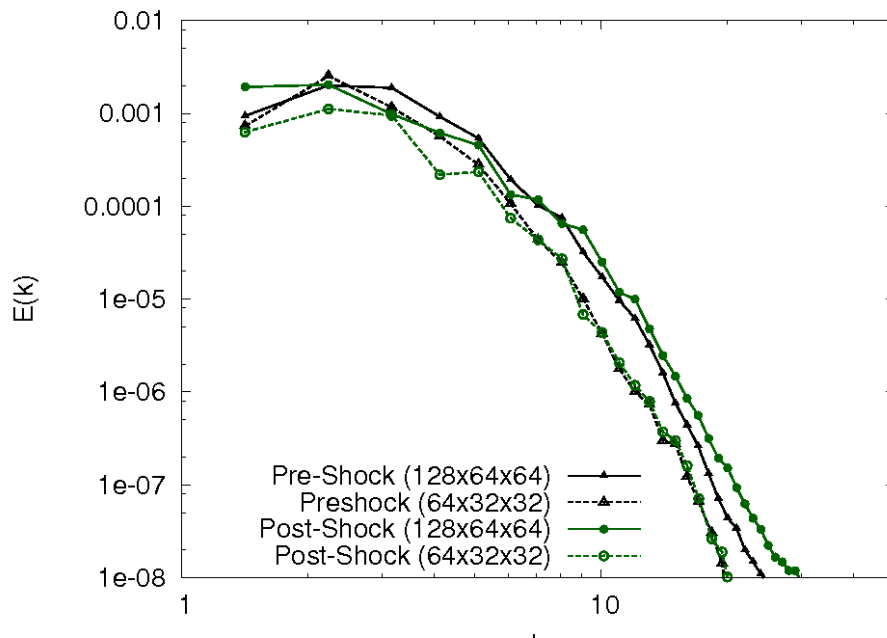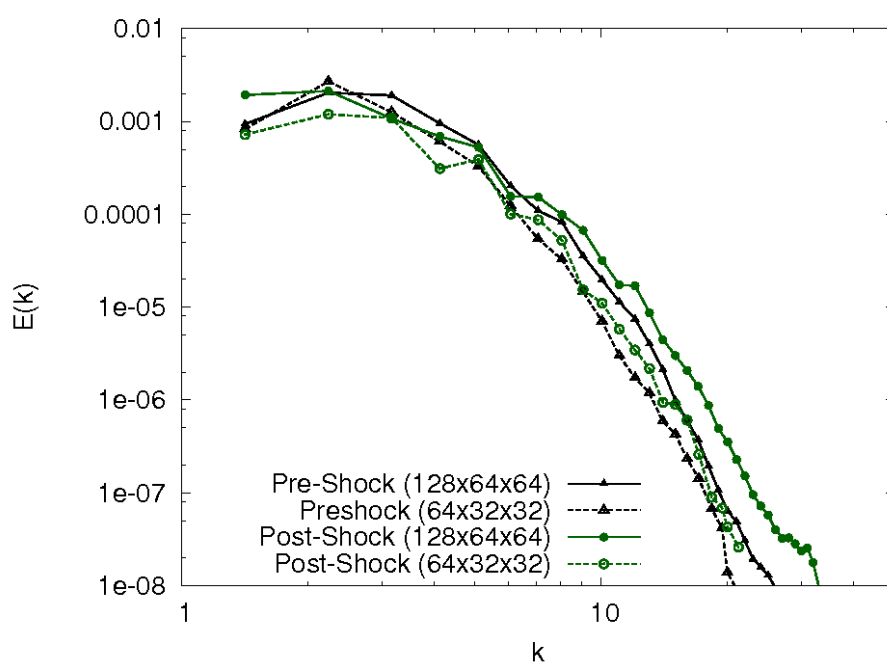
Figure 4.30: Streamwise RMS pressure fluctuations: (i) CRWENO5 ($128 \times 64 \times 64$ grid (ii) CRWENO5 ($64 \times 32 \times 32$ grid (iii) WENO5 ($128 \times 64 \times 64$ grid (iv) WENO5 ($64 \times 32 \times 32$ grid

numerical schemes and not the flow physics, the jitter is not used. However, the simulations are run for a large duration to ensure that statistically relevant quantities are obtained.

Solutions are obtained with the TVD-RK3 time-marching scheme on two grids – $64 \times 32 \times 32$ (with $16 \times 32 \times 32$ points in the sponge zone) and $128 \times 64 \times 64$ (with $32 \times 64 \times 64$ points in the sponge zone). The simulations are carried out at a Taylor microscale Reynolds number of $Re_\lambda = 50$. Figure 4.29 shows the solution obtained by the CRWENO5 scheme on the fine grid. The isosurfaces of the second invariant of the velocity gradient tensor are shown, colored by the vorticity magnitude. The figure also shows the $x - z$ cross-section of the mesh, especially the stretched mesh downstream of the domain of interest. It is observed that the turbulent fluctuations

(a) WENO5
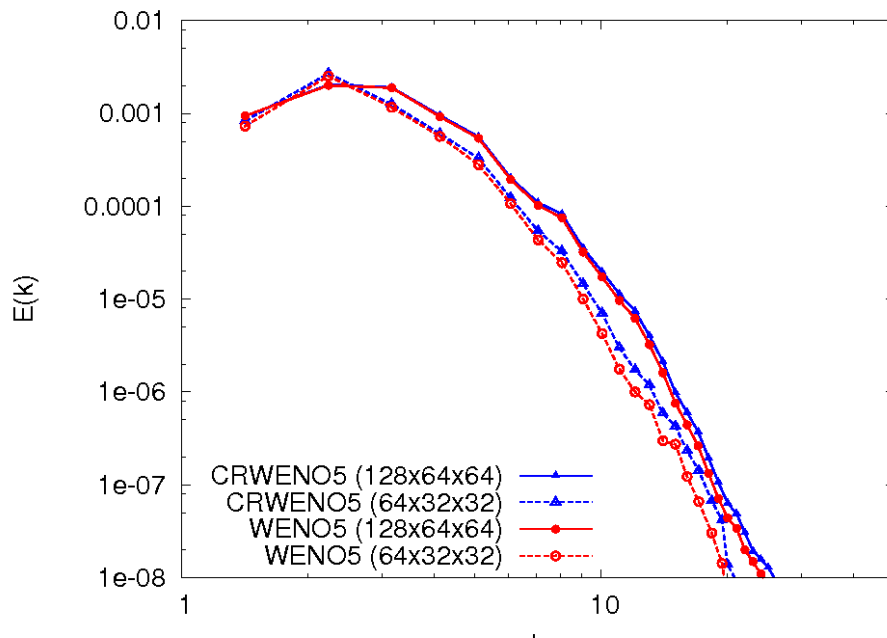
(b) CRWENO5

Figure 4.31: Pre- and post-shock energy spectra for the shock-turbulence interaction are damped out successfully in the sponge zone due to a combination of the grid-stretching and the sink term.
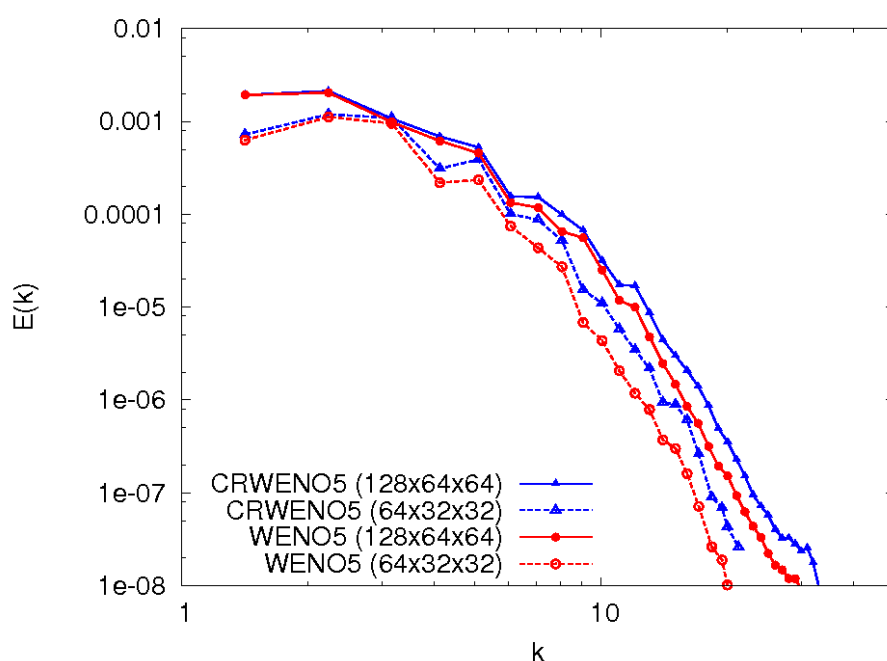
Figure 4.30 shows the streamwise variation of the pressure fluctuations (RMS) for the solutions obtained by the CRWENO5 and WENO5 schemes. Statistical quantities are calculated by averaging in time and homegeneity directions (y and z). Results are shown for the WENO5 and CRWENO5 schemes for both the grids. The interaction with the shock wave amplifies the turbulent fluctuations and this is observed for both the schemes. The solution obtained by the CRWENO5 scheme on the coarse grids predicts a higher magnitude of fluctuations as compared to the WENO5 scheme, especially downstream of the shock. The two schemes predict nearly identical levels of turbulence upstream of the shock for the fine grid. However, the CRWENO5 scheme predicts a marginally higher magnitude of the fluctuations downstream of the shock. These observations indicate that the CRWENO5 scheme is less dissipative for flow fluctuations characteristic of turbulent flows, as compared to the WENO5 scheme.

A comparison of the kinetic energy distribution with respect to the wavenumbers before and after the shock wave indicates the length scales that are amplified by the shock wave. Figure 4.31 shows the pre- and post-shock energy spectra for solutions obtained with the CRWENO5 and WENO5 schemes. The spectra are obtained for the fluctuations on stream-normal slices at $x = -1$ (pre-shock) and $x = 6$ (post-shock). Both schemes show an amplification of the smaller length scales on the fine grid, as is consistent with theoretical predictions [80]. However, on a coarse mesh, the CRWENO5 is able to capture the energy amplification at intermediate and high wavenumbers, but the WENO5 scheme yields solutions that do not show this amplification.

(a) Pre-shock

(b) Post-shock

Figure 4.32: Comparison of the energy spectra for solutions obtained by the WENO5 and CRWENO5 schemes

Figure 4.32 compares the solutions obtained by the WENO5 and CRWENO5

schemes on the two grids. At the pre-shock location (Fig. 4.32(a)), the energy spectra for the solutions obtained by the two schemes agree well for the fine grid. The CRWENO5 scheme shows an improved resolution of the intermediate and higher wavenumbers on the coarse grid. At the post-shock location (Fig. 4.32(b)), the CRWENO5 schemes shows an improvement on both grids, compared to the WENO5 scheme. The smaller length scales are less dissipated for solutions obtained with the CRWENO5 scheme.

4.5 Summary of Chapter

The numerical properties of the CRWENO schemes are analyzed and demonstrated on simplified systems in the previous chapters. This chapter discusses the integration of these schemes to a structured, finite-volume Navier-Stokes solver and the application to practical flow problems. The baseline algorithm solves the Navier-Stokes on curvi-linear, finite-volume meshes, including overset meshes with relative motion. Spatial reconstruction is carried out using the third-order MUSCL scheme and the fifth-order WENO scheme, both of which are non-compact. In addition to these, the fifth-order CRWENO scheme is added to the solver. Second-order central differences are used for the viscous terms. The TVD-RK3 time-marching scheme is used for simple domains while the implicit BDF2 scheme is used problems where the CFL criterion is too restrictive. Dual time-stepping is used with the BDF2 scheme for time-accurate problems. The algorithm includes the Spalart-Allmaras model with the RANS formulation for turbulent flows while direct numerical simulations

are possible by removing the turbulence model.

The CRWENO5 scheme is applied and validated on curvilinear meshes by solving the steady, turbulent flow around the RAE2822 airfoil. A good agreement with experimental results is observed. The scheme is also validated on overset meshes with relative motion by solving the unsteady flow around a pitching SC1095 airfoil in a wind tunnel. The solution-dependent weights treat the hole region inside overset meshes as a discontinuity since it contains non-physical flow values; and thus, the CRWENO5 scheme is successfully able to decouple the solution in the flow region from the hole region. Based on these validations, the scheme is applied to the low Reynolds number flow around the NACA0005 airfoil undergoing simultaneous pitching and plunging motion. This is representative of flapping-wing-based micro-air vehicles. A modified two-dimensional DDES approximation is used as the turbulence model and the CRWENO5 scheme results in significant improvements in the resolution of near-blade flow structures, and shed vortices in the wake.

The steady flow around the ONERA-M6 wing and the unsteady flow around the two-bladed Harrington rotor are solved to validate the scheme for three-dimensional flows and demonstrate its numerical properties. The integrated forces are validated with experimental data. The solutions obtained by the CRWENO5 scheme are compared to those obtained by the MUSCL3 and WENO5 schemes. In both cases, the CRWENO5 scheme is able to preserve the strength and structure of the tip vortices over large distances due to its lower numerical errors. This indicates that this scheme is well-suited for aerodynamic problems where a well-resolved solution of the flowfield is desired.

The high spectral resolution of the CRWENO5 scheme and its non-oscillatory nature make it suitable for direct numerical simulation of compressible, turbulent flows. Two canonical flow problems are considered – the decay of isotropic turbulence and the shock – turbulence interaction. The decay of an isotropic turbulent flowfield is characterized by a transfer of kinetic energy to smaller length scales. The solutions obtained by the CRWENO5 scheme are compared to those obtained by the WENO5 scheme. It is observed that the CRWENO5 scheme shows higher resolution and lower dissipation for the higher wavenumbers. Further improvements are observed in the resolution by using the alternative formulations for the non-linear weights. The interaction of a normal shock with an isotropic, turbulent flowfield is representative of the interaction of shock waves with turbulent boundary layers. The turbulence intensity is amplified across the shock wave and higher wavenumbers are energized through this interaction. Solutions obtained using the CRWENO5 scheme show lower dissipation of the turbulent fluctuations, especially at higher wavenumbers, compared to those obtained by the WENO5 scheme.

Chapter 5

Closure

Hyperbolic conservation laws govern many physical systems and the solutions often times involve a large range of length and time scales. The focus of this dissertation is on the development of a high-order spatial reconstruction scheme for problems involving a range of length scales. One such example is compressible, turbulent flows, which are governed by the Navier-Stokes equations. The numerical simulation of such problems requires the accurate modeling of small length-scales, as well as non-oscillatory behavior across discontinuities that are characteristic of hyperbolic PDEs. Compact interpolation schemes are known for their higher spectral resolution and the ability to resolve smaller length scales than non-compact schemes. In the presence of discontinuities, a modification is required to ensure non-oscillatory behavior. Several such schemes are presented in the literature that seek to construct non-oscillatory schemes with high spectral resolution.

The WENO schemes have been widely applied to the numerical solution of hyperbolic PDEs. Lower-order non-compact interpolation schemes are combined using solution-dependent weights such that the resulting scheme is higher-order accurate in smooth regions of the flow and non-oscillatory across discontinuities. Although high-order accurate WENO schemes have been constructed, they suffer from poor spectral resolution.

This dissertation introduces the CRWENO schemes that are constructed as solution-dependent combinations of lower-order compact interpolation schemes. The final scheme shares the non-oscillatory nature of the WENO scheme but has higher spectral resolution and lower dissipation and dispersion errors due to it being a compact scheme. The contributions and conclusions for this dissertation are presented in this chapter, as well as some indications for future research.

5.1   Summary and Conclusions

The numerical solution to a hyperbolic PDE using a conservative, finite-difference discretization is considered in this thesis. The CRWENO scheme is introduced for the high-order accurate, non-oscillatory reconstruction of the flux function at the grid interfaces. Fifth-order accurate CRWENO5 and CRWENO5-LD schemes are constructed in Section 2.2. Third-order compact interpolation schemes are identified at each interface and optimal weights are calculated such that the weighted sum is a fifth-order compact scheme. The weights are scaled by smoothness indicators that are identical to those of the WENO schemes. The final scheme is fifth-order accurate for smooth solutions, while across discontinuities, it yields non-oscillatory solutions. The smoothness-dependent non-linear weights go to zero for the constituent third-order schemes whose stencils contain discontinuous data. This results in a decoupling of the flux calculation across the discontinuity and spurious oscillations are avoided.

The numerical properties of the fifth-order compact schemes corresponding to

the non-linear CRWENO schemes are analyzed and compared to those of the non-compact scheme (that corresponds to the fifth-order WENO scheme). The leading error terms in the Taylor series expansion indicate that the compact schemes have dissipation and dispersion errors that are an order of magnitude lower than those of the non-compact scheme. The spectral properties of the schemes are analyzed by considering a periodic sinusoidal solution. The compact schemes have a higher bandwidth-resolving efficiency as well as lower dissipation for the wavenumbers that are resolved accurately.

The CRWENO schemes are applied to scalar conservation laws – the linear advection equation and the non-linear Burgers equation. Smooth and discontinuous solutions are considered to demonstrate the numerical properties of the schemes. The following observations and conclusions are made from the solutions to the scalar PDEs:

- The order of convergence and non-oscillatory behavior across discontinuites are verified for the CRWENO schemes, indicating that the non-linear WENO weights work well with the compact schemes.

- The absolute errors for the CRWENO5 and CRWENO5-LD are (1/10)th and (1/20)th, respectively, that of the WENO5 scheme for a smooth solution. This is consistent with the conclusions from the Taylor series analysis.

- The CRWENO5 and CRWENO5-LD schemes shows lower dissipation and phase errors at higher wavenumbers compared to the WENO5 scheme.

- Solutions obtained using the CRWENO schemes show reduced smearing of dis-

continuities and clipping of extrema. There is an improvement in the preservation of waveforms for large convection distances.

- Computational efficiency: The numerical cost of the CRWENO schemes is higher at the same grid refinement level due to the tridiagonal solution required at each iteration. However, the lower error imply that solutions with comparable errors can be obtained on a grid that is significantly coarser. Thus, the CRWENO schemes have a lower numerical cost when comparing solutions of the same accuracy.

In addition to the comparisons with the WENO5 scheme, the effects of alternative formulations for the non-linear weights are analyzed. The CRWENO5-JS scheme shows sub-optimal convergence for a smooth solution with critical points while the CRWENO5-M, CRWENO5-Z and CRWENO5-YC schemes recovered the optimal order of convergence. These alternative formulations for the weights significantly improved the resolution of discontinuities.

The extension of the CRWENO schemes to the Euler equations is presented in Chapter 3. The Euler equations govern the dynamics of inviscid flows and form a hyperbolic system of PDEs. The application of the CRWENO schemes to the primitive and conserved flow variables is trivial. In addition, the application to the characteristic-based reconstruction is discussed, which results in a block tridiagonal system of equations. Benchmark inviscid flow problems are solved and the following observations are made:

- The accuracy and order of convergence of the CRWENO schemes are veri-

fied for the system of equations for all three formulations – reconstruction of conserved, primitive and characteristic variables. The CRWENO5 and CRWENO5-LD schemes yield errors that are (1/10)th and (1/20)th that of the WENO5 scheme, respectively.

- The CRWENO schemes show a reduced smearing of shock waves and contact discontinuities. In particular, the CRWENO schemes show an improved resolution of small-length-scale density waves in the Shu-Osher problem due to the higher spectral resolution.

- The convection of an isentropic vortex over a large distance demonstrates the ability of the CRWENO schemes to preserve the vortex shape and strength for long-term convection.

- Computational efficiency: The CRWENO schemes are more efficient than the WENO scheme for the reconstruction of primitive and conserved variables. However, the reconstruction of characteristic variables requires the solution of a block tridiagonal system where the size of the block increases with the number of dimensions. Thus, a characteristic-based CRWENO scheme is less efficient than the WENO scheme.

The final observation indicates that the CRWENO schemes, in their present form, are not suitable for a characteristic-based reconstruction. Although the reconstruction of characteristic variables yield more robust solutions, reconstruction of primitive or conserved variables suffice for most practical applications involving viscous flows.

Finally, the CRWENO scheme is integrated with a structured, finite-volume Navier-Stokes solver for curvi-linear meshes and applied to flows with practical relevance (Chapter 4). The CRWENO5 scheme is applied to steady and unsteady flows around two-dimensional wings, and three-dimensions wings and rotors. The scheme is also applied to the direct numerical simulation of two canonical turbulent flows – the decay of isotropic turbulence and the shock-turbulence interaction. The spectral resolution of the numerical scheme is critical to model the energy transfer between the different length scales accurately. Comparisons are made with the non-compact fifth-order WENO scheme and third-order MUSCL scheme (with Koren's limiter). The following conclusions are drawn from the solutions:

- The CRWENO5 scheme is validated for curvi-linear and stretched meshes by solving the steady, turbulent, transonic flow around the RAE2822 airfoil.

- The CRWENO5 scheme is validated for a domain consisting of overset grids with relative motion. The unsteady flow over a pitching SC1095 airfoil in a wind tunnel is solved. Solutions on overset meshes require the partitioning of each mesh into field and hole points. The ability of the non-linear weights to decouple the solution in the field points from the non-physical solution in the hole points is verified.

- Lower-order schemes suffice for the accurate prediction of integrated airloads, for two-dimensional airfoils as well as three-dimensional wings and rotors. However, the CRWENO5 scheme shows an improved resolution of near-blade and wake flow features. The tip vortices shed from the wing or rotor convect

over large distances in the wake and the ability of the CRWENO5 scheme to preserve the strength and shape of these structures is demonstrated.

- The CRWENO5 scheme shows an improved resolution of the small length scales for both the isotropic turbulence decay and the shock-turbulence interaction. Solutions obtained by the CRWENO5 scheme predict higher turbulent intensities and a higher kinetic energy at high wavenumbers, compared to the WENO5 scheme.

Thus, to summarize, a high-resolution, non-oscillatory conservative compact differencing scheme is introduced in this dissertation. The numerical properties are assessed and verified for solutions to scalar conservation laws and the inviscid Euler equations. The scheme yields solutions with higher accuracy and resolution while maintaining non-oscillatory behavior across discontinuities. It is integrated into a finite-volume Navier-Stokes solver for curvilinear meshes and applied to practical flow problems. The scheme shows significant improvements in the resolution and preservation of flow features such as vortices and turbulent eddies. Based on the results presented in this dissertation, the CRWENO schemes can be considered as a robust, high-order accurate algorithm for the numerical simulation of compressible, turbulent flows.

5.2   Future Work

The CRWENO schemes, as presented in this dissertation, are observed to be robust and yield non-oscillatory, high-resolution solutions to practical problems.

However, there are some open questions that can be the subject of future research. Some possible algorithmic improvements are as follows:

- Convergence for steady airfoil: The application of the CRWENO5 scheme to the steady, turbulent flow around the RAE2822 airfoil is described in Section 4.3.1. Although the solution agrees well with experimental data, the residual does not converge beyond a couple of orders of magnitude. This behavior is also observed for the reconstruction of characteristic variables. One direction of future research is the improvement of convergence behavior for steady problems.

- Implementation of non-linear weights: The alternative formulations for the WENO weights and their effects on the solution are discussed in this dissertation in the context of the CRWENO schemes (Sections 2.7 and 3.5). Significant improvements are observed over the original formulation given by Jiang and Shu, including alleviation of ϵ-sensitivity and resolution of discontinuities and extrema. However, the author feels that there is scope for further improvement in the implementation of the WENO weights, especially to improve the convergence behavior across stationary shock waves and for steady flow around airfoils.

- Extension to non-uniform meshes: Several problems of practical relevance require the solution on a domain discretized by curvilinear meshes with non-uniform grid spacing. The schemes described in this dissertation are derived for a grid with uniform spacing. Although the scheme yields robust solutions

for curvilinear meshes, the order of accuracy and spectral resolution suffer. Thus, a significant gain in the resolution of the solution is expected from the derivation and implementation of the CRWENO schemes on non-uniform meshes.

- Derivation and implementation of a ninth-order CRWENO scheme: The CR-WENO5 scheme demonstrates that non-linear weights of the WENO schemes may be applied to compact interpolation schemes to yield non-oscillatory schemes with a high spectral resolution. Higher-order CRWENO schemes can be derived; however, increasing the order of convergence while maintaining the tridiagonal structure will not result in a significant increase in spectral resolution. A penta-diagonal ninth-order CRWENO scheme will significantly improve the spectral resolution as well as the accuracy and the order of convergence.

- Parallelization: Issues regarding the parallelization of the CRWENO schemes are not discussed in this thesis. Most of the solutions presented are obtained on a single processor. Solutions to three-dimensional flows presented in Sections 4.3.4 and 4.3.5 are obtained using a coarse-grain parallelization of the domain. The internal boundaries are treated similar to physical boundaries with the solution in ghost cells specified through exchange of information between processors. The medium and fine-grain parallel implementation of the CR-WENO schemes is expected to reduce the computational cost of the schemes. Although the reconstruction step requires tridiagonal solutions due to the im-

plicit nature of the scheme, the flux along each grid line in each dimension may be calculated independently. Thus, a substantial speed-up is possible by implementing a fine-grain parallel CRWENO scheme.

In addition to these, there are some applications where the CRWENO schemes can yield improved solutions:

- Flow around rotorcraft: Section 4.3.5 demonstrates the application of the CR-WENO5 scheme to the unsteady flow around the Harrington two-bladed rotor. An improvement is observed in the near-blade and wake flow features. Based on these results, the CRWENO5 scheme can be applied to the flow around a rotorcraft operating in ground effect. Solutions to such flows require the accurate preservation of the wake vortices as they interact with each other and the ground plane. Thus, a high-resolution scheme with minimal dissipation is required preserve the tip vortices as they convect in the wake. The CRWENO5 scheme can be used with vortex-tracking grids [89] to yield high-order accurate solutions.

- Immersed boundaries: The successful application of the CRWENO5 scheme to overset grids indicate their suitability (without major modifications) to domains involving immersed bodies. Solutions on such domains involve the partitioning of the domain into field points that are inside the flow and hole points that are inside the body, and the application of no-slip boundary conditions at appropriate interior points. This is similar to the procedure followed for overset grids. The validation of the CRWENO5 scheme for immersed bodies

would allow its application to a large number of flows, including flows around complete rotorcraft (wing and fuselage).

Bibliography

[1] R.J. Leveque, *Finite volume methods for hyperbolic problems* (Cambridge University Press, Cambridge, UK, 2002).

[2] C.B. Laney, *Computational gasdynamics* (Cambridge University Press, Cambridge, UK, 1998).

[3] C. Hirsch, *Numerical computation of internal and external flows*, Vols 1 and 2 (Wiley Publishers, 1988).

[4] S.K. Godunov, "A difference scheme for numerical computation of discontinuous solutions of equations of fluid dynamics," Mat. Sb. **47**, 271 (1959).

[5] P. Roe, "Approximate Riemann solvers, parameter vectors and difference schemes," J. Comput. Phys. **27**, 1 (1978).

[6] B. van Leer, "Towards the ultimate conservative difference scheme V. A second order sequel to Godunovs method," J. Comput. Phys. **32**, 101 (1979).

[7] A. Harten, "High resolution schemes for hyperbolic conservation laws," J. Comput. Phys. **49**, 357 (1983).

[8] P. Colella, P.R. Woodward, "The piecewise parabolic method (PPM) for gas dynamical simulations," J. Comput. Phys. **54**, 174 (1984).

[9] A. Harten, B. Engquist, S. Osher, S. Chakravarthy, "Uniformly high order essentially non-oscillatory schemes, III," J. Comput. Phys. **71** 231 (1987).

[10] C.-W. Shu, S. Osher, "Efficient implementation of essentially non-oscillatory shock capturing schemes," J. Comput. Phys. **77**, 439 (1988).

[11] C.-W. Shu, S. Osher, "Efficient implementation of essentially non-oscillatory shock capturing schemes, II," J. Comput. Phys. **83**, 32 (1989).

[12] X. Liu, S. Osher, T. Chan, "Weighted essentially non-oscillatory schemes," J. Comput. Phys. **115**, 200 (1994).

[13] G.-S. Jiang, C.-W. Shu, "Efficient implementation of weighted ENO schemes," J. Comput. Phys. **126**, 202 (1996).

[14] D.S. Balsara, C.-W. Shu, "Monotonicity preserving weighted essentially non-oscillatory schemes with increasingly high order of accuracy," J. Comput. Phys. **160**, 405 (2000).

[15] C.-W. Shu, *Essentially non-Oscillatory and weighted essentially non-Oscillatory schemes for hyperbolic conservation laws* (ICASE Report 97-65, 1997).

[16] A.K. Henrick, T.D. Aslam, J.M. Powers, "Mapped weighted essentially non-oscillatory schemes: Achieving optimal order near critical points," J. Comput. Phys. **207**, 542 (2005).

[17] R. Borges, M. Carmona, B. Costa, W.S. Don, "An improved weighted essentially non-oscillatory scheme for hyperbolic conservation laws," J. Comput. Phys. **227**, 3191 (2008).

[18] M. Castro, B. Costa, W.S. Don, "High order weighted essentially non-oscillatory WENO-Z schemes for hyperbolic conservation laws," J. Comput. Phys. **230**, 1766 (2011).

[19] N.K. Yamaleev, M.H. Carpenter, "Third-order energy stable WENO scheme," J. Comput. Phys. **228**, 3025 (2009).

[20] N.K. Yamaleev, M.H. Carpenter, "A systematic methodology for constructing high-order energy stable WENO schemes," J. Comput. Phys. **228**, 4248 (2009).

[21] A.A.I. Peer, M.Z. Dauhoo, M. Bhuruth, "A method for improving the performance of the WENO5 scheme near discontinuities," Appl. Math. Lett. **22**, 1730 (2009).

[22] C.-W. Shu, "High Order Weighted Essentially Nonoscillatory Schemes for Convection Dominated Problems," SIAM Rev. **51**(1), 82 (2009).

[23] D. Gottlieb and S.A. Orszag, *Numerical analysis of spectral methods* (SIAM, Philadelphia, 1977).

[24] C. Canuto, M.Y. Hussaini, A. Quarteroni and T.A. Zang, *Spectral methods in fluid dynamics* (Springer-Verlag, New York, 1987).

[25] S.K. Lele, "Compact finite difference schemes with spectral-like resolution," J. Comput. Phys. **103**, 16 (1992).

[26] E. Weinan, J.G. Liu, "Essentially compact schemes for unsteady viscous incompressible flows," J. Comput. Phys. **126**, 122 (1996).

[27] R.V. Wilson, A.Q. Demuren, M.H. Carpenter, *High-order compact schemes for numerical simulation of incompressible flows* (ICASE Report 98-13, 1998).

[28] A. Lerat, C. Corre, "A residual-based compact scheme for the compressible Navier-Stokes equations," J. Comput. Phys. **170** 642 (2001).

[29] J.A. Ekaterinaris, "Implicit, high-resolution compact schemes for gas dynamics and aeroacoustics," J. Comput. Phys. **156**, 272 (1999).

[30] T.K. Sengupta, G. Ganeriwal, S. De, "Analysis of central and upwind compact schemes," J. Comput. Phys. **192**, 677 (2003).

[31] J.S. Shang, "High-order compact-difference schemes for time-dependent Maxwell equations," J. Comput. Phys. **153**, 312 (1999).

[32] C. Lee, Y. Seo, "A new compact spectral scheme for turbulence simulations," J. Comput. Phys. **183**, 438 (2002).

[33] S. Nagarajan, S.K. Lele, J.H. Ferziger, "A robust high-order compact method for large eddy simulation," J. Comput. Phys. **191**, 392 (2003).

[34] D. Gaitonde, J.S. Shang, "Optimized compact-difference-based finite volume schemes for linear wave phenomena," J. Comput. Phys. **138**, 617 (1997).

[35] M.H. Kobayashi, "On a class of Padé finite volume methods," J. Comput. Phys. **156**, 137 (1999).

[36] L. Gamet, F. Ducros, F. Nicoud, T. Poinsot, "Compact finite difference schemes on non-uniform meshes. Application to direct numerical simulations of compressible flows," Int. J. Numer. Meth. Fluids **29**, 159 (1999).

[37] M.R. Visbal, D.V. Gaitonde, "On the use of higher-order finite-difference schemes on curvilinear and deforming meshes," J. Comput. Phys. **181**, 155 (2001).

[38] R.K. Shukla, X. Zhong, "Derivation of high-order compact finite difference schemes for non-uniform grid using polynomial interpolation," J. Comput. Phys. **204**, 404 (2005).

[39] B. Cockburn, C.-W. Shu, "Nonlinearly stable compact schemes for shock calculation," SIAM J. Numer. Anal. **31**, 607 (1994).

[40] H.C. Yee, "Explicit and implicit multidimensional compact high-resolution shock-capturing methods: formulation," J. Comput. Phys. **131**, 216 (1997).

[41] N.A. Adams, K. Shariff, "A high-resolution hybrid compact-ENO scheme for shock-turbulence interaction problems," J. Comput. Phys. **127**, 27 (1996).

[42] N.A. Adams, "Direct numerical simulation of turbulent compression ramp flow," Theor. Comput. Fluid Dyn. **12**, 109 (1998).

[43] S. Pirozzoli, "Conservative hybrid compact-WENO schemes for shock-turbulence interaction," J. Comput. Phys. **178**, 81 (2002).

[44] Y.-X. Ren, M. Liu, H. Zhang, "A characteristic-wise hybrid compact-WENO scheme for solving hyperbolic conservation laws," J. Comput. Phys. **192**, 365 (2003).

[45] X. Deng, H. Maekawa, "Compact high-order accurate nonlinear schemes," J. Comput. Phys. **130**, 77 (1997).

[46] X. Deng, H. Zhang, "Developing high order weighted compact nonlinear schemes," J. Comput. Phys. **165**, 22 (2000).

[47] S. Zhang, S. Jiang, C.-W. Shu, "Development of nonlinear weighted compact schemes with increasingly higher order accuracy," J. Comput. Phys. **227**, 7294 (2008).

[48] Z. Wang, G.P. Huang, "An essentially nonoscillatory high order Padé-type (ENO-Padé) scheme," J. Comput. Phys. **177**, 37 (2002).

[49] L. Jiang, H. Shan, C.Q. Liu, "Weighted compact scheme for shock capturing," Int. J. Comput. Fluid Dyn. **15**, 147 (2001).

[50] M.P. Martín, E.M. Taylor, M. Wu, V.G. Weirs, "A bandwidth-optimized WENO Scheme for the direct numerical simulation of compressible turbulence," J. Comput. Phys. **220**, 270 (2006).

[51] G.A. Sod, "A survey of several finite difference methods for systems of nonlinear hyperbolic conservation laws," J. Comput. Phys. **27**, 1 (1978).

[52] P.D. Lax, "Weak solutions of nonlinear hyperbolic equations and their numerical computation," Comm. Pure App. Math. **7**, 159 (1954).

[53] P. Woodward, P. Colella, "The numerical simulation of two-dimensional fluid flow with strong shocks," J. Comput. Phys. **54**, 115 (1984).

[54] O. Inoue, Y. Hattori, "Sound generation by shock vortex interactions," J. Fluid Mech. **380**, 81 (1999).

[55] S. Zhang, Y.T. Zhang, C.-W. Shu, "Multistage interaction of a shock wave and a strong vortex," Phys. Fluids **17** (11), Paper 116101 (2005).

[56] A. Chatterjee, S. Vijayaraj, "Multiple sound generation in interaction of shock wave with strong vortex," AIAA J. **46** (10), 2558 (2008).

[57] P. R. Spalart, S. R. Allmaras, "One-equation turbulence model for aerodynamic flows," Proceedings of the 30th AIAA Aerospace Sciences Meeting and Exhibit, Reno, NV, Jan 6-9 (1992).

[58] J. Dacles-Mariani, G. G. Zilliac, J. S. Chow, P. Bradshaw, "Numerical/experimental study of a wingtip vortex in the near field," AIAA J. **33** (9), 1561 (1995).

[59] S.M. Medida, J.D. Baeder, "Numerical prediction of static and dynamic stall phenomena using the $\gamma - \overline{Re_{\theta_t}}$ transition model," Proceedings of the 67th AHS Annual Forum, Virginia Beach, VA, May 3-5 (2011).

[60] B. Koren, "Upwind schemes, multigrid and defect correction for the steady Navier-Stokes equations," Proceedings of the 11th International Conference on Numerical Methods in Fluid Dynamics, Willamsburg, VA, (1988).

[61] R. Warming, R. Beam, "On the construction and application of implicit factored schemes for conservation laws", SIAM-AMS Proc. **11**, 85 (1978).

[62] T. Pulliam, D. Chaussee, "A diagonal form of an implicit approximate factorization algorithm," J. Comput. Phys. **39**, 347 (1981).

[63] A. Jameson, S. Yoon, "Lower-upper implicit schemes with multiple grids for Euler equations", AIAA J. **25** (7), 929 (1987).

[64] S. Yoon, A. Jameson, "Lower-upper symmetric-Gauss-Seidel method for the Euler and Navier-Stokes equations," AIAA J. **26** (9), 1025 (1988).

[65] T. Pulliam, "Time accuracy and the use of implicit methods," Proceedings of the 11th AIAA Computational Fluid Dynamics Conference, Orlando, FL, July 6-9 (1993).

[66] Y. Lee, J. D. Baeder, "Implicit hole cutting - A new approach to overset grid connectivity," Proceedings of the 16th AIAA Computational Fluid Dynamics Conference, Orlando, FL, June 23-26 (2003).

[67] G.R. Srinivasan, J.D. Baeder, "TURNS: A free-wake Euler/ Navier-Stokes numerical method for helicopter rotors," AIAA J. **31** (5), 959 (1993).

[68] V.K. Lakshminarayan, *Computational investigation of microscale coaxial rotor aerodynamics in hover, Ph.D. Dissertation, University of Maryland, College Park, MD (2009).*

[69] A. Rohde, "Eigenvalues and eigenvectors of the Euler equations in general geometries," Proceedings of the 15th AIAA Computational Fluid Dynamics Conference, Anaheim, CA, June 11-14 (2001).

[70] P.H. Cook, M.A. McDonald, M.C.P. Firmin, *Aerofoil RAE 2822 - Pressure distributions, and boundary layer and wake measurements* (Experimental Data Base for Computer Program Assessment, AGARD Report AR 138, 1979).

[71] S. Tatsumi, L. Martinelli, A. Jameson, "A new high resolution scheme for compressible flows past airfoil," AIAA Paper 95-0466 (1995).

[72] X. Su, D. Sasaki, K. Nakahashi, "Efficient implementation of WENO scheme on structured meshes", Proceedings of the 25th Computational Fluid Dynamics Symposium, Osaka, Japan, December 19-21 (2011).

[73] K.W. McAlister, S.L. Pucci, W.J. McCroskey, L.W. Carr, *An experimental study of dynamic stall on advanced airfoil sections*, Vol. 2 (NASA Technical Memorandum 84245, 1982).

[74] W. Yuan, R. Lee, E. Hoogkamp, M. Khalid, "Numerical and experimental simulations of flapping wings," Intl. J. Micro Air Vehicles **2** (3), 181 (2010).

[75] V. Schmitt, F. Charpin, *Pressure distributions on the ONERA-M6-wing at transonic Mach numbers* (Experimental Data Base for Computer Program Assessment, AGARD AR 138, 1979).

[76] R.D. Harrington, *Full-scale-tunnel investigation of the static-thrust performance of a coaxial helicopter rotor* (NACA-TN-2318, 1951).

[77] E.M. Taylor, M.P. Martn, "Stencil adaptation properties of a WENO scheme in direct numerical simulations of compressible turbulence," J. Sci. Comp. **30** (3), 533 (2007).

[78] C.K.W. Tam, J.C. Webb, "Dispersion-relation-preserving finite difference schemes for computational acoustics," J. Comput. Phys. **107**, 262 (1993).

[79] S. Lee, S.K. Lele, P. Moin, "Direct numerical simulation of isotropic turbulence interacting with a weak shock wave," J. Fluid Mech. **251**, 533 (1993).

[80] S. Lee, S. K. Lele, P. Moin, "Interaction of isotropic turbulence with shock waves: effect of shock strength," J. Fluid Mech. **340**, 255 (1997).

[81] K. Mahesh, S.K. Lele, P. Moin, "The influence of entropy fluctuations on the interaction of turbulence with a shock wave," J. Fluid Mech. **334**, 353 (1997).

[82] J. Larsson, S.K. Lele, "Direct numerical simulation of canonical shock/turbulence interaction," Phys. Fluids **21** (12), Paper 126101 (2009).

[83] R.S. Rogallo, *Numerical experiments in homogenous turbulence* (NASA Technical Memorandum 81315, 1981).

[84] N.N. Mansour, A.A. Wray, "Decay of isotropic turbulence at low Reynolds number," Phys. Fluids **6** (2), 808 (1994).

[85] T. Colonius, S. Lele, P. Moin, "Boundary conditions for direct computation of aerodynamic sound," AIAA J. **31**, 1574 (1993).

[86] J. B. Freund, "Proposed inflow/outflowboundary condition for direct computation of aerodynamic sound," AIAA J. **35**, 740 (1997).

[87] S. Lee, P. Moin, S.K. Lele, *Interaction of isotropic turbulence with a shock wave* (Report TF-52, Thermosciences Division, Department of Mechanical Engineering, Stanford University, 1992).

[88] K. Mahesh, P. Moin, S.K. Lele, *The interaction of a shock wave with a turbulent shear flow* (Report TF-69, Thermosciences Division, Department of Mechanical Engineering, Stanford University, 1996).

[89] V.K. Lakshminarayan, J.D. Baeder, T. Kalra, S. Thomas, "Methodological Improvements for Computational Study of Hovering Micro-Rotor in Ground Effect," Proceedings of the 20th AIAA Computational Fluid Dynamics Conference, Honolulu, HI, June 27-20 (2011).